Exploring root cell wall stiffness by nanoindentation in Arabidopsis thaliana under abiotic stress

Harinderbir KAUR

THÈSE

Pour obtenir le grade de

DOCTEUR DE L'UNIVERSITÉ GRENOBLE ALPES

École doctorale : CSV- Chimie et Sciences du Vivant
Spécialité : Biologie Structurale et Nanobiologie
Unité de recherche : Institut de Biologie Structurale

Exploration de la rigidité de la paroi cellulaire des racines par nanoindentation sous stress abiotique chez Arabidopsis thaliana.

Exploring root cell wall stiffness by nanoindentation in Arabidopsis thaliana under abiotic stress.

Présentée par :

Harinderbir KAUR

Direction de thèse :

Jean-Luc PELLEQUER — Directeur de thèse
Université Grenoble Alpes

Rapporteurs :

Valérie LEGUé
PROFESSEUR DES UNIVERSITES, Université Clermont Auvergne
Lorena REDONDO-MORATA
CHARGE DE RECHERCHE, INSERM

Thèse soutenue publiquement le **12 mai 2023**, devant le jury composé de :

Wim BURMEISTER PROFESSEUR DES UNIVERSITES, UGA	Examinateur, président
Daniel NAVAJAS PROFESSEUR, Universitat de Barcelona	Examinateur
Valérie LEGUé PROFESSEUR DES UNIVERSITES, Université Clermont Auvergne	Rapporteure
Lorena REDONDO-MORATA CHARGE DE RECHERCHE, INSERM	Rapporteure
Jean-Luc PELLEQUER INGENIEUR HDR, CEA	Directeur de thèse

In the memory of **AFM**

Dimension 3100.....

you will always live through our scientific work.

Acknowledgement

I would like to thank all the people who contributed to helping me achieve this research and accompanied its proper completion. I wish to express my deepest gratitude to my supervisor Dr. Jean-Luc Pellequer for believing in me, without whose contribution, this work would not have been possible. His undying optimism and continual encouragement motivated me every single day to accomplish this project. His friendly guidance throughout my PhD work has been invaluable, especially in teaching me the concept of trimechanic theory or discussing about the cell wall structure and mechanics. I am grateful for his immense patience and support during my tough times when I was sick for months.

I am grateful to the reviewers of my Ph.D. thesis Prof. Valérie Legué and Dr. Lorena Redondo-Morata who took out their precious time for being part of my Ph.D. committee while providing great comments. I am thankful to Prof. Daniel Navajas, who is 'hands down' the most well-established experienced researcher in the field of lung mechanics, for being part of my jury. A big thanks to Prof. Wim Burmeister for supporting this thesis and accepting being part of Ph.D. committee at the very last minute, thank you for saving the thesis crisis.

The gratitude continues with a special thanks to Jean-Marie Teulon who taught me to work with AFM. I would always look up to him during calibration related issues, which he always dealt with calm and patience. I am thankful for his knowledge, which he was always willing to patiently share.

I am particularly indebted to our collaborators from CEA Cadarache: Dr. Thierry Desnos and Dr. Christian Godon for having several discussions, unending support and guidance throughout this Ph.D. work. Thank you for always providing timely supply of seeds and other reagents without any delay whenever asked for. The exchanges we had over meetings, phone calls and e-mails were fruitful and none of the scientific publications could've been possible without you two. Thank you!!

A special thanks to Wendy for being a part of this project. You're an inspiration to me, being a woman, a researcher, I relate myself to you. Grateful for your contribution towards identifying issues and problems with indentation fitting of the force curves and solving it. You saved this project with your intellectual mindset and immense research study. It would have never been accomplished if it wasn't you.

I am grateful for being a part of Phys2Biomed ITN network, headed by Prof. Alessandro Podesta and managed by Antonia. It was always a great pleasure to be a part of a remarkable research network. My secondments helped me in improving my scientific skills while complimenting my Ph.D. work. I am thankful to Prof. Manfred Radmacher whose challenging questions motivated me to further improve my protocol while looking for all the answers during my one-month, pre-COVID, secondment at Bremen University. I am thankful to Dr. Felix Rico for accommodating/welcoming me for almost three months in his lab in Marseille and letting me perform indentation experiments independently on their AFM instrument. My Marseille secondment would have been incomplete without the co-operation from LGBP Lab

and their head Dr. Ben Field to whom I am thankful for providing access to their facilities to grow my plants for indentation experiments. I thank Dr. Nuria Gavara for hosting my one month secondment at Barcelona University where I learned decellularization of plants from one of her students and my friend Dr. Maria Leonor Narciso with whom I enjoyed working with. I am thankful to Dr. Kevin Bielawski and Massimiliano Berardi for hosting me at O11 Amsterdam and taking time out of their busy schedules for supporting my research work and helping with long-time consuming experiments.

A special thanks to my CSI committee, Dr. Claude Verdier at LiPhy Grenoble, Dr. Chloe Zubieta at CEA Grenoble and Dr. Arnaud Millet at INSERM Grenoble, for taking the time every year, reading my report and providing encouraging remarks. My last CSI was impromptu, but still you all supported me without any hesitation.

I acknowledge Ms. Christine Lancelon-pin of CERMAV-CNRS lab for helping with ESEM images of plant roots. I am also thankful to Dr. Christine Moriscot and Benoit Gallet from MEM group for teaching me preparing TEM samples of plant roots and in imaging of root slices by TEM.

A big thanks to Olivia Ravet for helping me with all my missions for the entire duration and taking care of all the administrative work during my sick leave.

A warm expression of thanks to my Grenoble family Dr. Shifali Singh, Dr. Vaibhav Jaiswal, Dr. Ranjana Yadav, Kunwar Amit Singh, Antik Ghosh, Smita Morade, Abhishek Mahajan, Mayur Mangukiya and Jijo Joseph Thanolil for always being around. I will always cherish the bond I shared with all of you. Robin, your constant support and encouragement kept me going on even on the darkest days. Thank you for always being there, believing in me when I didn't believe in myself, for always being proud of me.

To the three pillars of my existence in this world: I would like to thank my mom and dad who supported me in every possible manner and made sure that I performed well at all times. I'm grateful to my sister who encouraged me at all times and took care of me like my mother after my surgery, for loving me limitless. Thank you all for constantly pushing me to fly high, reaching out for sky.

Finally, I must acknowledge the financial support from European Union's Horizon 2020 research and innovation programme under the Marie Skłodowska-Curie grant agreement No 812772, Project Phys2BioMed and ANR project BioPhyt -18-CE20-0023-03.

Summary

Life on earth would not be possible without plants. Human activities have resulted in Global warming with climate change affecting the plant health. Use of excessive fertilizers and insecticides leads to degradation of soil quality. Plant roots are the first one to detect changes in soil composition and react accordingly. One of the most common causes of soil degradation is phosphate deficiency and acidic nature of the soil, causing metal solubilization, resulting in root growth inhibition and decrease in crop production.

The phenomenon of root growth inhibition is widely studied in the presence of iron and aluminum. However, little is known about the mechanics involved in root growth inhibition in presence of metals. Our work aims at quantifying the change of the nanomechanical response of living plant roots in presence of metals. In particular, we are interested in the relationship between the root growth arrest phenotype and a possible change in the stiffness of the external primary cell wall of the transition zone of *Arabidopsis thaliana* root.

In this research work, we established a robust experimental protocol to measure the external primary cell wall of Arabidopsis using nanoindentation experiments with atomic force microscopy (AFM). Force-distance curves are the output of vertical nanoindentation experiments by an AFM cantilever. A contact-based mechanical model (Sneddon for axisymmetric AFM tip) was applied to extract the elastic modulus (Young's modulus) from force-distance curves.

A significant part of this work focused on obtaining a robust protocol that introduces minimum impact from external factors such as root growth, root immobilization, or root nanoindentation. With this protocol, we analyzed iron or aluminum stress at different concentrations, plant root stiffness, and plant root growth. In our experimental conditions, results revealed that in a low concentration of iron and aluminum ($\leq$ 10 µM), no effect on the root growth and on the stiffness was observed. However, at high concentration (> 10 µM and $\leq$ 20 µM) of Fe or Al, higher stiffness values are observed, but without a detectable root growth arrest. Root growth arrest is determined by measuring the length of plant roots. Surprisingly, when both the metals (Fe and Al) are combined at 10 µM each, a large cell wall stiffness is observed concomitantly with a total root growth arrest. The major change in the observed phenotype when Al is present with Fe suggested that malate could be involved in the observed effect. Thus, we measured the stiffness change in Arabidopsis mutant (*almt1*) deficient in malate exudation. In the same experimental conditions as wild type, the combined presence of Fe and Al did not alter the cell wall stiffness and no root growth inhibition was observed.

All these observations helped us to present a speculative model where the change in stiffness of the external primary cell wall has a double origin. First, in presence of sufficient individual metals (10-20 µM), the accumulation of highly charged Fe^{3+} and Al^{3+} bind to negatively charged pectin. Such a binding induces a change in pectin stiffness. Second, in the presence of both Fe and Al, the exudation of malate caused by the presence of Al increases the accumulation of Fe^{3+} in the apoplast, which in turn activate a redox-couple response, such as reactive oxygen species, that triggers a root growth arrest, with an increase in cell wall stiffness. These results are also supported by a change in cell wall deformability as determined by the recently developed trimechanic theory.

Resumé de la thèse

Les activités humaines provoquent un changement climatique qui affectent entre autre la santé des plantes ainsi qu'une dégradation de la qualité du sol. Les racines des plantes sont les premières à détecter les changements dans la composition du sol et à réagir en conséquence. L'une des causes les plus courantes de la dégradation des sols est la carence en phosphate et la nature acide du sol, qui entraînent la solubilisation des métaux, ce qui a pour conséquence l'inhibition de la croissance des racines et la diminution de la production agricole. Le phénomène d'inhibition de la croissance des racines est largement étudié en présence de fer et d'aluminium. Cependant, les aspects mécaniques impliqués dans l'inhibition de la croissance des racines en présence de métaux sont peu connus. Notre travail vise à quantifier le changement de la réponse nanomécanique des racines de plantes vivantes en présence de métaux. En particulier, nous nous intéressons à la relation entre le phénotype d'arrêt de la croissance des racines et un changement possible de la rigidité de la paroi cellulaire primaire externe de la zone de transition de la racine d'*Arabidopsis thaliana*.

Dans ce travail de recherche, nous avons établi un protocole expérimental robuste pour mesurer la paroi cellulaire primaire externe d'Arabidopsis en utilisant des expériences de nanoindentation avec la microscopie à force atomique (AFM). Les courbes force-distance sont le résultat d'expériences de nanoindentation verticale par un levier AFM. Un modèle mécanique basé sur le contact (Sneddon pour une pointe AFM axisymétrique) a été appliqué pour extraire le module élastique (module d'Young) des courbes force-distance.

Une partie importante de ce travail s'est concentrée sur l'obtention d'un protocole robuste qui nous a permis d'analyser l'impact du fer ou de l'aluminium à différentes concentrations, la rigidité de la racine de la plante et la croissance de la racine de la plante. Dans nos conditions expérimentales, les résultats ont révélé qu'à une faible concentration de fer et d'aluminium ($\leq$10 µM), aucun effet sur la croissance et la rigidité des racines n'a été observé. Cependant, à des concentrations élevées (>10 µM et $\leq$20 µM) de Fe ou d'Al, des valeurs de rigidité plus élevées sont observées, mais sans arrêt détectable de la croissance des racines. De manière surprenante, lorsque les deux métaux (Fe et Al) sont combinés à 10 µM chacun, une grande rigidité de la paroi cellulaire est observée en même temps qu'un arrêt total de la croissance des racines. Le changement majeur dans le phénotype observé lorsque l'Al est présent avec le Fe suggère que le malate pourrait être impliqué dans l'effet observé. Nous avons donc mesuré le changement de rigidité chez un mutant d'Arabidopsis (*almt1*) déficient dans l'exsudation du malate. Dans les mêmes conditions expérimentales que le type sauvage (10 µM), la présence combinée de Fe et d'Al n'a pas modifié la rigidité de la paroi cellulaire et aucune inhibition de la croissance des racines n'a été observée. Toutes ces observations nous ont permis de présenter un modèle spéculatif dans lequel le changement de rigidité de la paroi cellulaire primaire externe a une double origine. Premièrement, en présence d'une quantité suffisante de métaux individuels (10-20 µM), l'accumulation de Fe^{3+} et Al^{3+} hautement chargés se lie à la pectine chargée négativement. Cette liaison induit une modification de la rigidité de la pectine. Deuxièmement, en présence de Fe et d'Al, l'exsudation de malate causée par la présence d'Al augmente l'accumulation de Fe^{3+} dans l'apoplaste, qui à son tour active une réponse redox, telle que les espèces réactives de l'oxygène qui déclenche un arrêt de la croissance de la racine, avec une augmentation de la rigidité de la paroi cellulaire. Ces résultats sont également étayés par une modification de la déformabilité de la paroi cellulaire, déterminée par la théorie trimécanique récemment développée.

Contents

List of figures

Figures 1-5, 1-8, 1-9, 1-10, 1-22, 1-23, 2-13, 3-12, 3-14, 3-15, 3-17, 3-18, 3-19, 3-20 were designed by Harinderbir Kaur.

Figures 2-8, 2-9 were designed by Jean-Luc Pellequer.

Figures 5-2 was designed by Christian Godon.

List of tables

Abbreviations

3PCS: Three Parallel-Connected Spring

AFM: Atomic Force Microscopy

ALMT1: ALUMINIUM ACTIVATED MALATE TRANSPORTER 1

AT: Arabidopsis thaliana

ATP: Adenosine triphosphate

CEA: Commissariat à l'énergie atomique et aux énergies alternatives

CERMAV: "Centre de recherches sur les macromolécules végétales » Grenoble

CFW: Calcofluor White

CP: Contact Point

CW: Cell Wall

D3100: Dimension 3100 AFM

DAPI: 4',6-diamidino-2-phenylindole

DMT: Derjaguin, Muller, & Toporov model

Dx: cantilever deflection (m)

DZj: Indentation depth of zone j

Ê: Effective Young's modulus

EBM : Equipe "Environnement, Bioénergies, Microalgues et Plantes » Cadarache

EGTA: ethylene glycol-bis(β-aminoethyl ether)-N,N,N',N'-tetraacetic acid

ESEM: Environmental Scanning Electron Microscopy

EtOH: Ethanol

EZ: Elongation Zone

F: Force (N)

FD: Force Distance

FDC: Force Distance Curve

FeXAlY: X µM of Fe and Y µM of Al

GA: Glutaraldehyde

GRP: Glycine-rich protein

HEPES: N-(2-Hydroxyethyl)piperazine-N'-(2-ethanesulfonic acid)

HG: homogalactorunan

HRGP: Hydroxyproline-rich glycoprotein

IBS : « Institut de Biologie Structurale » Grenoble

ICP-MS: Inductively Coupled Plasma Mass Spectrometry

ITN: Innovative Training Network (EU Programme)

JKR: Johnson, Kendall, & Roberts model

JPK: AFM instrument provider

k: spring constant (N/m)

$K_{C,j}$: Spring constant of the Fc force of depth-zone j

$k_{T,j}$: stiffness measure for the material indented through the depth-zone j

LAI : « Laboratoire Adhésion et Inflammation » Marseille

LPR1: LOW PHOSPHATE ROOT1

LR: Lateral Root

NWX: Nanowizard version X

PCW: Primary Cell Wall

PDMS: Polydimethylsiloxane

PDR2: PHOSPHATE DEFICIENCY RESPONSE 2

PE: Poly-Ethylene

PFA: paraformaldehyde

PHEM: Buffer made of PIPES, HEPES, EGTA

-Pi : absence of additional Pi

Pi : Inorganic Phosphate

PI: Propidium Iodide

PIPES: piperazine-N,N'-bis(2-ethanesulfonic acid)

PLA: Poly-Lactic Acid

PNP: Pyrex-Nitride Probe

PR: Primary Root

PSA: Pressure Sensitive Adhesive

RAM: Root Apical Meristem

REA: Root Extension Arrest

RGA : Root Growth Arrest

RGI: rhamnogalacturonan I

RGII: rhamnogalacturonan II

ROS: Reactive Oxygen Species

$r_{S,j}$: relative strength of tip-shape nanomechanics

RSA: Root Structure Architecture

RT: Room Temperature

S: Sensitivity of photodiode (V/m)

SAM: Shoot Apical Meristem

SCN: Stem Cell Niche

SCW: Secondary Cell Wall

SD: Standard Deviation

SDC: Sodium Deoxycholate

SDS: Sodium Dodecyl Sulfate

SEM: Scanning Electron Microscopy

SNAP: Standardize Nanomechanical Afm Procedure

SPM: Scanning Probe Microscopy

STOP1: SENSITIVE TO PROTON RHIZOTOXICITY1

TEM: Transmission Electron Microscopy

TRIS: 2-Amino-2-(hydroxymethyl)propane-1,3-diol

UB : « Universitat de Barcelona »

WT: Wild Type

Z_1: First indentation zone

INTRODUCTION TO PLANT BIOMECHANICS AND IMPACT OF METALS ON THEM.

1 Introduction

Our research interest dealt with measuring mechanical properties on the roots of Arabidopsis. Before introducing the root structure or cell wall of *Arabidopsis thaliana*, let me first present you to the nanomechanical properties, which were incorporated in this work based on Atomic force microscopy.

1.1 AFM and contact mechanics

Mechanics serves as an important regulator on how tissue homeostasis is achieved and maintained (Ayad, Kaushik, and Weaver 2019). Elasticity of the extracellular matrix influence the changes in the mechanical properties of the cell. Changes in the mechanical properties of the cell or tissue lead to various pathologies and diseases (Lekka et al. 1999). While there are several methods to characterize cell or tissue mechanics such as micropipette aspiration (Hochmuth 2000), optical tweezers (Zhang and Liu 2008), deformability cytometry (Otto et al. 2015), Brillouin microscopy (Prevedel et al. 2019), Atomic force microscopy (AFM) probe indentation has one of the most versatile approaches allowing high-accuracy measurements of forces and deformations (Krieg et al. 2019). AFM probably has the widest contribution to cell biology and its mechanics (Sokolov, Dokukin, and Guz 2013; Kilpatrick, Revenko, and Rodriguez 2015; Gavara 2017; Chen et al. 2023).

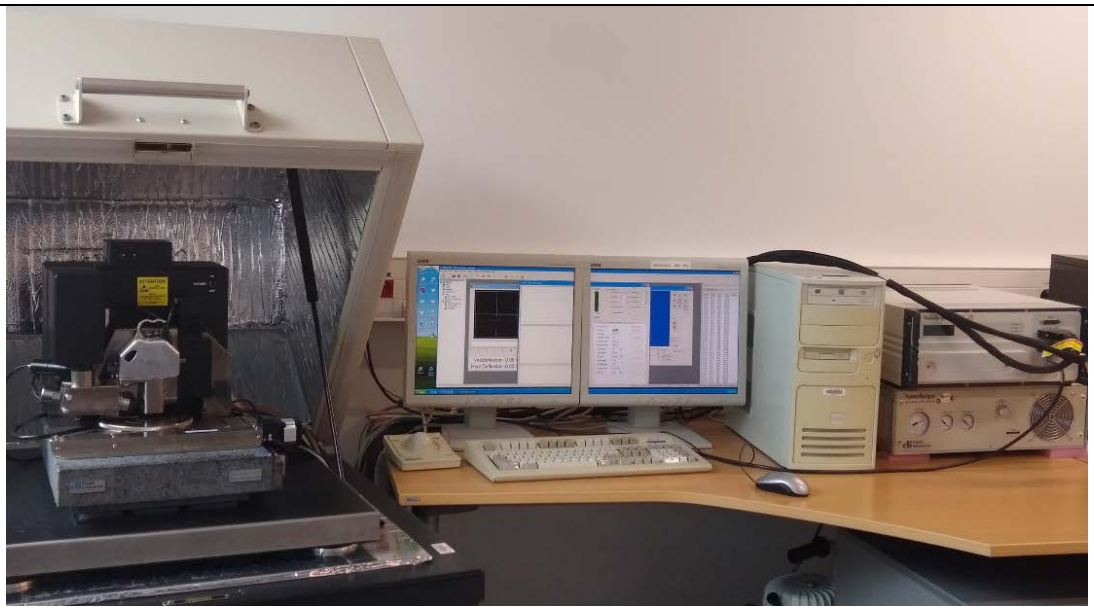

Figure 1-1: Complete Veeco Dimension 3100 AFM used in our study.
The system is composed of three components: the AFM head with the piezo systems (on the left), the AFM controllers (on the right), and the computer system that runs the instrument. A compressor below the table is used to maintain the anti-vibration table beneath the AFM head system.

Atomic Force Microscope was invented by IBM scientists in 1986 (Binnig, Quate, and Gerber 1986) which is a derivative of the scanning tunneling microscope designed in the early eighties (Binnig et al. 1982). AFM belongs to the scanning probe microscopy (SPM) family. It has the ability to demonstrate resolution of fractions of a nanometer, which is 1000 times better than the optical diffraction limit. The information is acquired by "feeling" or "touching" the surface with a mechanical probe. Piezoelectric elements facilitate accurate and precise movements, enabling a precise scanning. Very conveniently, AFM uses the same principle to perform surface imaging, receptor-ligand interactions, and surface indentations (Figure 1-1). In addition to that, AFM is capable of working in liquid medium with high spatial and force resolutions, which lead to its great potential to study soft biological samples under physiological conditions (Sirghi et al. 2008).

1.1.1 Principle of AFM and instrumentation

Fundamentally, AFM works on the basis of feeling the surface with a mechanical probe. This mechanical probe is called cantilever, which is attached to the piezo scanner. Although tipless cantilever exist, usually cantilevers have a sharp tip beneath their free end, which is generally made of silicon/silicon nitride. The size and shape of the tip determines the experiment. For imaging, very sharp tip of a few nanometer radius are preferred (Pyne and Hoogenboom 2016) whereas for unbinding (force spectroscopy) experiments, a larger tip of several 10s of nm is preferred (Teulon et al. 2011). When this tip is brought closer to the sample surface, the attractive/repulsive forces between the sample and the tip leads to the deflection of the cantilever towards/away from the surface. This deflection is translated according to the Hooke's law (Eq.1) that establishes the relationship between the force which is directly proportional to the deflection sensitivity measured in m/V and the deflection (in V) (Mueller 2016). This principle is applied to all modes of AFM.

$F = k * S * \Delta x$ …… (Eq.1)

where: F = Force [N], k = Cantilever specific spring constant [N/m], S = Sensitivity of the position-sensitive photodetector [m/V], Δx = Deflection [V].

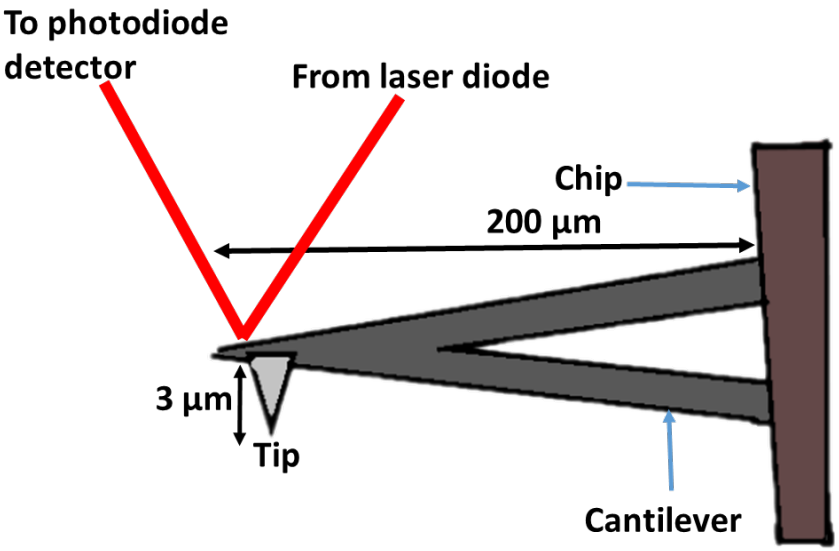

Figure 1-2: AFM indentation probe with red lines depicting laser deflection.
The black arrow show the measurement of PNP tip, which has been used in our experiments. Drawn not to scale.

The chip of the cantilever is attached to the piezoelectric scanner, which allows the precise positioning of the cantilever in the vertical direction (z-axis). Changes in the cantilever deflection are actually measured by a laser beam, which is focused on the extreme end of the cantilever (Figure 1-2). Reflection of the laser is focused on a photodiode where changes in the laser deflection are converted to an electrical signal. The incident position on the photodiode changes and hence, the voltage read out in the form of cantilever deflection. Force is obtained when the system has been calibrated (S) and the cantilever deflection (Δx) can be multiplied by the cantilever spring constant (k). The importance of the calibration of AFM instrument is described in the next section.

1.1.2 Calibration of cantilever and tip selection

In a classical instrument, a measure is made by a readout (usually by the eye) from an output produced according to a calibrated scale. In such a case, the uncertainty of measurement is simply due to the quality of the reference scale and the error in the readout. A similar context applies to AFM where a recent analysis of errors in AFM indentation experiments has been published (including valuable information in the supplementary data) (Schillers et al. 2017). Calibration needs to be done carefully in order to acquire correct measurements. Indeed, multiple factors can affect the variability of the data even if we use the same tip, such as

different AFM instruments, transparency of the liquid buffer or the gold coating that affects the reflectivity of the laser.

Equation 1 explains the goal of the calibration: to obtain *F* knowing Δx, it is necessary to define *k* and *S*. The standardized SNAP method describes the process of obtaining a calibrated system using pre-calibrated cantilevers (Schillers et al. 2017) and allows you to perform a non-contact calibration. However, the availability of pre-calibrated cantilevers remains low for sharp tips and it is not trivial to perform the pre-calibration on common commercial cantilevers without specific instruments such as interferometers. Therefore, in our case and before starting AFM indentation experiments, it is mandatory to perform the calibration of the cantilever by measuring the deflection sensitivity.

Most of the time, calibration is done when the tip of the cantilever interacts with a very hard surface like glass, which is considered as infinitely stiff. This is called contact-based calibration to indicate that there is a physical contact between the tip and the surface, which may damage a very thin tip. By performing a single force-distance curve (Figure 1-3); we obtain a linear relationship between z-piezo movement (usually in nm) versus cantilever deflection (usually in V). By taking the slope of this curve, we obtain the conversion factor S' (V/nm) that translates AFM internal readout (V) into a distance (nm). However, the conversion factor in Eq. 1 requires the inverse of S' (it is often called Inverted Optical Lever Sensitivity), so S = 1 / S'.

After calibrating the deflection sensitivity, it is necessary to determine the spring constant of the cantilever. Again, if we do not have pre-calibrated cantilevers, we used the thermal method and the equipartition theorem to estimate the spring constant k. When running a thermal tune in AFM, the power spectrum shows peaks at different frequencies. Normally the very first peak, which is normally the largest peak of the spectrum, is selected and integral under the peak is computed. Stiffness of the cantilever is calculated by combining integral value with the Boltzmann constant and the room temperature/liquid buffer temperature (Hutter and Bechhoefer 1993). By its name (thermal method), it is clearly a statistical approach, and consequently it should be performed a couple of times to make sure that results are consistent. Although it is reasonable to compute an average value for k, in practice, we often keep the currently computed value if it falls into the range observed in previous reading.

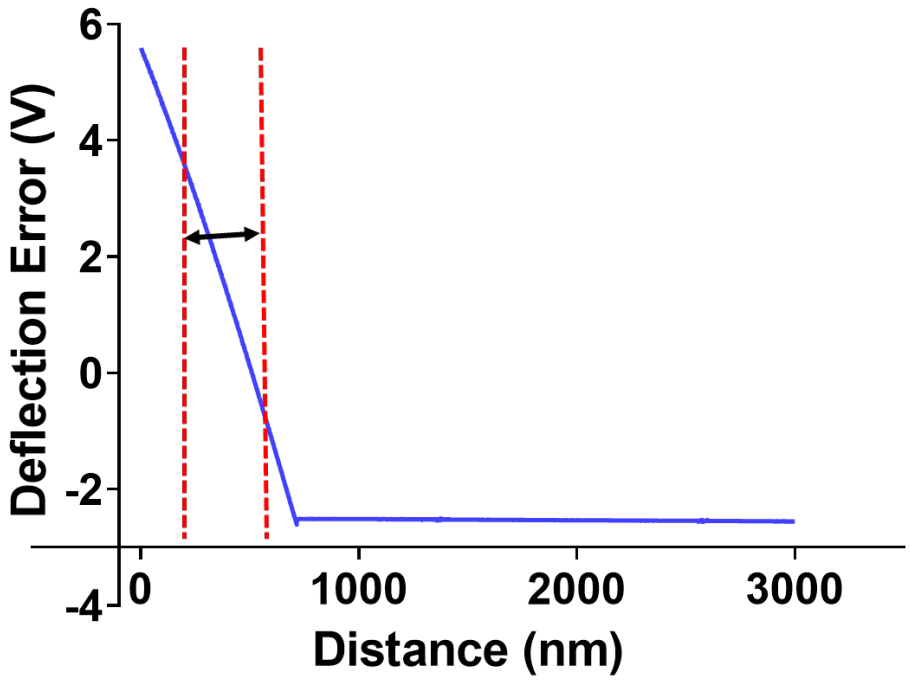

Figure 1-3: Deflection vs distance curve.
Figure shows when AFM tip hits the glass surface for the calibration of probe, a sharp deviation is observed. Deflection sensitivity is calculated from the slope of this curve in nm/V. Observe the sharp deviation when the tip hits the hard surface.

There are wide range of biological samples on which indentation experiments are done. Due to the variability in the elasticity of the samples, it becomes important to choose appropriate tips according to the sample's behavior. For soft materials, large spherical tips are used to avoid deep penetration while knowing precisely their size (Chighizola et al. 2021; Norman et al. 2021). However, a parameter is rarely discussed in nanomechanical experiments, i.e., the relationship between the tip size and the heterogeneous surface structure of the biological sample. By applying a large spherical tip over a soft sample, we obtain a global average response; however, if we apply a finer tip (not too sharp) we can then probe a local response. If the surface of a sample is nm-size heterogeneous (like plant cell wall components), it is reasonable to use nm size pyramidal tip as well.

Another parameter, which can be considered, is that of the cantilever's spring constant. Cantilever's spring constant should be selected according to the sample's 'expected' stiffness range. It becomes helpful if the expected stiffness range of the sample is known. Indeed, if we indent a hard surface with a softer cantilever, then the cantilever will bend easily without any deformation on the sample. On the contrary, a stiffer cantilever can easily deform the material

but no deflection will be recorded by photodiode. If elasticity of the sample is unknown, it is always better to start with the low spring constant and gradually increasing until expected indentation is not obtained (Norman et al. 2021).

1.1.3 AFM imaging and force modes.

As described before, most traditional AFM cantilevers have a sharp tip at its end, which is used to scan the sample surfaces. Scanning can be done in various modes depending on the application. There are three major imaging modes based on which AFM can operate depending on the tip motion (Magonov and Reneker 1997; Main et al. 2021)

1) **Contact mode**: This is the original mode of AFM. The tip is scanning a surface in continuous contact with the sample. There are two versions: a constant height or a constant force imaging. In the first case, the feedback loop is switched off and the raw cantilever deflection is recorded. In the constant force, a feedback loop is active, i.e., it pushes the z-piezo up and down depending upon the topography of the sample; these ups and downs are then assembled to make a topography image. The contact mode is the most damaging to the sample. Thus, only low spring constant cantilevers are used for it.
2) **Tapping mode**: Because of the limitation of contact mode, a softer alternative has been devised (Zhong et al. 1993). Here the cantilever oscillates at a resonance frequency (usually 10-100s of kHz) having intermittent contact with sample. The damping of this oscillation amplitude between the sample and the tip is monitored and recorded when operated in tapping mode. This mode is best suited for fragile biological soft systems and can be operated in liquid environment (Radmacher et al. 1994).
3) **Peak Force tapping mode**: This mode is preferred for soft samples while preventing tip or sample degradation. Compared with the tapping mode, the peak force tapping (and similar modes found in different instrument manufacturers) does not use the resonance frequency but a fixed off-resonance frequency (a couple of kHz) to oscillate the cantilever. Variations in this imaging mode among manufacturers concern mostly the shape of the driving oscillation (triangular, sinusoidal …). This mode is also called a very fast force distance mode as it is perceived as a succession of force distance curves (Main et al. 2021).

AFM **force mode** is the fundamental mode of this technique. Because the force mode is used in a collecting fashion, it is also known as force spectroscopy. This force mode describes the relationship between the motion of the z-piezo scanner (up and down) and the cantilever deflection. We have already seen such a force-distance (FD) curve during the calibration of the optical sensitivity. Let us describe this FD curve in more details. First, in most systems, a FD curve contains two "curves": approach and retract, both representing a single FD cycle (down and up). On a hard substrate, both approach and withdraw curves should overlap. This is, however, rarely the case on soft biological systems in liquid environment. We can describe the seven phases of a single FD curve (Figure 1-4):

1) As the cantilever approaches the surface towards the sample, the cantilever does not experience any interaction force and thus the deflection is null.
2) When the tip comes near to the sample, it experiences the attractive forces (like Van der Waal's forces) which ends up in a contact between the tip and the sample. This position is called the contact point (CP).
3) The tip is now in contact with the sample while the z-piezo continues its travel downward. The cantilever bends and this is the indentation part of the curve. On a hard substrate, the deflection is a straight line (as used in the calibration step), but on a soft sample, the indentation curve is more round.
4) The indentation continues until the maximum force or the maximum z-piezo ramp is reached. This marks the end of the approach curve and onset of the retraction, i.e., withdraw curve.
5) The cantilever moves upward (in the opposite direction of the approach curve). The cantilever bends in an opposite direction as well, i.e., the deflection decreases. Ideally, on a hard substrate, retract and approach curves should overlap, but hysteresis is very common on biological samples or samples that do not behave purely elastically.
6) A particular property of biological samples is the strong adhesion between the tip of the cantilever and the sample. This adhesion is clearly seen as a negative peak in the FD curve while the cantilever is moving away from the surface. At some point, the pulling energy is stronger that the adhesion energy and the tip detaches itself from the sample. Often, a complicated pattern is observed for the tip detachment (two major events in Figure 1-4).

7) Lastly, the tip is detached from the surface and free again from any interaction forces; consequently, the deflection is again null.

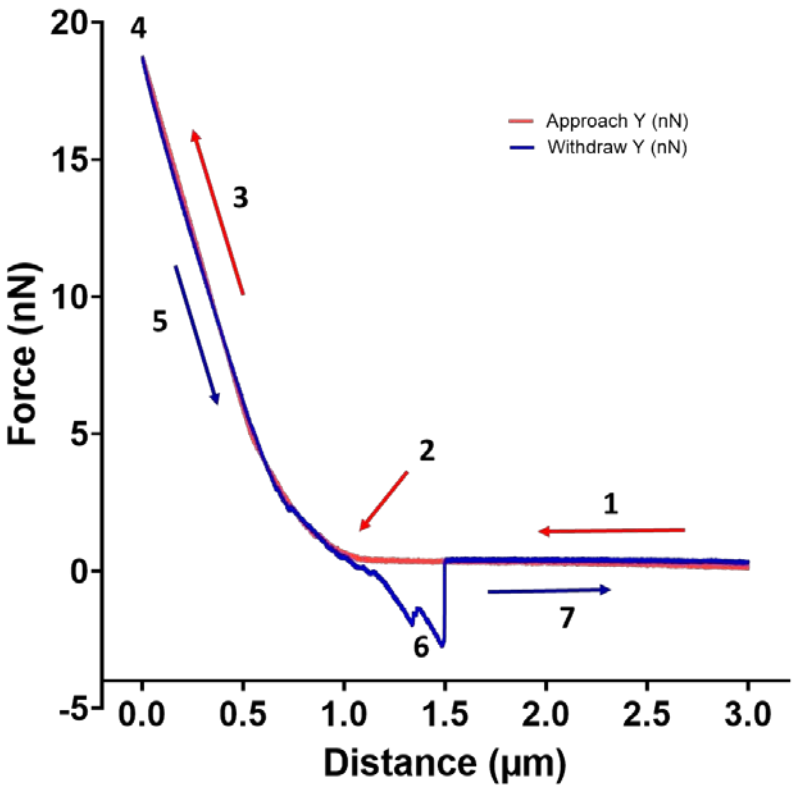

Figure 1-4: Force-Distance curve extracted from one of our datasets on plant roots.
The approach and retract curves are shown in red and blue, respectively. Labels are used in the seven phases of the FD curve. In our nanomechanical analysis, only the approach curve was of interest.

1.1.4 Stiffness, elasticity and mechanical models

There is some confusion in the literature about the mechanical terminology; so, let us describes this terminology. Stiffness is the resistance of a solid body to deformation by an applied force. Stiffness is an extensive material property (depends on the size, shape, amount of material and boundary conditions) of the solid body. A material is said to be elastic if it deforms under stress and returns to its original shape when the stress is removed. The elastic modulus is an intensive property (does not depend on the size, shape, amount of material, boundary conditions, etc.) of the material. A very fundamental principal to keep in mind is that the higher the elasticity of a material is, the lower its deformability is. A common-sense description of elasticity uses the words: soft and hard. It is often found in the literature that

high elasticity is also called stiff although stiffness and elasticity do not share the same units: N/m for stiffness and N/m² (or Pa) for elasticity.

A possible origin of the confusion is that all mechanical measurements involved stiffness, i.e., the resistance to deformation of a material. Accordingly, we are all performing stiffness experiments. However, as mentioned above, stiffness is an extensive property and therefore cannot be used to characterize a given material. It should be clear now that a material could have a large elastic constant and remains soft (this is the case of AFM cantilever where k could be as small as 0.05 N/m but with an elastic constant of GPa for silicon). In nanomechanics, one of the goals is to characterize the elasticity of a material. By definition, the elasticity is characterized by a constant, known as the Young's modulus. It is defined as the ratio between stress and strain ($E = \sigma / \varepsilon$); the stress is defined by a pressure (N/m²) and the strain is a dimensionless fraction of elongation. Although it is easy to obtain the pressure σ with AFM, it is more difficult to extract the elongation ε. Consequently, most of the time we need to use mechanical models to derive the elastic constant or Young's modulus.

The initial problem of contact mechanics were first studied by Hertz (1881) and Boussinesq (1885). However, it is only in 1965 that a modern description of surface deformation by the normal pressure against its boundary of a rigid punch was numerically accessible (Sneddon 1965). Most contact-based mechanical models used in the literature use the equation derived by Sneddon, although they can be called Hertz when referring to spherical indenters. The major breakthrough of Sneddon has been to develop a methodology based on integral transforms for several axisymmetric indenter geometries, with conical/pyramidal, flat, paraboloid tip shape model (Sneddon 1965) where two sample relationships are shown in Figure 1-5.

As for any model, there are a couple of restriction due to the approximations made for establishing the above relationships. Both models (spherical and axi-symmetric) assume that the material is elastically homogeneous and the radius of indenter is infinitely smaller than the sample surface. These models do not take into account the adhesion forces between the indenter and the sample (Kontomaris and Malamou 2022; Chen et al. 2023). Adhesive interactions are either studied using the DMT model [stiff samples, small-radius indenters and materials with weaker adhesive properties (Derjaguin, Muller, & Toporov, 1975)] or the JKR model [soft samples, large-area indenter and strong adhesive properties (Johnson, Kendall, &

Roberts, 1971)]. Another assumption is that the sample is infinitely thick which limits the indentation depth of thin samples. However, force correction formulas have been described to solve the problem of thin samples (Dimitriadis et al. 2002; Gavara and Chadwick 2012; Garcia and Garcia 2018). One of the last restrictions is the fact that the indentation should be performed normally to the sample surface, which is more or less the case for AFM on flat samples.

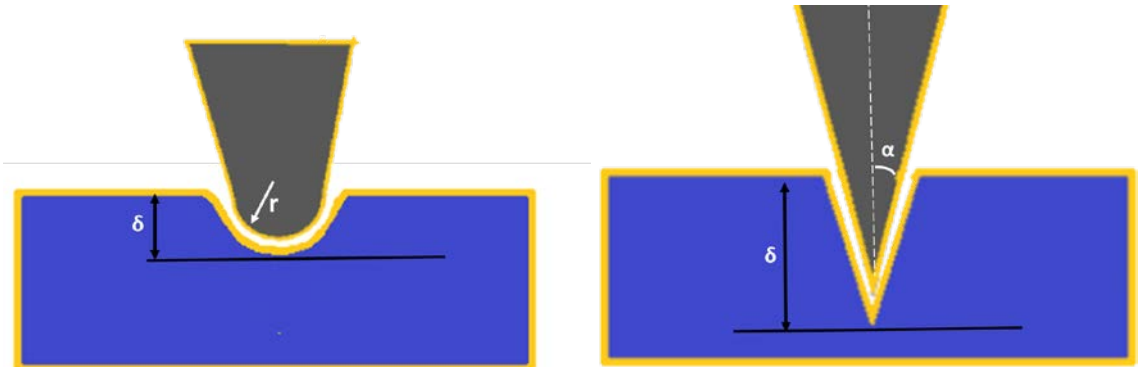

"Sneddon paraboloid or Hertz model"

$$F = \frac{4}{3} \cdot \frac{E}{1-\nu^2} \cdot \sqrt{r} \cdot \delta^{3/2}$$

"Sneddon asymmetric model"

$$F = \frac{2}{\pi} \cdot \frac{E}{1-\nu^2} \cdot \tan\alpha \cdot \delta^2$$

Figure 1-5: Contact-based model representation.
Figure showing relationships between cantilever shape and indentation of a flat sample.
E = Young modulus; ν = Poisson's ratio; r = tip radius of curvature for spherical indenter; α = opening half angle for conical indenter; δ = indentation depth.

To determine the Young's modulus value using a FD curve, it has to be first converted into a force-indentation curve. The force-indentation curve represents the true indentation curves since the recorded raw FD curve represents the z-piezo movement. Indeed, part of the "round" curve in step 2 of the FD curve (Figure 1-6) is due to both the indentation depth and the bending of the cantilever. Consequently, to extract only the indentation depth, it is necessary to remove the cantilever bending contribution from the total FD curve (Carl and Schillers 2008). This step is linked with the definition of the contact point. Once the force indentation curve is obtained, a simple quadratic fitting (in case of pyramidal tips) is applied and the fitting problem can be summarized by the equation 2:

$F = a \bullet \delta^2$ where a is the slope of the quadratic curve. (eq. 2)

It is then easy to extract E since all other parameters are known (Figure 1-6).

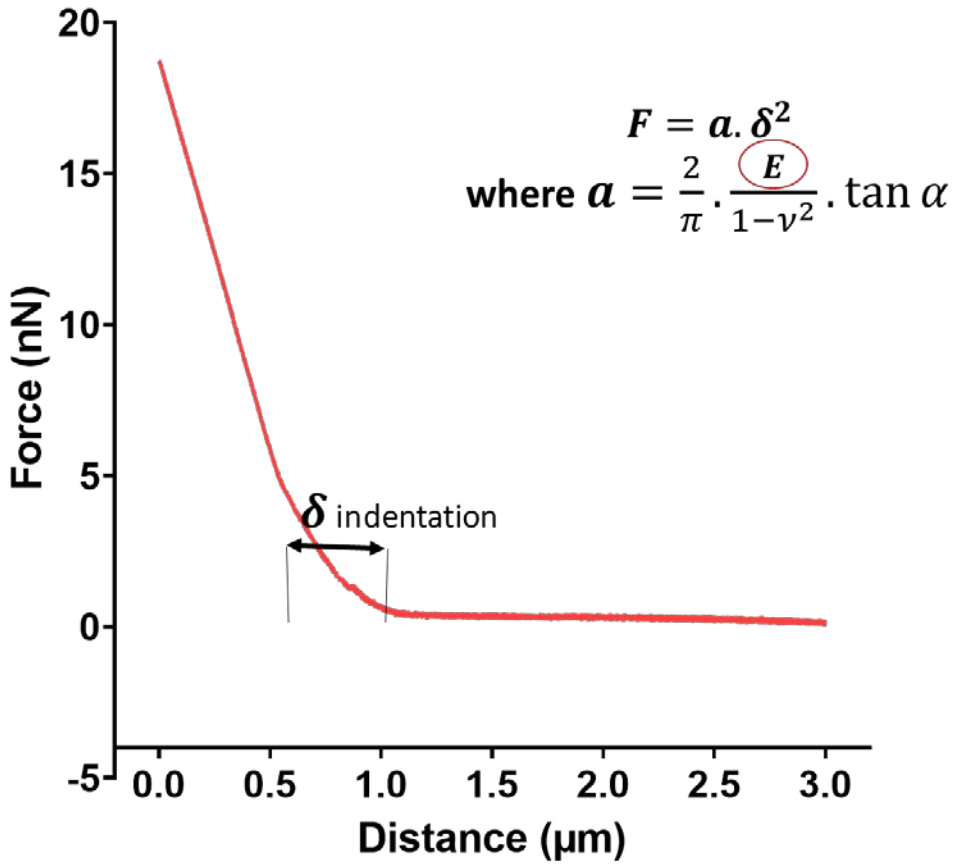

Figure 1-6: Principle of curve fitting and determination of the Young's modulus (E).
The force-distance approach curve is shown in red. The zone labeled by the $\delta_{indentation}$ indicates the region used to build the force-indentation curve with the contact point located on the right side of the label. The master equation of the fit and the corresponding slope value are also shown. α is the known half open angle of the tip and ν is the Poisson ratio kept at 0.5 assuming the incompressibility of biological sample.

1.1.5 Point of contact and data analysis

In a contact-based model, one of the critical and controversial parameter is the positioning of the contact point (CP), i.e. the exact moment where the AFM tip touches the surface of the sample. Its positioning will influence the so-called fitting of the indentation curve. Because of its importance, it has been often decided that the contact point should be also fitted, and consequently, not arbitrarily defined. The problem we found is that the fitting of the indentation curve (necessary to obtain the elasticity constant or the Young's modulus), which includes the contact point, relies on one of the weakest limitation of nanomechanical experiments that is the homogeneity of the sample. During our research various programs were used to extract the critical E value: Force v1 from (Lekka et al. 1999); AtomicJ from (Hermanowicz et al. 2014).

In general, such contact-based software processed the data by extracting force indentation curve first from FD curve and then determining the contact point. Then appropriate model is applied to the force indentation curve, according to the tip shape geometry and Young modulus is calculated from the fit. Processing of the curves is possible in two ways: manual or automatic. In manual mode, a user picks up the contact point to fit the force indentation curve, which leads to error prone data if contact point is not well placed. Although it seems that consecutively recorded FD Curves are similar in shape, but they are not identical. This leads to displacement of the contact point from one curve to another, which is hard to identify by eye. In automatic mode, there is no manual picking and curves are fitted according to the user selected procedure. However, in this method also, true contact point is often missed by the procedure, which will consequently impact the fitting data. In both the cases, software tends to fit the data in a best possible way, albeit flaws in the correct placement of the CP remains (Hermanowicz et al. 2014); a direct consequence of inhomogeneity of biological tissues. Almost all the standard methods have a similar approach and work on fitting the Sneddon model with a single force-indentation curve while the sample itself is heterogeneous.

1.1.6 The trimechanic theory

The trimechanic theory was developed by Shu-wen W. Chen to answer a critical question of how to analyze force-indentation curve along the vertical depth (Chen et al. 2023). Although there are many alternative theories in nanomechanical studies (contact-based models, hyper-elastic models, shell models and more), most of the nanomechanical experiments are analyzed using a contact-based model of Sneddon (Sneddon 1965). Thus, the trimechanic theory was developed to respond to this limitation.

In brief, the theory describes the mechanical behavior of a sample by a sum of three physical responses: a constant, a linear, and a non-linear. The idea is to observe local variations of these three responses along the vertical depth of the indentation. One key step in the trimechanic theory was the identification of depth-homogeneous zones. This was performed by the analysis of the so-called stiffness curve, that is the derivative of the indentation curve along the depth calculated using the classical Savitzky-Golay filter (Savitzky and Golay 1964). According to Sneddon, such a data-driven curve should be linear when using an axi-symmetric conical (or pyramidal) AFM tip. The lack of a straight line indicates a lack of homogeneity in

the nanomechanical response of the sample. Therefore, each time the slope of the stiffness curve changes (defined by the angle of linear section fitting, (Chen et al. 2023)), the sample stiffness changes and we assign a new zone in depth.

Thus, in the trimechanic theory, multiple depth zones are defined and individually analyzed. At the first zone, the constant response of the sample is null according to the contact point definition. In our case, the contact point is simply defined by a change in the force response above a given threshold (a very classical approach used in the field). We need not to worry about the "correct" positioning of the contact point, except that we always follow the same identification rule and does not change upon the quality of the indentation curve fitting. In the second zone, the current force at the entry of the zone is not zero anymore; it becomes our constant force response according to the trimechanic theory. A critical improvement in the depth analysis (over other methods such as stiffness tomography (Roduit et al. 2009) is the strict application of the Sneddon's boundary conditions that state that the tip-shape dependent fitting of the indentation curve must start at a zero force and a zero force gradient (stiffness). In the trimechanic theory, the true novelty is to reset the stiffness at each beginning of indentation-depth zone. Consequently, the stiffness value, defined by the stiffness curve, is used to subtract this linear contribution (stiffness) to the total indentation curve. Then, what is left from the total curve is the true non-linear contribution of the sample upon the axi-symmetric AFM tip indentation; it could be easily fitted by a quadratic curve as required by the Sneddon's formula (Sneddon 1965).

Because of the novelty of this theory, not every corner has been investigated. Consequently, only the first indentation zone was studied in our plant experiments. Besides, since it occurred near the end of my work, I started to use AtomicJ, and the classical Sneddon contact-based model, to analyze all my force-curve experiments.

1.2 Arabidopsis thaliana

In this section, I introduce the characteristics and traits of *Arabidopsis thaliana* (AT) plant. Its unique properties make it suitable for most of the research work in plant labs. In addition, I briefly introduce the root structure architecture as my research exclusively focused on the roots.

When I started working on *Arabidopsis thaliana*, I thought that this plant is grown specifically only in plant labs. To my surprise, it turned out that this plant had a very broad distribution on Earth's surface. We may find *Arabidopsis* vegetation throughout Europe, Asia and North America (Meinke et al. 1998; Kramer 2015).

The earliest mention about *Arabidopsis* dates back to 1577, described by the physician Johannes Thal [Lat Johannes Thalius]. It was renamed *Arabis thaliana* by Carl Linnaeus in 1753, mentioned and featured in the Species Plantarum II. The modern name by which we know today i.e., 'Arabidopsis thaliana (L.) Heynh' was given by Gustav Heynhold. (Meinke et al. 1998; Koornneef and Meinke 2010; Kramer 2015).

Arabidopsis is a small rosette flowering plant that belongs to mustard family of *Brassicaceae* with a height of not more than one meter (that of matured plant). The roots of this plant grow easily as it does not establish any relationship with nitrogen-fixing bacteria. In addition, unlike other flowering plants, the roots of *Brassicaceae* family do not undergo mycorrhiza or rhizobial symbiotic association. These distinct characteristics lead to natural expansion of this plant under different living conditions (disturbed or exposed soil). It is estimated that AT divergence from a common ancestor is ~5 M years ago. The divergence occurred before or during the transition from warm to colder temperature. AT is recognized as native to Western Eurasia and is a colonizer and pioneer plant of poor, stony or shallow soils, in nutrient-poor sandy meadow and forest habitats. AT re-colonized central Europe from glacial refuge in the Caucasus possibly accompanying the spread of human farming from the near east (Kramer 2015).

1.2.1 Arabidopsis revolutionary movement: 1930- 2000

The extensive research on Arabidopsis started during 1930s when Friedrich Laibach began collecting seeds from over 150 different natural varieties. In as early as 1943, it was proposed to adopt *Arabidopsis* as a model organism for plant science (Provart et al. 2016). Laibach founded the Arabidopsis information service seed bank in 1960s. A new portal for seed resources can be found with the 'The Arabidopsis Information Resource' (Huala et al. 2001).

Many ecotypes of AT were collected for experimental analysis, but later only Columbia and Landsberg were accepted standard ecotypes for genetic and molecular studies. The first irradiation on AT was done in 1947 by Erna Reinholz, but the first mutant was produced by György Rédei in 1957 named Landsberg erecta mutant. Later, Rédei selected a single plant (not irradiated) as a reference new line called Columbia. In 1975, Rédei again proposed AT as a plant model '*Arabidopsis* as a genetic tool' (Redei 1975). Many important developments took place in 1980s and 90s at the genetic level. Long-term research goals were discussed among researchers with the aim of sequencing the entire genome by the end of the decade. It was in 2000 that the whole genome of *Arabidopsis* was published (Arabidopsis Genome 2000). AT has a small genome sequence of 157 Mbp (shorter than other Arabidopsis plants with 207 Mbp for *A. lyrata*) which greatly facilitated the sequencing. This milestone was instrumental in making AT as a universal 'reference/classical model' in plant sciences. The advances made in the research of AT, may help in solving agriculture related problems which eventually impacts industries and human health.

Apart from complete sequenced genome, other factors favored AT to become a classical model. It has a very short generation time of 6-8 weeks ranging from seed germination, flowering, until the harvesting of the very first seeds (Meinke et al. 1998). They can tolerate extreme hot or dry conditions by producing de-hydrated seeds for effective defenses. It is observed that the seeds of *A. thaliana* are comparably long-lived and highly viable than those of *A. halleri* and *A. lyrata* (see Figure 1-7) (Kramer 2015). Besides, AT is highly synchronized in the seed pod formation i.e., producing much higher number of seeds that are smaller in size than other close relatives (ideal for mutagenesis or stock maintenance).

The morphological organization of AT primary roots is simple. It contains a central stele with systematically four easily identifiable layers involving a single and specialized cell type:

epidermis-> cortex-> endodermis-> pericycle (cortex is the biggest cells in diameter) (Kramer 2015).

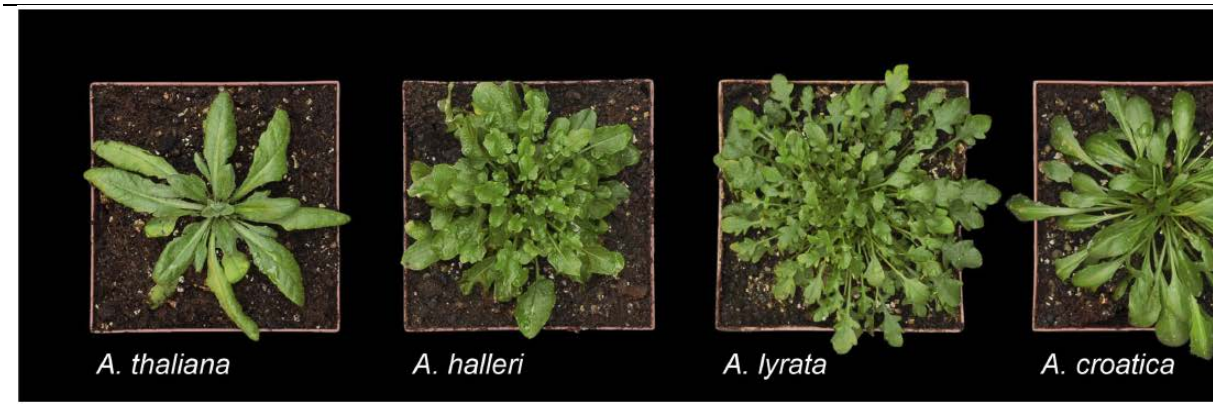

Figure 1-7: A. thaliana and a subset of species from its sister clade.
From left to right: ***A. thaliana*** *(Col),* ***A. halleri*** *(ssp. halleri; individual Lan5, Langelsheim, Harz, Germany),* ***A. lyrata*** *(ssp. lyrata; selfing accession Great Lakes, North America), and* ***A. croatica*** *(Baške Oštarije/ Ljubičko brdo/ Croatia). A. thaliana was grown from seed to early reproductive stage, and the other species were propagated vegetatively and grown for 3–6 months. The individuals shown here do not reflect the large intraspecies morphological diversity, particularly in leaf shape, among different accessions of A. halleri and A. lyrata. Adapted from (Kramer 2015).*

1.2.2 Root development and the impact of soil

Our research project focused on the roots of AT. Before proceeding to understand the structural organization of roots, it is important to understand the soil resources and their impact on the root development. Soil distribution is uneven on the earth's land surface. Almost one third of land's surface is arid in nature. Soil compaction poses a challenge in agriculture where root growth reduces because of its inability to penetrate into the hard soil. This largely affects the plant productivity. Various factors like harsh climatic changes, nutrient limitation, soil acidity, salinity largely govern the root system architecture (RSA) of the plant. Changes in RSA determine the ability of the plants to exploit those resources. Roots dynamically respond to localized availability of the soil resources through merismetic activity (Lynch 1995; Pandey et al. 2021). It is easy to imagine the future impact of global climate change on soils, which will greatly provide an additional stress to plant roots.

Root development is highly sensitive to environment that modifies the intrinsic genetic program affecting the fundamental morphology of a plant's root system. In fact, the primary root (PR) is established during embryogenesis, while the lateral roots (LRs) originate from the PR post embryonically (Figure 1-8). The temporal and spatial variations in the supply of soil

nutrients such as nitrogen (N), phosphorus (P) and iron (Fe) have a major influence on root growth and architecture, these nutrients alter root patterning through particular signal transduction pathways. Changes in the RSA throughout time finally determine root plasticity and allow plants to adapt efficiently to environmental constraints (Sanchez-Calderon et al. 2005; Gruber et al. 2013).

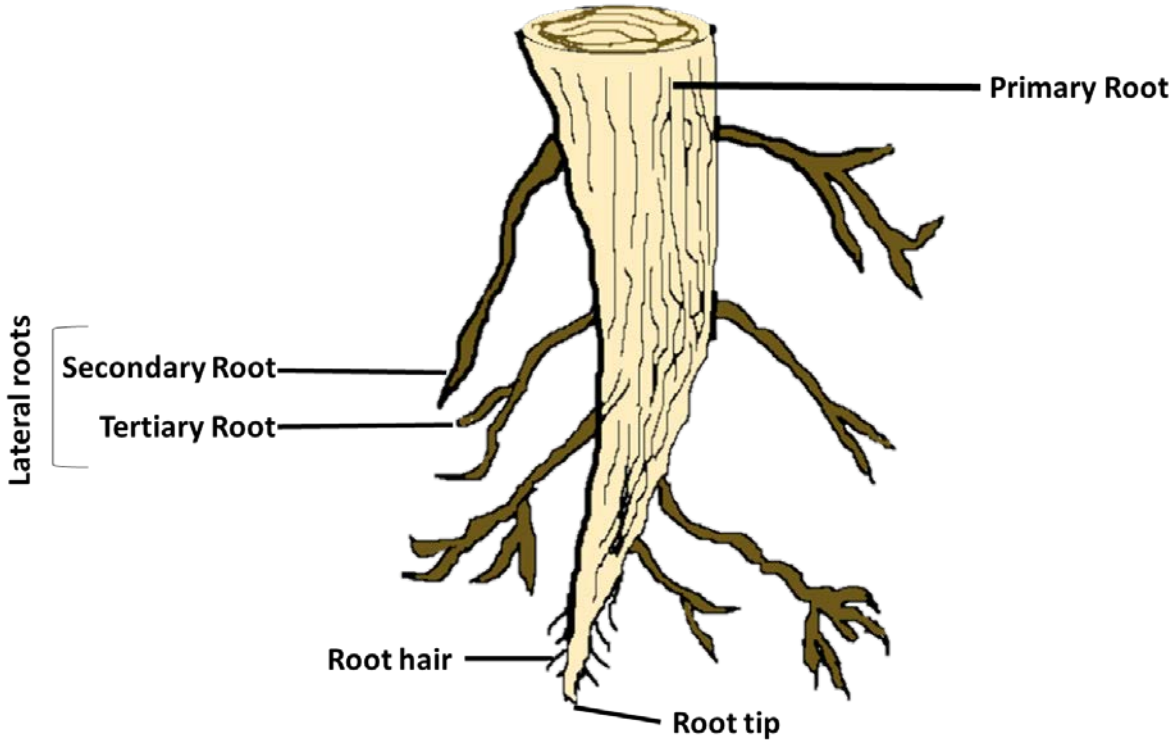

Figure 1-8: An overview of root structure architecture.
Roots are divided mainly into three parts: Primary, lateral and root hairs. Further, lateral roots can be distinguished into secondary and tertiary roots.

There are many challenges when it comes to study plant roots. Although we do grow plant in agar medium in our labs, it is relatively difficult to observe, quantify and interpret root architecture in external environmental conditions. Roots grow in soil in an opaque medium and the soil environment itself is very complex, posing challenges to root researchers. Roots interact with a wide array of physical, chemical, and biological factors in the soil that vary in time and space.

1.2.3 Root structure and cell organization in roots

In most of the vascular plants, root tip plays an important role. New root tip keeps on growing throughout their life. Roots provide nutrients and water to the rest of the plant system. They can be categorized into three zones mainly cell division zone (including root cap), elongation zone and lastly cell differentiation zone as shown in Figure 1-9 (Cliffsnotes 2023).

1.2.3.1 Root zone differentiation

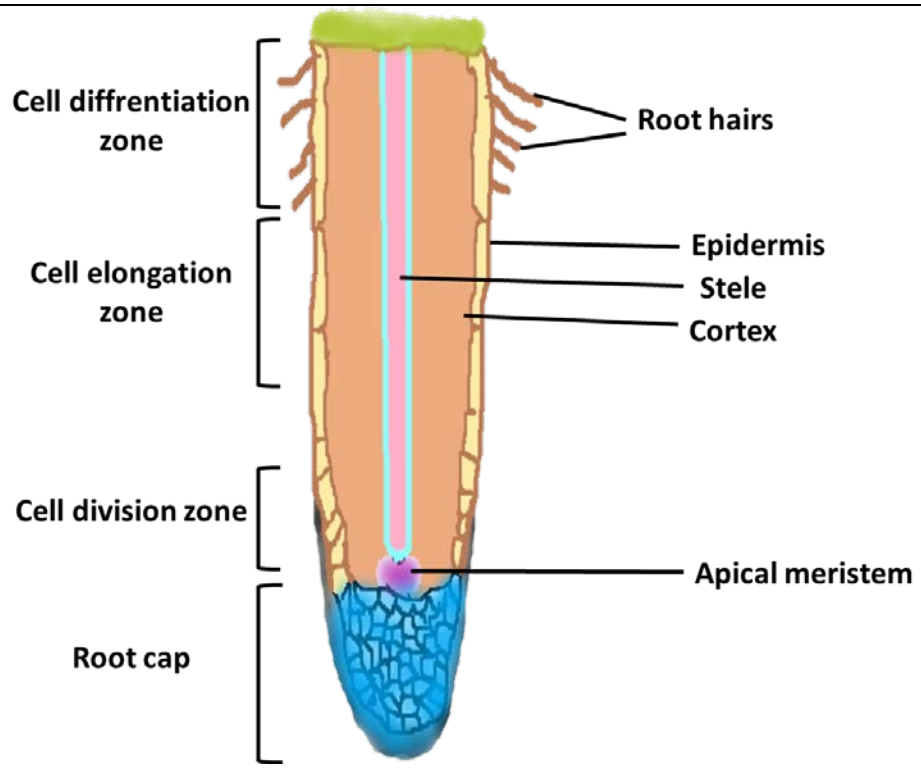

Figure 1-9: Different activity zones in AT plant root.

The very first part is the root cap, which is the home to stem cells, also called stem cell niche (SCN). The cells in this zone continuously divide while penetrating through the soil. A very rigid layer surrounding the root tip protects the cells from underneath abrasion and assists the root to push through the soil. Root tip secretes a substance called mucigel, which lubricates the root more smoothly and protect the cells from drying out. Root cap senses the light in some way and responds in the opposite way, thus guiding the growth away from sunlight in addition to gravity, which directs the root downwards (Scheres, Benfey, and Dolan 2002).

Immediately comes the cell division zone where cells divide relatively slow and displaces these cells upward in the cell file. Here cells arrange themselves parallel to the root axis. The apical

meristem of the root forms three primary meristems: epidermis; xylem and phloem whereas the ground meristem gives rise to cortex (Scheres, Benfey, and Dolan 2002).

Elongation zone is a special zone where cells do not divide but elongate i.e., the cells stretch themselves while enlarging the vacuoles. This expansion actually is responsible for directing root cap and apical tip downwards through the soil. This phenomenon is actually apparent in epidermal cells (Scheres, Benfey, and Dolan 2002).

The point from where we see the very first root hair marks the beginning of cell differentiation zone. Here the cells differentiate into specialized cell types and allows the formation of root hair or secondary roots.

1.2.3.2 Cellular differentiation of root layers

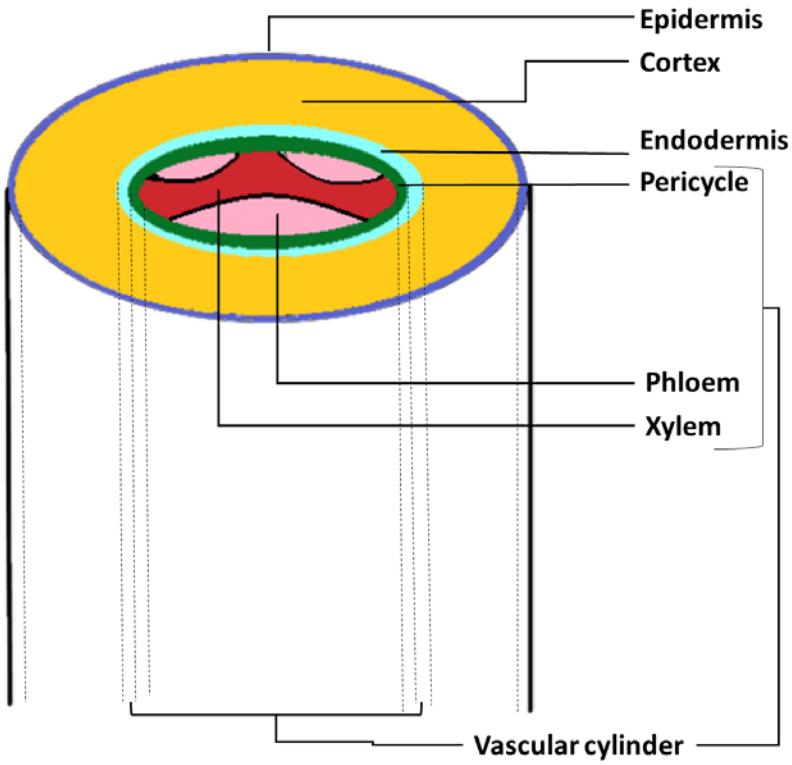

Figure 1-10:Transversal section of Arabidopsis thaliana roots showing different layers.

As mentioned before, *Arabidopsis* has a relatively simple organization of the root layers involving single layer of each specialized cell. All those differential layers in the root system arise from cell division region. The simple anatomy of AT roots compose of single radial layers

of epidermal, cortical, endodermal and pericycle cells surrounding vascular tissues, as shown in Figure 1-10 (De Lucas and Brady 2013).

Epidermis consists of epidermal cells making outer protective layering of roots. It provides a large surface area along with root hairs, through which movement of nutrient take place (Sánchez-Calderón, Ibarra-Cortés, and Zepeda-Jazo 2013).

Cortical layer or outer cortex is made of parenchyma cells that gives mechanical support. These cells are tightly packed and are impermeable to water and other nutrients.

Endodermis is the innermost layer of cortex. The distinguished part of this layer is responsible for forming ion barrier. It regulates absorption and translocation of materials in and out of the vascular system. Like the cortical layer, the endodermis layer is always made of eight cells, which facilitates their identification in transversal microscopic layers (Dolan et al. 1993).

Last cylindrical layer, the Stele also known as vascular cylinder, includes the pericycle and vascular tissues (xylem and phloem). Pericycle layer is a cylinder of parenchyma cells in the stele immediately after endodermis. In this region, cells maintain their merismetic properties, i.e. cells are able to divide and localized division gives rise to lateral roots (Sánchez-Calderón, Ibarra-Cortés, and Zepeda-Jazo 2013).

1.3 Cell wall composition and architecture

Universally the two main features shared by all the eukaryotic cells are cytoskeleton and plasma membrane. In plants and fungi, there are two additional features: the cell wall (CW) and the turgor pressure (Geitmann 2006). Cell wall and turgor pressure are both involved in the irreversible expansion of plant cells (Lockhart 1965). In addition, the immobilization of plants is mainly possible because of the presence of cell wall in plants. Cell wall is responsible for regulating growth and expansion at the cellular level while the middle lamella are responsible for connecting one cell to another. Although morphogenesis occurs at the tissue level, cell wall mechanical properties are controlled at the cellular level through the deposition and chemical modification of cell wall material (Routier-Kierzkowska et al. 2012; Hamant and Haswell 2017)

Today, even if all the components of cell wall are well known, it is still not possible to understand the nature of bonds and interactions, which makes it possible to build up a complete cell wall model. Numerous methods have been explored to understand the reasons behind this characteristic cell wall stiffness. Although cellulose remains the main load bearing component, there could be other factors that can contribute to the stiffness for example cellulose-cellulose, cellulose-matrix or cellulose-xyloglucan-cellulose bonds that may contribute to mechanical strength of cell wall (Burgert and Keplinger 2013; Cosgrove 2016).

In this introduction, we will only focus our attention to cell wall properties and architecture directly linked to Arabidopsis-type of plants, i.e., only type I primary cell wall architecture. In this section, I will introduce the components of primary cell walls, and then I will briefly describe the plant cell wall organization.

1.3.1 Composition of CW

Although from a mechanical point of view, we consider the CW as a single heterogeneous entity, primary CW are usually described in terms of two structurally independent, but interacting, networks. The first network is made of cellulose in presence of crosslinking glycans (hemicellulose). The second network if made of matrix pectin polysaccharides in presence of proteins (Kerr and Bailey 1934). By its function, CW has also been called plant extracellular matrix (Roberts 1989). The composition and description of both networks is further explained.

1.3.1.1 Cellulose and hemicellulose

1.3.1.1.1 Cellulose

The central element of cell wall is cellulose, an ancient polymer that first appeared in bacteria, albeit not in their CW, rather as an extracellular material used for adhesion to host cells or a flotation device. CW is made up by the building blocks of sugar polymers with variable interconversions indicating the presence of 13 different monosaccharides Figure 1-11 (Albersheim et al. 2011).

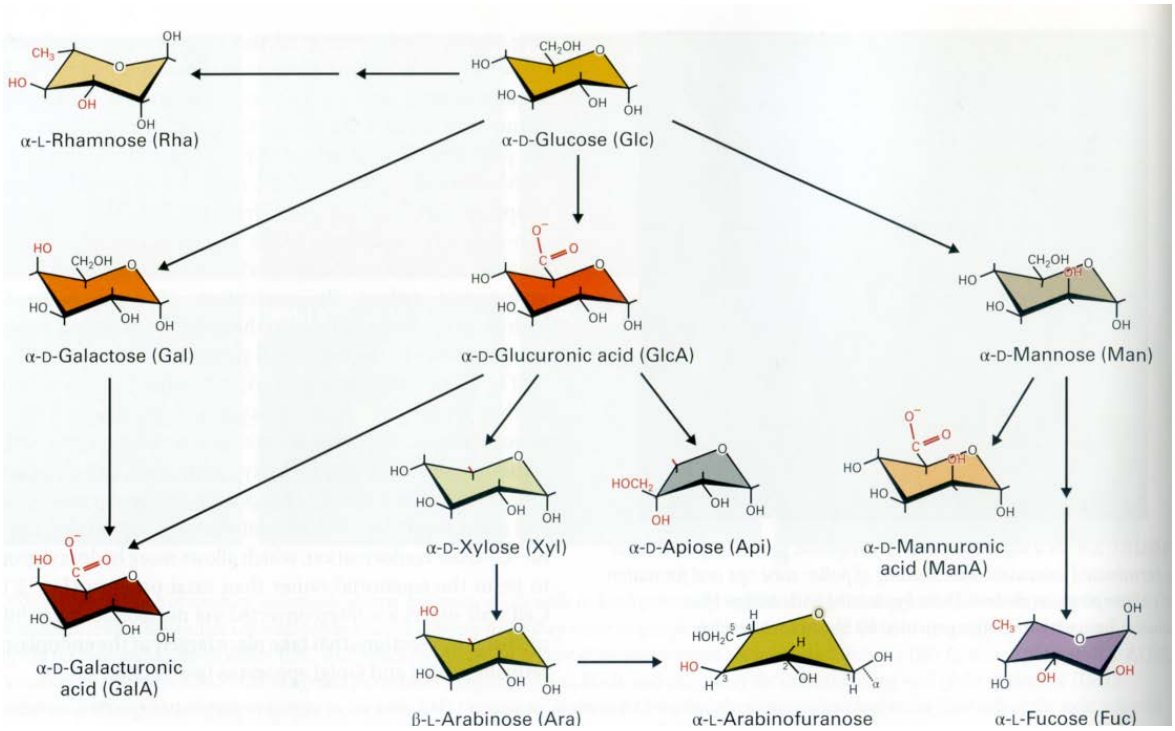

Figure 1-11 : Monosaccharides linked into cell wall polymers derived from glucose.
Modifications needed to convert D-glucose into other sugars are highlighted in red. Bonds represented in red show the negative charges (Buchanan, Gruissem, and Jones 2015).

Cellulose is built by an assembly of monosaccharides derived from glucose (glucan). Cellulose is made of a so-called 1-4 β-D-glucan assembly where the repeating unit is the cellobiose (Figure 1-12). A simple change in the glucan connection, i.e., 1-3 β-D glucan produces callose, which has a different role in plant cell walls, in particular to the stiffening of CW.

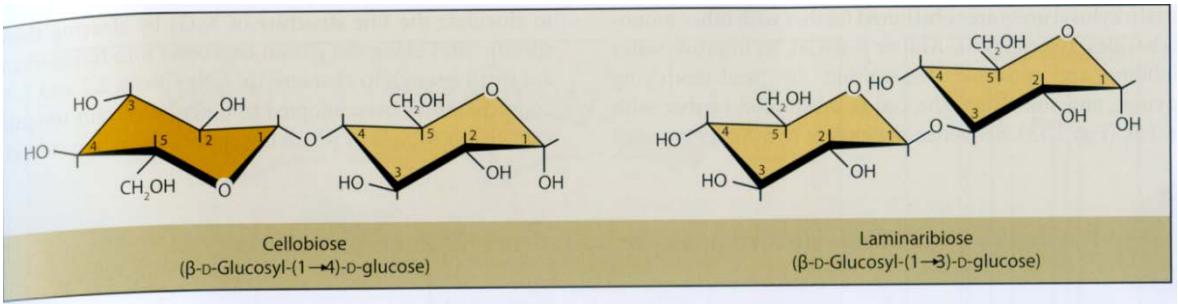

Figure 1-12 : Structural illustration of cellobiose and laminaribiose.
The (1-4)-ϐ-D-linkage of cellobiose inverts the glucosyl unit about 180° relative to each other, whereas the (1-3)-ϐ-D linkage is slightly askew (Buchanan, Gruissem, and Jones 2015).

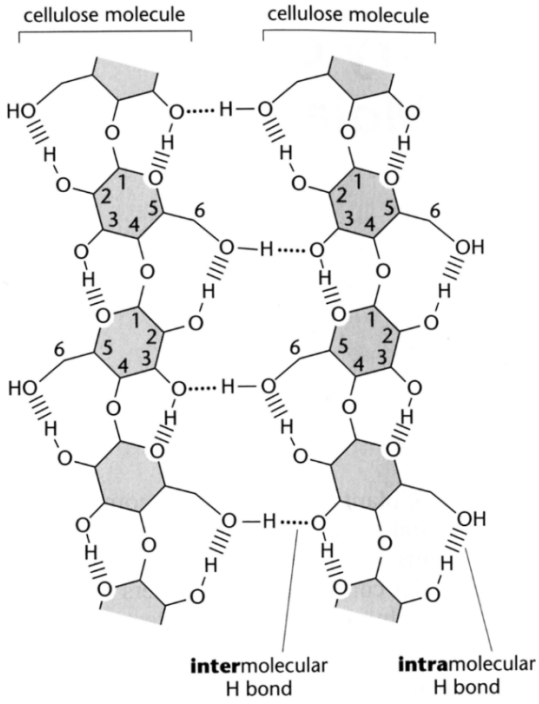

Figure 1-13 : Unit structure of microfibril.
Parallel arrangement of atoms in of several (1→4)-ϐ-D-glucan chains that binds through hydrogen bonds both side to side and top to bottom to each other (Albersheim et al. 2011).

Cellulose represents about 15-30% of the dry mass of primary CW (Cosgrove 1997). It exists essentially as microfibrils that are para-crystalline assemblies of several dozen single chains, which are thought to originate from Algae (Buchanan, Gruissem, and Jones 2015). It is estimated that a microfibril of 24 chains has a diameter of 3.3 nm whereas the presence of 36 chains increases the diameter to 3.8 nm. A single microfibril is made of several thousand units totaling a 2-3 µm long structure (Cosgrove 2005). It should be noted that microfibrils do not

assemble from their edges but they partially overlap at different positions, which allows a final production of hundreds of µm-long fibers. From x-ray structures, the glucan chains in cellulose are arranged parallel to each other Figure 1-13. The same hydrogen-bond network is present during the interaction of cellulose and hemicellulose (Albersheim et al. 2011).

1.3.1.1.2 Hemicellulose

The hemicellulose is often described as cross-linking glycans (Keegstra et al. 1973), i.e. a class of polysaccharides that can bind to cellulose microfibrils with hydrogen bonds, thereby producing a meshed network (Valent and Albersheim 1974). New models of CW also suggest that hydrophobic interactions and physical entanglement between hemicellulose and loose cellulose fibrils are important structural contributions (Park and Cosgrove 2012). Hemicellulose can be separated from CW using concentrated alkali solutions (Cosgrove 2005) or enzymes (glucanases). There are two major cross-linking glycans: xyloglucan, which is the major cross-linking of all eudicots (includes Arabidopsis), and glucuronoarabinoxylan. The structure of xyloglucan are composed of branched chains of 1-4 β-D glucose with 2 or 3 α-D xylose units, attached at the O6 position of the glucose, and sometimes galactose or fucose units (Buchanan, Gruissem, and Jones 2015). Its average length is about 200 nm (Carpita and Gibeaut 1993). In general, the length of xyloglucans is longer than the spacing between the cellulose microfibrils i.e. 20-40 nm, which makes it possible for them to link the microfibrils together (Cosgrove 1997). The structure of hemicellulose is quite similar to that of cellulose, which makes it possible to bind to cellulose. However, the branches and other modifications in their structure prevent them from forming microfibrils by themselves, which differentiate them from cellulose (Cosgrove 2005).

1.3.1.2 Pectin matrix

The second network in the composition of CW is much more diverse than the first network. They determine wall porosity and provide charged surfaces that modulates cell wall pH and ion balance, regulating cell-cell adhesion at the middle lamella, and alerts plants of infection. Cell wall enzymes bind to this charged surface of the pectin network, limiting their activities to local regions of the wall. By limiting wall porosity, pectin can restrict cell growth, thereby regulating access of wall-loosening enzymes to their glycan substrate (Buchanan, Gruissem,

and Jones 2015). Pectin matrix can be easily extracted from CW using Ca^{2+}-chelators or by de-esterification agents such as Na_2CO_3 or diluted alkali (Cosgrove 2005).

The pectin matrix contains a diverse class of uronic acid-rich polysaccharides and present a high-degree of structural branching. The two fundamental constituents of pectin are homogalactorunan (HG) and rhamnogalacturonan I (RGI) which are both homopolymers of about 200 units or about 100 nm long (Figure 1-14, Figure 1-16). HG is composed of xylogalacturonan (Figure 1-15) and rhamnogalacturonan II (RGII, unrelated to RGI). RGII is present in Arabidopsis and makes cross-links using boron atoms (Figure 1-17), thus HG and RGII are linked together in a single polymer (Goldbach and Wimmer 2007). HG is produced as methyl-esterified polymers (neutral) and requires the action of pectin methylesterases to reveal the acidic charge of uronic acids. Then, Ca^{2+} can link two antiparallel chains of HG.

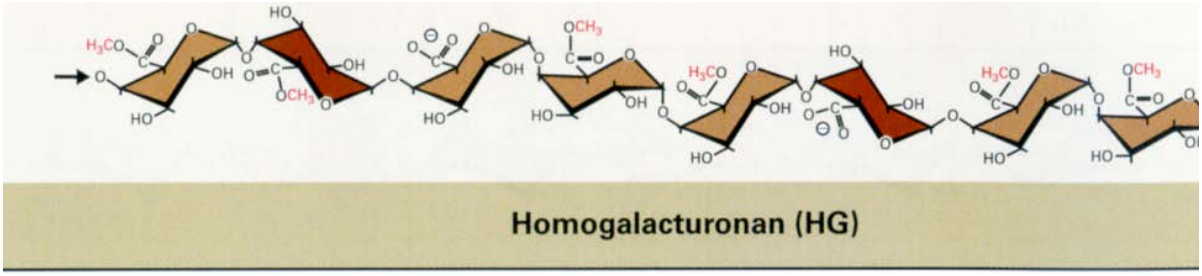

Figure 1-14 : Structure of homogalaturonan.
Red color bonds showing highly charged sites for binding. Image source (Buchanan, Gruissem, and Jones 2015).

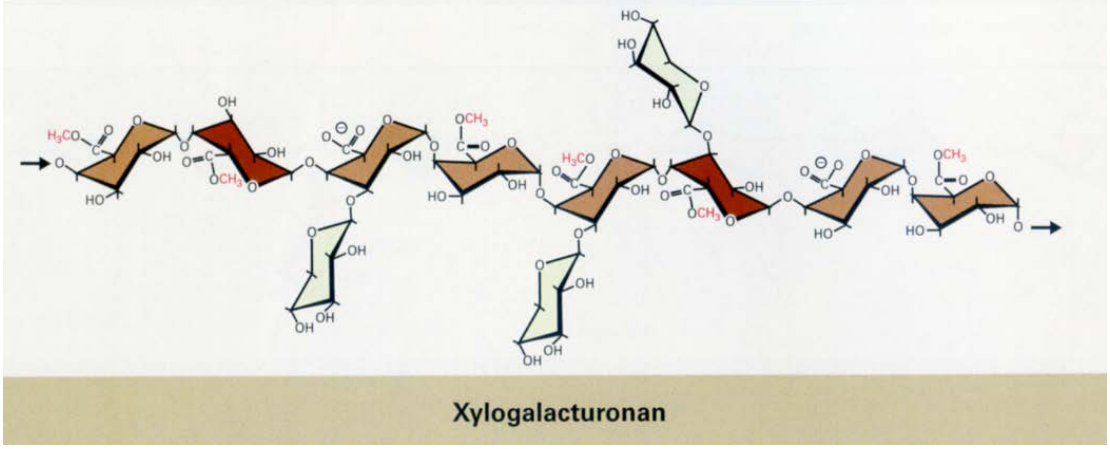

Figure 1-15 : Structure of xylogalacturonan.
Xylogalacturonans are separate class of HG with appendant α-D-Xyloglucan units at O-3 position of about half of Galacturonyl units (Buchanan, Gruissem, and Jones 2015).

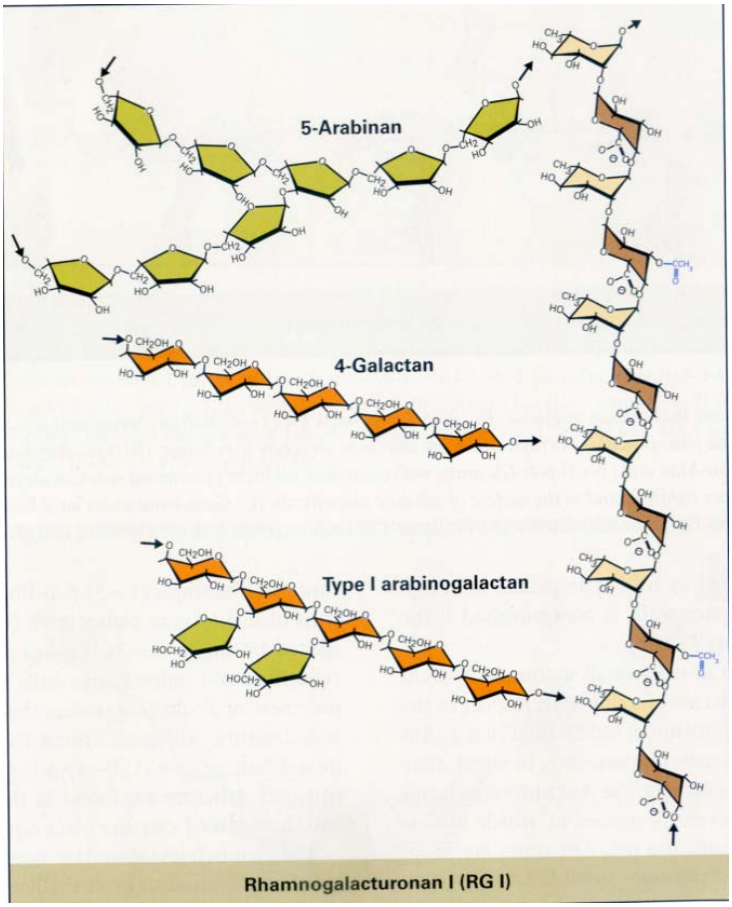

Figure 1-16 : Molecular structure of RG(I).
RG(I) has repeating sub units of →2) α-L-rhamnosyl1-(1→4-α-D-galacturonyl disaccharides with long side chains of arabinans and arabinogalactans (Buchanan, Gruissem, and Jones 2015).

1.3.1.2.1 Relationship of cations and pectin

In AT elongation zone, there is a different bonding status of pectin in central cells, which are de-esterified, compared to external cell pectin, which are mostly methyl-esterified (Palin and Geitmann 2012). It appears clearly that the presence of negatively charged pectin (de-esterified) is able to make cross-links with Ca^{2+}, whereas uncharged pectin (methyl-esterified) cannot. There is a general agreement that the amount of *in muro* dimethyl-esterification correlates with the stiffening CW through homogalacturonans (Wolf, Hematy, and Hofte 2012). In fact, responsible enzymes in esterification, pectin methyl esterases, may all promote CW stiffening, loosening, degradation, and signaling (Wolf, Hematy, and Hofte 2012). Pectin may also bind directly metals, such as Al, during the Al-induced rapid inhibition of root elongation (metal sequestration in CW) (Yang et al. 2016), but also with Fe in phosphate-

deprived conditions (Hoehenwarter et al. 2016). The degree of methylation of CW pectin contribute to genotypic difference in Al resistance in maize (Eticha, Stass, and Horst 2005).

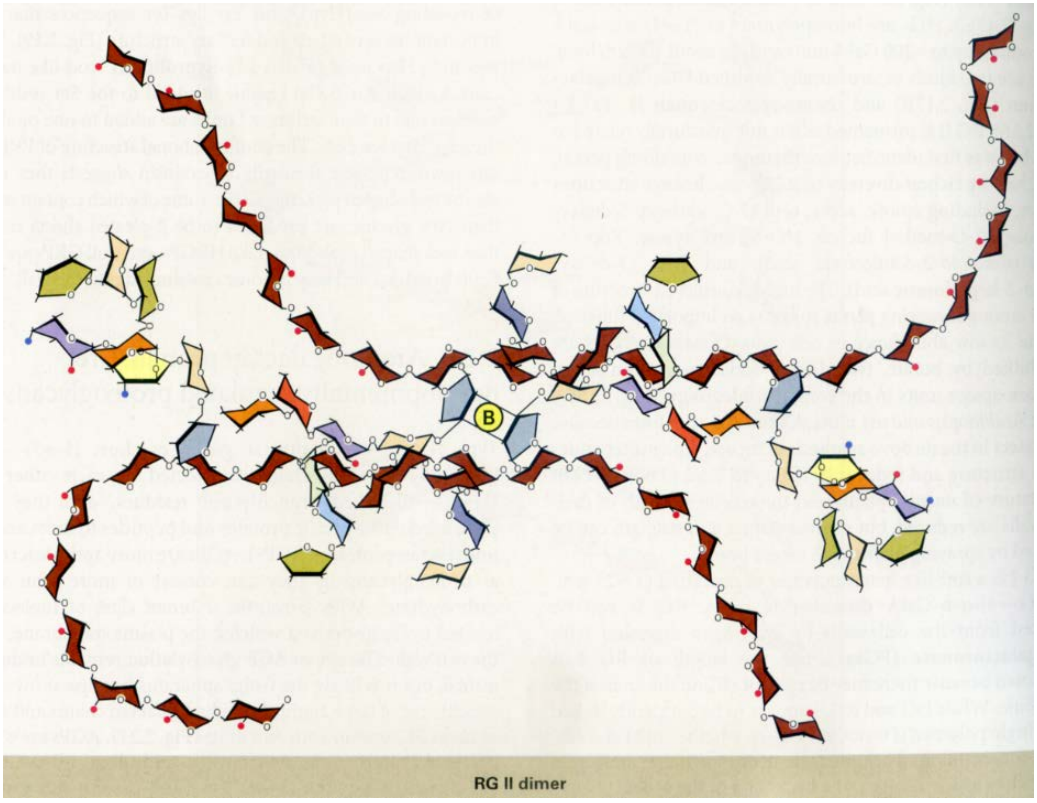

Figure 1-17 : Structural illustration of RG(II) dimer.
RG(II) is a complex pectin domain containing 11 different sugar residues and forms dimer through borate esters (Buchanan, Gruissem, and Jones 2015).

Boron is one of the structural component of CW for non-graminaceous plants (like AT) and helps in crosslinking pectin (Figure 1-17) and in reducing the pore size of CW (Fleischer, O'Neill, and Ehwald 1999). Boron-based complexes between rhamnogalacturonanII and galactosylated xyloglucan contribute to the tensile strength of CW in AT (Kobayashi, Matoh, and Azuma 1996; Ryden et al. 2003). It shows the importance of pectin in CW morphogenesis since pectin chemistry may initiate a non-uniform softening, which may be an initial step that precedes stress-induced stiffness of CW (due to turgor) growth (Bidhendi and Geitmann 2016).

The pectin matrix contains constitutive proteins in CW (Showalter 1993) such as hydroxyproline-rich glycoproteins (HRGPs), proline-rich proteins (PRPs), or glycine-rich

proteins (GRPs). CW-related proteins are believed to play a central role in remodeling CW extensibility that mediates cell expansion or cell plasticity (Le Gall et al. 2015). A notable important HRGP is the extensin family of proteins that contains many glycosylation on hydroxyl-proline residues and is involved in CW cross-linking (Fry 1986). It is often difficult to extract these proteins from CW because they may be covalently attached to it.

1.3.2 Plant cell wall organization

It should be clear that CW is heterogeneous not only in its constitution, but also across the various areas of the plant including roots of Arabidopsis (Somssich, Khan, and Persson 2016). Knowledge of the primary cell wall organization is continuously improving with a growing evidence of the importance of the role of pectin, notably with possible direct interactions with cellulose fibers (Cosgrove 2014). Cell wall is differentiated into two types (1) Primary cell wall (PCW) outer layer and (2) Secondary cell wall (SCW) inner layer.

1.3.2.1 Secondary cell wall

It has been observed that secondary cell walls are more rigid and thicker than primary cell walls. This is in part due to the continuous insertion of cellulose microfibrils into the cell wall. SCW is less hydrated when compared to PCW. SCW makes a waterproof shield, with a decrease in pectin components and thus containing a larger proportion of cellulose. In addition, other polysaccharides such as lignin take a significant part in the constitution of SCW. Consequently, SCW accumulates mostly at the late-stage of cell extensions, leaving only the PCW responsible for cell expansion and growth (Rongpipi et al. 2018; Bidhendi and Geitmann 2019).

1.3.2.2 Features of primary cell wall

The thickness of primary CW is between 80 and 100 nm for meristematic and parenchymatic cells (Figure 1-18) (Albersheim et al. 2011). It is rather difficult to find accurate information regarding the thickness of external primary CW (our major interest in this work). Values ranging from 100 nm to 1 µm can be found (Derbyshire et al. 2007). It should be emphasized that water is also a major constituent of CW (Gaff and Carr 1961), up to 65% in growing

primary walls (Jackman and Stanley 1995), since essential chemical reactions do occur directly with the cell wall. Water is also obviously required to transport ions across the cell wall.

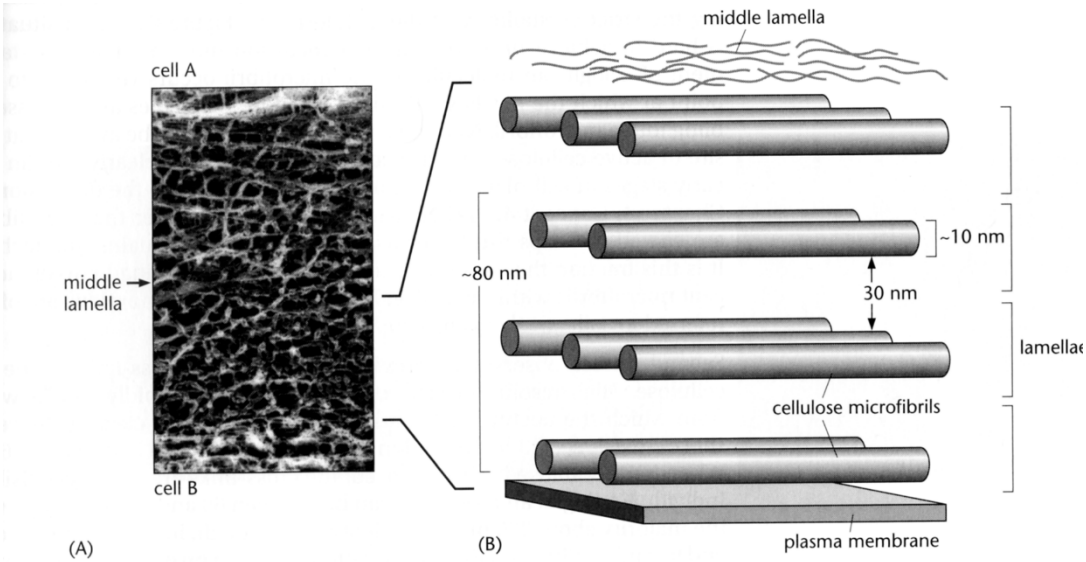

Figure 1-18 : Structural organization of Arabidopsis thaliana cell wall.
(A) An electron micrograph of two primary Arabidopsis cell walls and their intervening middle lamella. Each wall is about 100 nm thick.
(B) Schematic diagram, drawn to scale, showing the probable arrangement of cellulose microfibrils and lamellae within the walls shown in (A). Each wall can probably accommodates only around four lamellae. Figure adapted from (Albersheim et al. 2011).

Cellulose microfibrils are the stiffest component of CW and provides load-bearing role, and their orientation creates a mechanical anisotropy, which in turn restricts cell expansion in the microfibril direction (Majda et al. 2017). The spacing of cellulose microfibrils was measured around 20-40 nm (McCann, Wells, and Roberts 1990) and the intertwining of cellulose, hemicellulose, and pectin has been pictured by Carpita et al. (Carpita and Gibeaut 1993). The conceptual view of layer hierarchy in CW organization is possibly due to the fact that cellulose is produced by a complex machinery (Cellulose Synthase) located at the cytoplasmic membrane of the cell whereas hemicellulose or pectin are exported in the apoplast (Lampugnani et al. 2018). Nascent microfibrils are thus “injected” into the apoplast from the cell just above the membrane. Cellulose microfibrils orientation follows that of cellular microtubules, which in turns orient microfibrils perpendicularly to the long axis of the cell (Paredez, Somerville, and Ehrhardt 2006).

1.3.2.3 Organization of primary cell wall.

The textbook view of the structural organization of the primary cell wall is shown in Figure 1-19. Cellulose microfibrils can be viewed as making multiple layers of a flat assembly (lamellae, Figure 1-19 (Scheller and Ulvskov 2010)). The number of lamellae is not necessarily a fixed number for all plants species or all organs. As seen in Figure 1-20, hemicellulose (crosslinking glycans) binds to cellulose microfibrils creating a connected mesh (Somerville et al. 2004). Xyloglucan and cellulose network provides a balance between extensibility and strength requirement by the primary cell wall (Whitney et al. 1999). In CW, xyloglucan chains bind to cellulose microfibrils using hydrogen bonds (Valent and Albersheim 1974). In sycamore cells, it has been found that xyloglucan binds to cellulose with hydrogen bonds and to pectin polysaccharides with covalent bonds (Bauer et al. 1973). Finally, although the middle lamella is principally made of pectin, it is clear that pectin components also fill up the space made around cellulose and hemicellulose, reinforcing the control of the CW pore sizes. This convenient static view of CW should not be confused with a certain immobilization of its components. It is known for a long time that cell walls are dynamic structure (Heyn 1940) that still escape our full understanding.

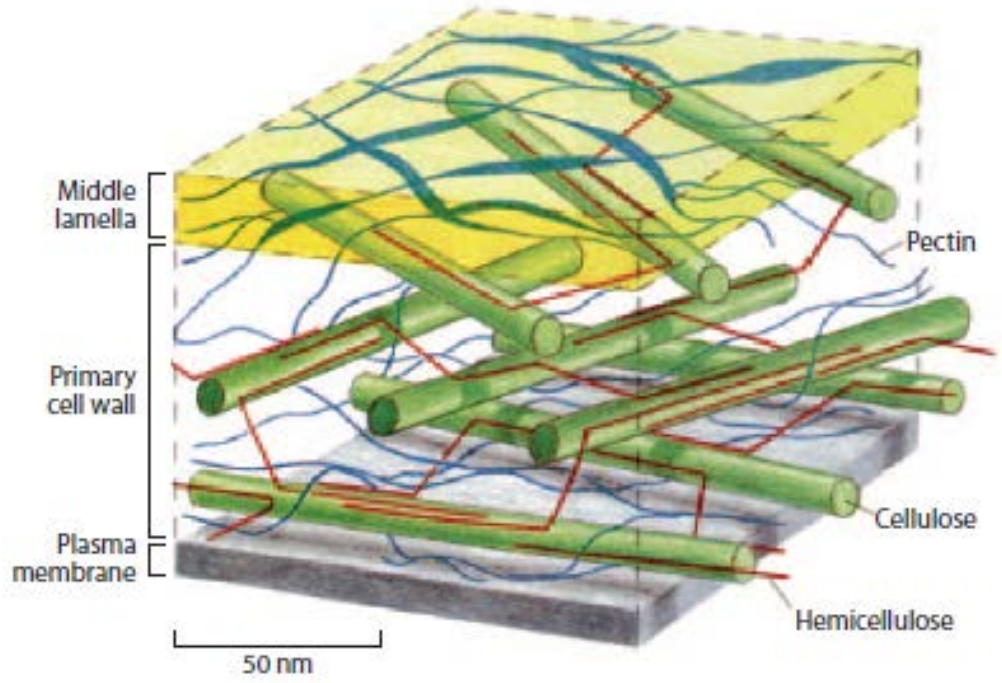

Figure 1-19 : Illustration of the structure of the primary cell wall.
Image source (Scheller and Ulvskov 2010).

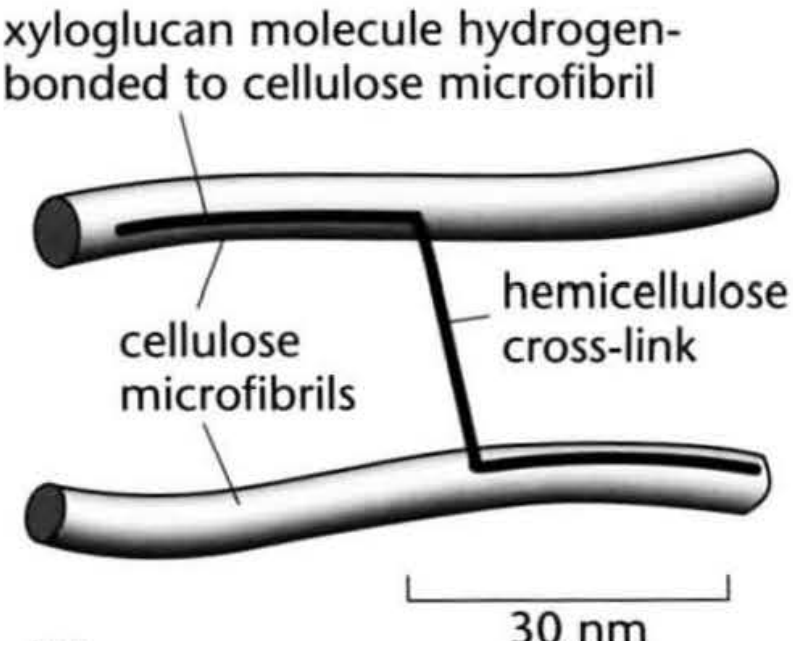

Figure 1-20 : Schematic representation of how hemicellulose molecules form cross-links. About 30 nm long, between adjacent cellulose microfibrils (Albersheim et al. 2011).

1.3.3 Summary

As a summary of plant cell walls, we can say that plant cells devotes ~10% of their genomes to CW biogenesis and that:

- CW is a dynamical extracellular matrix compartment
- CW constraints the shape of plants
- CW limits the rate and direction of cell growth
- CW is assembled of multiple layers: a primary cell wall and a secondary cell wall in vascular plants to improve their rigidity
- CW is highly organized and composed of polysaccharides and proteins
- CW in between two neighboring cells is separated by a middle lamella that is rich in pectin
- CW contains signaling molecules as well as enzymes
- CW participate in secretion of defense molecules.

1.4 Cell wall dynamics and mechanics

1.4.1 Cell wall dynamics

Plant cell wall is a dynamically remodeling system that needs to support growth and to be the first line of defense (Houston et al. 2016). In the previous section, we discussed about the CW architecture, which is a necessary step toward understanding molecular mechanisms behind plant cell growth through changes in cell mechanics and water uptake (Park and Cosgrove 2012).

The architecture of plant CW is required to be strong and rigid for supporting the plant. But it should also be lenient to allow for a controlled cell expansion (Bashline et al. 2014). Cell wall and turgor pressure are the two factors that are involved in the irreversible expansion of plant cells (Lockhart 1965). Such expansion involves various mechanical principles in cell extension, CW architecture, CW loosening or CW stiffening (Schopfer 2006). It is known that the cell growth starts with the extension of the CW, which in turns reduces the cell turgor and finally initiate the uptake of water to maintain the expansion of the cell (Bruce 2003). The idea of elasticity and plasticity can be traced back to 1940s in the works of A.N.J Heyn in relation to the plant growth (Heyn 1940). At that time, the word “plasticity” was commonly used to describe the adaptability of CW, but the terminology of viscoelasticity has been suggested a better use to the observed changes in the mechanical properties of CW (Nolte and Schopfer 1997).

Way back in 90s, Arabidopsis genes related to morphological changes were investigated by a combination of microscopy and molecular genetics (The Arabidopsis Genome Initiative 2000), but the knowledge about forces affecting Arabidopsis root cell remains limited (Akita et al. 2020). In summary, CW must be considered more as a living organ than a dead structure of the cell (Heyn 1940).

The dynamics of CW is illustrated by the multinet theory suggesting that new microfibrils are deposited continuously transversally on the inside of CW. During growth, there is a rearrangement of CW texture going from a perpendicular to a more longitudinal texture of elongated cells. This re-orientation only affects outer layers while inner layers remain more or less in transverse orientation (Roelofsen 1958). It follows that CW is involved in cell growth

with re-orientation of cellulose (Probine and Preston 1962). This model of orientation of cellulose microfibrils, from a perpendicular to a parallel orientation, has been confirmed by real-time imaging (Anderson et al. 2010). Cellulose microfibrils are fabricated by the cellulose synthase. A functional association between cellulose synthase and the dynamics of cellular microtubules has been demonstrated (Paredez, Somerville, and Ehrhardt 2006). However, it has been clearly shown that the production of material for CW synthesis is not coupled to the cell elongation rate (Refregier et al. 2004). It follows that cellulose is continuously deposited within the CW independently of cell expansion.

A particular important concept for our work is that using stress-strain diagrams, it has been shown that cessation of coleoptile growth is due to the loss of CW plasticity, i.e. an increase of CW stiffness, and not a loss of turgor pressure (Kutschera 1996). One of the origins of our work in nanomechanics of plant roots is the corollary statement, i.e., a loss of CW plasticity (increased stiffness) is a marker with the root growth arrest phenotype. More explicitly, our biophysical enquiry aims to determine the structural mechanisms underlying the stiffness increase during root growth arrest. Although there are many biophysical approaches to study micro and nanomechanics on plant CW to investigate the elasticity, viscoelasticity, viscosity, and plasticity of growing plants (Burgert and Keplinger 2013), in our work we essentially focus on atomic force microscopy (AFM).

1.4.1.1 Plant cell growth and cell wall loosening

Cell growth is defined by an irreversible increase in cell volume and surface area, but, upon environmental stress, a reduction of cell growth (by CW stiffening) is commonly observed in plants (Schopfer 2006). During plant growth, some cell enlarges 10-to-1000 fold in volume (Cosgrove 1997) that is regulated by external stimuli such as temperature, light, water, xenobiotics, as well as internal factors such as growth hormones (Preston and Hepton 1960). The complexity of cell wall growth results in a poorly-known pathways and mechanisms that control root CW plasticity (Somssich, Khan, and Persson 2016).

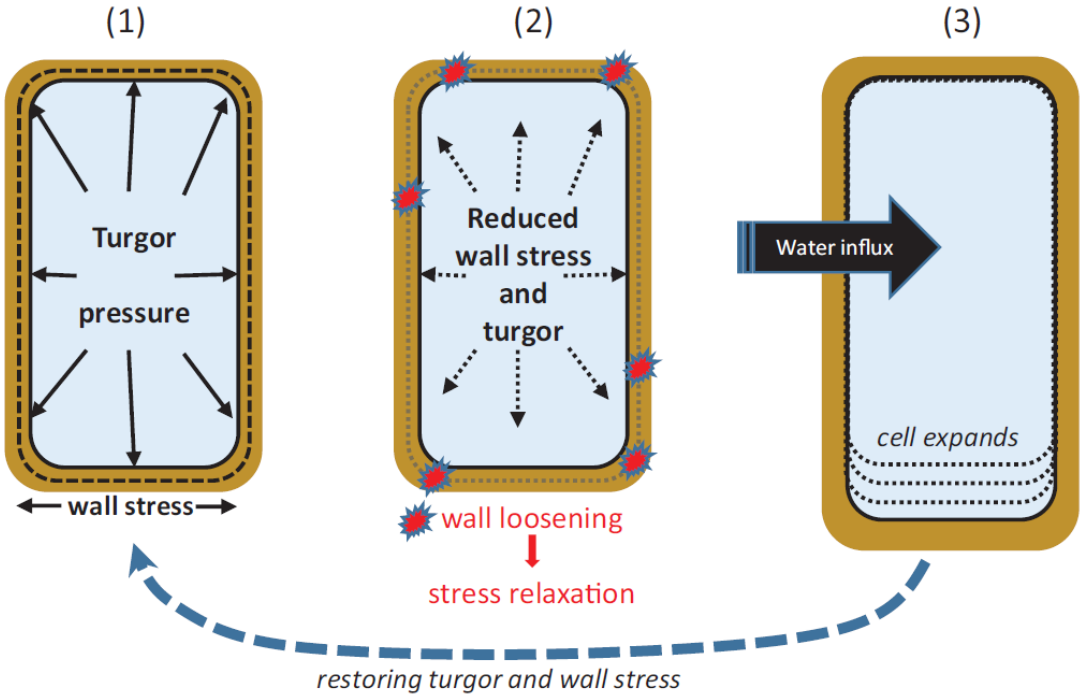

Figure 1-21: Biophysics of plant cell growth.
Illustration of the concept of wall stress relaxation and its connection with turgor pressure and induced water flows. (1) In a well-hydrated non-growing cell, the cell reaches osmotic equilibrium, with wall stresses counter-balancing the outward force of turgor pressure against the wall. (2) Growing cell walls are loosened, resulting in a reduction in cell wall stress and turgor pressure. This means that elastic elements in the cell wall shrink because of the slippage or bond breakage caused by wall loosening. (3) In response to the reduced cell turgor and water potential, water flows into the cell, elastically expanding the wall and restoring turgor and wall stress. This process is illustrated as discrete steps, but relaxation, water influx, volume enlargement, and turgor restoration occur simultaneously. Figure adapted from (Cosgrove 2016).

It is commonly admitted that the driving force of wall extension is the turgor pressure generated by the protoplast (Figure 1-21). The plant growth paradigm stipulates that growth be seen as a result of CW stress and CW mechanical properties (due to turgor pressure) (Lockhart 1965). In addition, growth requires biochemical loosening of CW that includes the breaking of cross-links in CW polymers (Lockhart 1967). In short, any changes that affect non-covalent binding forces between CW polymers is a potential cause of CW loosening (Talbott and Ray 1992). Cell expansion should not be confused with plant growth as an increase in cell production in the meristem is also correlated in root elongation (Beemster and Baskin 1998). Loosening CW agents include expansin, a 25 kDa protein with no-known enzymatic activity but that are believed to disrupt non-covalent bonding of CW polysaccharides (Edelmann 1995), cellulases to produce additional microfibrils, xyloglucan endo-transglucosylases/hydrolases (XTH), and hydroxyl radicals (•OH) that are produced locally in

CW by cell wall peroxidases from O_2^- and H_2O_2 (Cosgrove 2005). Other agents include the important role of Ca^{2+} that are suspected to disrupt pectin structures and favoring CW extensibility (Peaucelle, Braybrook, and Hofte 2012) or acidification caused by auxin which in turns increase the activity of expansins (Kierzkowski et al. 2012; Wang et al. 2013). Interestingly, acid-increased extension is inhibited by the presence of low concentration of metal ions (McQueen-Mason 1995).

1.4.1.2 Root growth arrest and CW stiffening

Previously we have seen that cell wall softening is a pre-requisite for cell expansion. Is it safe to postulate that CW stiffening is a key mechanism in the root growth arrest phenotype? What are the mechanisms of CW stiffening? The usual suspects should be all cross-linking capabilities in the CW: hydrogen bonds, ionic bonds with Ca^{2+} ions, covalent ester or ether bonds, and van der Waals interactions (Buchanan, Gruissem, and Jones 2015). The role of Ca^{2+} in plant growth is well known and it has been shown that an increase in Ca^{2+} inhibits growth and stiffens the CW (Tagawa and Bonner 1957; Cramer and Jones 1996) whereas a decrease in Ca^{2+} promotes CW extensibility and growth (Heath and Clark 1956; Weinstein et al. 1956). One creep-extension analysis showed that Al accumulation in the CW provoked a reduction of CW extensibility in wheat roots (Ma et al. 2004). An additional component in CW locking is the family of extensins (HPRGs) which lock polymers similarly to cloth pins. The incorporation of extensins into the CW appears as a preliminary step for blocking expansion (Carpita and Gibeaut 1993). Besides, another major actor in CW stiffening is the peroxidase family and their associated reactive oxygen species (ROS).

It has been shown for some time that peroxidases participate in the rigidification of CW; notably by converting feruloyl side chains to diferuloyl crosslinks (Fry 1979). Such oxidative crosslinks provide the irreversibility in cell elongation in the presence of O_2 and active peroxidases (Hohl, Greiner, and Schopfer 1995). This has been shown on rice (Tan et al. 1991) and maize (Hohl, Greiner, and Schopfer 1995) coleoptiles. Cell wall rigidification, which determines the growth response to an initial stress, has been shown to involve both basic and acidic peroxidases (Gaspar et al. 1985). Similarly, in the elongation zone where H_2O_2 could be detected directly in the CW, an increase in peroxidase activity was detected during the production of diphenoyl phenolic crosslinks (Goldberg et al. 1987). Cell wall-bond peroxidases

have been involved in the formation of isotyrosine bonds between glycoproteins such as extensins or diferulate bridges between polysaccharides. These peroxidase-driven crosslinking contribute to stiffening the CW during growth and reduce the rate of cell elongation (Fry 1986). In corollary, the presence of ascorbate, a peroxidase inhibitor, contributes to the elongation of roots in onions (Cordoba-Pedregosa et al. 1996). It has been suggested that the ascorbate reduces O_2 to H_2O_2 (non enzymatically) and Cu^{2+} into Cu^{+} provoking the production of $^{\bullet}OH$ by reaction of H_2O_2 and Cu^{+} leading to oxidative scission of polysaccharide chains (Fry 1998).

Peroxidase are thus considered as growth limiting and to stiffen CW by crosslinking their constituents (Dunand, Crevecoeur, and Penel 2007). However, contradictory effects have been observed between a role in cell elongation and growth restriction by consuming or releasing H_2O_2 and ROS ($O_2^{\bullet -}$, $^{\bullet}OH$) (Passardi, Penel, and Dunand 2004). For instance, ROS production was linked with an increase in Ca^{2+} influx which increases the root growth, but when extracellular Ca^{2+} is chelated, then the root growth rate decreases by 10-fold (Foreman et al. 2003). A dual effect of hydroxyl radicals ($^{\bullet}OH$) was observed by either activating crosslinking in CW through the activation of peroxidases or loosening the CW (and thus increase growth) by polysaccharide cleavage (Fry 1998). A most likely explanation for the opposite role of ROS production on cell growth is the dynamics in CW modification in which both stiffening and loosening are at competing equilibrium. A new hypothesis of CW remodeling under stress suggests that upon increase in ROS, there is a growth arrest whereas if the ROS production persists in time, then the growth restart due to the production of $^{\bullet}OH$ that breaks CW components without the requirement of peroxidases (Tenhaken 2015).

1.4.2 Cell wall mechanics

1.4.2.1 AFM to investigate cell wall stiffness

Experiments based on AFM stiffness tomography were useful in observing cell expansion where cell wall loosens only at specific regions, showing simultaneous existence of stiffer and softer regions in the cell wall (Radotic et al. 2012). In addition, results show that the walls of Arabidopsis cells in growth phase are much stiffer (0.6 MPa on average) than they are at the beginning and end of the growth process (0.1–0.2 MPa on average). These results prove the heterogeneous stiffness distribution at the cellular level. In addition, it is seen that the

thickness of the cell wall keeps on varying continuously. It appeared that the thickness varies between 1.2 - 2.1 µm, with a minimum on days 4, 17, and 20 and a maximum on day 10. This variable cell wall thickness partly influence cell wall stiffness (Radotic et al. 2012). Thus, the magnitude of the mechanical stress in the cell wall is related to the turgor pressure, the composition and organization of the cell wall, and the interface between the cells (Hayot et al. 2012).

1.4.2.2 Literature review on cell wall mechanics

As listed above, many factors affect cell wall stiffness. Atomic force microscopy can be instrumental in providing useful contributions with or without being combined with other quantitative methods/techniques. There are different aspects, which makes AFM-based indentation experiments, at either micro or nanoscale, to be explored.

1.4.2.2.1 In-vivo plant mechanics: AFM on living cells and tissues.

Preliminary studies based on indentation on living meristems have been performed (Milani et al. 2011; Peaucelle et al. 2011). Using large spherical AFM tip of 1 and 5 µm radius, it has been shown that a decrease in the tissue stiffness was a result of pectin de-methylesterification, i.e., the removal of CH_3 groups releasing a net negative charge in uronic acids. Chemical changes lead to changes in tissue mechanics, while changes in tissue mechanics were associated with organ initiation (Peaucelle et al. 2011). In the same year, Milani *et al.* characterized the elastic modulus of living shoot apical meristem (SAM) along with AFM imaging using a nanotip in this case (10-40 nm radius). In fact, to our knowledge the very first use of NuSil 1356 was mentioned in this article to immobilize the living meristem to study mechanics. It was based on their research that we implemented the use of same medical grade adhesive to keep plant seedlings intact. This research work suggested that shallow indentations done with sharp indenters provide us with the elastic modulus of cell wall, independently of the influence of turgor pressure (Milani et al. 2011).

Nanoindentation experiments do not distinguish the influence of the turgor pressure from the effects associated with deformation of the cell wall. Forouzesh *et al.* combined finite element simulations with nanoindentation experiments, where they treated the cells in plasmolyzed and turgid situation, to characterize the turgor pressure of cells *in vivo* while explicitly

separating the cell-wall properties from the turgor pressure effects (Forouzesh et al. 2013). Quantification of turgor pressure at tissue level from living tissues (onion epidermal peels) and single cells have also been studied (Routier-Kierzkowska et al. 2012; Beauzamy, Derr, and Boudaoud 2015). In the study of Beauzamy *et al.*, they implemented their own mechanical model to deduce turgor pressure and elastic moduli from single force displacement curve (Beauzamy, Derr, and Boudaoud 2015).

Apart from studying turgor pressure and elastic moduli, viscoelastic properties are also being studied in single living cells *in vivo*. With extensive computer modeling, storage (stiffness) and loss (loss of energy) parameters were determined by nanoindentation (Hayot et al. 2012).

Live cell imaging combined with AFM-based cell mechanics was used in modelling of cell wall. In particular, it has been successful in observing microtubule alignment along the maximal tensile stress direction within the cell wall during cell growth (Sampathkumar et al. 2014).

1.4.2.2.2 AFM on root tissues.

The main goal of our study is to know more about mechanical experiments on living plant tissues specifically roots of *Arabidopsis thaliana*. To our knowledge, the very first work on living Arabidopsis roots was initiated in 2012 to understand mechanical properties of living epidermal cells. Force-distance curves were collected from different root zones to study effects of surface heterogeneity or cell wall properties. Many questions arose during this preliminary work such as the immobilization of the sample and on its living state (Fernandes et al. 2012).

Our laboratory got involved in stiffness measurement of living *Arabidopsis thaliana* seedling roots in 2014. The context of this work was linked to a particular plant phenotype: root growth arrest (renamed in our study as root extension arrest) in connection with a deficiency in inorganic phosphate (Pi) (Balzergue et al. 2017). At this time, it was hypothesized that a phenotype linked to root growth should likely have some mechanical signatures. It was decided to perform nanomechanical indentations to extract elastic properties of living plant roots, on both wild type and mutants. The AFM work was initiated by Dr. Christian Godon in the CEA Marcoule who designed the original protocol; improvement of this protocol was one of the important task of my thesis. The conclusion of this preliminary work indicated that a metal stress due to Fe (unleashed by the absence of Pi in the growth media (Godon et al.

2019)) contributed to stiffen the external primary cell wall of plant roots. It was also demonstrated that the stiffening was concomitant with the action of peroxidase enzymes that were likely produced in response to reactive oxygen species (Balzergue et al. 2017).

More recent works that explored cell wall stiffness in growing Arabidopsis roots where roots grew on glass micropillar supports revealed a variable heterogeneity in cell wall stiffness at different zones and on different observation days (Akita et al. 2020). Lastly, a recent work analyzed the contribution of Arabidopsis TETRATRICOPEPTIDE THIOREDOXIN-LIKE 1 (TTL1) gene in the tolerance to osmotic stress. It was found that using the characterization of the stiffness of epidermal cell wall that TTL1 might play a role in the cell expansion during root growth. (Cuadrado-Pedetti et al. 2021).

1.4.2.3 Indentation techniques and their importance

The overall heterogeneity on the root surface comes from the organization of the cells that are joined together by the extra cellular matrix. Consequently, the overall stiffness of a tissue is not homogeneous, even at a single cell level (Peaucelle et al. 2011). In addition, shallow indentation is useful in calculating elastic modulus of the CW; while deeper indentations are probably useful for quantifying turgor pressure. In both the cases, the deformability of the overall surface structure does gets affected by superposition of all layers (Bidhendi and Geitmann 2019). The entanglement between turgor pressure and cell wall constituents makes it difficult to perform proper indentation experiments. For such a particular curved samples (the root), a cellular force mechanic instrument has been devised to help probing both section of plants: internal vacuole pressure and external cell wall by allowing a large range in indentation force (up to µN, (Routier-Kierzkowska et al. 2012)).

Thus, it is critical to design carefully indentation experiments that includes the indenting technique, the location of indentation, the choice of the indenter, and the calibration of the indenting technique. Calibration methods and issues are presented in section 2.6.6. The selection of the indenter remains a critical choice in nanomechanical experiments. There are three parameters for AFM indenters: stiffness, shape, and size. Regarding the stiffness, one is constrained by the stiffness of the sample. For stiff biological samples such as plant roots, which requires up to 10 nN pressure force, a spring constant around 0.1 N/m is appropriate. The size and shape is somewhat linked to commercially available cantilever where large tips

(radius > 100 nm) are often spherical or paraboloid probes. The advantage of large probes is to provide an overall surface stiffness, which is somewhat less sensitive to the nanoscale heterogeneity in the tissue surface. However, in our study, since we concern more about the nanoscale organization of the cell wall constituents, sharper tips (up to 40 nm) are satisfactory. For simplicity in the analysis of elastic properties, it is better to take an axisymmetric tip (square pyramid) with a well-defined half-opening angle. However, the exact shape of the indenter (pyramidal tip) still remains ambiguous at its apex; a major inconvenient for axisymmetric tips.

The work already done in this field provided us with some knowledge of cell wall surface, curvature effect, choosing suitable indentation tip, indentation depth limit, etc... All these factors were helpful in improving the experimental design by designing a robust protocol having least error prone data while targeting quantitative analyses.

1.5 Root response in the presence of metals

1.5.1 Phosphate deficiency and its consequences

Phosphorous is an important structural component of nucleic acids, phospholipids, and has a key role in cellular energetics through ATP. It is an essential micronutrient, fundamental for plant growth and development (Chiou and Lin 2011; Waidmann, Sarkel, and Kleine-Vehn 2020; Chen et al. 2022).

The problem of phosphate starvation is quite common and the second most limiting factor for biomass consumption (Abel 2011). About 70% of our cropland is phosphate deficient (Abel 2011; Waidmann, Sarkel, and Kleine-Vehn 2020). Plant root structure architecture (RSA) is highly responsive to phosphate availability in soil, in the form of inorganic phosphate ($H_2PO_4^-$ or Pi) (Chiou and Lin 2011). Availability of inorganic phosphate (Pi), which is the major form that plant roots absorb, is very low due to low mobility and high fixation, particularly in acidic soils (Chen et al. 2022). Pi often gets converted to organic phosphate by microorganisms or by interacting with cations (Chiou and Lin 2011; Waidmann, Sarkel, and Kleine-Vehn 2020). As a result, it becomes immobile in nature leading to uneven distribution and low accessibility.

In Arabidopsis, Pi deficiency results in the reduction of primary root (PR) length, while promoting lateral root elongation rate and root hairs (Sanchez-Calderon et al. 2005; Abel 2017). Plants can sense low Pi situation immediately and start responding by rapid cessation of cell elongation (<2 h) in the transition zone and inhibiting of cell division (<2 days) in the RAM (Abel 2017; Balzergue et al. 2017). Many studies link ROS accumulation under low Pi with reduction in PR length via cell death in meristem (Waidmann, Sarkel, and Kleine-Vehn 2020). As an alternative P fertilizer is thought to improve the yield of the crops but the efficiency of P fertilizer is low (10-25 %). Moreover, excessive application of P fertilizer results in a series of environmental problems such as water eutrophication (Chen et al. 2022). However, some plants tend to grow in Pi deficiency like maize or rice (Ward et al. 2008), which basically illustrate the ill-definition of Pi deficiency.

Apart from phosphate deficiency, another environmental issue is that of the acidic soils. Almost one third of our cropland is acidic in nature. Acidic soil leads to the solubilization of the metals in their oxidized ionic forms such as Fe^{3+}, Al^{3+} facilitating their entry inside the root

leading to metal toxicity. Metals target the root apex and their accumulation restrain the ability of the roots to absorb water and nutrients (Ward et al. 2008; Chen et al. 2022).

Thus, phosphate starvation under low pH situation leads to metal accumulation in plants, mainly aluminum and iron, thereby decreasing of primary root growth (Bournier et al. 2013).

In the last 20 years, it was found that root inhibition in –Pi situation was due mainly to excessive iron accumulation in the root tip (Svistoonoff et al. 2007; Ward et al. 2008). When iron is removed from Pi deficient medium, roots continue to grow. However, when Pi is removed in which Fe concentration remains unchanged, primary root growth is inhibited (Sanchez-Calderon et al. 2005; Ward et al. 2008). The presence of metals in low Pi situation leads to metal-Pi bonds, and Pi is thought to be released back to the soil in this metal-Pi bonds (Foy, Chaney, and White 1978; Abel 2017). It was suggested that manipulating iron concentrations can thus improve the crop production (Ward et al. 2008).

1.5.2 Role of iron and aluminum under phosphate deficiency in low pH.

Under normal situation when iron deficiency is sensed by plant roots, they release organic acids (OAs) in the rhizosphere that lowers the pH level. Organic acids, which are released during this phase, mainly citrate and malate, enable the capture of solubilized metal such as iron to improve their entry into the root system. Citrate appears to be a natural carrier of Fe regarding intra plant transportation. The solubility of iron depends on both their redox status and the environmental pH. While ferrous iron (Fe^{2+}) is soluble in neutral pH, ferric iron (Fe^{3+}) is insoluble (Morrissey and Guerinot 2009). Thus, soils do not lack Fe per se, but it may not be easily available to plants or when grown on alkaline soils (Brown 1978).

The above phenomenon occurs under sufficient phosphate concentration explaining the uptake of iron under normal conditions. However, under phosphate deficiency, the extent of root inhibition depends mostly upon the Fe concentration and pH value (Svistoonoff et al. 2007; Ward et al. 2008; Bournier et al. 2013). In short, root tip senses low Pi condition, not by detecting the concentration of Pi but by detecting the presence of increasing concentration of metals.

From our collaborators in CEA Cadarache, it was shown that both Fe and Al, trigger the accumulation of STOP1 (SENSITIVE TO PROTON RHIZOTOXICITY1) transcription factor in the nucleus, which further activates the transcription of the malate transporter gene ALMT1

(ALUMINIUM ACTIVATED MALATE TRANSPORTER 1) (Godon et al. 2019). STOP1 is not activated at higher pH more than 5.5 (Le Poder et al. 2022). Activation of ALMT1 leads to malate exudation. It is thought that exudation of small organic acids promotes plant growth by solubilizing scarcely available Pi and Fe nutrients, or by forming non-toxic complexes with Al^{3+} cations. However, malate efflux appears to inhibit elongation of root cells under –Pi by forming Fe-malate chelation participating in plant Fe Homeostasis (Balzergue et al. 2017; Mora-Macias et al. 2017). It has been found that malate chelates with iron to accumulate it in the apoplast region in the extension zone (EZ) and the stem cell niche (SCN) (Muller et al. 2015). Malate-Fe chelation within the apoplast leads to redox cycling of Fe mediated by the apoplastic ferroxidase LPR1 (LOW PHOSPHATE ROOT1), and possibly blue-light, in a Fenton-like reaction, generating reactive oxygen species (ROS). ROS accumulation leads to peroxidase dependent stiffening of the cell wall of the EZ (Muller et al. 2015; Naumann et al. 2022).

LPR1 protein is a multicopper oxidase with ferroxidase activity. LPR1 expression leads to apoplastic Fe^{3+} accumulation in the root apex and transition zone, which correlate with the sites of reactive oxygen species (ROS) generation and callose production (Muller et al. 2015; Abel 2017; Balzergue et al. 2017). Simultaneously, the PDR2 (PHOSPHATE DEFICIENCY RESPONSE 2) ATPase gets disrupted, which further down regulates the root patterning transcription factors SHORT ROOT and SCARECROW (Chiou and Lin 2011; Godon et al. 2019). The Fe^{2+}-oxidizing activity is said to target cell wall modifications to adjust RAM activity (Naumann et al. 2022). Eventually, the change in phosphate to iron ratio leads to remodeling of the root system architecture (Godon et al. 2019). In summary, PDR2 and LPR1/LPR2 are activated and expressed under Pi deficiency leading to primary root growth arrest (Svistoonoff et al. 2007; Chiou and Lin 2011; Balzergue et al. 2017). Deficient mutants *stop1* and *almt1*, in low phosphate and in presence of Fe, reduced the accumulation of Fe in the EZ, which allowed the plant to grow almost normally (Balzergue et al. 2017).

Of major interest to our work, accumulation of Al in CW, most likely interacting with pectin, has been suggested as early as 1995 (Horst 1995; Chang, Yamamoto, and Matsumoto 1999). Because of the net charge of Al^{3+} and the presence of negatively charged uronic acid-based saccharides in pectin, their interaction is normally expected. If so, it should be also expected for Fe^{3+} to bind to pectin, as it is known that Fe3+ accumulates in cell wall (Bienfait, Vandenbriel, and Meslandmul 1985). Such accumulation of metals has been accompanied

with an increase in CW stiffness (Ma et al. 2004). A summary of the growth arrest phenotype with the following actors: Pi, Al, and Fe, is presented in Figure 1-22 for WT roots and for mutants in Figure 1-23.

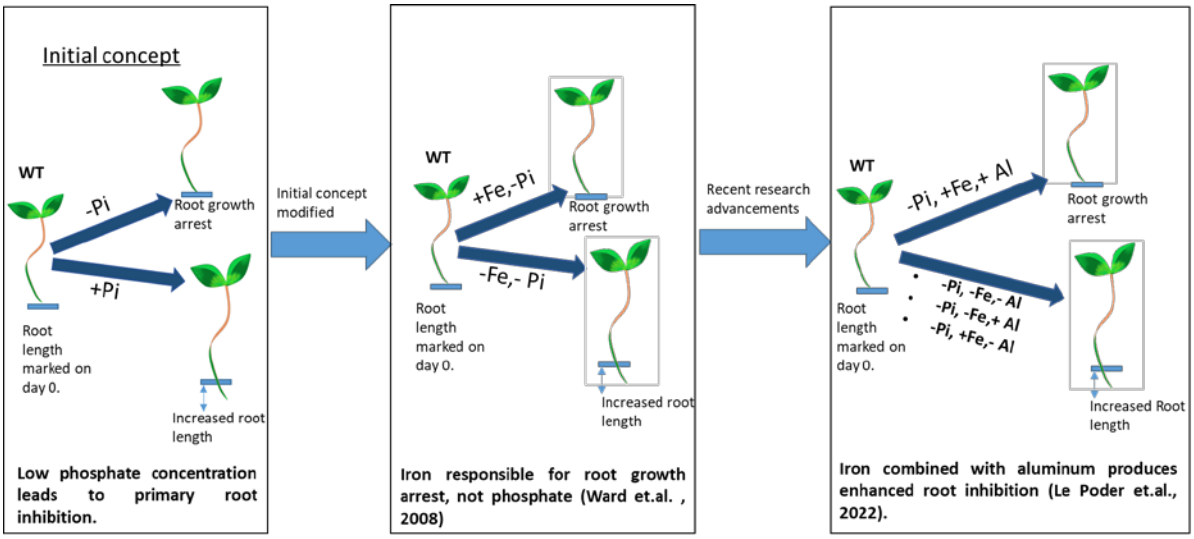

Figure 1-22: Plant root behavior in response to the presence of iron and aluminum.
Initially phosphate starvation was considered responsible for primary root growth inhibition. However, later on it was found that iron in low phosphate situation is responsible for root inhibition, and root grows normally in phosphate starvation in the absence of iron. Recently, it has been observed that iron when combined with aluminum leads to iron accumulation and eventual root growth inhibition.

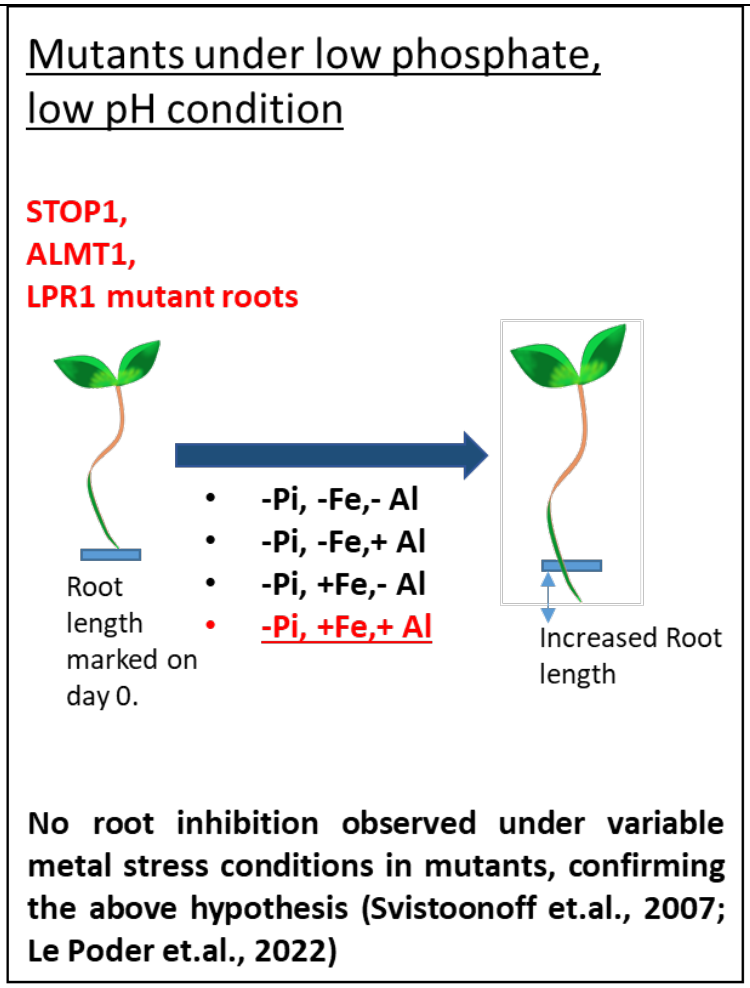

Figure 1-23: Mutant root tested under various stress conditions.
For more information and understanding, mutant roots were tested in stress conditions. STOP1-ALMT1 pathways were confirmed when their individual mutant roots were subjected to iron and aluminum combined stress, root growth was observed in both the cases. LPR1 mutants were tested in the presence of iron where root growth was observed, pointing towards the participation of LPR1 in WT for root inhibition.

However, as of today, there is no clear relationship between the accumulation of metals in plant roots, the possible stiffening of external primary cell wall, and the root extension arrest phenotype. As toxicity is intimately linked with the concentration of toxic elements, we plan to study the effect of various concentration of individual metals (Fe, Al), or their combination, on the stiffness response of the transition zone of Arabidopsis roots and observing a possible correlation with the root extension arrest.

MATERIAL AND METHODS

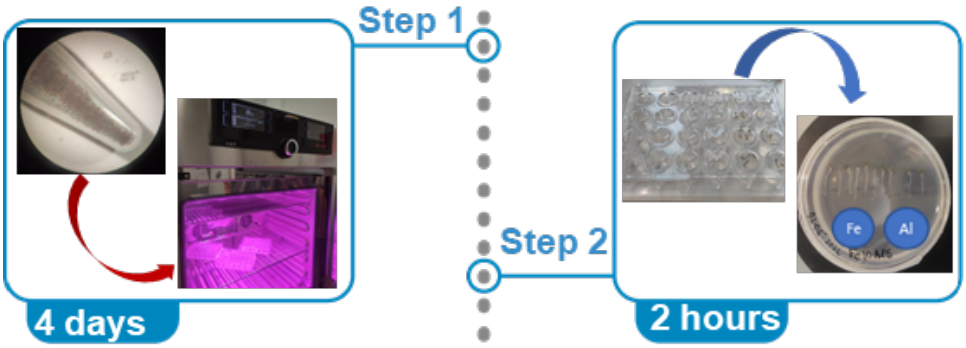

Step 1
Sow *A. thaliana* seeds on horizontal agar plates

Step 2
Transfer 4-days-old seedlings on Petri dishes with metallic stress

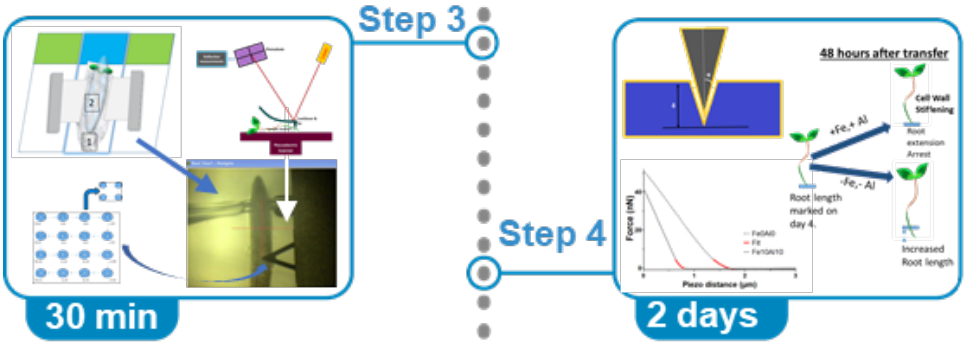

Step 3
Fix seedlings on glass slides and perform nano-indentation experiments with AFM

Step 4
Analyze force-distance curves to obtain elastic parameters and record phenotype (root length).

2 Materials and Methods

This chapter details the step-by-step guide of the complete protocol for measuring the stiffness of plant roots. The framework is inspired from the protocol manuscript that is attached in the annex 2 of this thesis. This protocol includes precautions, warnings, and additional notes that are useful for the reproduction of this work. I would like to acknowledge the existence of a preliminary protocol that was established by Dr. Christian Godon in 2014 and already published (Balzergue et al. 2017). The refinement of the protocol took me almost two years to reach its final content.

2.1 Materials

2.1.1 Biological materials

We used Arabidopsis thaliana L. (Heynh.) lines of Columbia (Col-0) or the Col^{er105} backgrounds as specified in (Bonnot et al. 2016). The *almt1*-51 mutant was previously published (Balzergue et al. 2017). Seeds were always provided by Dr.Thierry Desnos, CEA Cadarache.

2.1.2 Reagents

Caution When handling the reagents wearing of lab coat and gloves is advised. Follow the waste disposable rules as per your institute and country's safety guidelines. Reagents should be stored and prepared according to the manufacturer's recommendation. Refer to the appropriate material's safety data sheet.

1. 0.1 mM Cobalt chloride $CoCl_2$ (provided by T. Desnos, CEA Cadarache)
2. 0.1 mM Copper sulphate $CuSO_4$ (provided by T. Desnos, CEA Cadarache)
3. 0.47 mM Magnesium sulfate $MgSO_4$ (provided by T. Desnos, CEA Cadarache)
4. 0.5 mM Potassium iodide KI (provided by T. Desnos, CEA Cadarache)
5. 0.67 mM Calcium chloride $CaCl_2$ (provided by T. Desnos, CEA Cadarache)
6. 0.79 mM Boric acid or Hydrogen borate H_3BO_3 (provided by T. Desnos, CEA Cadarache)
7. 1 mM Sodium molybdate Na_2MoO_4 (provided by T. Desnos, CEA Cadarache)
8. 1.89 mM Potassium nitrate KNO_3 (provided by T. Desnos, CEA Cadarache)
9. 10 mM Manganese(II) sulfate $MnSO_4$ (provided by T. Desnos, CEA Cadarache)
10. 2.1 mM Ammonium nitrate NH_4NO_3 (provided by T. Desnos, CEA Cadarache)

11. 5 mM Zinc sufate $ZnSO_4$ (provided by T. Desnos, CEA Cadarache)
12. Agar sigma powder Sigma-Aldrich (A7921 Lot BCBZ7284)
13. Aluminium Chloride (provided by T. Desnos, CEA Cadarache)
14. Ethanol absolute (#4145872, Carlo Erba, Val de Reuil, France).
15. Iron chloride: $FeCl_2$: 15 M stock solution (Sigma, 44939)
16. MES-(2-(N-morpholino)ethanesulfonic acid, (Sigma, M8250)
17. Milli Q water (MilliQ, Direct8)
18. Potassium hydroxide (Sigma-Aldrich, 221473)
19. Saccharose (MPbio, 02904713-CF)
20. Sodium Dodecyl Sulfate (SDS) solution at 0.05 % (Sigma, L4390).

2.2 Equipment

1. Artificial LED light box: Indoor Led, 45W, 169 LEDs, 276 x 276 x 14 mm, full spectrum (www.cultureindoor.com).
2. Atomic Force Microscope, Dimension 3100 (Bruker, Santa Barbara, USA).
3. Atomic force microscope, JPK Nanowizard IV (*provided by INSERM Marseille*).
4. Autoclave machine.
5. Binoculars: Nikon SMZ800N, Nikon C-PS stand, Nikon plain 1X lens.
6. Cantilevers: The Pyrex-Nitride Probe (PNP-TR-50, NanoWorld AG, Neuchatel, Switzerland). (cant #2) has 200 µm-long silicon nitride cantilevers and integrated oxide sharpened, pyramidal tips with a height of 3.5 µm (and a 4 µm edge set-back), a resonance frequency of 17 kHz, and a 70 nm-thick gold coating.
7. Cover slips (Glass 24 x 40 mm): Agar Scientific (AGL462440-1).
8. Crystallization plate: Hampton Research, VDX plate HR3-140 (well capacity 3.5 ml, Area/well = 2 cm^2, plate dimension: 15 cm x 10.8 cm x 2.2 cm).
9. Eppendorf™ tubes: 1.5 ml safe lock tubes, Eppendorf, (0030.120.086).
10. Falcon™ tubes: 50 ml, Polypropylene graduated, conical bottom, blue screw cap, sterile, Greiner Bio-One, (227261).
11. Glass bottle: Duran, Ref. Dutscher no° 818014407
12. Glass slides: Knittel Glass, Braunschweig, Germany. Reference no. VS1137#1FKB.01 (ground edges 90˚, StarFrost 3 x 1 inch).

13. Laminar flow hood: Faster air, U.K., FlowFAST H 09 SA7010 (Horizontal Laminar Flow Cabinet, 3ft/0.9m).
14. Microtape: Euromedis, Neuilly-sous-Clermont, France, Anapore (9.14 m x 1.25 cm).
15. Microwave: 30L, 900w, Severin (mw7825.
16. Nanoscope V controller (Bruker, Santa Barbara).
17. Peltier-cooled incubator: Memmert, Schwabach, Germany, IPP 110+.
18. Petri dish: FALCON, (353004), 60 x 15 mm style.
19. Pipette motor: Starlab Ergo one FAST, (S7166-0010).
20. Pipette tips: Tipone (S1111-0700), 200 µl.
21. Pipette tips: Tipone, (S1111-6701), 1000 µl blue graduated tip.
22. Pipette: Gilson, SKU, (FA10003M) PIPETMAN L P20L (2-20 µL, Metal Ejector).
23. Pipette: Gilson, SKU, (FA10005M) PIPETMAN L P200L (20-200 µL, Metal Ejector).
24. Pipette: Gilson, SKU, (FA10006M) PIPETMAN L P1000L (100-1000 µL, Metal Ejector).
25. Probe holder: DTFML-DD (Bruker, Santa Barbara).
26. Screw cap: black polypropylene, open top, thread 8-425, Thermo Scientific (C4013-3A).
27. Screw thread: red PTFE / white silicone, septa for 12x32 mm standard, Thermo Scientific (C4013-60).
28. Silicone adhesive: NuSil Technology LLC, Carpinteria, CA, USA. NuSil MED1-1356.
29. Syringe filters: Millipore Millex-GV, (SLGV033RB, 0.22 µm, PVDF, 33 mm, gamma sterilisable).
30. Syringe needle: Terumo Neolus. (NN-2138R, 0.8x40mm).
31. Thermal gloves: Versa touch, knitted thermal gloves with PVC dots, oracle code 115106, ASP = 256363
32. Tweezers (to pick seedlings): Techni tool, Excelta 1-S Tweezers (Style 1s, Fine, Slender, Stainless Steel, 4.5").
33. Tweezers: Techni-Pro SMD Tweezers (758TW401, Style SM104, Anti-Acid/Anti-Magnetic, Stainless Steel, Bent, 4.7").
34. Vials: Thermo Scientific 2 (C4013-2, 12x32 mm, AMB Screw thread vials)
35. Wooden sticks.

2.3 Software.

1. Atomic J (Hermanowicz et al. 2014), https://sourceforge.net/projects/jrobust/.
2. ImageJ (Schneider, Rasband, and Eliceiri 2012), https://imagej.nih.gov/ij/ and its plugin Neuron J. (Meijering et al. 2004), https://imagescience.org/meijering/software/neuronj/.
3. AFM Software For force acquisition, Nanoscope_7.3 by Bruker.
4. Prism, v5 or v8, GraphPad, https://www.graphpad.com/.

2.4 Reagent set up

While preparing and handling the reagents, it is advised to wear gloves all the time. Glassware should be clean and dry (preferably baked) before use. At the end of preparation, they should be filtered through 0.22 µm membrane filters.

2.4.1 MES Buffer (pH 5.6)

MES Buffer (pH 5.7) (170 mM stock solution = 3.62 g in 100 mL H20); adjust the pH with 10 N KOH. Filtrate (0.2 µm) and store at 4 °C.

2.4.2 Nutrient solution preparation

Nutrient solution was supplied by T. Desnos (CEA, Cadarache). Detailed measurement of individual solutions is provided here.

Preparation of individual stock solutions of each nutrient

1. 1 M $MgSO_4$, $7H_2O$ (246.5 g in 1 L milliQ H_20). Filtrate (0.2 µm) and store at 4 °C.
2. 1 M NH_4NO_3 (80 g in 1 L milliQ H_20). Filtrate (0.2 µm) and store at 4 °C.
3. 1 M KNO_3 (101.1 g in 1 L milliQ H_20). Filtrate (0.2 µm) and store at 4 °C.
4. 1 M $CaCl_2$, $2H_2O$ (147 g in 1 L milliQ H_20). Filtrate (0.2 µm) and store at 4 °C.
5. 10 mM KI (166 mg in 100 mL milliQ H_20). Filtrate (0.2 µm) and store at 4 °C.
6. 100 mM H_3BO_3 (618 mg in 100 mL milliQ H_20). Filtrate (0.2 µm) and store at 4 °C.
7. 1 M $MnSO_4$, H_2O (6.76 g in 40 mL milliQ H_20). Filtrate (0.2 µm) and store at 4 °C.
8. 1 M $ZnSO_4$, $7H_2O$ (28.7 g in 100 mL milliQ H_20). Filtrate (0.2 µm) and store at 4 °C.
9. 25 g/L Na_2MoO_4, $2H_2O$ (1.25g in 50 mL milliQ H_20). Filtrate (0.2 µm) and store at 4 °C.
10. 2.5 g/L $CuSO_4$, $5H_2O$ (125 mg in 50 mL milliQ H_20). Filtrate (0.2 µm) and store at 4 °C.
11. 2.5 g/L $CoCl_2$, $6H_2O$ (125 mg in 50 mL milliQ H_20). Filtrate (0.2 µm) and store at 4 °C.

Table 2-1: Composition of the 50X nutrient solution stock (1L)

Reagent	Final concentration	Amount
$MgSO_4$, $7H_2O$	23.4 mM	23.4 mL
NH_4NO_3	103 mM	103 mL
KNO_3	94.5 mM	94.5 mL
$CaCl_2$, $2H_2O$	33.5 mM	33.5 mL
KI	25 µM	2.5 mL
H_3BO_3	39.3 mM	39.3 mL
$MnSO_4$, H_2O	523 µM	523 µL
$ZnSO_4$, $7H_2O$	251 µM	251 µL
Na_2MoO_4, $2H_2O$	52 µM	400 µL
$CuSO_4$, $5H_2O$	7.3 µM	728 µL
$CoCl_2$, $6H_2O$	5.26 µM	500 µL
milliQ H_2O	n/a	701.398 mL
Total	n/a	1L

Filtrate (0.2 µm) and store it at 4 °C.

2.4.3 Agar media preparation

a) Pour 4 g of agar powder in 500 mL glass bottle.
b) Add 2.5 g of sucrose to the bottle.
c) Add 500 mL of milliQ H2O water and stir to dissolve the powders.
d) Take the bottle to laminar hood.
e) Open new sealed 10 mL pipette.
f) Add 10 mL of the solution nutritive to the bottle in the sterile laminar flow hood with the help of pipette.

   Note: Nutrient solution is maintained in sterile environment and in the refrigerator

g) After adding the nutrient solution, seal the bottles with the autoclave tape.
h) Place in an autoclave for sterilization (120˚C, 30 min). After autoclave swirl gently the bottle while it is still warm. This helps agar to dissolve uniformly and is not separately solidified. Figure 2-1 below shows how it happens after autoclave.

Note: After autoclave, the sterilized materials are opened in the clean laminar hood only. It is better to make small batches of agar bottles instead of big bottles (e.g. 1L) because repetitive heating leads to loss of water and increase salt concentration.

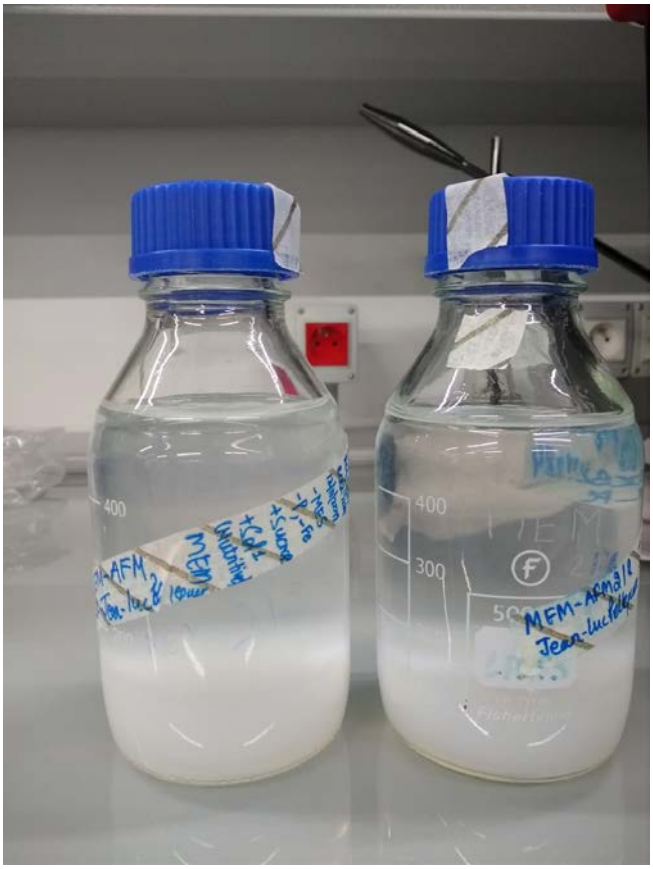

Figure 2-1: Picture showing bottle with solidified agar after autoclave.
If it happens, reheat (not boil) the bottle again to get uniform consistency of agar media.

2.4.4 Growth solution

Table 2-2: Growth solution components

Reagent	Final concentration	Amount
50X nutrient solution	n/a	20 mL
Sucrose	5 g/L	5 g
MES solution	3.4 mM	20 mL
milliQ H_20	n/a	960 mL
Total	n/a	1000 mL

Nutrient solution added in sterile condition.

2.4.5 Other individual stock solutions

a) 500 µM phosphate solution (KH_2PO_4 (1 M stock = 13.61 g in 100 mL milliQ H_20). Filtrate (0.2 µm) and store at 4 °C.
b) 10 µM $FeCl_2$ solution (10 mM stock = 0.12 g in 100 mL milliQ H_20). Filtrate (0.2 µm) and store at 4 °C.
c) 10 µM $AlCl_3$ solution (10 mM stock = 0.13 g in 100 mL milliQ H_20). This stock solution should be prepared with caution in a fume hood (use gloves and safety glasses) as the addition of water to the $AlCl_3$ powder releases vapor of hydrochloric acid. Furthermore, this solution must be prepared in a glass beaker as the dissolution of $AlCl_3$ is exothermic. Slowly add the water onto the powder and swirl the beaker until complete dissolution of the powder (few minutes). Do not autoclave this solution; store at 4 °C.

2.5 Equipment set up

2.5.1 Laminar flow hood.

Laminar flow hood protects our workspace, when dealing with sterile biological reagents or samples, from dust and air borne contaminants by maintaining a constant unidirectional flow. Reagent preparation and growth media preparation are done using a laminar hood. We need to activate the hood before using.

a) Open the screen and press power button to start and set.
b) Wait for the calibration.
c) When the speed is 0.40, the hood is ready to use.
d) Clean the surface with 70% ethanol before to avoid any previous contamination if it is present.
e) We should always wait for 5 minutes before using the hood.

2.5.2 Peltier cooled incubator

After sowing the seeds in growth media using laminar hood, plants are kept in Peltier cooled incubator for four days. Following are steps mentioned to activate the program.

a) Peltier cooled incubator (Memmert IPP+ 110), Figure 2-2, is an instrument which controls the temperature of the chamber and regulates it.

b) A LED light box is inserted at the top of the incubator.

c) This artificial light box has a mixture of red (600-630 nm), blue (470 nm), and white color (3000 K – 6500 K) of LED lights, which corresponds to a “full spectrum”.

d) Both chamber and LED lights are programmed with a timer set up.

e) Temperature in the day programmed to 24˚C and LED lights turn on for 16 hours. In night, lights turn off with the temperature of 21 ˚C.

f) Software based program is activated to run custom-made settings as mentioned above.

Note: It takes 24 hours for the program to start. We need to turn on the machine one day before use.

Figure 2-2: Peltier-cooled incubator to grow Arabidopsis thaliana seedlings
Light is provided by an added indoor LED box (purple light). The day/night program on the incubator requires the development of a short running sequence of events using a Memmert proprietary software (AtmoCONTROL 2.9.2.0 29/01/2019). Importantly, on the IPP+ 110, when activating the program, it automatically starts at the beginning of the programed cycle (likely the morning), which implies that the program must be activated 24 hours before use.

2.5.3 Pressure sensitive silicon adhesive (NuSil)

NuSil is a pressure sensitive adhesive (PSA) that has a property to stretch while polymerizing. It has a composition of 50 % of silicone and 50 % of ethyl acetate. It has a low viscosity (245 mPa•s), which makes it easy to pipet. Ethyl acetate evaporates with time leaving behind only silicone that gets polymerized with time. NuSil adhesive tends to polymerize with time when stored in any plastic material (ethyl acetate is also stored in dark glass bottles). If they are stored with half-empty bottle for longer duration, the air inside the bottle can lead to partial drying of the adhesive. Thus, NuSil must be stored in glass aliquots of 1 mL. One of the great advantages of NuSil is its high viscosity that allows relatively easy manipulation. These glass vials are filled up to the brim with NuSil, then sealed with a rubber-seal cap tightly. To fill the vials, it is necessary to use a sealed syringe instead of classical pipette tip. This way they are stored in small quantities and last long. For three-year experiments, almost ¾ of the 1L glass bottle is used.

Note1: We prefer NuSil over other adhesives because it has a particular characteristic of stretching while drying, which was not reproduced with other PSAs. For the nanomechanical experiment, it is crucial that the end of the root tip is appropriately fixed on the glass slide since measurements are performed about 500 µm from the root tip. Because of the root capping, the tip of the root hardly bends like the rest of the root. This macroscopic increase in elasticity of the root tip was the major source of the attachment of root tips on glass slides.
Alternative: The NuSil used in our work is difficult to obtain because of logistical issues with the supplier that hardly deliver small bottles. However, alternative PSA exists and we also tried Silicolease PSA 408 (cat #117149, Elkem, France), but was not pursued due to the higher viscosity (from 40,000 to 120,000 mPa•s compared to 245 mPa•s for NuSil) and the change of solvent (toluene).

2.5.4 AFM set up.

2.5.4.1 AFM instrument

Indentation experiments are performed in liquid medium with a Bruker Dimension 3100 AFM Scanning Probe Microscope (Figure 2-3). This AFM allows a large stage in which large samples

could be positioned beneath the AFM cantilever. Before starting measurements, several preparation steps need to be performed each time.

2.5.4.2 Probe holder

A special probe holder is required when experimenting AFM cantilever in fluid, see Figure 2-4. This holder is designed to allow the laser light to reflect of the cantilever in solution while keeping the scanner tube from coming into contact with the fluid environment. We used DTFML-DD probe holder, which is capable of holding triangular PNP cantilever well enough during indentation experiments.

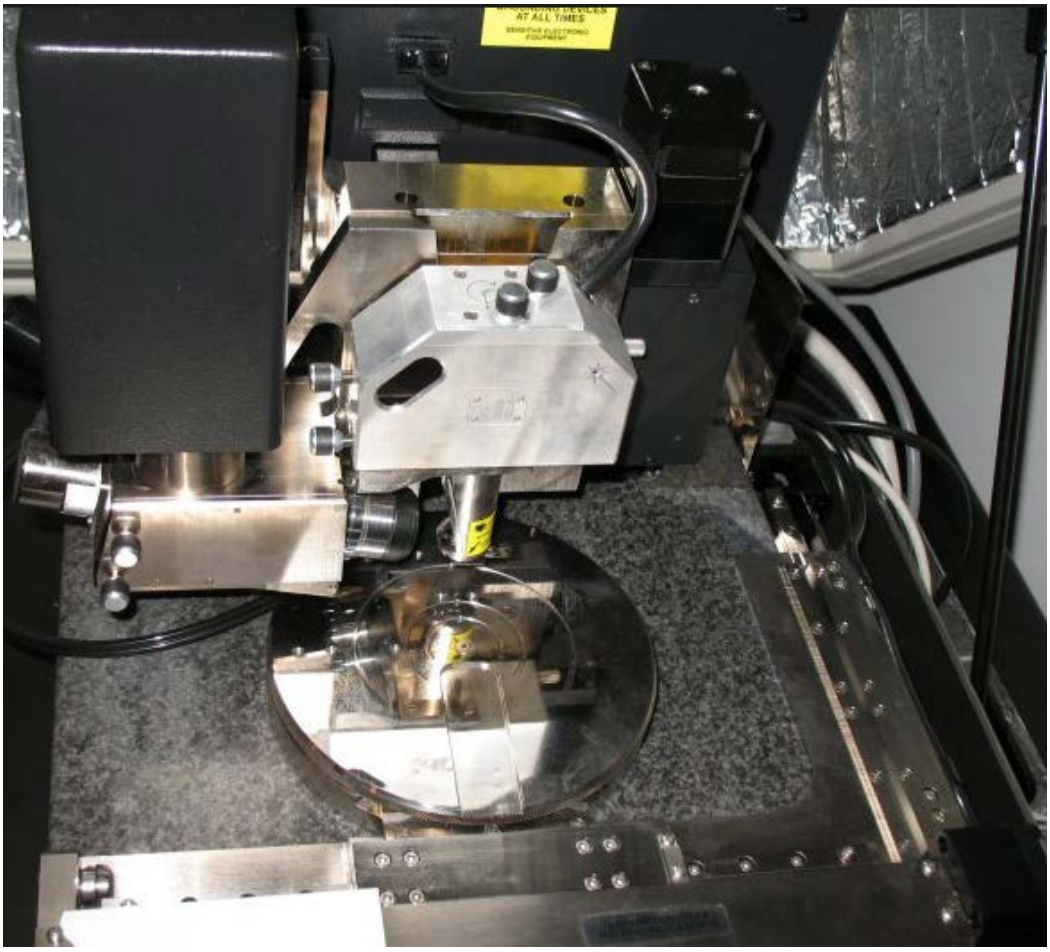

Figure 2-3: AFM Dimension 3100 SPM.
Instrument used for measuring nanomechanical response in plants A large motorized stage (center steel circle) allows easy adjustment of very large samples. The piezo scanner is displayed vertical and perpendicular to the stage while the digital camera is on the left side of the picture.

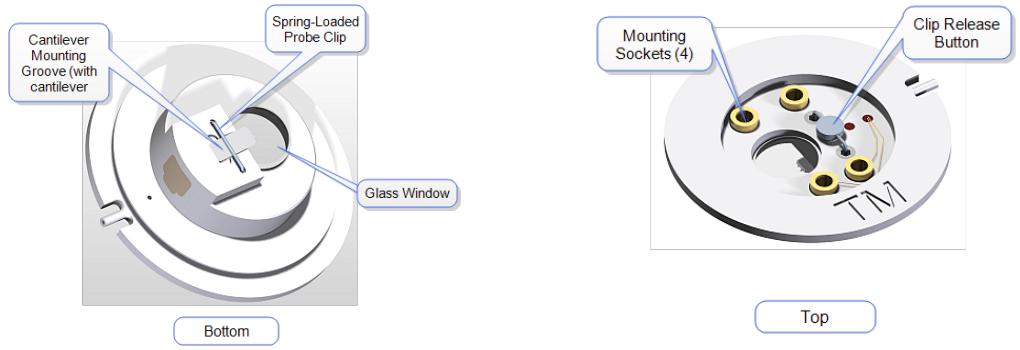

Figure 2-4: DTFML-DD liquid probe holder bottom and top view.
Bottom view showing the groove where the probe is mounted and clipped by a a U-shape spring. The Top part shows the 4 sockets which are fixed to the piezo scanner and the clip release button, which when pressed releases the cantilever (Bruker Corporation 2011).

2.5.4.3 Cantilever set up

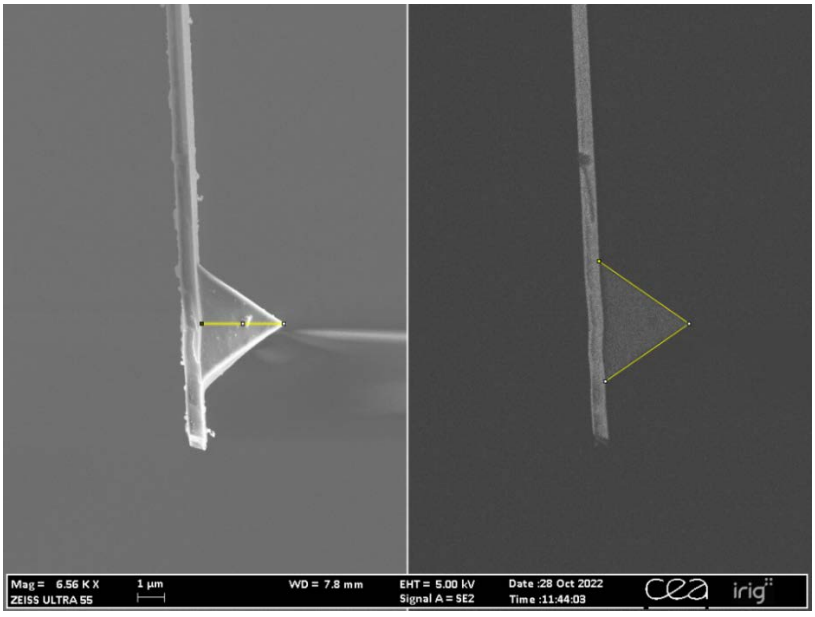

Figure 2-5: Scanning electron microscopy image of a used PNP-TR cantilever.
A secondary electron image is on the left and a backscattered electron image is on the right. Tip height and opening angle are highlighted in yellow and were measured using ImageJ: 3.05 µm in height (left) and an opening angle of 69.27°. The manufacturer's data indicates a tip height of 3.5 µm and a half-opening angle of 35°. Image acquired by Daphna Fenel (IBS/MEM) with the help of Bérangère Moreau from the CEA Grenoble (IRIG/DEPHY/MEM/LEMMA).

We used Pyrex nitride cantilevers (PNP) tips during the whole duration of our experiments. The PNP tip has a square pyramidal symmetry, its low sharpness (~10 nm nominal radius), a half-opening angle of 35°, which was verified by SEM measurements, and a proper spring constant for stiff plant root tissues (nominally 0.08 N/m). An SEM image shown in Figure 2-5.

The total mass of such a cantilever is about 130 ng, a very negligible mass compared to a single seedling root (~0.5 mg).

2.5.4.4 Laser Alignment

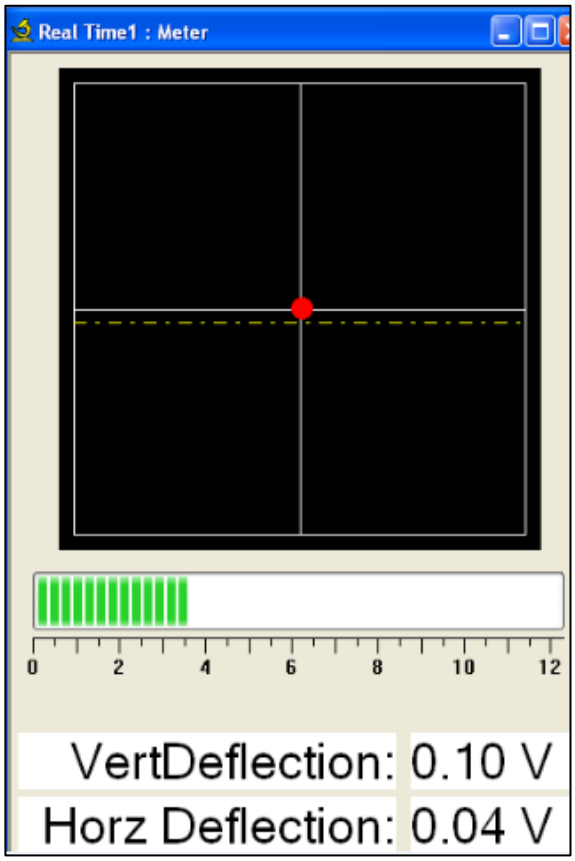

Figure 2-6: Laser alignment representation
Here the red dot shows the laser position. Laser is initially centered with a maximum signal strength (SUM in green bars, ~3.5 V) is achieved for good quality of data acquisition.

Laser alignment is important in regulating signal/noise ratio, cantilever deflection etc., useful in acquiring better calibration and thermal parameters. It helps in defining the quality of our data. Laser positioned on the top of cantilever is reflected on to photosensitive detector, in which the change in reflection position modifies the voltage read out signal.

Focusing the laser on the top of cantilever tip is done manually with the help of the camera. Once the laser is aligned on the cantilever, we verify there is an appropriate laser sum signal displayed on the image monitor (see Figure 2-6). Typical laser sum values are 3.5-4V in liquid medium. The laser signal is centered using the photodetector adjustment knobs located on

the left side of the Dimension head. The position of the laser is denoted by a red dot on the detector schematic as shown in Figure 2-6**.**

2.5.4.5 Additional parameters

AFM runs with a Nanoscope V controller and the Nanoscope 7.3 software using the picoforce module. Indentation of plant root surface was performed with approach-retract curves using a ramp size of 3–4 µm, a scan rate of 0.5 Hz, and 4096 points per curve. Ramp size was adjusted using a relative set-point threshold so that an indentation of about 0.5 µm was achieved.

2.6 Detailed nano mechanical measurements

Note: From seed sterilization step until preparation of liquid growth solution step, perform all the steps under the laminar flow hood wearing gloves.

2.6.1 Plant growth/ seed harvesting

During our project, seeds were harvested and supplied by Thierry Desnos (CEA, Cadarache).

2.6.2 Seed sterilization

As the seeds are harvested in the natural climate, they tend to have some contaminations by bacterial or fungi spores. Thus, sterilization becomes necessary after harvesting. In general, seeds are not uniform in size. The large ones have more probability to germinate than the smaller ones as the later are not mature enough. To homogenize the germination rate and seedling size, small seeds were screened out with a nylon mesh. Normally after harvesting, seeds are stored in small 'labelled' glassine seeds envelope. In order to store seeds for longer duration it is better to store at 4°C freezer in low hygrometry.

Caution: Do not use plastic for storage due to static effect.

a) Pour small quantity of seeds (an equivalent of around 50 µL or less) in the Eppendorf tube.
    i. It is better to label the Eppendorf with the name of the seed line on it with date.
    ii. Cover the label with Para film or tape so that the label does not fade out.

b) Add 1 mL of washing solution (SDS 0.05%, EtOH 70%) using sterile pipette tip.

Additional information: Seeds are cleaned and sterilized in a sterile environment. SDS has detergent like properties, which helps in cleaning the seeds. However, higher concentration of SDS should not be used as it can denature the sample leading to seed coat breakdown.

c) Close the cap and invert the tube upside down for 2-3 minutes gently to expose all the seeds with the liquid solution.
d) Let the seeds settle down afterwards.
e) Now, place the pipette to bottom of the Eppendorf, push two times in the washing solution gently so that seeds are suspended to the sidewall of the Eppendorf.
f) Carefully pipette out the liquid with the help of the tip and discard; avoid taking out the seeds!
g) Wash seeds with 1 mL of ethanol (96%). Gently shake Eppendorf for 1 min minimum. Pipette out the ethanol similar way as the previous step; avoid taking out the seeds!
h) Dry the seeds. Keep the Eppendorf open for at least 1 hour under the laminar flow hood, or until dry.
i) Before storing seeds, check for their dryness after sterilization. Seeds are kept at room temperature for short storage, and in 4°C with low hygrometry for long storage.

   Note: Any moisture content left afterwards affect the germination capacity. If not dried enough, the moisture content left, can damage the outer seed coat, opening it before germination.

j) Sterile seeds can be stored for up to 3 months. When kept for a longer time, the germination rate decreases with time, and seeds do not germinate synchronously.

2.6.3 Culture plate preparation

The seedlings need to be grown for four days before nanomechanical experiments. Traditionally, seedlings are grown in large Petri dishes. Instead, we found that the plants grow

better in crystallization plates, in particular regarding straightness of roots. It is important to have straight root ends for indentation experiments to avoid any external stiffness caused during growth i.e., root curling effect. These crystallization plates are suitable for growing plants for 4-5 days only.

2.6.3.1 Heating the agar

a) Normally agar solidifies at room temperature form. Slightly unscrew/loosen the lid of the bottle without fully opening it.

   Caution: Opening the lid in air will make the solution non-sterile. Remember to loosen the cap slightly. If not, bottle will burst during heating (it is important to wear a protective glove and goggles). Normally when it is heated with lid closed, it become difficult to open the bottle later because of the pressure.

b) Place the bottle in microwave at full power.

   Note1: Timing for heating is proportional to the volume of the solution in the bottle. Take out the bottle after 1-2 minutes or when it is partially melted. Swirl gently for 2-3 minutes. It helps to even out the heat and dissolve agar completely. The goal is to melt and not boil agar. If needed, place it back into the microwave for 30-40 seconds each time.
   Note2: Excessive heating can lead to water evaporation, which changes the concentration of nutrients.
   Important: While heating, make sure to wear thermos-protective gloves to handle the hot bottle and not burn yourself.

2.6.3.2 Preparing culture plate (perform all steps in laminar flow hood)

a) In a 50 mL falcon bottle, add 30 mL of melted agar solution and 600 µl of MES buffer solution.
b) Add 3 µL of $FeCl_2$ from 10 mM stock. Final $FeCl_2$ concentration = 1 µM. In all our experiments, there is a minimum concentration of Fe of 1 µM.

c) Falcon tube is used here so that it is easy to mix well all the solutions. Gently invert upside down the tube to mix well.
d) Pour carefully medium solution to the wells of crystallographic plate up to the brim.
e) Allow the medium to cool down at room temperature until solidifies.
f) Spread the seeds onto the medium and align them evenly with a sterile wooden stick. Approximately 10-12 seeds in each well.

Note1: If more seeds are poured, they will have less space to grow and they reduce the amount of nutrients available for each seedling.
Note2: To adjust extra seeds in case many seeds are poured accidently in one well, keep two wells without seeds.

g) Slightly dip the seeds inside agar so that the seeds have better contact with agar. This helps the roots to grow downwards and straight.
h) Pour some water in 2 or 3 empty wells of culture plate to keep high hygrometry for next 4 days.
i) Seal the plate with the micro-pore tape. Porous nature of the tape allows aeration and prevents water evaporation outside the plate.
j) Place the plate in Peltier cooled incubator for next 4 days with a day/night cycle of 18/6 hours and corresponding temperature of 24°C/21°C.

Additional Information: When preparing media, one should always take care of precision while scaling/measuring various ingredients. Agar has the property to thicken when it gets cold which makes a solid base replicating like a soil base. Sugar within the medium is responsible for affecting plant growth. It is the major component in the structure of the cell wall. Solution nutritive is a mixture of various minerals, which are essential for growth, present in the soil naturally.

2.6.4 Transfer media preparation

To stress seedlings with various abiotic metal stresses, seedlings need to be transferred from their original growing conditions to the stress conditions. These Petri dishes are prepared on the day of the experiment.

For stress medium, (in case of Fe10Al5 condition):

a) Use small Petri dish of 60 x 15 mm style.
b) Label the bottom of the petri dish with the stress conditions including date.
c) Add 15 ml of melted agar and 300 µl of buffer solution. Add 5 µM of $AlCl_3$ (or 7.5 µL from 10 mM stock), 10 µM of $FeCl_2$ (15 µL from 10 mM stock).

Note1: Petri dish is further checked after 24 - 48 hours for observing the phenotype.

Note2: Petri dishes are kept in the incubator throughout the whole experiment. Seedlings are systematically transferred to a Petri dish for 2h. Either the Petri dish is regular agar or it contains agar plus a metal stress (Fe or Al, or both).

2.6.5 Attach cantilever to the scanner

Nanomechanical experiments are performed with an atomic force microscope, here with respect to Dimension 3100 in our case.

a) Using the binocular and dedicated tweezers, gently lift the cantilever tip from the cantilever box and place it straight into the groove of the liquid cell holder.

Note: Improper fitting of the cantilever might lead to the error prone thermals data for the tip. In case of incorrect sensitivity characterization, the thermal tuning will provide an erroneous cantilever spring constant. Figure 2-7 shows the poor data acquisition due to improper fitting of the cantilever.

b) Attach the liquid cell holder to the piezo scanner. In case of the Dimension 3100, lift the piezo significantly upward (away from the sample)

Note: Make sure that the scanner is far from the sample stage so that the tip does not hit the surface below and breaks.

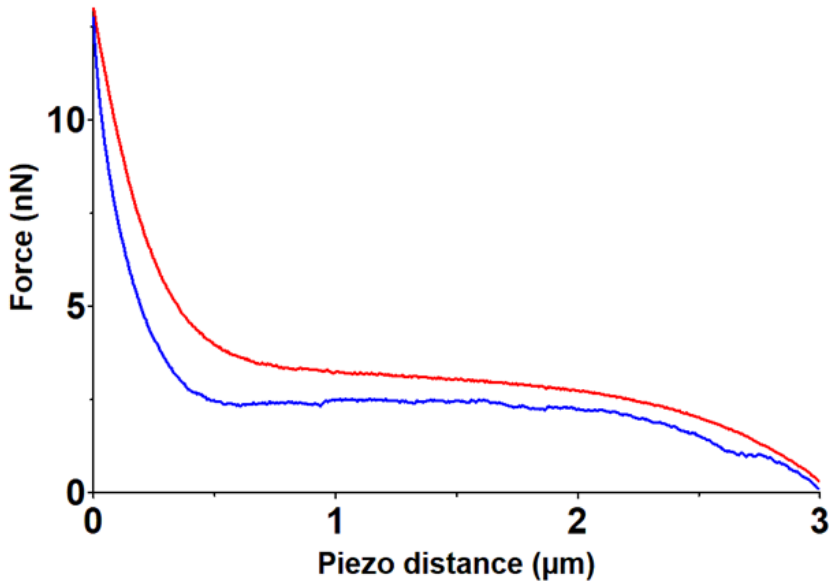

Figure 2-7: Example of a FD curve with a bent baseline.
The approach and retract curves are in red and blue, respectively. The total ramp size is 3 µm while the maximum applied force is about 13 nN. Sometimes such a bending is a sign of a poor set-up in the optical AFM system. Other reasons could also explain the non-flat baseline such as a cantilever still in contact with the surface at the end of the retract ramp. If such a FD curve is obtained during the calibration, then re-adjust the cantilever in the probe holder and restart the calibration procedure.

2.6.6 Calibrate the AFM system

2.6.6.1 Perform calibration in air.

a) Adjust the laser beam on the tip while preserving the highest sum
b) Perform a contact-based force-distance curve (ramp size of 3 µm, frequency of 0.5 Hz, 4096 points per curve).
c) Determine the deflection sensitivity by measuring the slope of the curve in contact with the surface.
d) Repeat the previous step several times until sensitivity values are constants.
e) Perform a thermal tuning to determine the spring constant of the cantilever.
f) Save the computed spring constant and repeat the previous step until the spring constant valuess are uniform.

2.6.6.2 Perform calibration in liquid

a) Repeat previous step but in liquid environment
b) For the Dimension 3100, only the deflection sensitivity can be performed in liquid.
c) Set the sensitivity values obtained in liquid as final values.
d) If the AFM system can perform thermal tuning with frequencies below 1 kHz, then also perform the thermal tune in liquid, otherwise, keep the spring constant obtained during the previous calibration in air.

Note: Keep the cantilever in liquid medium for an hour before measuring deflection sensitivity to avoid any artefacts due to temperature variation.

2.6.7 Fixing plant root on glass slide

2.6.7.1 Glass slide set up

a) Take two standard glass slides plus two rectangular cover slips and assemble them as shown in Figure 2-8**.**
b) Take a micropore tape and place it over the cover slip to stick to the glass slide.

Note: make sure that both the coverslips are at the same height in the middle of the slide and that 2/3rd of width is touching the slide and 1/3rd of it is outside the slide.

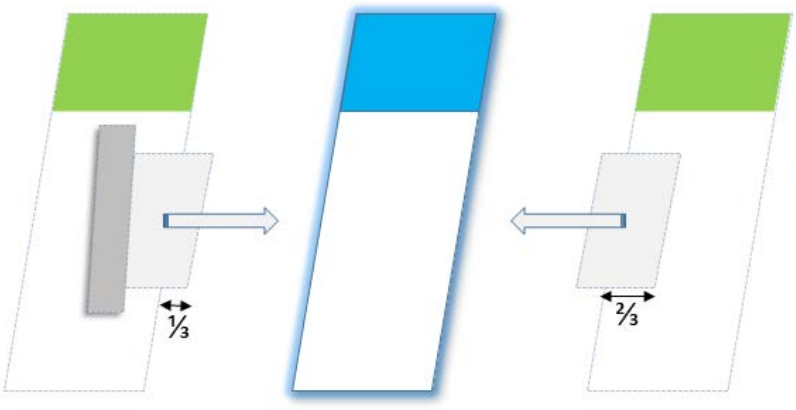

Figure 2-8: Principle of assembly of glass slides.
Procedure to mount plant seedlings for further mechanical analysis with AFM. Cover slips glued to the green Starfrost glass slides are colored in light gray. A small piece of micropore tape (dark gray, only on the left slide for clarity) is used to fix the cover slips.

c) Take a third glass slide and place it in the middle of the other two glass slides such that a little rectangular space is left in between (Figure 2-9).

d) At one end of the glass slide, deposit a drop of silicone adhesive approx. 100-150 μL.

e) After depositing, the NuSil on glass slide spread it with the help of another cover slip (square #1, Figure 2-9) dragging upwards to the other end. When we spread a drop of NuSil on the glass slide, it has the thickness of the cover slip and is evenly distributed.

Note: Do not add more than two drops. More amount will lead to longer polymerization time.

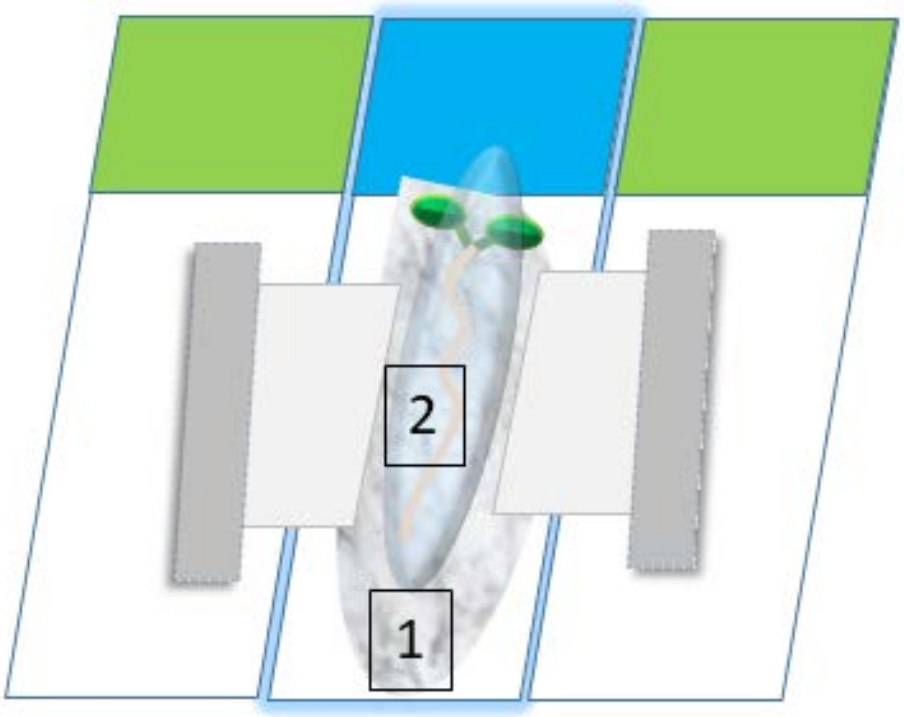

Figure 2-9: Principle of mounting plant seedling on glass slides.
The goal of this setup is to deposit a uniform layer of NuSil glue on the middle glass slide. The adhesive layer shown in light gray and labeled with the number 1. A long primary root in orange and two green cotyledons schematizes the seedling. The seedling is finally covered with a growth medium shown in light transparent blue color and labeled with the number 2. Cover slips are in light gray whereas micropore tapes are in dark gray.

f) After spreading NuSil wait for 20-25 seconds, so that the adhesive starts polymerizing, yet it is still wet for the sealing purpose. The goal is to place the root on the adhesive when it is semi-solid so that it stays on the surface and does not dip into the adhesive.

Note: It might be tempting to place the plant sooner. Sometimes the plant can dip inside the NuSil and can affect its living state, in particular due the presence of un-evaporated ethyl acetate.

g) Take one seedling from the Petri dish and, using a dedicated tweezer[1]; gently lift it from the shoot area preferably under the cotyledon without pinching the seedling.

Note1: If not lifted properly, this might lead to breakage of the plant into two pieces. In case of longer roots, it might be stuck inside the agar gel and extra caution is required to extract the seedling from the agar. Always lift from the cotyledon part because that area has the center of mass. This way the root can balance itself during the transfer from the Petri dish to the glass slide.

2.6.7.2 Depositing seedling on a glass slide

a) Place the plant on the slide such that the root tip is laid first, followed by the shoot part.

Caution: Gently place the root on the glass slide. Affinity of NuSil might lead to misplacement. Also, roots are very fragile and light, which might lead to misplacement.
Note: Pay attention to the face of the root that is in contact with agar during the transfer time of two hours. Because it is transferred just for two hours and in that period, the side touching the metal-excess agar is most likely to experience the full stress level than the whole root itself. It is best to present the side of the root that was in contact with agar to the top access of the glass slide, i.e., facing the tip of the cantilever. We have experienced a reduced heterogeneity in our data after such trick.

b) The root is laid down very straight so that it is easy to do the indentation on straight part of the transition zone. In case the root is bend around the transition zone, it is difficult to perform indentation around that area.

[1] NuSil is a glue and it is difficult to fully remove from the tweezer. Thus, the tweezer would not be able to be used for picking cantilevers for instance.

Note: The curl effect makes the root rounded and more stretched as shown in Figure 2-10. In some cases, some part of the tissue might be under the cantilever, which will not allow the cantilever to take the measurements properly as it might not touch the desired area. Also note that the cantilever support may also touch the NuSil glue before the tip is reaching the surface of the root.

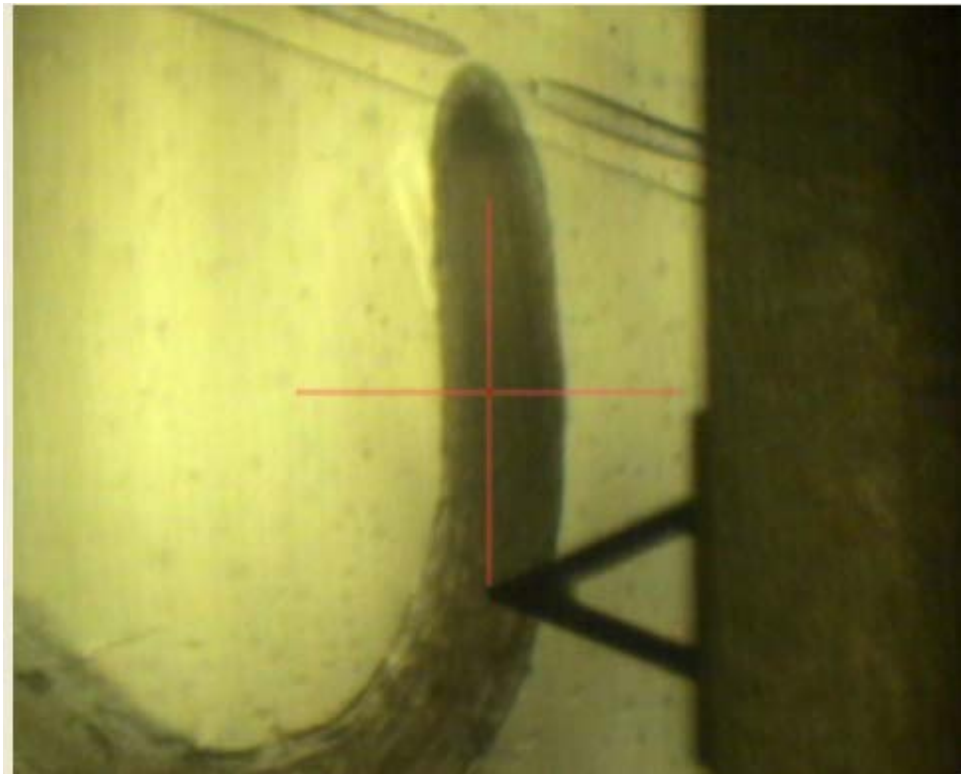

Figure 2-10: Image showing a bend root fixed on a glass slide.
We found that such bending leads to high elasticity values of the external cell wall structure. The curvature often comes from the growing condition, likely induced by gravitropism. This is likely the most inconvenient aspect of growing seedlings in vertically oriented growing agar plates.

c) Fastening the seedling root by sealing it with the semi-solid adhesive present on the glass slide, starting from the top, then the middle and the very end (root tip) to prevent any movement of the root Figure 2-11

Note1: Sealing by adhesive is done such that the height shall remain constant throughout the slide. With an excess of adhesive, the tip may touch the adhesive during the positioning

under the AFM scanner or the edge of cantilever support may also touch the adhesive that will bias nanomechanical measurements.

Note2: The sealing starts from the top just to make sure of the stiffening of the glue. A minimum of three seals is required so that the root does not move, Figure 2-11.

a) b)

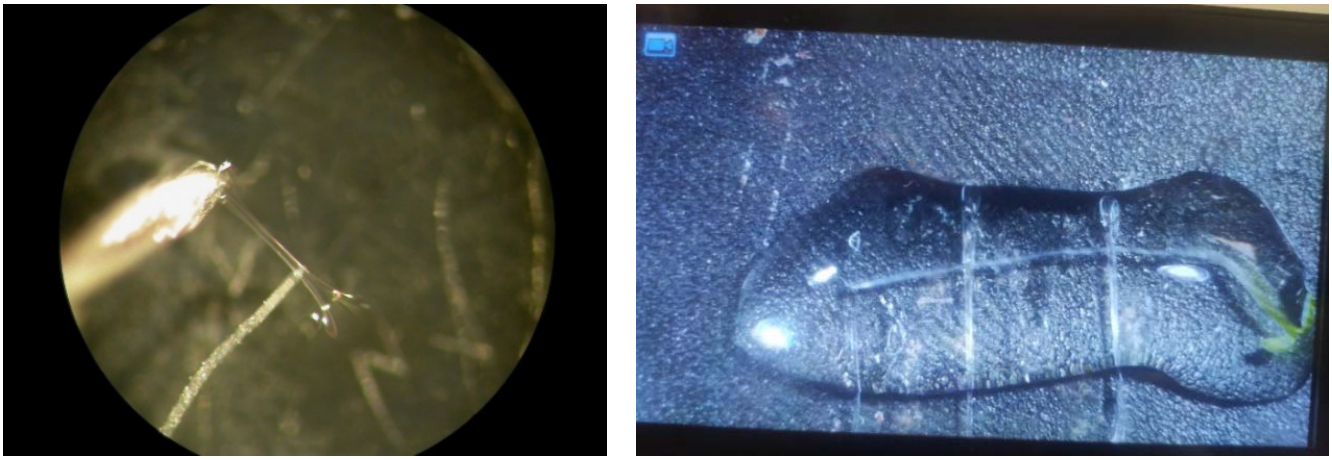

Figure 2-11: Optical magnification of deposited seedling roots on adhesive.
a) A thin needle (bright color on the left) is used to fasten the position of the root on the adhesive by picking hardening adhesive over the root. Several fastening strips are required along the root but keep a significant room for the investigation zone, which is about 500 µm from the root tip. b) Root sealed by NuSil as seen under the binoculars.

d) Only 50-100 µm of the root tip area is sealed, while preserving the elongation zone which our desired area, Figure 2-12.

e) Immediately cover entirely the plant root (at least 100 µL) with growth solution (square #2, Figure 2-9) (Figure 2-11) to prevent drying during measurement. Make sure to cover the root tip first as it is the most sensitive part of the plant. The system is ready for measurements.

Caution: Do not use water to cover the root, as it will generate an osmotic stress on immobilized root.

f) The mounted seedling is positioned under the AFM so that the plant is still alive and experiment on living root tissues can be performed, Figure 2-12.

2.6.8 Nano-indentation on the living root tissues

Note: Although the seedling is alive, the horizontal position is not its favorable for plants. Consequently, the experiment should be performed as quickly as possible. A time longer than 30 min gave us unpredictable results as global stress may occur within the root.

a) Before positioning the plant root under the AFM cantilever, retract the piezo to a safe distance between the cantilever and the plant root.
b) Lift the scanner head carefully and insert the glass slide with the plant root. Buffer is already on the top of the root, thus carefully lower the scanner head so that the cantilever will not bend upon contact with liquid (adding a drop of buffer on the cantilever is usually necessary to have a smooth insertion in liquid).
c) Orient the glass slide, so that the root orientation is close to vertical and its tip is on the top of the camera, Figure 2-12.

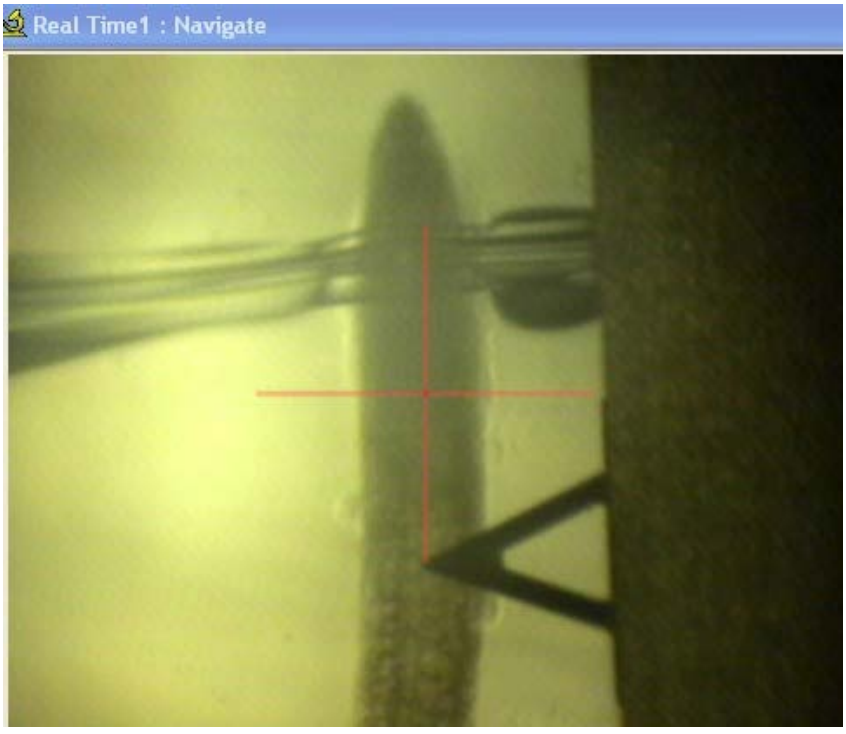

Figure 2-12: Picture showing how the root are laid down for better measurements.
The sealing with NuSil should be very thin so that cantilever head is not touching the sealing. After sealing carefully, place the glass slide under the piezo scanner. At this point also, we need to rotate the glass slide ourselves so that the root tip is under the cantilever as seen through the camera. This step is facilitated by the large stage of the D3100 AFM.

d) The target working area is located approximately 500 µm away from the root tip. This distance can be estimated knowing the length of the PNP cantilever (about 200 µm). Use the stage positioning controls to move the cantilever on the right zone.

Note: Because the root is pseudo-cylindrical and the PNP tip height rather small (~3.5 µm), it is not advised to probe the root beyond the longitudinal median line of the root. Note that there is small setback of the tip on PNP cantilever (4 µm), see Figure 2-5 in equipment set up section 2.5.4.

e) Focus the camera so that the root surface is clearly visible.
f) After placing the root under the scanner, wait for few minutes for laser to stabilize.
g) Centre the laser spot at (0,0) position. Keep deflection set point to 2.5 V.
h) Make a new folder for each node and mention co-ordinate of it in the filename.
i) Lower the piezo down manually until the root is clearly visible, then start engaging.
j) When the surface is detected, then run continuous force-distance (FD) curves to adjust the ramp parameters. With the Dimension 3100, we have to modify the z-ramp start so that our 3 µm long ramp could be performed correctly. With our open-loop scanner, we did not use a trigger force threshold, and consequently, the ramp must be manually adjusted prior a full record.
k) With appropriate FD curves, start collecting and recording curves.
l) Because of the limited time (before plant roots display additional stress signals), we can only probe a limited number of areas. Our best protocol contains 16 physically different areas (called nodes) and each node is composed of a matrix of 2 x 2 FD curves spread with 50 nm of distance between each point, Figure 2-13.
m) Withdraw the cantilever every time after the recording of the curves and engage again after changing the piezo offset co-ordinates.

Note: Performing a large-scale displacement on the top of a root (Nano-Indentation on the living root tissues, step 5 µm). Because of the inherent curvature and topography of a plant root, it is not advised to move long distance (> 1 µm) using piezo scanner offsets. We

found that withdrawing the cantilever works best on our system. It will avoid any tip damage. Re-engage at each measurement node. This practice helps in a better landing of the tip at the correct spot, fewer plant surface scratches, and less cellulose fibers deposition on the tip. All these parameters lead to better data acquisition.

n) After completion of all the 16 points, take a screen shot of the plant root under the cantilever for the record.

o) Move piezo upward to a safe distance and discard the glass slide.

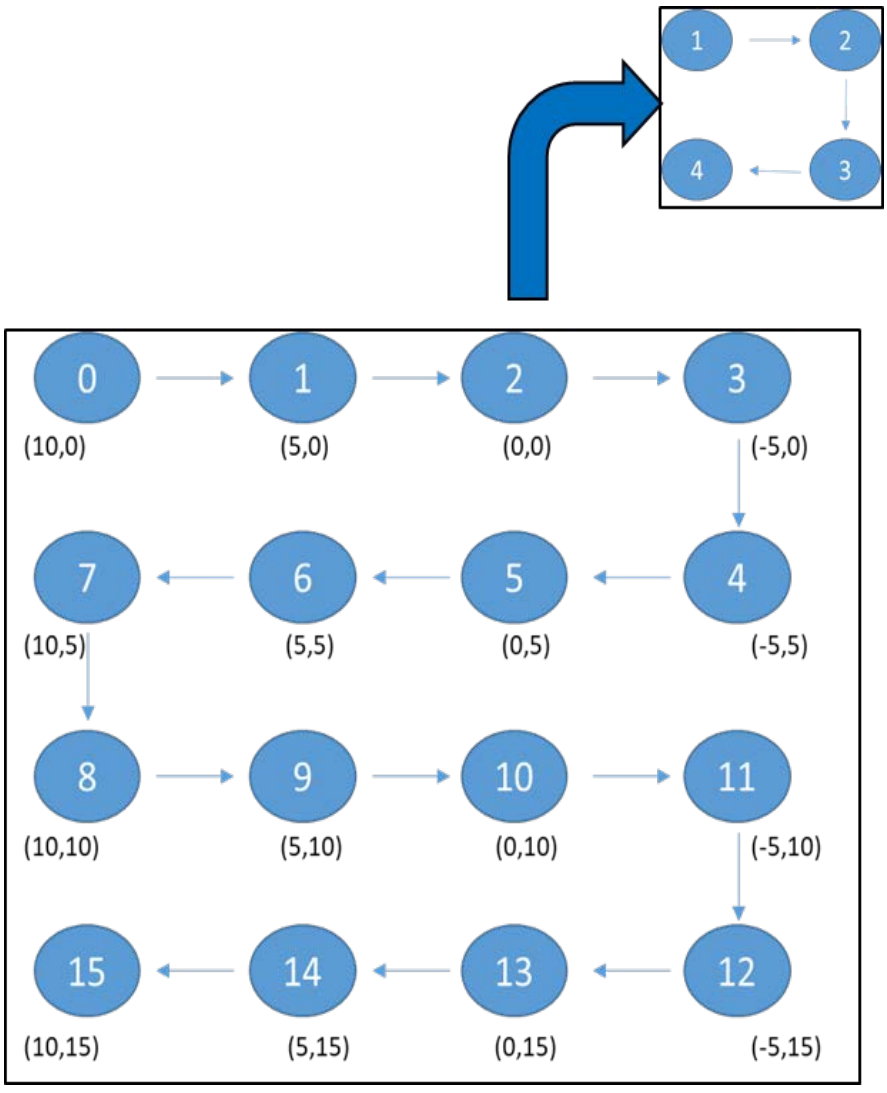

Figure 2-13: Final matrix strategy used to collect force-distance curves.
It starts at position 0 and proceed according to thin blue arrows. Offsets of the piezo scanner at each node of the matrix are indicated below (values in µm). At each node, a submatrix of 2 x 2 FD curves are recorded. Do not forget to update filenames at each node in order to keep track of the matrix (it helps during the data analysis).

2.6.9 Prepare plant roots for phenotype confirmation

a) With the remaining roots, not taken for the indentation experiment, transferred them to the Petri dishes containing stressed medium or control medium, try to align them properly and mark the position of the root tip with a pen.
b) Observe phenotype (root growth or no root growth) after 24 hours and take a photograph.

2.6.10 Root length measurement

a) We measure the root length 48 hours after the transfer to have a clear distinction between growth and no growth.

   Note: The reading of the plant root phenotype in our experiment is the root extension (measured in mm). Sometimes, plant seeds have different germination “power” and some seedlings may grow slower or faster. Always try to transfer roots of similar length so that their rate of growth would be similar. This will help in overcoming any errors when measuring root length the next days.

b) Take pictures of the whole roots under stressed and non-stressed conditions Figure 2-14. Do not forget to add a ruler in the field of view to calibrate the length measurement with ImageJ.
c) Export these pictures to imageJ where they can be opened with the NeuronJ plugin. The NeuronJ plugin allows you to trace the root paths with the computer mouse. The standard length unit is in pixels.

2.6.11 Data analysis

The contact-based mechanical model has already been discussed in the introduction section 1.1.4 and 1.1.5. Here, only the steps based on data analysis have been mentioned.

a) Force-distance curves were analyzed by AtomicJ (Hermanowicz et al. 2014).

Parameters that best suited the fit of our indentation curves were: robust exhaustive contact estimator with the robust (LTA) fitting method following the Sneddon model for pyramidal tips of 35° opening, Figure 2-15.

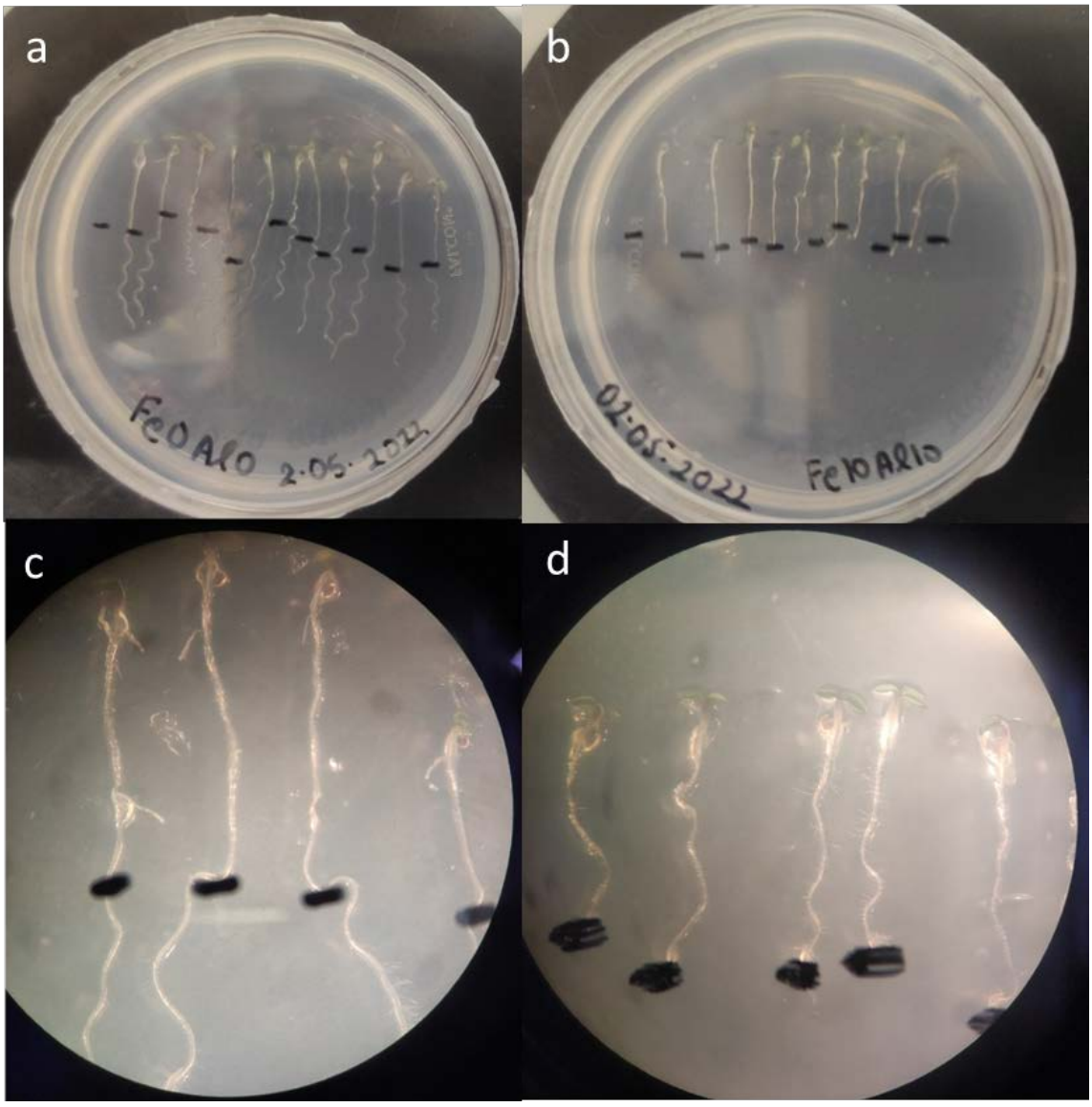

Figure 2-14: Root extenstion phenotypes.
(a) Control that shows a normal root extension in absence of metallic stress. (b) Root extension arrest phenomenon when roots are exposed to iron and aluminum stress of 10 µM each. (c-d) Roots seen under the binoculars in case of Fe0Al0, Fe10Al10 respectively. The black mark is drawn at the extrimity of the root at the end of the AFM measurement, directly on the Petri dish cover. If plants grow, then their root tips are beyond the black marks.

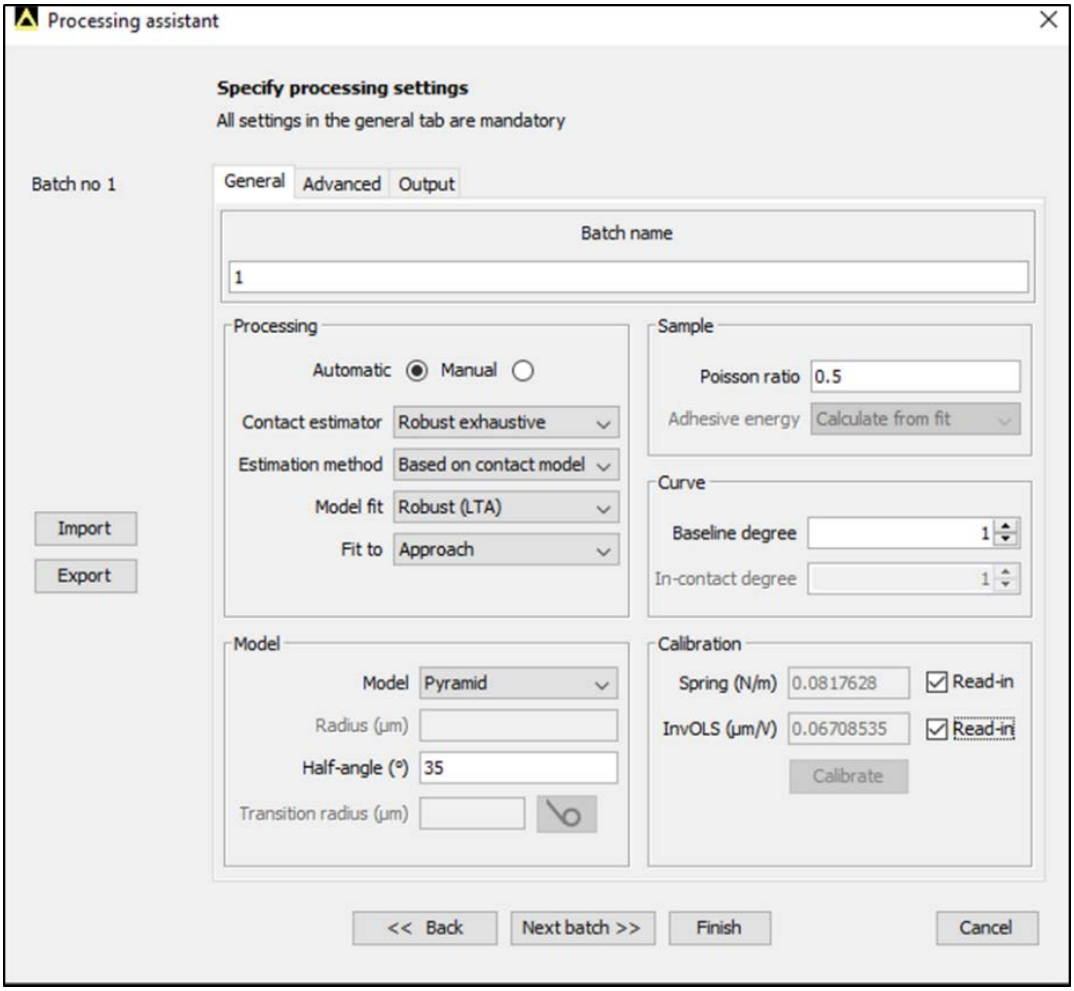

Figure 2-15: Screen shot of AtomicJ interface.
Showing all the parameters which are implemented to FD curves for the analysis of our data with AtomicJ. It has a wide range of fitting parameters, which can be found in processing section in the drop down menu based on our data curves.

b) The force in indentation approach curve was capped to 5 nN.

c) We regularly observed that curves showing a poor fitting were "poor" acquisition data; it was decided to remove all fitting data having a fitting quality $R^2 < 0.9$.

d) Data is saved in excel worksheet after analysis for consulting the data in future for all the curves.

e) The overall summary of the data is saved in a set called descriptive analysis. Those statistics were saved in excel and further copied to GraphPad Prism for further statistical analysis.

2.6.12 Outliers

a)

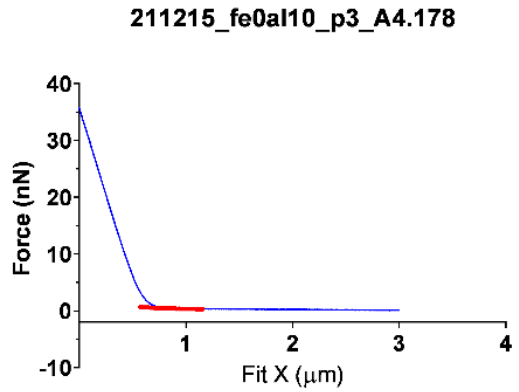

b)

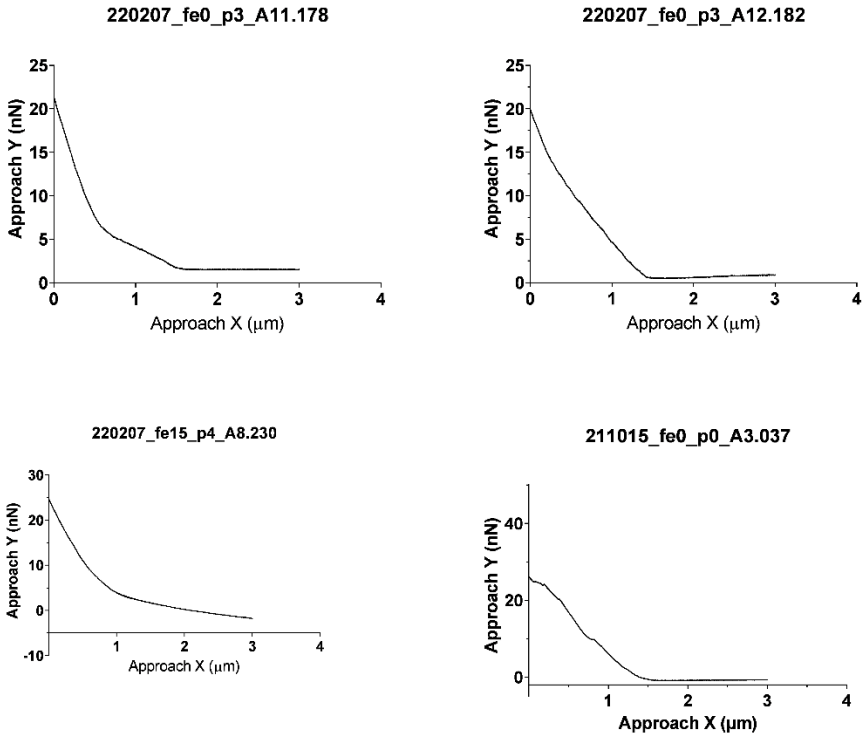

Figure 2-16: Force-distance curves that are excluded from the AtomicJ analysis.
a) Example of a fine curve but with a poor fitting. Thus, instead of changing its contact point manually, the curve was deleted due to non-respecting R^2 threshold. b) Examples of curves excluded from the analysis according to visual checking. It can be seen that these curves do not have a good approach with several slopes or tilted baselines. These curves indicate that the nanomechanical measurement were not properly acquired by the AFM technique.

While the data was filtered out based on R^2 values, there were some cases where their might be a good curve with a bad indentation fitting and vice versa. Thus, it was important to observe the force curves manually and remove unsatisfactory curves (Figure 2-16). In general, 5-10 curves were deleted manually for each plant. In case the overall number of deleted curves is greater than 30, then the whole plant is rejected based on poor data acquisition. This was one of the disadvantages of AtomicJ as poor fitting was quite common, essentially due to poor contact point assignment. Below are various examples of bad curves acquired during data recording and later discarded.

2.6.13 Statistical analysis and plotting

We adopted a hierarchical and redundant approach by duplicating local data (the final protocol is a 4-times repeat, a 2 x 2 matrix) with a sufficient number of acquired nodes (16 in the final protocol). If the sought property (let's say the Young's modulus) of a single FD curve is outside an acceptable average range (we used a 2 sigma range around the mean), then the FD curve is discarded among the 2 x 2 matrix. If more than half curves are discarded per node, then the node is discarded. A distribution histogram of Young's modulus values obtained at each node of all plants revealed a log-normal distribution. This is not particularly rare in biology (Millet 2021). Consequently, we decided to compute the geometric mean of all nodes of a plant and provide this single value for a single plant, Figure 2-17. A quick survey of other averaging methods did not change the overall conclusions of the work.

During our statistical analysis, non-parametric Mann–Whitney t-tests were used to evaluate the statistical significance of elastic constants in different experimental conditions using as null hypothesis that there is no difference between each condition. A p-value was calculated by Graphpad Prism 8.0 using an α-threshold of 0.01. Box plots with min-max whiskers were drawn by Graphpad Prism 8.0.

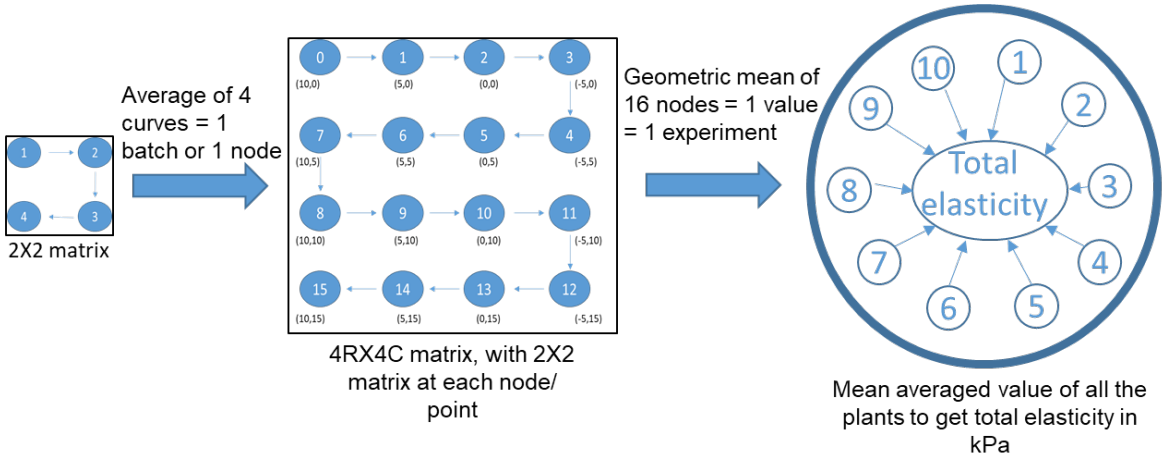

Figure 2-17: Hierarchical statistical analysis done with the help of GraphPad Prism.
During data acquisition 2 x 2 matrix with 4 FD curves were acquired at each of the 16 nodes. During data analysis, values of interest of the 16 nodes were geometrically averaged to have a single value per plant per experiment. In the end, arithmetical mean of all the 10 plants of a given experimental condition (blue circle) is calculated and used for further statistical analysis

2.7 Additional information & other procedures

2.7.1 Advantage of crystallization plate over Petri dish

a) b)

Figure 2-18: Disadvantage of using petri dish
(a) 4-days-old AT plants in Petri dish where we can see most of the root end curved which makes them unsuitable for indentation experiments. (b) 4-days-old plants germinated in crystallization plate. The idea of switching from Petri dishes to crystallographic plates was initiated during a discussion with Anne-Emmanuelle Foucher (IBS/EPIGEN).

During our initial set of experiments, plants were grown in a Petri dish deposited vertically in the growing chamber Figure 2-18 (a). The wriggling of 4-days-old AT plants is clearly seen.

Some plants have a curved effect at the root tip. When these roots were analyzed, they had unexpectedly high elasticity values, likely due to gravitropism effect.

2.7.2 ESEM on plant roots.

We performed Environmental Scanning Electron Microscopy (ESEM) (Figure 2-19) on plant roots to understand and find out more about the root surface. Although there are many images of *Arabidopsis* investigated before, we wanted to specifically see the root surface and cell organization for day-4 seedlings. We visited CERMAV-CNRS lab, Grenoble, where Ms. Christine Lancelon-Pin helped us with the imaging.

Figure 2-19: Quanta FEG-250 environmental SEM instrument used for high-resolution imaging at room temperature.

It is still not possible to image living plant root tissues with ESEM. However, there was no pre-preparation of the sample required prior to imaging Figure 2-20. This was the main advantage of ESEM where no metal coating was needed unlike SEM, thus, less time consuming. Samples were imaged with 98.8 % of humidity. The sample is placed on a small circular glass slide with a double-sided carbon tape. The plant root is laid above the carbon tape. The specimen chamber is closed, and then roots are imaged. Measurements were done both in air and in humid conditions; roots placed in air are shown in Figure 2-20.

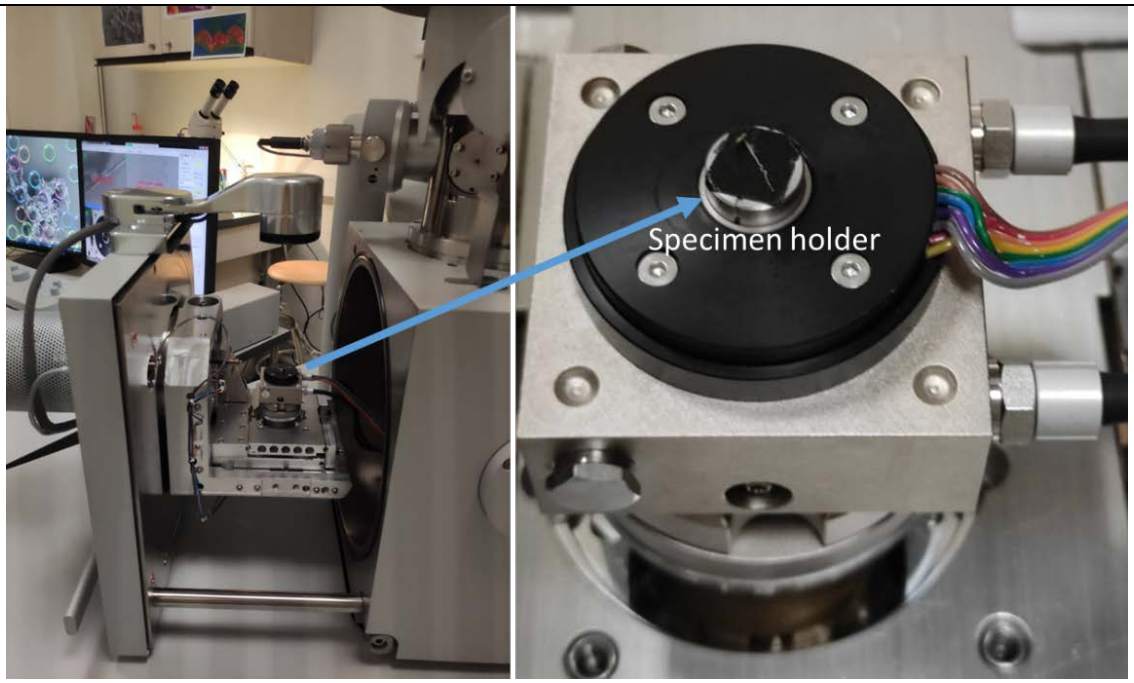

Figure 2-20: Specimen chamber of Quanta FEG-250.
It is opened to put the sample over the specimen holder as shown in the second picture, which is zoomed where the samples are placed in air, and later closed. ESEM is capable of taking images of wet samples that are non-conductive in high vacuum mode. However, a carbon tape is always required to evacuate electrons.

2.7.3 TEM on plants roots

We tried to prepare samples for Transmission Electron Microscopy (TEM) to image the external primary cell wall of roots and particularly its thickness. Normal roots are grown until day 4 and transferred to the stress/control media. We prepare the samples of 5-days-old plant roots. Initially, a standardized protocol was followed by the cellular electron microscopy team of IBS EM platform. Later on, the protocol changed a couple of times to improve the sample handling, image quality, and focusing in the transition zone. TEM images were taken with the help of Christine Moriscot (IBS/MEM). After a couple of trials, the finalized protocol contains

three main steps: processing, embedding and polymerization. During the whole process it is strictly required to wear lab coat and gloves. Perform all the steps under the laminar hood.

Processing

a) Fixation: Prepare a fixation solution before. It is composed of Paraformaldehyde (PFA) 2% and Gluteraldehyde (GA) 0.2 %.

   For 10 mL of solution, add 2.5 mL of 8% PFA and 0.08 mL of 25% GA.

   Roots were taken out from agar media and dipped directly into this solution. Then Petri dish was kept for 2 hours on a rotator at the room temperature (RT).

   This step is done to preserve the sample and to prevent further deterioration so that it appears as close as possible to the living state, although close to dead now. This method stabilizes the cell structure with minimum alteration to cell morphology and volume. Glutaraldehyde is often used as the fixative in TEM. Because of glutaraldehyde fixation, the protein molecules are covalently cross-linked to their neighbors.

b) Rinsing: Sample is rinsed with the buffer (PHEM) 0.1 M pH 7.4, two times at RT to maintain the pH of the sample. PHEM buffer is a mixture of PIPES 60 mM, HEPES 25 mM, EGTA 10 mM and $MgCl_2$ 2mM.

   Note: While rinsing, we need to be careful while discarding the liquid buffer through pipette tube, while keeping the roots in the Petri dish.

c) Post fixation: A secondary fixation with 1% osmium tetroxide (OsO_4) and 1.5% of Potassium ferrocyanide (KFeCN). OsO4 binds phospholipid head regions creating contrast with the neighboring protoplasm (cytoplasm). Tissue proteins, which are stabilized by OsO4 are not coagulated by alcohol during dehydration. Samples are kept for one hour on a rotator in a petri dish.

d) Rinse: Osmium treated roots are washed with H_2O twice for 5 minutes each time.

   Make sure to discard the water carefully according to institution safety rules as it contains traces of osmium, which is highly toxic.

e) Staining contrast: Treat the plants with 0.5% of Uranyl acetate in 30% of ethanol for 30 minutes. Heavy metals like uranium and lead are used to give contrast between different structures. Thus, adding more electron density to the internal structures Figure 2-21.

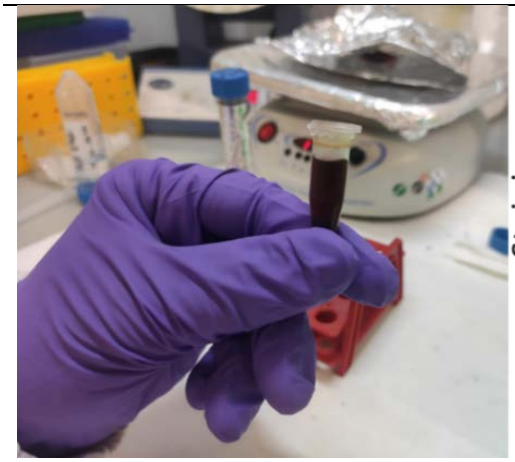

Figure 2-21: Staining roots with 0.5% of Uranyl acetate and 30% of ethanol solution.

f) Rinse: Again, the roots are rinsed two times for 5 minutes each time.

g) Dehydration: The water content in the tissue sample replaced with an organic solvent at different percentages.

Samples are rinsed consecutively with 30%, 50%, 70%, and 90% of ethanol for 10 minutes each time. Then again, rinse with 100% of Ethanol, 3 times for 10 minutes.

h) Substitution and infiltration: After rinsing with alcohol, pour 50% EPON^{TM} resin + 50% ethanol solution on plants for 2 hours, on a rotator.

After 2 hours remove the solution and add 100% EPON^{TM} resin for 1 hour. Again, add 100% resin solution for overnight. Epoxy resin is used to infiltrate the cells. It penetrates the cells and fills the space to give hard plastic material, which will tolerate the pressure of cutting.

<u>Embedding:</u>

i) Embedding done using flat molds. Samples were again washed and new resin was added. Then, the samples along with resin were poured in silicon holders.

j) Let the resin polymerize for two days at a temperature of 60°C in an oven, Figure 2-22.

Polymerization:

Figure 2-22: Roots embedded inside polymerizedresin blocks. (Black thread like structures).

k) Sectioning: Resin blocks shown above are sectioned on ultramicrotome with a glass or diamond knife. For best resolution, the sections must be 30 nm to 60 nm, Figure 2-23.

Note: Thin sections are cut so that the electrons are semitransparent to the electronic beam.

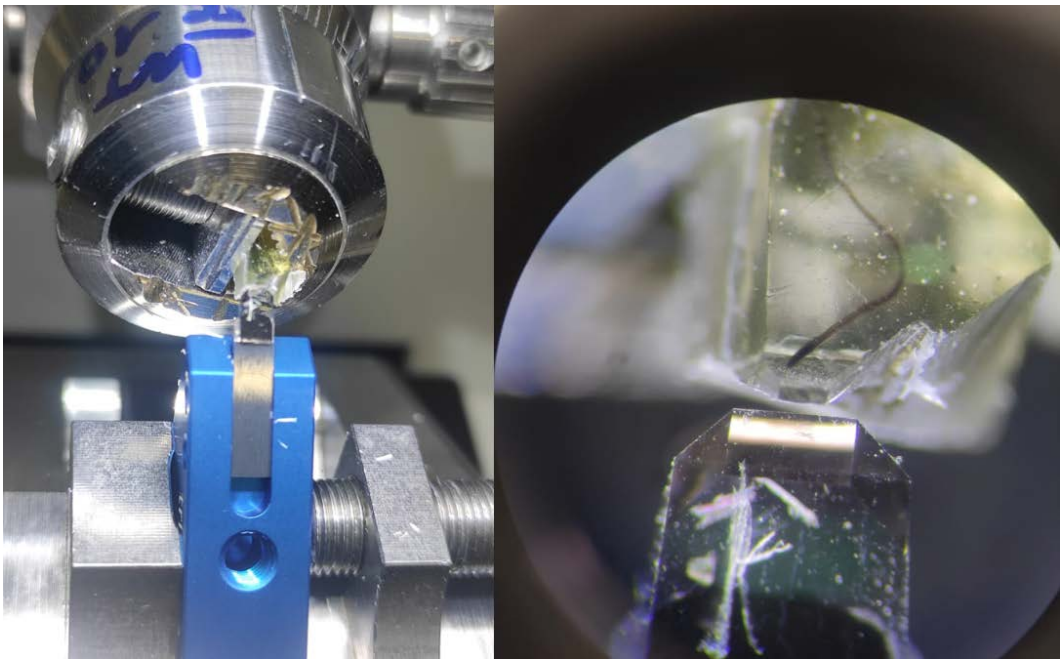

Figure 2-23: Ultramicrotrome instrument with the diamond cutter.
On the right, we can see the zoomed image as seen from binoculars where the diamond cutter is cutting the raisin block. The black color thread like structure inside the block is that of the root.

l) Sections float onto a surface of liquid held in trough below and remain together in a form of ribbon. Freshly distilled water is used to fill the trough. These sections are then collected onto a copper grid and viewed under the microscope. All these steps have been performed by Christine Moriscot (IBS/MEM) Figure 2-23, Figure 2-24.

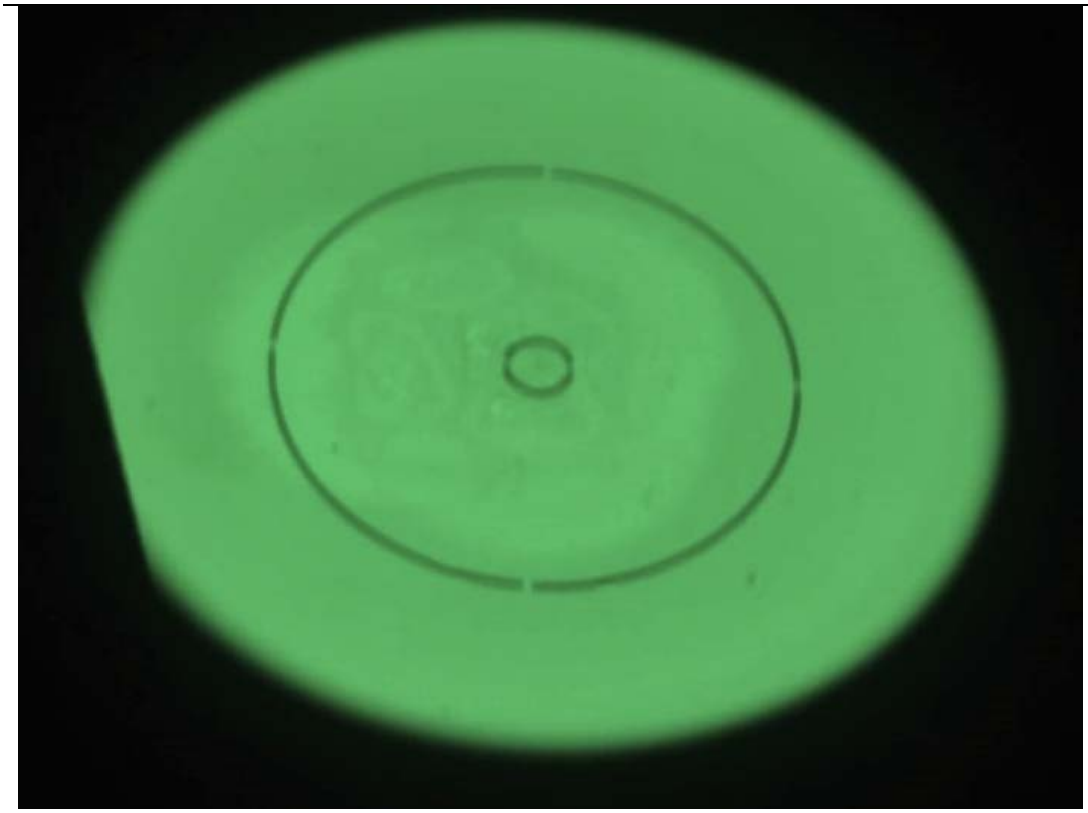

Figure 2-24 : Arabidopsis root tissue image on phosphorescent screen.
When seen through horizontal slicing of the root structure, the phosphorescent screen is useful in locating us the cell structure on a root slice followed by bombardment of the electrons to get image

2.7.4 Decellularization on plant roots

One month of secondment was done in University of Barcelona, under the supervision of Nuria Gavara (UB) and the help of Maria-Leonor Narciso (UB/ITN), to get training on decellularization of plant roots. It was intended to perform indentation on stressed and control roots after decellularization to characterize cell wall behavior in absence of cell and

thus turgor pressure. Although no indentation experiment has yet been performed, they are expected to be done before the end of the project.

This protocol is partially based on the already developed and published protocol of decellularization on lung tissues on which the host lab was actually working on (Narciso et al. 2022).

Protocol:

Note: Several roots treated at the same time.

a) Take an empty culture plate to perform washings.
b) Pour milliQ water in two wells.
c) Place the plants in the wells.
d) Set the timer for 10 minutes.
e) Repeat the washing for another 10 minutes.
f) Two washes are enough before treating them with a detergent solution.
g) Prepare detergent solution.
    i. Add 2% of SDS solution i.e., 0.4g for 20 mL of detergent preparation.
    ii. Vortex to dissolve detergent granules well.

    Note: A comparison was made between two detergents SDS and SDC initially to finalize the most effective one. It turns out that both the detergents showed similar cell removal and neither showed any observable decreases in cellulose signal, so we decided to use SDS for further experiments.

h) Plants are treated twice for 30 minutes (1h in total).
i) Roots are rinsed with water thereafter 3 times for 5 minutes each time to remove any detergent traces.
j) Prepare DNase I solution. DNase I solution is prepared as follows for 10 mL:
    i. Add 10 mg of $CaCl_2$ and $MgCl_2$ to 10 ml of milliQ water (final concentration of 9 and 10.5 mM, respectively).
    ii. Add 100 µl of Tris-buffer solution (10 mM, pH 7.5). Vortex nicely.

iii. Then add 3 mg of DNase to it.

About DNase: It is always stored in freezer. Take out required amount of DNase and quickly place it back into the freezer. It is highly susceptible to absorb humidity from the air.

After adding DNase, gently rotate the falcon tube up and down so that DNase is dissolved. Do not vortex after adding DNase.

k) Add DNase I solution to cover plants and keep for 40 minutes at 37 °C in incubator.

l) Rinse DNase 3 times with water for 5 minutes each time.

m) Remove excess water at the end of 3rd rinsing.

n) Take out the roots from the culture plate and place them on a glass slide.

o) Mark the boundaries of the roots with the help of hydrophobic pen, so that less volume of liquid is required from here on.

p) Preparing the stain solution. Three indicators were used and tested for observing decellularization:

i. DAPI (4',6-diamidino-2-phenylindole): Add 2 drops of DAPI to 1ml of PBS solution as per the instruction manual provided with the package.

DAPI is blue-fluorescent DNA stain, which preferentially stain dead cells.

ii. PI (Propidium Iodide): Add 1 % of PI i.e., add 6µl to 594 µl of PBS.

PI is a red stain indicator used for staining nucleic acids just like DAPI labelling dead cells. In addition, it is used for staining the epidermal layer as well (Bidhendi, Chebli, and Geitmann 2020).

iii. CFW (Calcofluor White): Original concentration of CFW is 20 mg/mL. As it is highly concentrated, we add 1 µl of CFW per 999 µl i.e., 0.1%.

CFW stain is a blue fluorescent stain that binds cellulose and chitin in cell wall of plants (Bidhendi, Chebli, and Geitmann 2020).

q) Normally it takes approx. 100 µl of the stain solution to cover the whole root. With the help of pipette tip, pour the liquid over the roots.

r) Cover it with the lid or perform the staining onwards steps in dark.

s) Stain for 15 min in case of DAPI, 10 min CFW, 7 min PI (or 10 minutes for both PI and CFW).

t) After staining, again rinse with water 4-5 times with 5 minutes of interval to remove the extra stain.

u) Remove excess water with filter paper.

v) Now take a pipette tip of 200 µl and dip the pipette tip in the viscous fluromount solution. Just release the extra drop with is attached to the tip over the plant root. Fluromount is used for mounting slides following immunofluorescent staining.

w) Gently place the cover slip on the sample slowly. It touches the liquid and spreads well while covering the whole root. Do not let any air bubbles trapped between coverslip and glass slide. Place the samples in dark and dry place for one day before imaging.

x) After mounting the slides, they are observed under the confocal microscopy for viewing decellularized roots with different exposure times based on different stains.

Summary of the Protocol

Sample preparation and immobilization

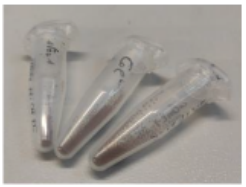

Seed harvesting and seed collection

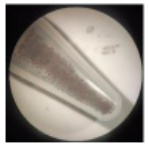

Seed sterilization
- Ethanol
- SDS

Preparation of *crystallography* culture plate
- Agar
- MES pH5.6
- Additives

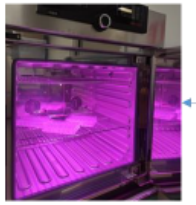

Seed germination
- 4 day incubation
- 16h/8h light & dark
- 24°C/21°C temperature

Transfer root to stress/ control media
- Agar
- MES pH 5.6
- Additives + Fe, Al

2 hours waiting time

Phenotype observed next day.

Root immobilization

Transfer on a glass slide + NuSil

Root under the AFM

Data acquisition and analysis

AFM Indentation

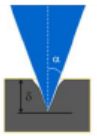

Recording of F-D curves

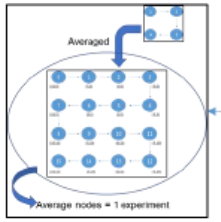

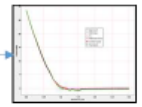

Calculation of Young Modulus value by AtomicJ.

$$F = \frac{2}{\pi} \cdot \frac{E_s}{1-\nu_s^2} \cdot \tan\alpha \cdot \delta^2$$

Selecting/Averaging node data

Plotting the values using graph pad

1 Plant = 1 value = 1 experiment

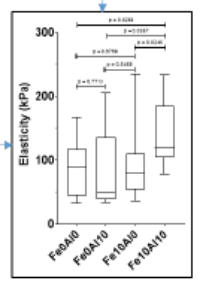

RESULTS:

DESIGN OF THE PROTOCOL

3 Results: Design of the protocol

In the previous chapter, we presented our final protocol that is designed to determine the cell wall stiffness when plants are transferred from control to stress conditions.

Multiple factors need to be taken care of when indenting over the live root samples in an easy and reproducible manner. For instance, it is challenging to keep the plants immobilized and hydrated while indenting close to their living state. Duration of experiment is also important; the deposition of seedlings on glass slides must be performed quickly with a fixation system that do not create a "growth arrest" phenotype. This chapter deals with the chronological evolution and advancements of the protocol, in response to an unexpected situation that, hopefully, occurred at the very beginning of the thesis.

3.1 Background to project

During preliminary tests in 2014, we initially used the presence and absence of inorganic phosphate ions (Pi) to create a metallic stress that led to a root growth arrest (RGA) phenotype. Later, a similar change in the phenotype was observed just by adding different concentrations of Iron alone, and a threshold of 6-8 µM of $FeCl_2$ was sufficient to create the desired stress (i.e. RGA). It was in 2019, at the very beginning of my thesis, when a change in the manufacturing of the Agar powder led to a drastic change in the phenotype. No root growth arrest was observed when Iron alone was added, even at 10 µM concentration, which was considered highly stressful for plant root growth in previous experiments. After mass spectrometry tests (ICP-MS at CEA Cadarache), it was observed that the new agar contains much less minerals than the earlier agar powder (the major change concerned the concentration of boron). Of major interest, was the presence of a few micrograms of aluminum (Al), in the earlier agar that were missing in the new agar. Our collaborators in CEA Cadarache decided to add 5 µM Al to all agar preparations and the usual RGA was recovered when using previous Fe concentrations. Thus, initially we added Al as a "compensating" supplement in agar, but soon we get curious about the role of aluminium alone as well as in combined form with iron, and their effect on the cell wall stiffness. In particular, the role of Al in the stiffening of the CW and its relation with RGA remains largely uncharted.

3.2 Preliminary results

Indentation experiments are performed on wild-type *Arabidopsis* seedlings. In initial experiments, the stress was caused by 10 µM $FeCl_2$ in the presence of 5 µM $AlCl_3$. At the beginning, the protocol for growing plants and data analysis was kept similar to that observed in 2017 (Balzergue et al. 2017). We performed force-distance curve analyses using the Force software (Lekka et al. 1999). Force distance curves were analyzed individually and their average values were taken as final data to plot. Here comparative results for Fe0Al0, Fe0Al5, Fe10Al0 and Fe10Al5 are plotted in Figure 3-1.

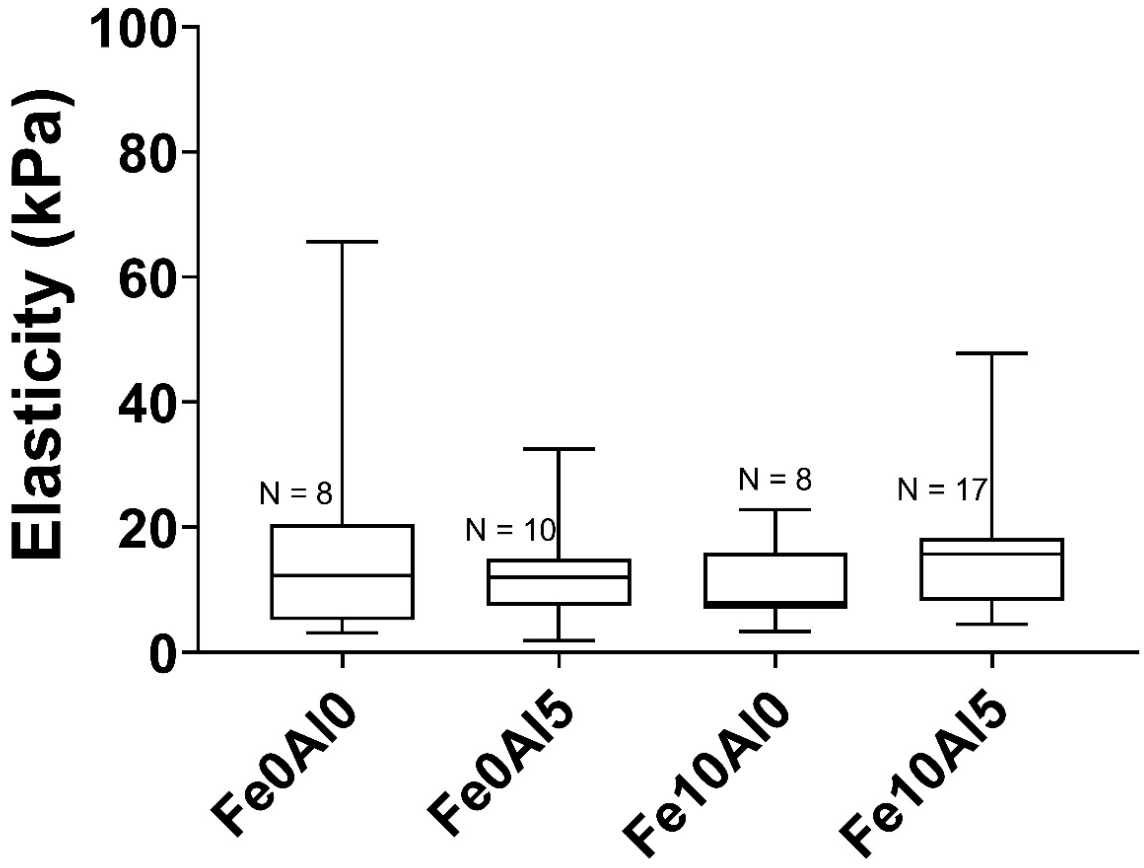

Figure 3-1: Elasticity values for WT plants in presence or absence of iron and aluminum.
Box-and-whiskers plot is shows for each condition the average elasticity expressed in kPa. The middle black line in the box indicates the median and the whiskers indicates the min and max values. N represents the number of plants. Force-distance curves were analyzed and the average of all elasticity values are pulled together in the plot.

Table 3-1: Early results of elasticity variation in plants.

Stress condition	Elasticity (in kPa)	
	Average ± SD	Median
Fe0Al0	17.8 ± 20.3	12.3
Fe0Al5	12.4 ± 8.5	12.1
Fe10Al0	10.7 ± 6.4	7.93
Fe10Al5	15.5 ± 10.3	15.7

In all the tested conditions, plants showed a varied level of stiffness, as judged by the large standard deviation values. Overall, elasticity values are similar and non-significantly different in all cases, see Table 3-1 (and Figure 3-1), in contrast to the previously published results (Balzergue et al. 2017). Consequently, our preliminary data was unclear and it prompted us to revise the experimental protocol systematically. While our home made nanomechanical analysis software was still at the developing stage, all the force distance curves shown further in this report are analyzed using AtomicJ (Hermanowicz et al. 2014) while plots were made by using GraphPad Prism version 8. In the following sections, I present all the exploratory work done to improve critical steps of the experimental protocol.

3.3 Immobilization of the sample

3.3.1 Root growth arrest

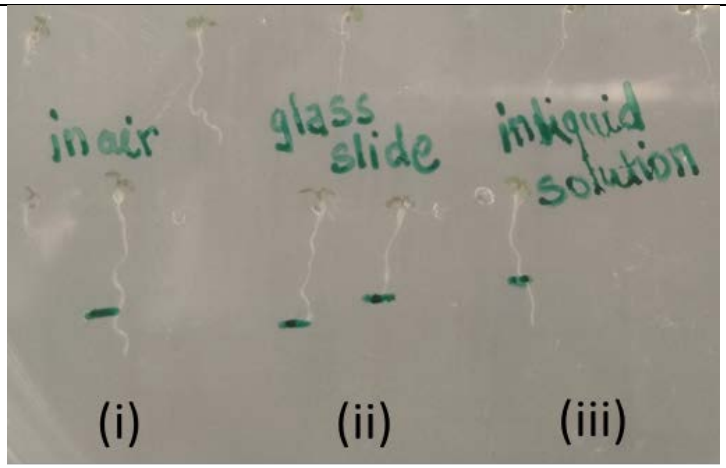

Figure 3-2: Plant root growth in three different conditions observed the next day
(i) Plant lifted from Petri dish and kept in air for one minute before putting back to the petri dish. Root growth is observed next day (ii) Plants left on a glass slide for few seconds before transferring back to the petri dish showing a root growth arrest. (iii) Plants kept in liquid growth solution for few minutes (~10 minutes) before transferring them to the petri dish.

To perform indentation experiments on a live tissue sample such as plant roots, it was important to fix the tissue firmly to a glass slide. Handling of seedlings on glass slides is a particularly sensitive step as it was observed that a seedling left one minute on a glass slide without liquid was unable to grow for several days (Figure 3-2). We performed this simple experiment to find out the maximum time by which the root faces stress. This observation was always kept in our mind while depositing the seedlings on a glass slide. Hence, we always considered that deposition must always be quick with a fixation system that do not create a "growth arrest" phenotype. Most importantly, our goal is to devise a methodology that is improve reproducibility.

3.3.2 Materials tested for fixing samples

Seedling roots need to be fixed on a glass slide before performing nanoindentation experiments. We tested several fixation methods: various tapes (double face AFM stickers, double face carbon tapes, standard scotch tape, micropore tape, Parafilm, Polydimethylsiloxane or PDMS) without any success due to the weak attraction of the plant root tip to the tape once placed in liquid medium. It was always difficult for us to seal or immobilize the root end (Figure 3-3). Theoretically, we already knew about the root cap covering the stem cell region, which offers a special skeletal coating protecting the stem cell region and provides a great rigidity in the root end. Among all the tested systems, the apparent most efficient was double face carbon tape, which immobilized, unfortunately, the whole root except the root cap.

3.3.3 Low melting agarose trials

Many research articles cited the use of low melting agarose to fix plant tissues or cells. This prompted us also to test the agarose ability. We have tested low melting agarose of varied concentration (2%, 4%, 8%) and several molecular components (methyl cellulose, poly-lysine, starch). Again, the main problem was the weak attachment of the root to these molecules in presence of liquid.

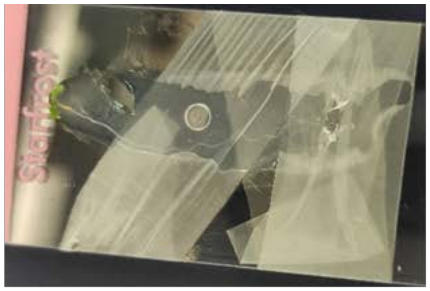

Figure 3-3: Trial tests done to immobilize root samples with various methodologies.
None of the tested methods were successful enough to immobilize the root especially the root cap. The major difficulty turned on when adding growth solution that made roots usually floating over the glass slide.

We also tested the possibility to perform experiment in air (in absence of liquid covering the root) since agarose medium are already composed of > 90% water content. Although, the agarose appears to maintain and stabilize the seedling appropriately, we faced the problem of heating agarose surface with the AFM laser beam used for the detection of cantilever deflection. The heating was sufficient to partially melt agarose that diffused all over the

surface of the root and end up with root movements, in addition to polluting the AFM cantilever during indentation experiments (Figure 3-4). This partial melting of agar was particularly prominent in our AFM instrument due to the large diameter of the laser beam.

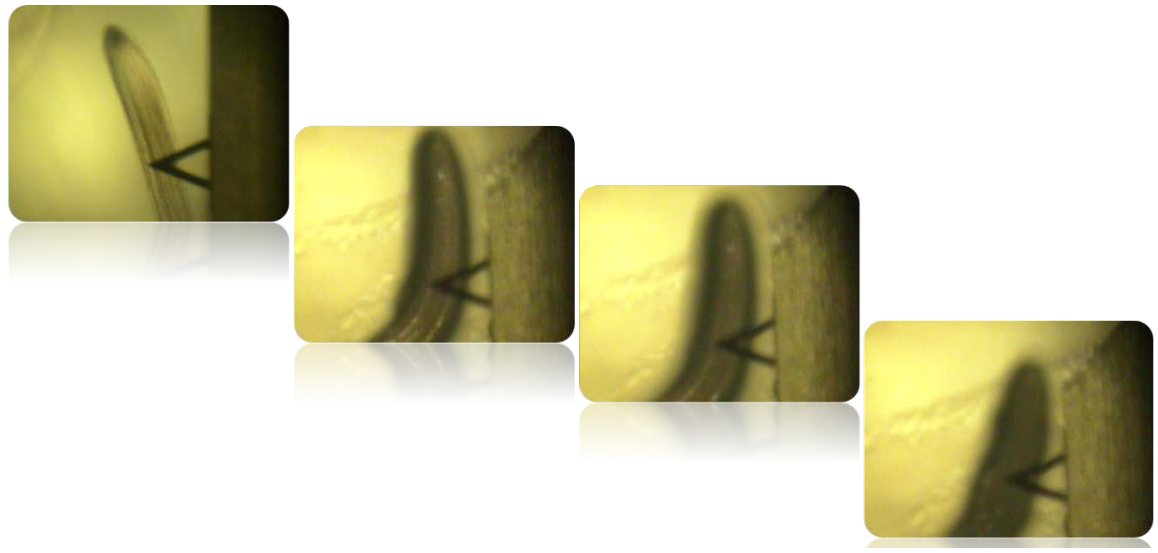

Figure 3-4: Gradual shifting of a root deposited on agarose when placed under the AFM. Root was placed atop the soft low melting agarose gel. The heat from the laser beam was enough to melt the agar gel below and displace the roots, while contaminating the AFM probe.

3.3.4 3D printing technique

In collaboration with Brice Poirier (CEA Grenoble, Y•SPOT), we designed and tested 3D micro-printing techniques to design micrometer size channels to deposit seedlings. We targeted simpler methods than the high-tech lithography (Akita et al. 2020). Various materials and designs were tested. A 3D-shape was built using different printers depending upon the material used (Figure 3-5). The 3D designs were made using Fusion 360° Autodesk software and converted to a file format compatible with 3D printers.

a) First, poly-lactic acid (PLA) plastic was used. PLA presents several advantages including a medium hydrophobicity that allowed us to deposit a few µL of liquid medium in the engraved channels followed by the deposition of seedlings. However, the width and depth of the designed channels could not be optimized to allow the seedling to be both located at the bottom but not too deep to be accessible by the AFM cantilever.

PLA Microcap slide

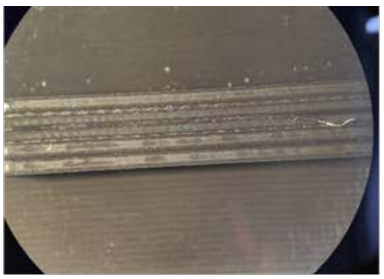

Root end coming out of trench

Resin microcap slide

Rough surface, water not reaching roots.

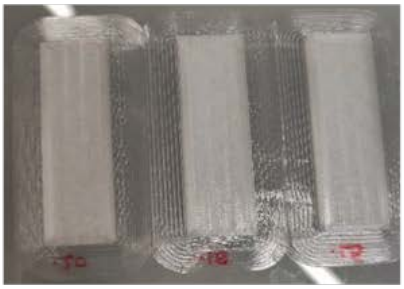

Co-polyester microcap slide. No trenches seen under this.

Resin made harp, quite brittle and light. Cannot confine root.

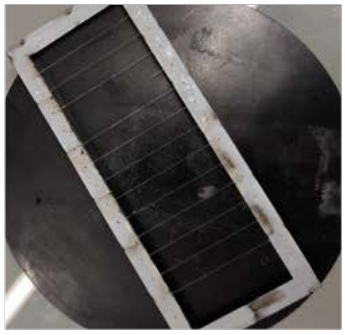

Harp made with fish threads. Design made by laser cutting having hole of few micron to insert fish thread.

Root end still not well fixed with harp.

Figure 3-5: 3D microprinting materials and designs tested for root immobilization.
The various 3D printers include 'Ultimaker S5' for PLA, 'Formlabs 2' for resin-based 3D print and 'Trotec 400 Flexx CO2 laser' for laser cutting. Normally it can take 2-3 hours or more to make a 3D print depending upon the complexity of the design.

b) Another design was performed with poly-ethylene (PE) plastics which unfortunately appeared completely transparent which was a real challenge for depositing white plant roots; this material was excluded.
c) A third design involved a resin-based component which was very smooth but turned out to be extremely hydrophobic and thus provoked a strong reaction on the root tip when the liquid medium is added. We tried to use various glues to maintain the root tip in the resin-based holder but unsuccessfully.
d) Fourth design was based on well-known "harp" design used to maintain mammalian tissues for microscopy-based experiments. This design takes advantage of the PLA-designed channels and a micro-printed "harp" which is used to lock down the root tip mechanically. To avoid adding too much pressure on the root tip, several thicknesses of the "harp" threads were tested (50 -100 µm). However, in reality none of the machines could produce such a fine threads of the promised micrometer scale. Wider threads pushed too much force on the root ends, enough for damaging the tissue.

3.3.5 Silicone pressure sensitive adhesive and toxicity tests

Initially, a silicon-based pressure sensitive adhesive (NuSil MEDI-1356) was used to fix seedlings on glass slides. The presence of 50% of ethyl acetate in this adhesive led us to test alternative methodologies. In the meantime, toxicity tests were performed with the NuSil MEDI-1356 on the seedlings. First, the ethyl acetate solvent was diluted at different percentage with liquid growth medium, deposited one minute on a glass slide, then remove from the glass and placed back in the culturing agar petri dish. From 20-50% ethyl acetate concentration, the plants were unable to grow for several days; however, from 1 to 10%, a growth was observed although reduced in the case of 10% (Figure 3-6). However, when the NuSil was deposited on a glass slides followed by a curing time of one or two minutes, it was possible to deposit a seedling for one min and removing it before placing it in the culturing petri dish and observing a classical growth (Figure 3-7). We thus demonstrated that the NuSil MEDI-1356, when polymerized, did not have any effect on seedling growth.

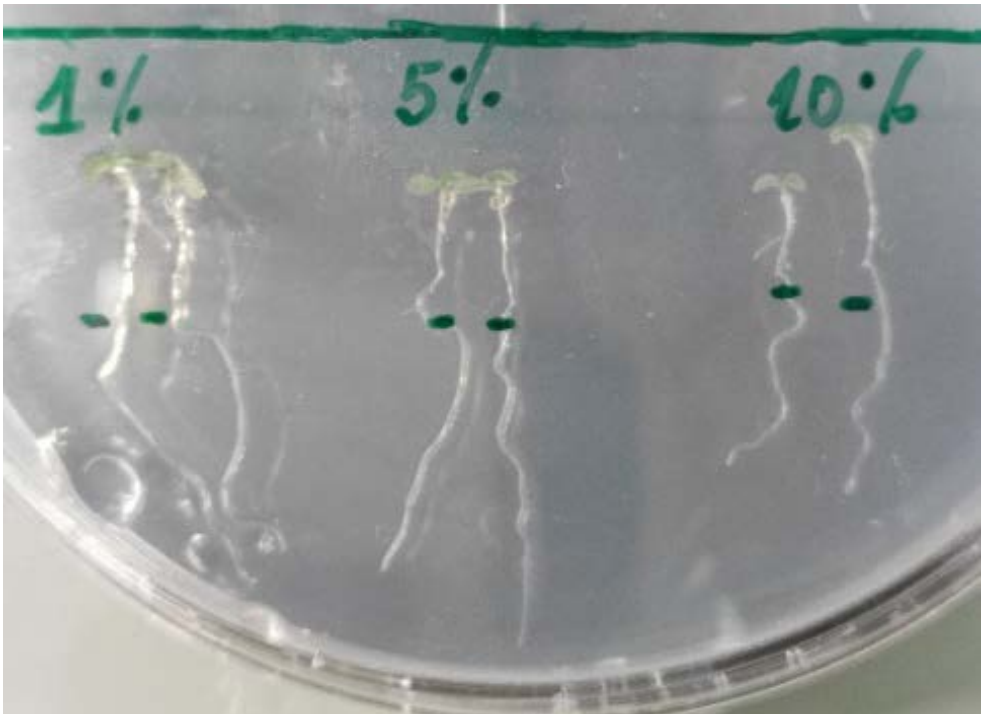

Figure 3-6: Different concentrations of ethyl acetate.
Root length decreases with increase in concentration.

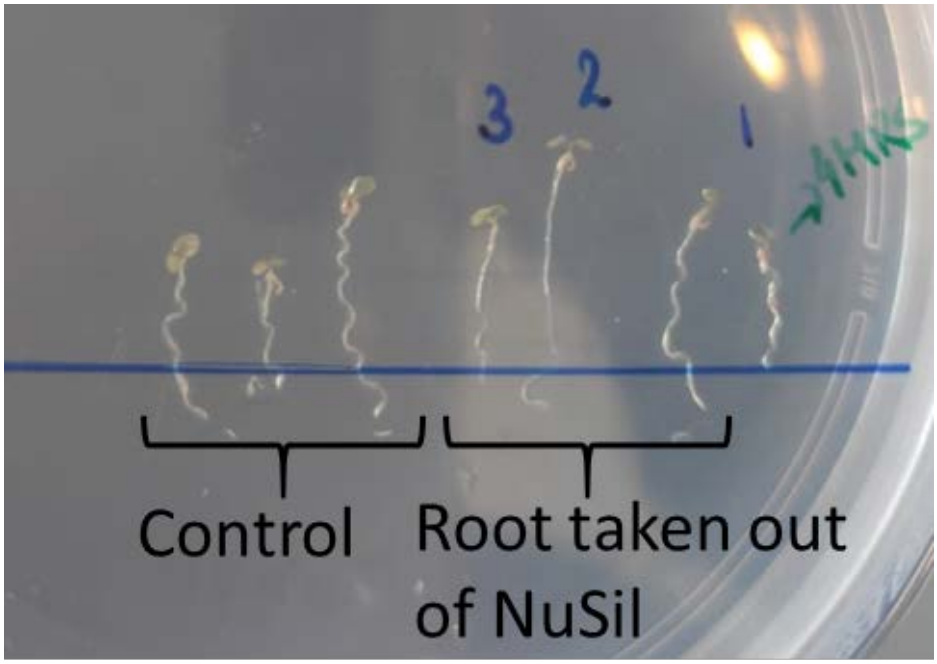

Figure 3-7: Roots kept in NuSil after curing, for 1-2 minutes.
No sign of stress is seen in both control and NuSil treated root. The green label shows the root kept for four hours under NuSil, but did not grow the next day.

The NuSil used in our work is hard to get because of logistic issues from the supplier that hardly deliver small bottles (or anything less than a barrel). However, alternative PSA exists and we tried Silicolease PSA 408 (cat #117149, Elkem, France), but was not pursued due to the higher viscosity (from 40,000 to 120,000 mPa•s compared to 245 mPa•s for NuSil) and the change of solvent (toluene). We finally prefer NuSil over other adhesives because it has a particular characteristic of stretching while drying, which was not reproduced with other PSAs. For the nanomechanical experiment, it is crucial that the end of the root tip is appropriately fixed on the glass slide and this is nicely performed by the fastening step (see full protocol).

3.4 Plant root surface analysis: ESEM &TEM images

While testing various 3D printing materials, we were investigating the physical structure of root surface to understand more about the cell structure and their organization. A brief introduction of Environmental Scanning Electron Microscopy was presented in protocol section 2.7.2. We hoped, likely naively, that environmental SEM would show us images of the native root surface.

3.4.1 Results of ESEM

ESEM images showed us how our root surface looked like in addition to the cell length measurement. It was possible to measure even the cell wall junction and its width, which was clearly visible (Figure 3-8). Although the roots were already dried, nevertheless, it still gave us an idea to imagine how the cells would be arranged if they were living. A large population of the cells crowded near the root tip show the uneven organization of the stem cells at the root cap. However, if we move further away from the root tip, we observe a more uniform arrangement of the cells, cell length varying around 40-50 µm (as measured with the help of ImageJ (Schneider, Rasband, and Eliceiri 2012)). These images were helpful in characterizing tissue surface and eventually the spacing of our matrix design.

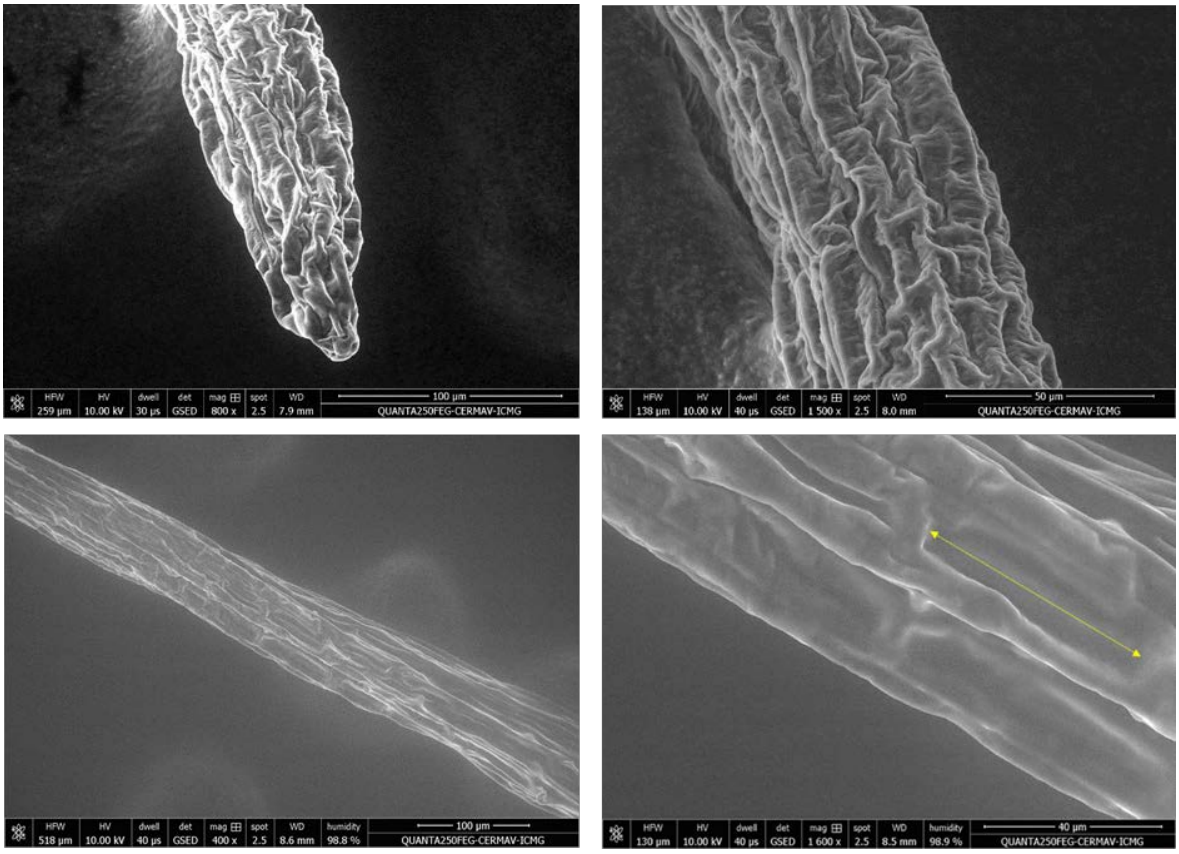

Figure 3-8: Dehydrated plant root surface imaged by ESEM.
Despites the absence of vacuum and the presence of 98% humidity, roots shrink due to clear dehydration. We, nevertheless, were able to measure total width and length of the cells of a 4-days-old Arabidopsis thaliana roots. The yellow arrow is approximately 40 µm in length.

3.4.2 Results of TEM

Another unknown criterion in root structure is the thickness of the external primary cell wall. Thus, we decided to prepare transversal slices of *Arabidopsis* root for direct observation in Transmission Electron Microscopy. Inside roots, it is trivial to measure the primary cell walls that separate cells. We found a classical value between 100 and 200 nm thickness (Figure 3-9). Unlike ESEM that image the outside, TEM provides us with the internal structure of 5-days-old *Arabidopsis thaliana* roots. Unfortunately, we did not have the equipment to ascertain that 500 µm of root tissue (transition zone) were cut-off before imaging with TEM. Consequently, we cannot be sure of the imaging region (Figure 3-9).

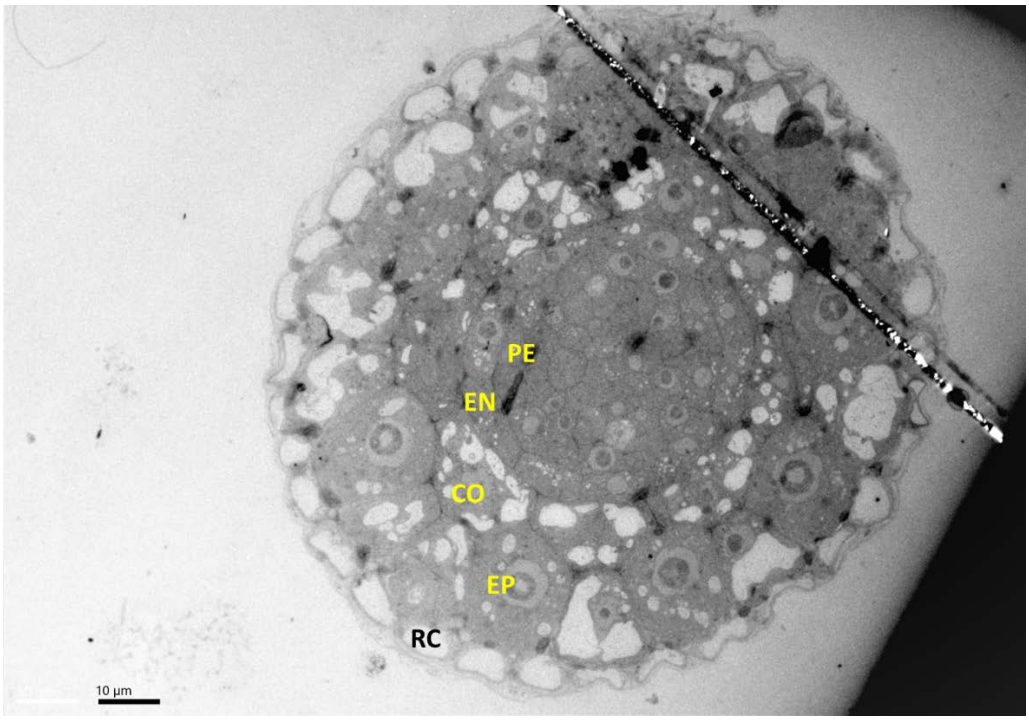

Figure 3-9: TEM image of a cross-section of Arabidopsis thaliana root.
Although the chemical treatment slightly damaged the external layer of the root, the image shows the classical circular layers present in Arabidopsis plant root. Outermost layer RC i.e. root cap of the plant cell appears in light gray whereas the inner layers i.e. epidermal layer (EP) and cortex (CO) appear in medium gray until the innermost layer endoderm (EN) followed by pericycle (PE) layer that encircle the central root cylinder, stele. Scale bar 10 µm.

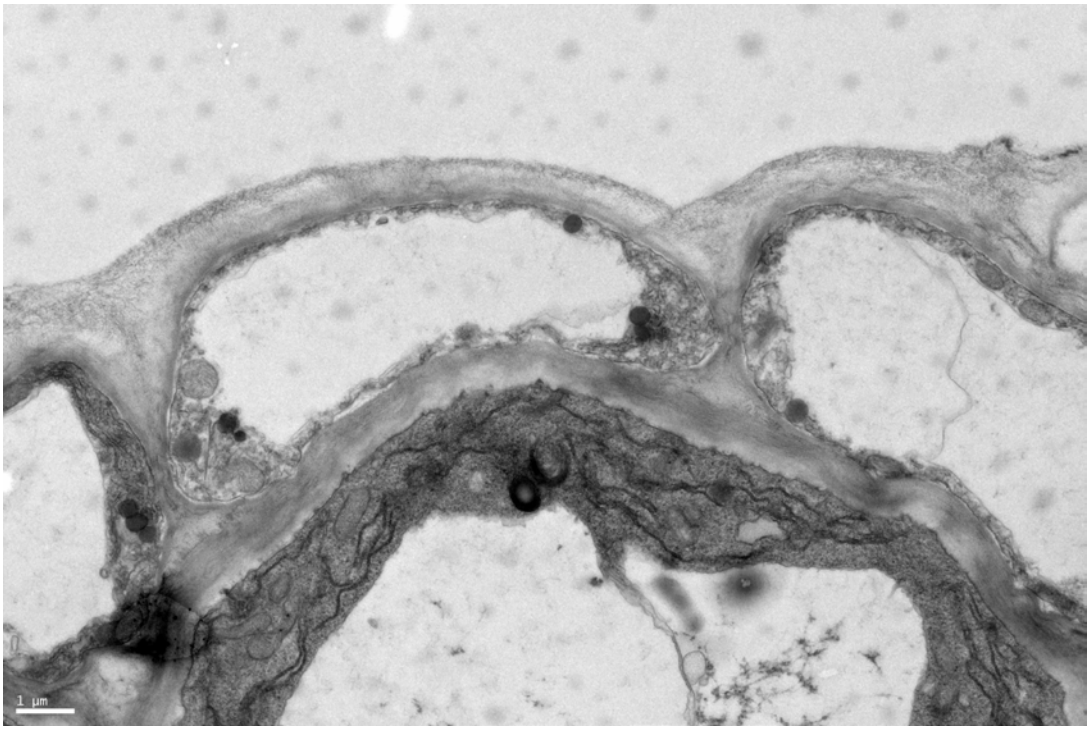

Figure 3-10: TEM image of epidermal layer of the plant root.
The thickness of the external cell wall of epidermal layer was approximately 800-900 nm, yet not homogeneous as measured by ImageJ. Scale bar 1 µm.

Different root layers in *Arabidopsis* can be seen in our TEM image (Figure 3-9). When observed more closely we can observe the epidermal cell layer, which is surrounded by thicker cell wall than the rest of the internal layers.

These images informed us about the external epidermal cell wall thickness in roots, which seemed to be quite variable and non-homogeneous, and consider that the experimentally probed cell wall of the transition zone can be up to 1 µm in thickness (Figure 3-10).

3.5 Plant topography and curvature: AFM

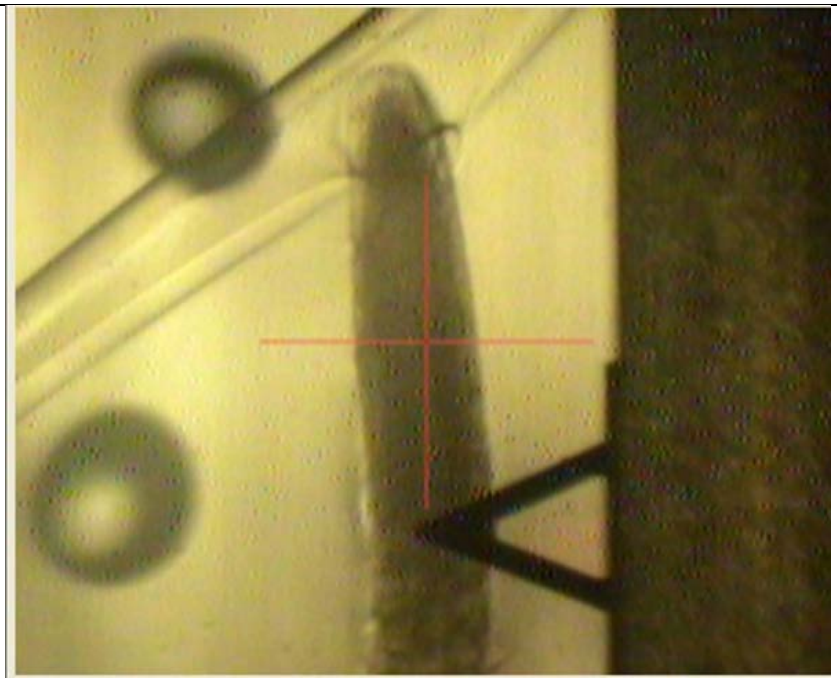

Figure 3-11: Optical view of a plant root under the cantilever.
The optical system of our AFM does not allow us to pinpoint the exact positioning of the cantilever tip over the plant root.

Despite improvement in the plant root immobilization and AFM calibration process, we still observed a considerable variation/heterogeneity in our nanomechanical measurements. Plant cell wall consist of macromolecular polymer chains interconnected in a non-uniform spatial distribution (see section 1.3). The circularity of plant roots and their surface roughness can contribute to the large range of stiffness values when analyzing with AFM (see Figure 3-1). While developing our protocol, we addressed this issue that is closely interlinked with the AFM tip used in our experiments. It is likely that the plant root surface is far from a smooth and

homogenous structure. We tried to image the root surface using AFM, but it remained a continuous failure with our lab's AFM.

As can be seen on the Figure 3-11, the optical system of our AFM does not allow us to pinpoint the positioning of the cantilever tip over the plant root. Since we could not image the surface of a root, we decided to perform a root surface analysis by performing indentation experiments over a transversal line across the plant root

3.5.1 Coarse root surface analysis

Indentation was done on a 40 µm horizontal line with a 5 µm gap between each point. We labeled a positive side that ranges from 20 µm to 1 µm (left side) and a negative side that ranges from -20 µm to -1 µm (right side) as shown in Figure 3-12. Elasticity measurements show that the positive side and the center (zero) generate a higher heterogeneity, i.e., a large standard deviation, than that observed with the right/negative side of the root (Figure 3-13).

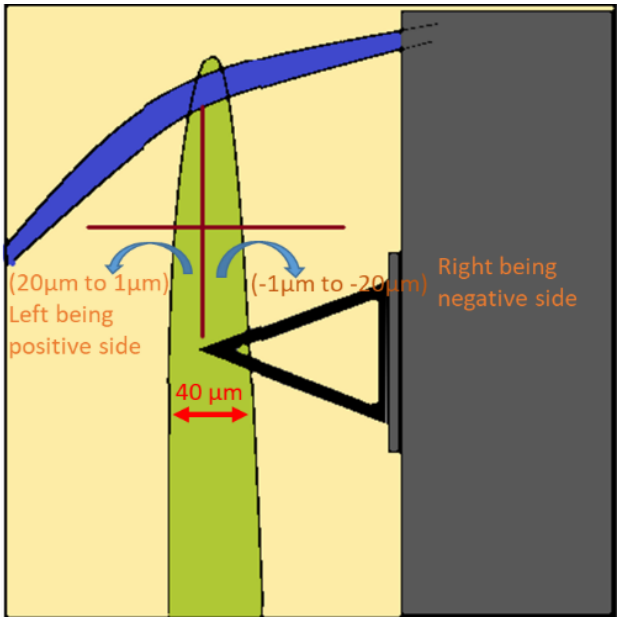

Figure 3-12: Figure showing indentation range in the coarse root surface analysis.
Please note that the co-ordinate orientation is based on the AFM offsetting system, which explains why negative values are found on the right side.

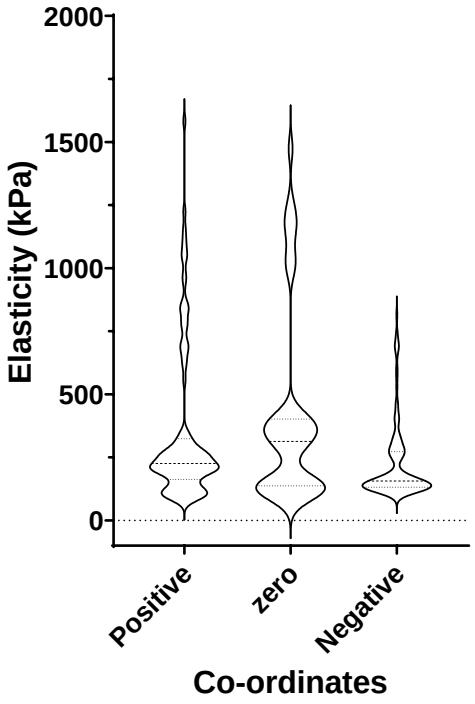

Figure 3-13: Results of coarse root analysis.
Figure showing positive side stiffer than the negative side. Data analyzed using AtomicJ.

A possible reason for the positive side being stiffer than the negative side could be interpreted as the cantilever head might be touching the root surface before the tip itself. This is due to the small tip height of our probe, which is approximately 3 µm. Thus, the total applied force will be different (a small tip versus a large cantilever); more importantly, the data analysis using a pyramidal tip shape is then inappropriate. On the negative side, which appears softer than the positive side, a putative contact with the side of the tip (instead of its apex) and the root surface may contribute to softer values, although we do not have any certainty of our interpretation. Thus, these peculiarities of the coarse surface analysis could be interpreted by the global shape of the plant root surface that is not totally cylindrical and smooth as shown in Figure 3-14.

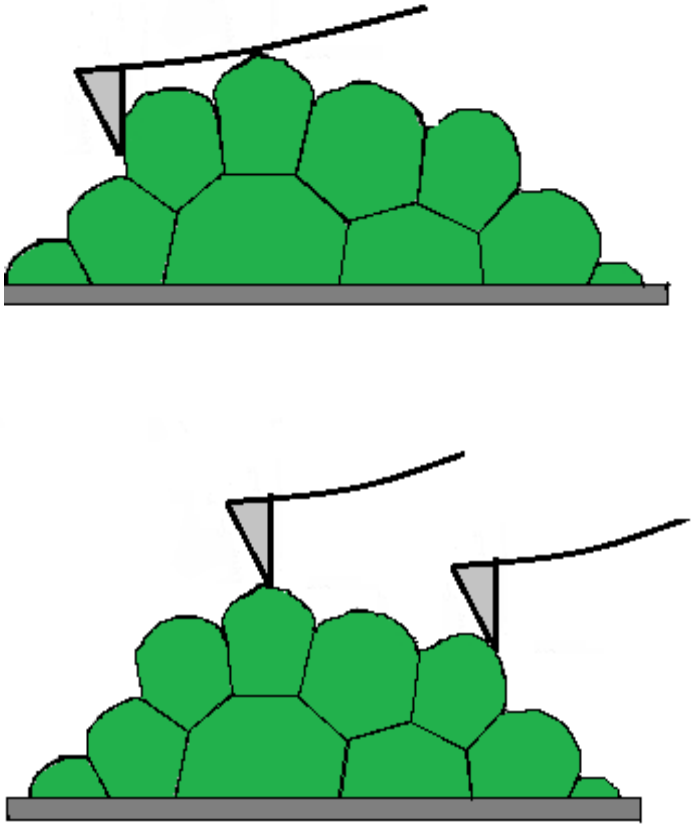

Figure 3-14: Limitation of the cantilever depicting error prone stiffer or softer values. The first figure is the schematic representation of the cantilever chip hitting the root surface instead of the probe (or nano tip) itself, which corresponds to the stiffer values. The second figure is showing two cases where the probe hits the root surface when the probe is placed at the apex of the root surface giving us more reasonable values, and the other case where the side of the probe touches the root surface giving pseudo soft values.

In order to reduce the impact of these errors, it was decided to position the physical end of the cantilever in the middle of the root surface using a ruler directly positioned on the computer screen. Due to the tip set back of a couple of µm from the end of the cantilever, the tip is thus slightly on the negative side.

3.5.2 Fine root surface analysis

To locate variations across a single cell or across two neighbor cells, we repeated a scanning over a 20 µm horizontal line with a step every 1 µm of distance and 5 curves recorded at each point (Figure 3-15). The goal is to observe sudden changes in elasticity and potentially attributes these changes to the primary cell wall organization on young plant roots. In particular, the elasticity of the region of cell-cell contact surfaces remains poorly characterized.

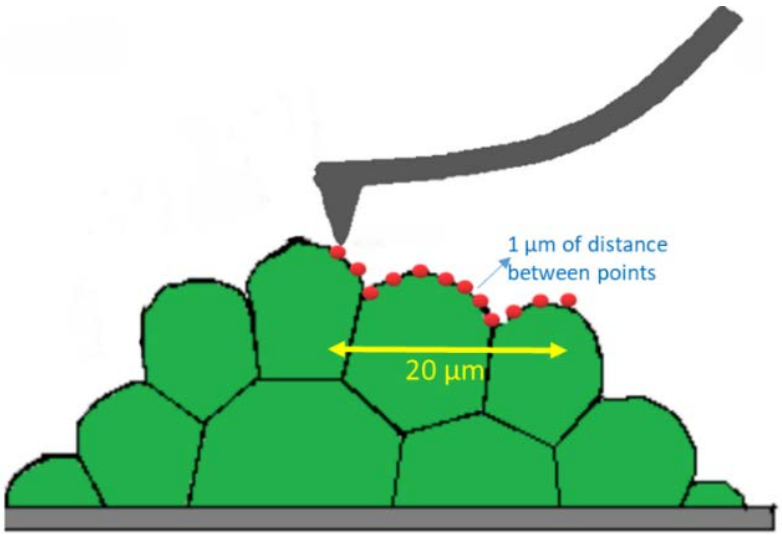

Figure 3-15: Pictorial representation of a fine root analysis.
Data points were taken along a 20 µm distance with a gap of 1 µm between two points.

Results are shown in Figure 3-16. The first observation is the smooth variation in the elastic property over the surface of plant cells. From this variation, we tried to identify some repetitive pattern knowing the 20 µm width of a single cell (Figure 3-8). The plant P4 provides a clue where both extremities of the horizontal line show a clear increase in elasticity (Figure 3-16). It suggests that these high values (up to 600 kPa) corresponds to cell-cell interactions. High values are also observed on other plants, but with a less clear pattern. Combining our

observation with previous observation (Peaucelle et al. 2011), we conclude that these very high values correspond to cell-cell interaction areas. These areas must be avoided for measuring the elastic response of plant roots and consequently we appropriately adapted the spacing of the nodes in our indentation protocol.

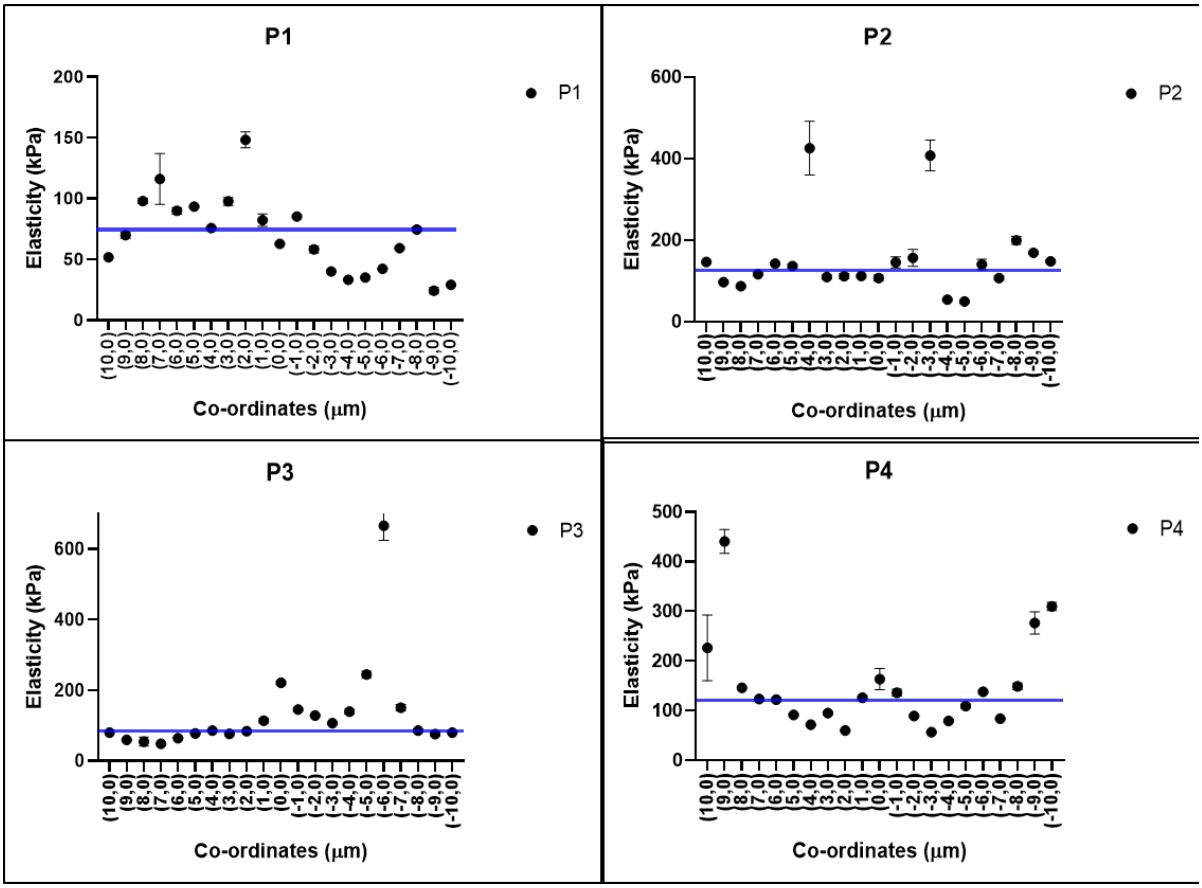

Figure 3-16: Results for a fine root surface analysis.
Box-and-whiskers plot of 4 different plants showing elasticity variation with a step size of 1 µm. Observe the smooth oscillation of values and the abrupt high values among the series of low value.

3.6 Development of the AFM measurement pattern

Because of the heterogeneity of plant root surfaces, force-curve distances cannot be collected randomly. It is clearly counter-intuitive as it is statistically sound to collect data randomly. The major problem of collecting data randomly is the collection time. In our AFM systems, it implies lots of withdraw and engaging from the AFM scanner that increases the recording time (without being certain that data are of good quality). As we mentioned before, collecting data

must be performed within 30 min. It is the main reason for designing a collecting protocol that insures us to collect a minimum set of force-distance curves in a reproducible way.

It is useful to introduce our nomenclature for the measurement pattern. We give the name of "matrix" the collection of multiple data points at different X,Y coordinates. We call "node" the location of multiple force-curve measurements. Thus, data collection is composed of a matrix build of several nodes, which themselves could be composed of a sub-matrix (or multiple curves at the same location). We briefly show the evolution of our collecting matrix over time.

3.6.1 First matrix

The very first matrix was designed to avoid local artifacts from the plant cell wall stiffness. We could not see exactly where the AFM cantilever touches the plant root so; we recorded force-distance curves on 9 different nodes as shown in Figure 3-17 and record 5 curves at every node and save the data. Although the idea of indenting 9 different areas seemed fine to us, the idea of indenting the same location five times did not seem to be convincing. That particular area accumulates stress and could likely be damaged during the recording.

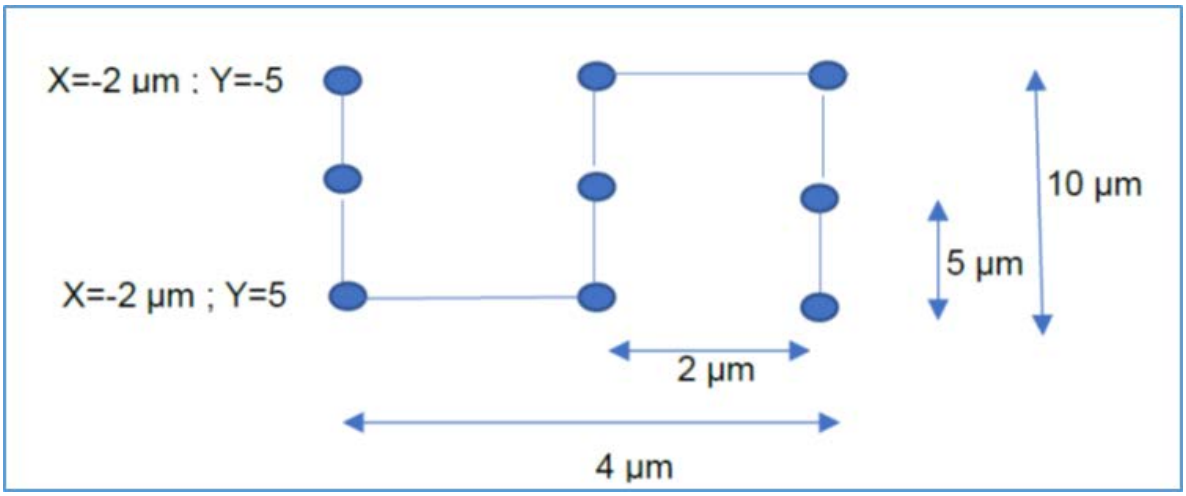

Figure 3-17: Schematic diagram of data collection using our first matrix.

Results from fine root analysis done by AFM (discussed in section 3.5) suggested a new matrix design by increasing the spacing between each node.

3.6.2 Second matrix

To compensate for the heterogeneity in the plant root surface, we decided to standardize the location of the matrix. The indentation location starts right before the start of the elongation zone, i.e. the transition zone of the plant, which is 500 µm away from the root tip. We also make sure to do indentation near the middle of the root surface. Ten nodes with a 3 x 3-point sub-matrix are recorded according to the arrangement shown in Figure 3-18. This auto-ramp acquisition of nine curves at each node helps to remove any kind of instrument drift thus making the data analysis more robust. A 5 µm of gap is set between each vertical point and 10 µm horizontally (Figure 3-18). The rationale behind this matrix system is to avoid the cell-cell interaction area. For instance, if one column has high values of stiffness, it could be assumed to be over a cell-cell junction, thus the other column will be in the middle of the cell region.

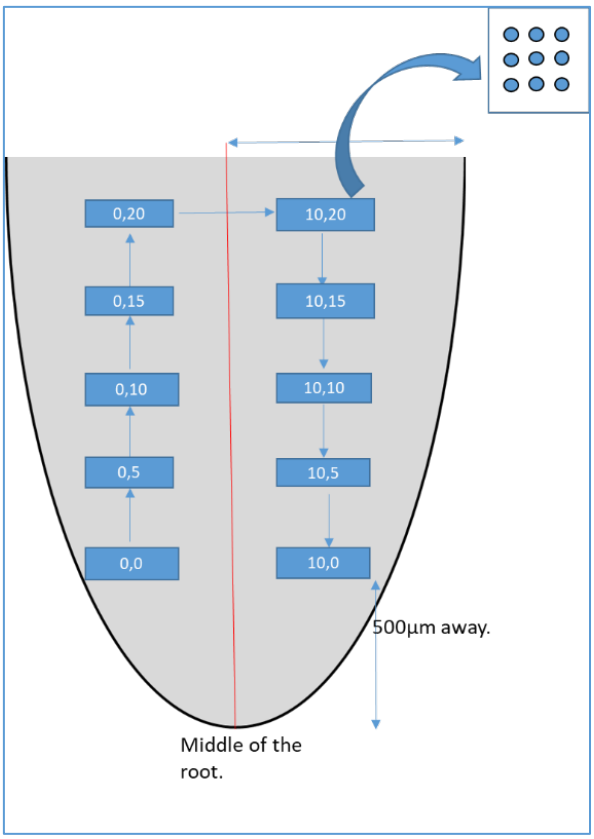

Figure 3-18: Schematic diagram of the second matrix.
This matrix was designed after obtaining ESEM and TEM images. A 3 x 3 matrix is recorded at each node with a spacing of 50 nm.

It turned out that this design of matrix took a lot of recording time. In addition, half of the data could be removed in case we hit cell wall junction. Another unexpected disadvantage of this design was that we might hit the same region again due to growing living roots. In any case, this design did not provide us the stability in data collection.

3.6.3 Third matrix

To compensate above problems another matrix was designed. It again started at 500 µm away from the root tip with an uneven zigzag pattern in order to avoid putative cell-cell junction area. The advantage was that the indentation area would always be different but, again, it took a lot of time to follow this pattern to avoid junction nodes (Figure 3-19).

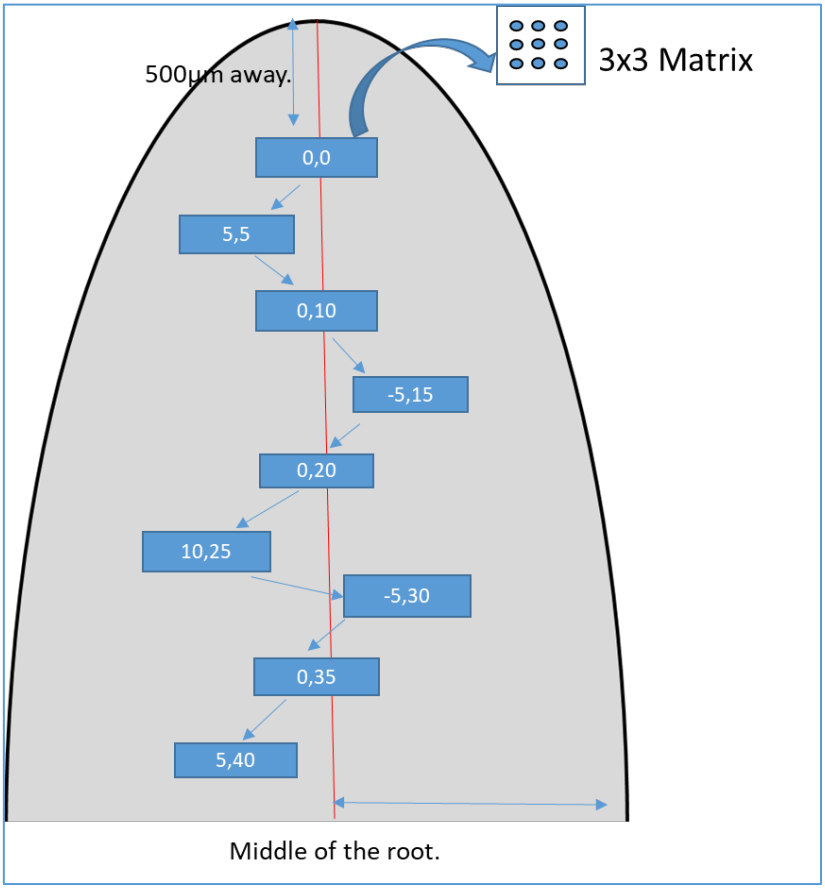

Figure 3-19: Schematic representation of the third matrix.
Indentation starts 500 µm away from root tip but in a non-uniform arrangement.

In addition, it was difficult to record a 3 x 3 sub-matrix on our instrument as we observed piezo drifting. This limitation was visible on our data as well. To overcome the time constraint, another matrix method was designed, but again 500 µm away from root tip and in the middle of the root.

3.6.4 Fourth matrix

The final validated matrix (Figure 3-20) is made of 16 nodes where each node consists of a 2 x 2 sub-matrix, indenting four different points 50 nm apart. It takes 20 minutes for acquiring all the necessary F-D curves per plant. The major advantage of this design resides in the acceptable loss of data if a row or a column measures data over cell-cell junctions. In the worst-case scenario, where one row and one column scan over a cell-cell junction, then only 7 nodes are discarded (leaving 9 nodes for data analysis).

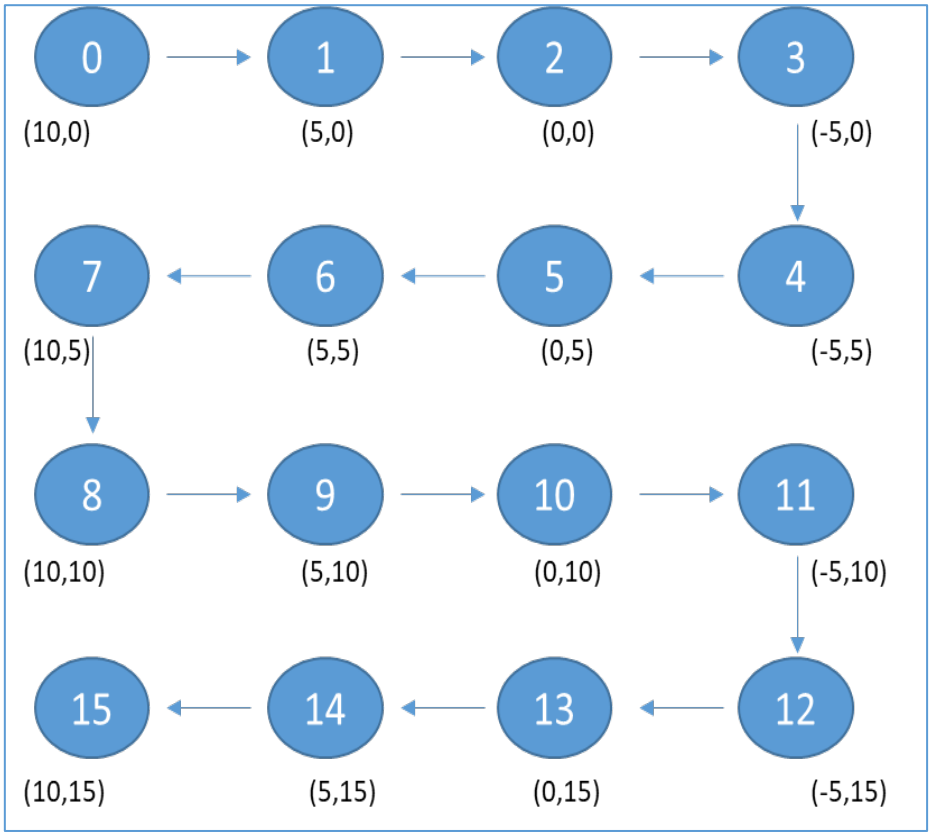

Figure 3-20: Schematic representation of the fourth and the final matrix.
The matrix is made of 16 nodes with 2 x 2 collection sub-matrix with a gap of 50 nm. Cantilever is placed at the middle of the root and 500 µm away from the root tip.

3.7 Decellularization on plant roots.

Measuring the external primary cell wall stiffness cannot be uncoupled from the turgor pressure of the epidermal cells. Because our goal is to measure the stiffness of plant roots in various experimental stress conditions, the protocol assumes that the turgor pressure did not change. However, one of the interests in this work is to identify putative changes in the structural organization of cell walls. It appeared to us that one way to analyze these changes could be done after removing all the cellular content of plant roots. We therefore contacted an ITN partner laboratory (Univ. Barcelona) to plan a secondment in Barcelona and test the possibility of decellularizing plant roots. During this month in Barcelona, we defined and tested a decellularization protocol (see methods chapter, section 2.7.4).

The success of the decellularization protocol was established after testing different concentrations of detergents and stains and exposure time under the fluorescence microscope. This protocol has been made once in Barcelona and here are the main results illustrated by fluorescence imaging. A major difficulty in plant root fluorescent imaging is the persistent auto-fluorescence in the blue light. As seen in the Figure 3-21, blue auto-fluorescence is quite prominent and does not label any specific area of the root.

Three stains were tested i.e. DAPI, PI and CFW. DAPI is used to stain nuclei. Native roots labelled with DAPI showed the presence of nucleus with other unspecific staining (Figure 3-22). After incubation of 1 hour with SDS followed by DNase action, most of the blue spherical labeling, which indicates nucleus, seems to disappear. However, the overlapping with native auto-fluorescence (Figure 3-23) led us to abandon the usage of DAPI for plant roots.

The propidium iodide (PI) is a large and charged molecule that is unable to cross membrane bilayers but can bind to DNA (and likely epidermal layers) in case of disrupted cellular structures. From our results, we observed a clear labelling in red of nucleus in normal roots as well as a continuous labeling of roots (Figure 3-24). After decellularization, the PI stained plants with only a specific binding to the central root cylinder (Figure 3-25). The absence of nuclear labelling suggest that cells have been efficiently removed in our decellularization experiment.

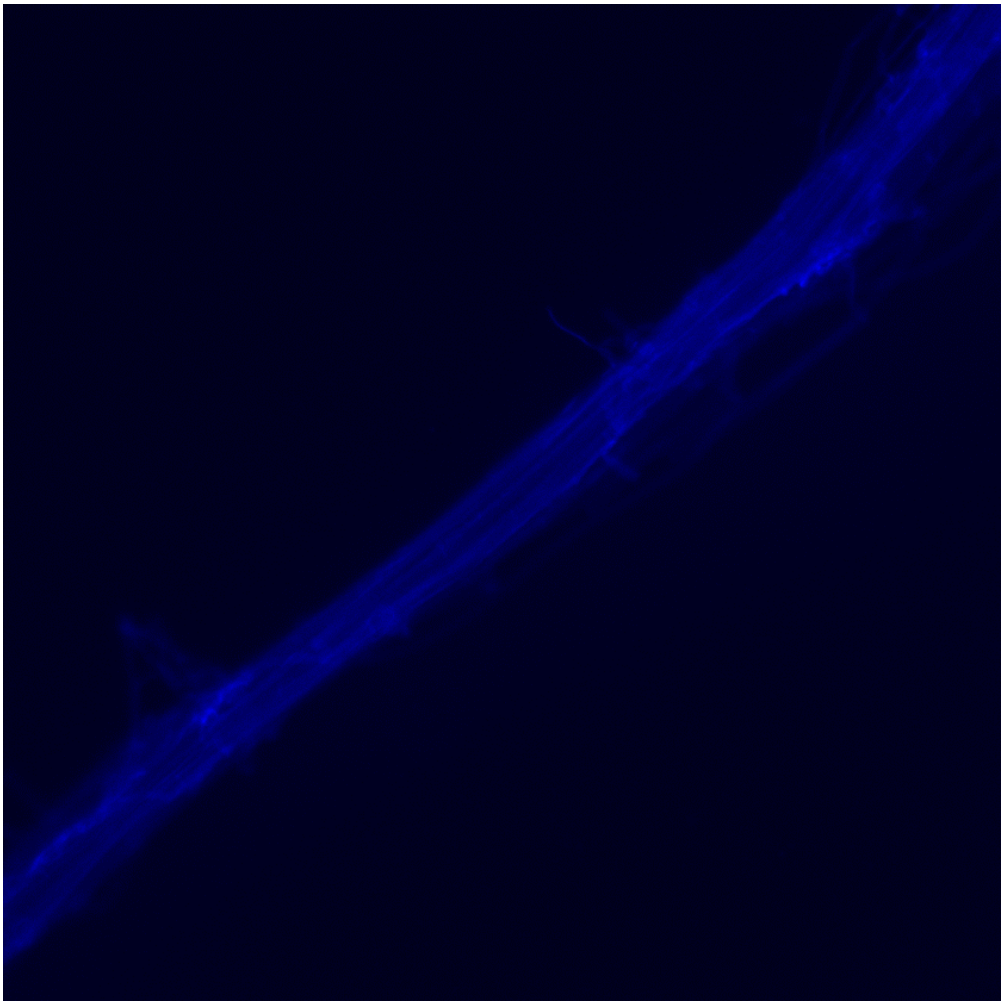

Figure 3-21: Plant root showing auto-fluorescence in the blue light.
Roots were not decellularized and not stained either. No specific labelling could be seen in this picture. The average width of a root is around 100-120 µm for 4-day old seedlings, which provides us an estimated scale bar of the image.

The third label is the calcofluor-white (CFW) that is specific of cellulose in the root structure. While observing fluorescent images, it is seen that CFW staining showed no reduction of signal between native (Figure 3-26) and decellularized roots (Figure 3-27). The presence of stain before and after decellularization suggests that the cell wall is conserved even after processing the roots by SDS and DNase (Figure 3-27).

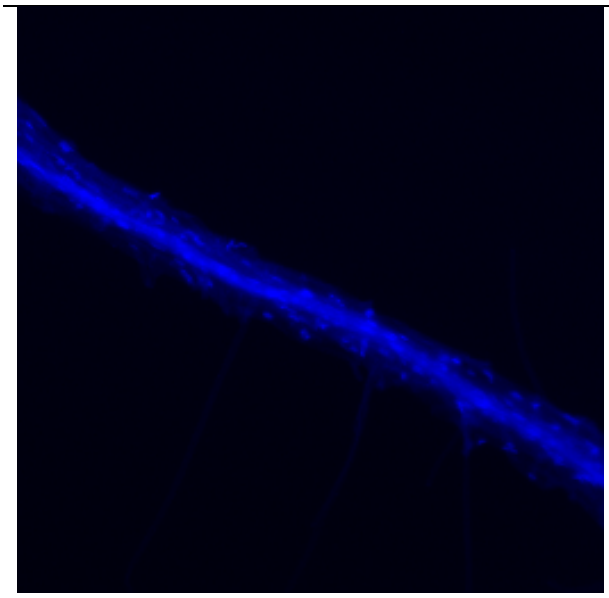

Figure 3-22: DAPI stained root in native form.
Small pseudo-spherical dots indicate the presence of nuclei. For an estimated scale bar refer figure 3-21.

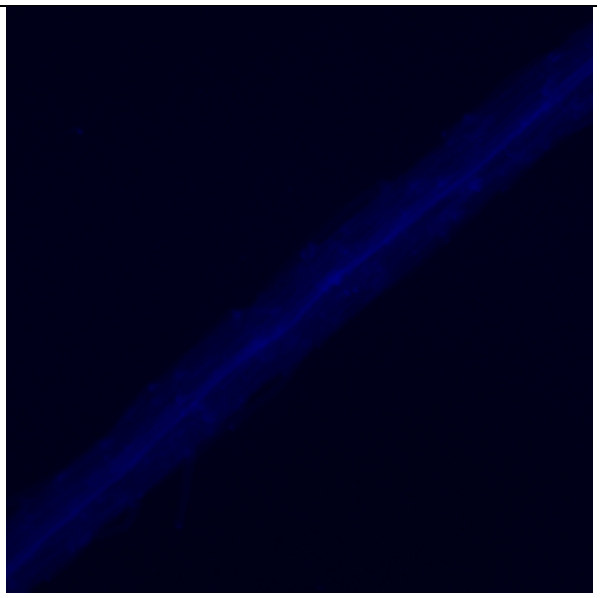

Figure 3-23: DAPI stained root after decellularization by SDS and DNase. For an estimated scale bar refer figure 3-21.

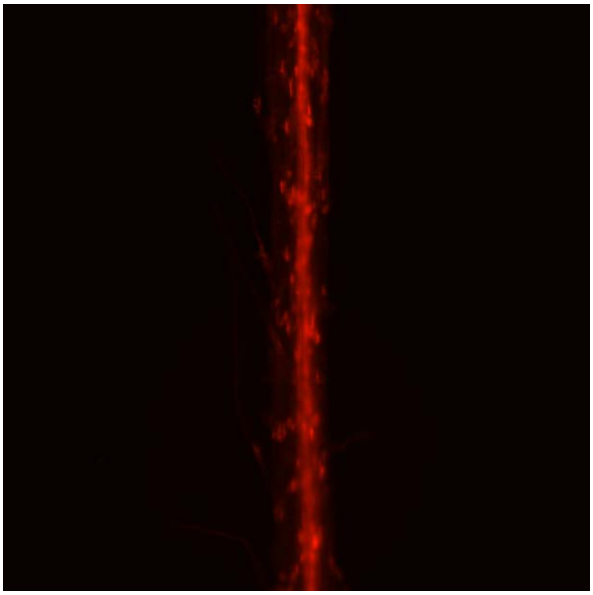

Figure 3-24: Native PI stained root.
Nuclei dots visible along with the root cylinder. For an estimated scale bar refer figure 3-21.

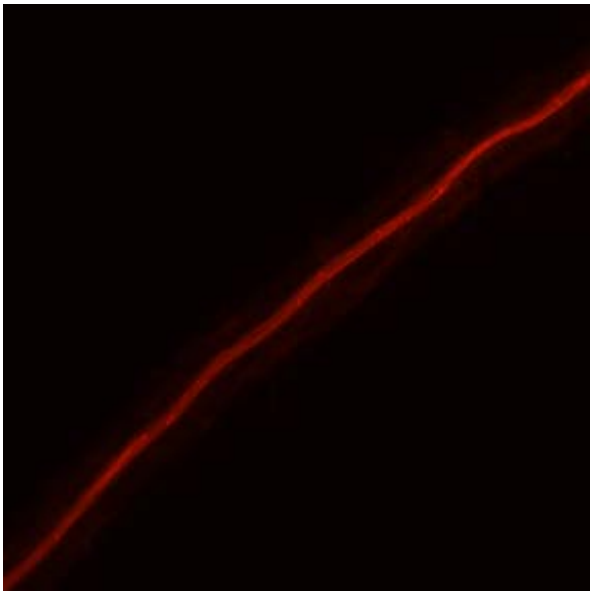

Figure 3-25: Decellularized root stained with PI.
Unspecific labeling of probably the stele of the roots with absence of nuclei stains. For an estimated scale bar refer figure 3-21.

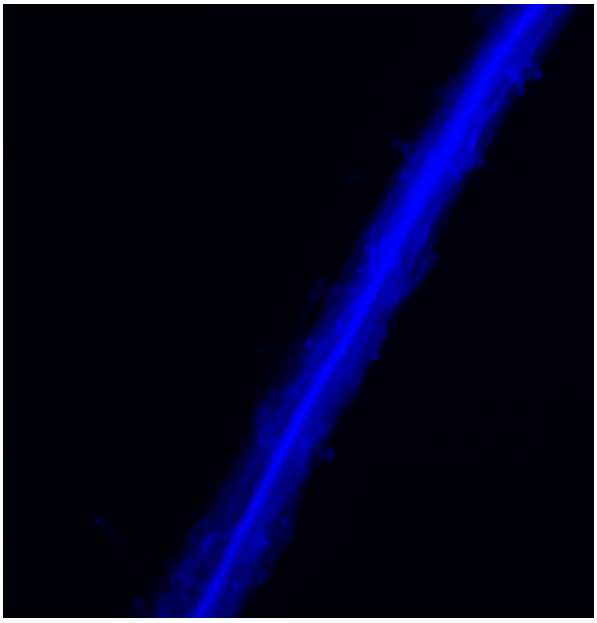

Figure 3-26: Native CFW stained root. For an estimated scale bar refer figure 3-21.

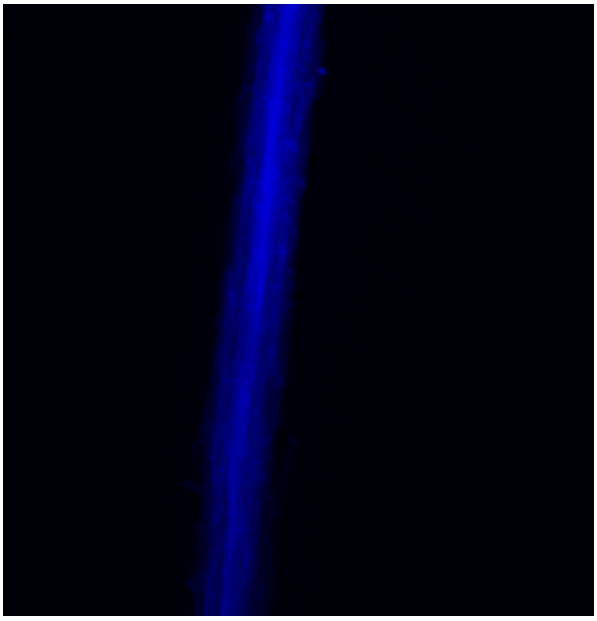

Figure 3-27: CFW stained root after decellularization. For an estimated scale bar refer figure 3-21.

The biggest obstacle during this time was the staining protocol of the plants. The root and root end were extremely thick (100-200 µm), which made imaging complicated.

With samples this thick, it is common to observe auto-fluorescence of the sample that can be difficult to distinguish from specific signal. To counteract this obstacle, we used higher concentration of stains so that the required exposure time would decrease, decreasing auto-fluorescence as well.

3.8 Conclusions

The complex arrangement of cell wall structure and the non-uniform distribution of cells in root lead to major heterogeneity in nanoindentation experiments. This chapter deals with all our efforts to achieve a robust protocol that increases the reproducibility in measured elastic parameters. Improvements were reached in the seedling growth methodology, the seedling fixation on a glass slide, and the strategy to collect force-distance curves. It is important to emphasize that the robustness is likely not obtained because of a single factor, but instead by a succession of little improvements. Nevertheless, several constraints remain in our protocol that are linked with the usage of the old Dimension 3100 AFM instrument. In particular, we could not use taller tips as PFQNM due our unfocused laser beam. In addition, the drift of the

open-loop piezo scanner of Dimension 3100 pushed us to develop redundant measurements to ascertain the collection of meaningful data. Finally, a major challenge (or risk) in our methodology is the usage of the NuSil silicon adhesive to fix seedlings on glass slides. Initially, we only considered the impact of NuSil on the living status of plants. This was cleared out by several tests, but the major difficulty remains in obtaining NuSil from a reliable commercial source. A practical reason, as explained to us, was the short shelf-storage period of NuSil that push providers to sell it in large quantity; a single 1 L bottle used in our study was just a given sample.

RESULTS:

NANOMECHANICAL RESPONSE OF ROOTS

4 Results: Nanomechanical response of roots

In this chapter, we present our indentation results on plant roots. Under –Pi condition, changes in epidermal cell extension can be observed initially 4 days after germination (Sanchez-Calderon et al. 2005). Although AFM can detect the changes on the root surface as early as 30 minutes after transfer in a stress condition, we performed our analyses with a two-hour stress period. In practice, and according to our previously detailed protocol, nanoindentation experiments are performed on day 4 (post-sowing), the identification of phenotype (root elongation) is performed at day 5, and quantification of root length is performed at day 6. The strict timing and the impossibility to halt the experiments after sowing make the project challenging in terms of planning.

The main objective of these nanoindentation experiments is to determine the relationship between metallic stress and root cell extension in plant roots. Experiments will be performed on *Arabidopsis* wild-type and mutant seedlings systematically in –Pi condition and at low pH, unless otherwise stated.

4.1 Results of Wild type (WT) Arabidopsis

Nano-indentation of our wild-type *Arabidopsis* roots are analyzed by treating them with different conditions of iron and aluminum. Metals are added in the µM range of concentrations and the labeling follows the rule: Metal[conc]Metal[conc]. For instance, a stress condition Fe0Al0 indicates that no metal is added to the stress condition whereas Fe10Al5 indicates that 10 µM $FeCl_2$ and 5 µM $AlCl_3$ are added. In this work, force-distance curves were analyzed by AtomicJ (Hermanowicz et al. 2014). Parameters are as follows: robust exhaustive contact estimator with the robust (LTA) fitting method following the Sneddon model for pyramidal tips of 35° opening (for PNP tip). The indentation approach force curve was capped to 5 nN. We regularly observed that curves showing a poor fitting were “poor” acquisition data; it was decided to remove all fitting data having a fitting quality $R^2 < 0.9$.

4.1.1 Control conditions

We considered our control condition when WT seedlings grow under non-stress conditions. The non-stress condition includes the absence of supplemented metals (Fe0Al0). Two sets are

included in our results: first, roots that were classically transferred from growing crystallization plates to Petri dishes for two hours; second, roots that did not follow the transfer step, i.e., the roots are directly taken from the crystallization plates and measured (Figure 4-1). We believed that there could be some amount of stress induced by transferring seedlings from growing plates to various experimental conditions. Thus, we performed a "no transfer" experiment as well to see if there is any significant change due to transfer condition or not.

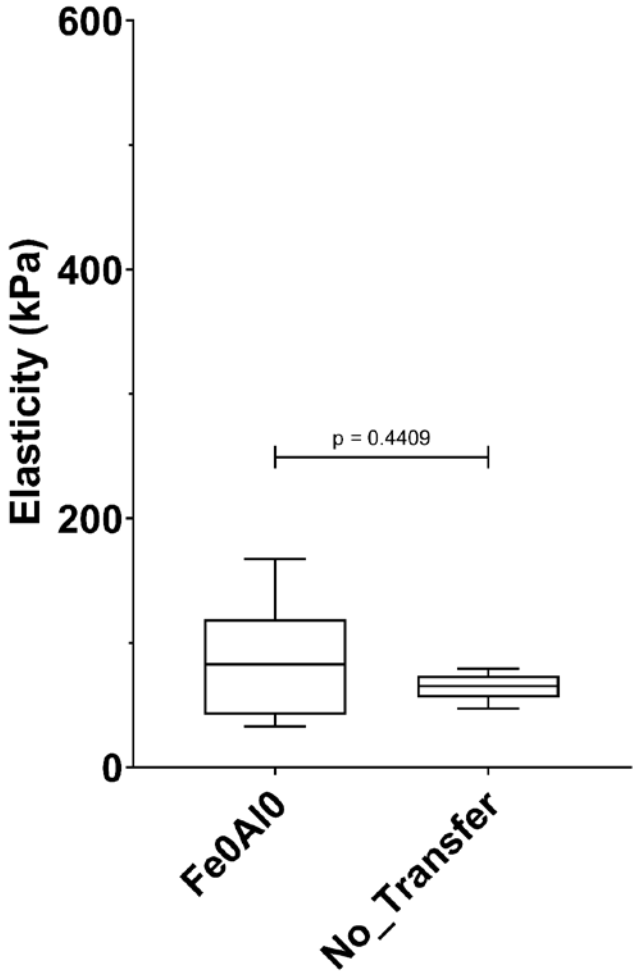

Figure 4-1: Elasticity values obtained for WT seedlings in control conditions.
Box-and-whiskers plot shows the average elasticity expressed in kPa. The middle black line in the box indicates the median and the whiskers indicate the min and max values. Force-distance curves were analyzed and the average of all elasticity values at the plant level constitute the plot. The nomenclature follows the metal stress conditions where Fe0Al0 implies no addition, 0 µM of Fe^{2+} and 0 µM of Al^{3+}, was added to the control conditions. No Transfer indicates that seedlings were not transferred from the growing plates to petri dish, and were measured directly after pick-up from growing plates.

A first observation is the large standard variation (SD) in the elasticity values of Fe0Al0 (Figure 4-1). This is a recurrent observation all along our work. There is clearly heterogeneity among seedlings and some heterogeneity in data acquisition (probing multiple areas on the root). It is important to remember that the data is compiled at the plant level and not by individual force-curve measurements. In further results, Fe0Al0 is considered as the control (including the transfer step) while comparing with other stress conditions.

Table 4-1: Elasticity values in control conditions.

Stress condition		Elasticity (in kPa)	
	Number of Plants	Average ± SD	Median
Control (Fe0Al0)	11	87.7 ± 45.3	82.8
No transfer (Fe0Al0)	5	64.9 ± 11.5	65.2

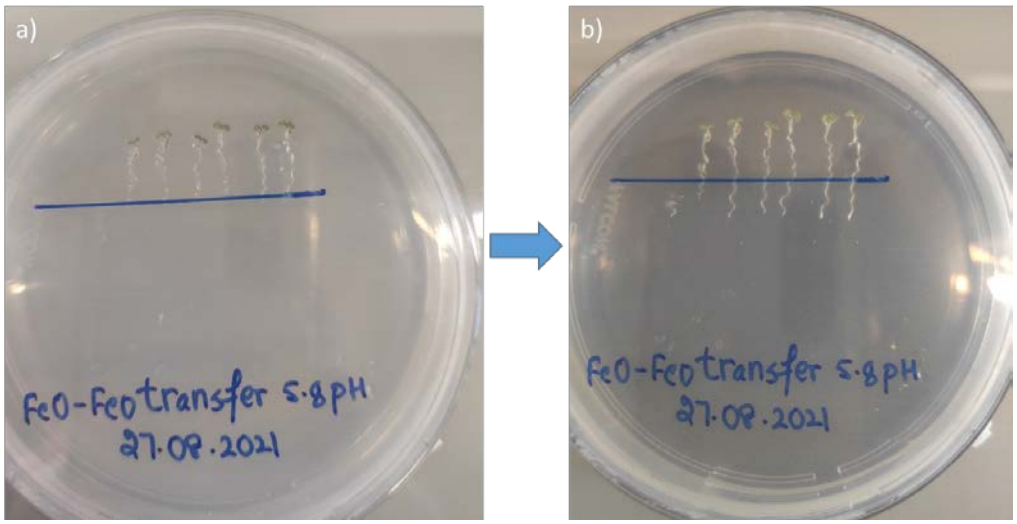

Figure 4-2: Root length phenotype showing root growth in Fe0Al0 condition.
a) Picture taken on day 4, when roots are transferred from crystallization plate to the petri dish, marked at the root end.
B) Picture taken on day 5 that shows the root growth when no metals are added.

Phenotype for "no transfer" roots cannot be presented here because they were taken directly from the crystallization plate and indented. Since it is not possible to remove fastened seedlings on glass slides, it is not possible to view and take pictures of these roots (they grew in the crystallization plates). For Fe0Al0 (control), roots were transferred from the crystallization plate to Petri dish as shown in Figure 4-2 (a) on day 4 and their root ends were marked. Root growth was observed on day 5 as shown in Figure 4-2 (b). We can clearly see

that the roots grow beyond the marked line. It is interesting to note that even in the same growing conditions roots develop with variable growth rate.

4.1.2 Nanomechanical response under aluminum stress.

In this section, we show the stiffening effect of the presence of aluminum on the plant root surface. The different concentrations were Fe0Al5, Fe0Al10 and Fe0Al20. A comparative plot shows all these conditions including the control (Fe0Al0). From our results, we see that there might not be a significant difference in the elasticity of plant root surface by adding 5 µM and 10 µM concentration of aluminum. However, 20 µM of aluminum shows considerably higher elasticity values (Figure 4-3). Our results lead to the fact that higher concentration of aluminum leads to higher cell wall stiffness.

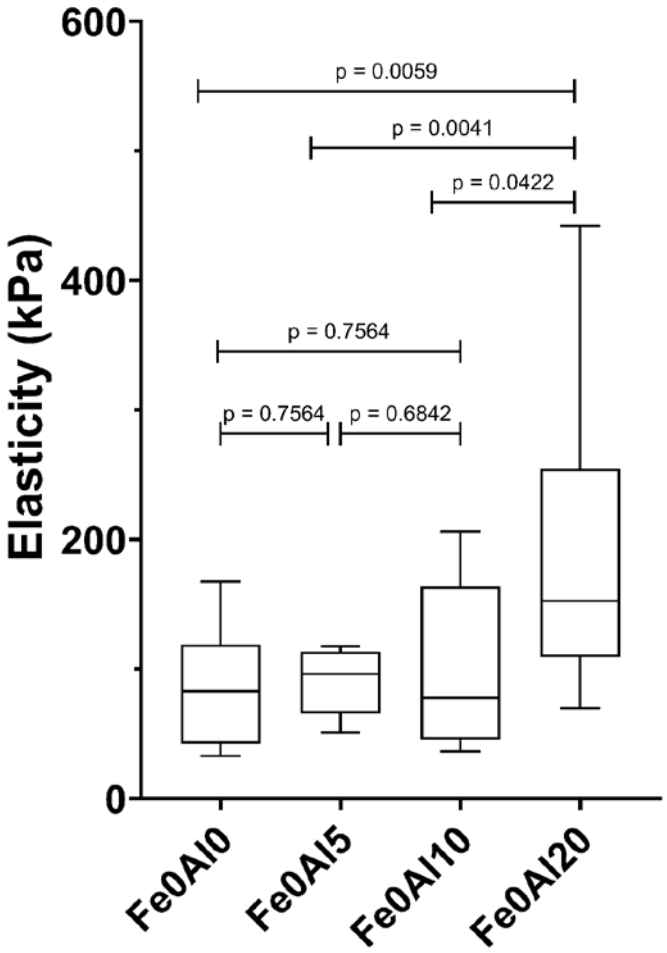

Figure 4-3: Elasticity values obtained for WT roots in the presence of aluminum.
There is no significant increase in the stiffness of Fe0Al5 and Fe0Al10 with the control Fe0Al0. However, a significant increase in stiffness is observed with the Fe0Al20 stress condition. For box-and-whiskers plot details refer to Figure 4-1.

Table 4-2: Elasticity values in aluminum stress condition.

Stress condition		Elasticity (in kPa)	
	Number of plants	Average ± SD	Median
Fe0Al0 (Control)	11	87.7 ± 45.3	82.8
Fe0Al5	10	91.1 ± 24.7	96.2
Fe0Al10	10	99.9 ± 65.9	77.7
Fe0Al20	13	186 ± 112	152.6

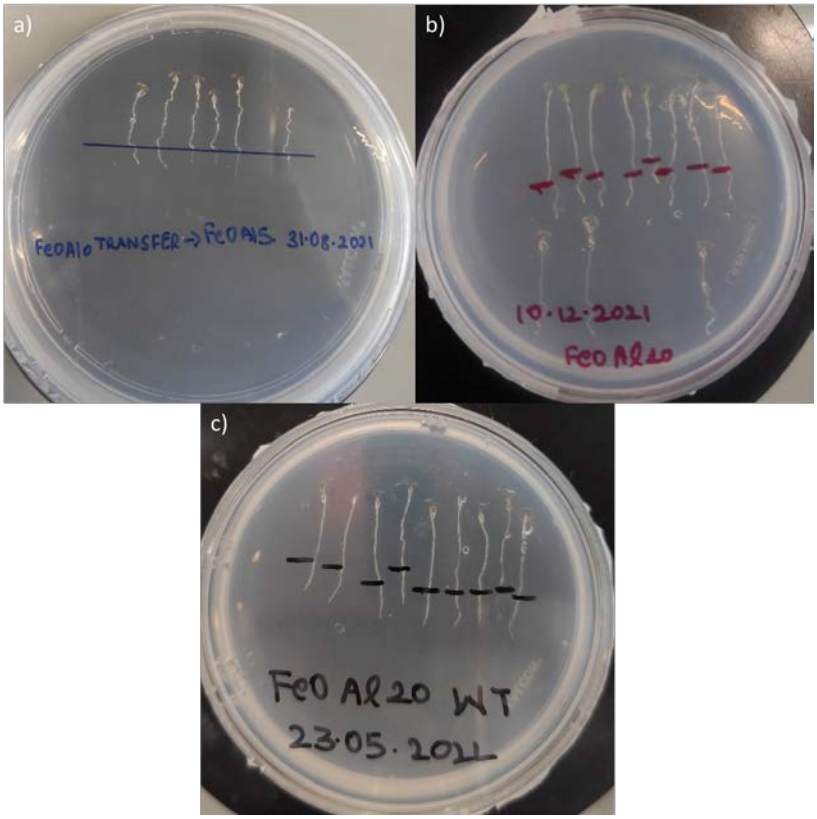

Figure 4-4: Root length phenotype in case of aluminum alone.
Root ends were marked on Day 4 and pictures were taken next day. Root growth on day 5 seen in case of a) Fe0Al5 b) Fe0Al10 and c) Fe0Al20.

Root growth in plants after adding aluminum can be seen in Figure 4-4. Despite the variability in the elasticity values, we observed a homogeneous root growth in all our phenotype results. Although aluminum is considered toxic for the root development, but it was still possible to observe root growth which seemed similar to that of control phenotype.

4.1.3 Nano mechanical response under iron stress

In this section, we show the stiffening effect due to the stress with the presence of iron. Different concentrations of iron were tested: Fe10Al0, Fe15Al0 and Fe20Al0 while comparing them with the control Fe0Al0 condition (Figure 4-5). We observed that elasticity values of Fe10Al0 are similar to that of Fe0Al0. Interestingly, if we add 5 µM more of $FeCl_2$ (Fe15Al0), we observed a significantly increase in elasticity when compared with that of Fe0Al0 or Fe10Al0 (Table 4-3). Furthermore, by adding 5 µM more to the previous concentration, we observed a further increase in the elasticity values. However, we found out that the overall elasticity of plant roots with Fe15Al0 is not significantly different from that of Fe20Al0, although the min-max range of Fe20Al0 is much larger than Fe15Al0 (Figure 4-5).

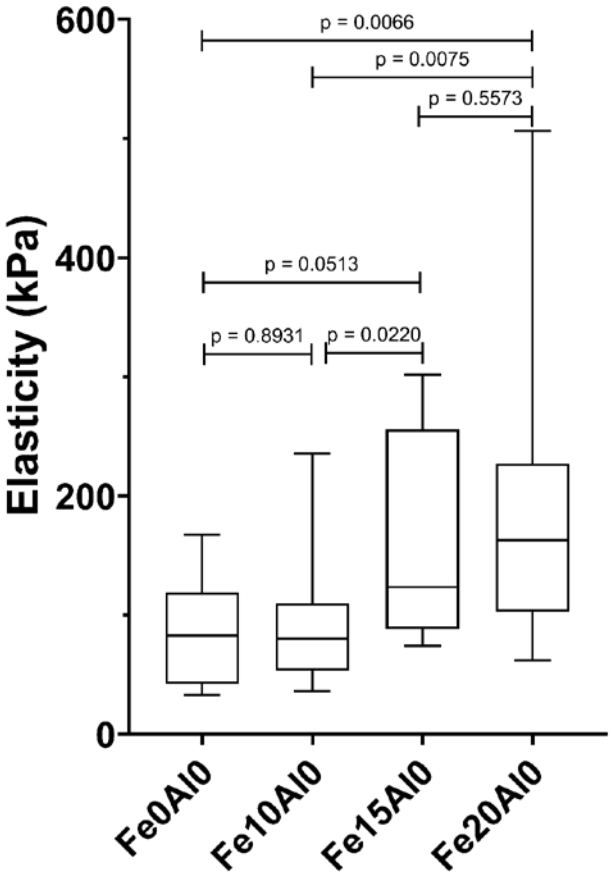

Figure 4-5: Elasticity values obtained for WT roots in the presence of iron. Although there is no significant increase in elasticity between Fe0Al0 and Fe10Al0, the conditions Fe15Al0 and Fe20Al0 show significantly higher elasticity values. For plot box-and-whiskers plot details refer to Figure 4-1.

Table 4-3: Elasticity values in iron stress conditions.

Stress condition		Elasticity (in kPa)	
	Number of plants	Average ± SD	Median
Fe0Al0 (Control)	11	87.7 ± 45.3	82.8
Fe10Al0	14	94.8 ± 56.7	80.2
Fe15Al0	10	157 ± 87.7	123.5
Fe20Al0	11	192 ± 122	162.7

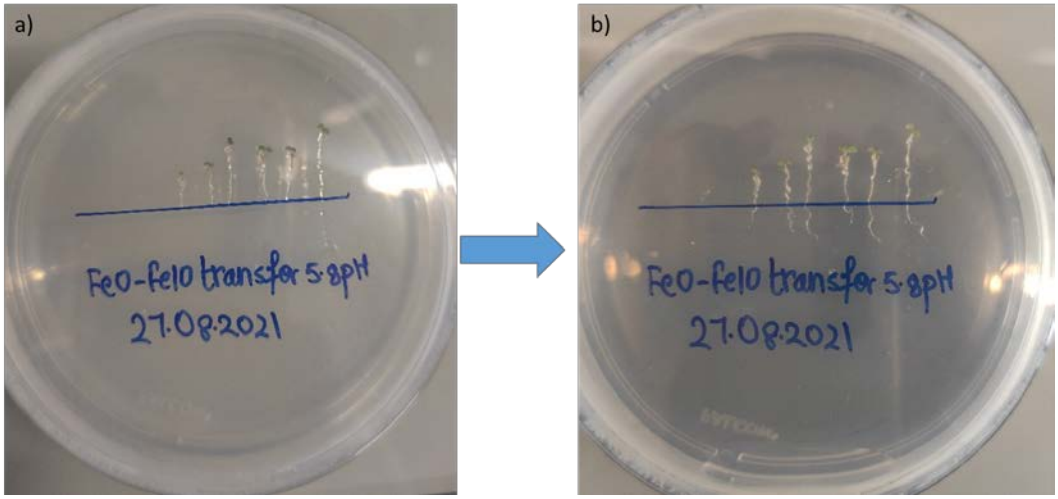

Figure 4-6: Root length phenotype of iron in Fe10Al0 stress condition.
Roots were transferred from crystallization plate to the petri dish on day 4 as seen in the first picture. The second picture of the same petri dish is taken on day 5 and shows the root growth next day for Fe10Al0 condition.

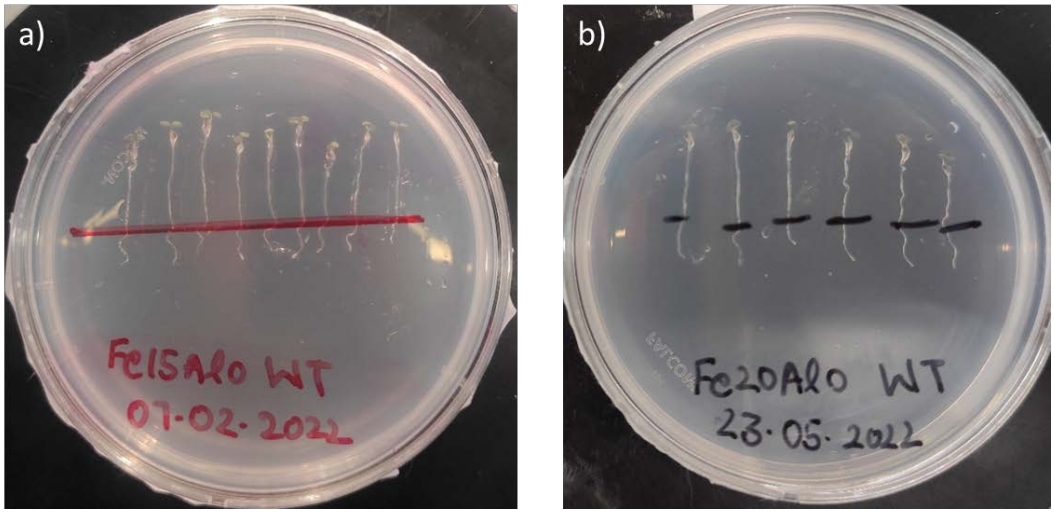

Figure 4-7: Root length phenotype in the presence of higher concentration of iron.
The first picture shows the root growth on day 5 for Fe15Al0 and the second picture in case of Fe20Al0. Root ends were marked on Day 4 and pictures were taken by camera on Day 5.

Figure 4-6 shows the root growth phenotype from day 4 (Figure 4-6a) to day 5 (Figure 4-6b). In Fe10Al0, root grows normally similar to that of Fe0Al0. Surprisingly, despites the higher elasticity values for the Fe15Al0 and Fe20Al0 conditions, the root growth behavior is similar to that of Fe0Al0 and Fe10Al0 (Figure 4-7).

From the results obtained with single metal stress conditions, we observe an increase in the stiffness of seedling roots when their individual concentration increases. However, no change in the root growth is observed, in apparent contradiction with our previous results (Balzergue et al. 2017).

4.1.4 Nanomechanical response under iron and aluminum

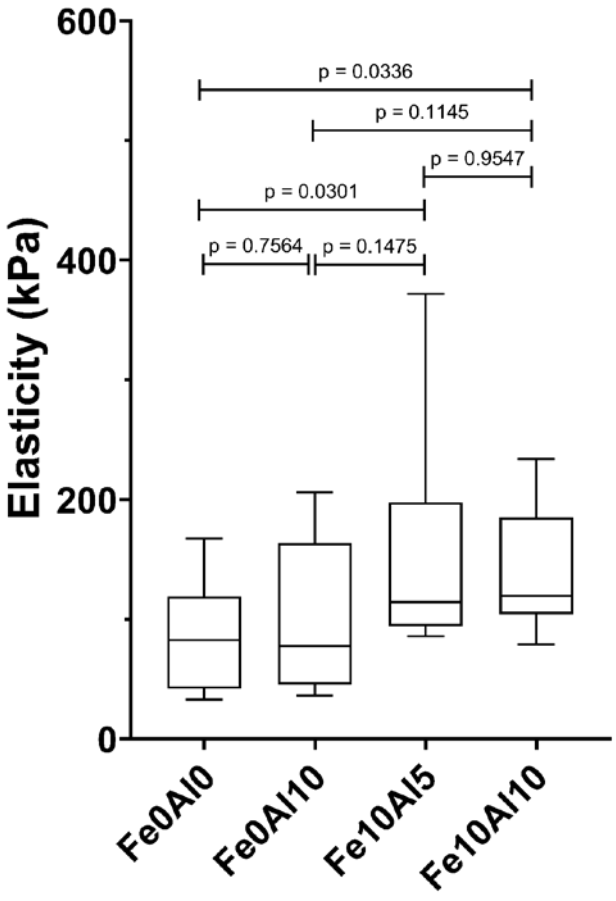

Figure 4-8: Elasticity values obtained for WT roots in the presence of iron and aluminum.
For plot box-and-whiskers plot details refer to Figure 4-1.

We now test the combined effect of iron and aluminum together on plant root surface (Figure 4-8) using two stress conditions: Fe10Al5 and Fe10Al10. The elasticity values are significantly higher when compared to control and Fe10Al0 (if we consider α threshold of 0.05), whereas the difference between Fe10Al5 and Fe10Al10 is not significant (Table 4-4).

Table 4-4: Elasticity values for combined effect of iron and aluminum stress condition.

Stress condition		Elasticity (in kPa)	
	Number of plants	Average ± SD	Median
Fe0Al0 (Control)	11	87.7 ± 45.3	82.83
Fe10Al0	14	94.8 ± 56.7	80.19
Fe10Al5	13	153 ± 84	114.2
Fe10Al10	11	141 ± 57	119.6

The very surprising result is that, despite a similar increase in stiffness between Fe20Al0 (or Fe0Al20) and Fe10Al5 (or Fe10Al10), a complete root extension arrest (REA) is observed for both conditions (Fe10Al5 and Fe10Al10) the next following days (Figure 4-9).

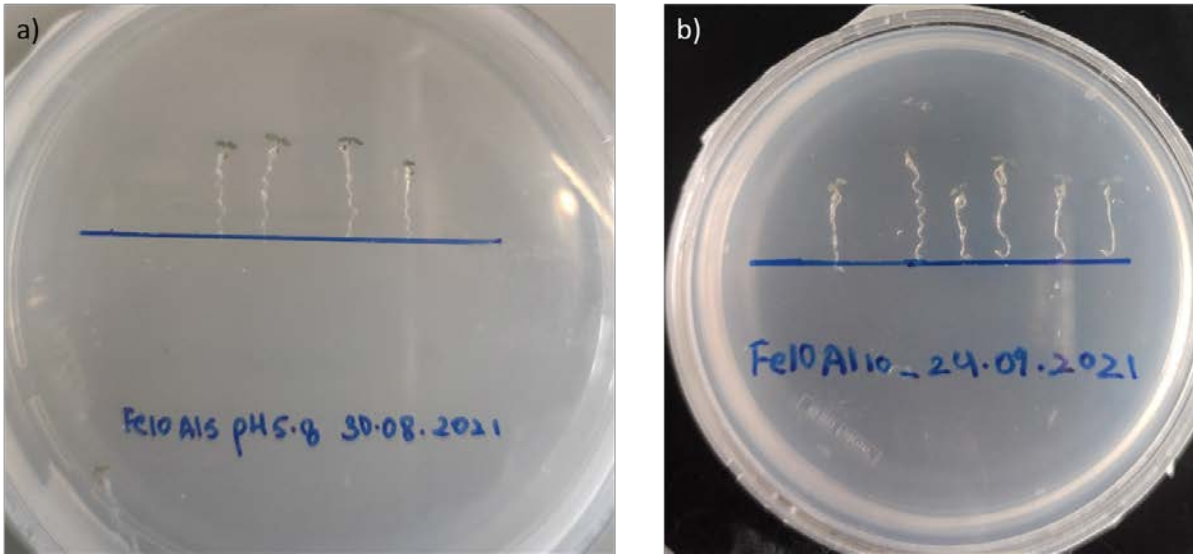

Figure 4-9: Root length phenotype in case of combined effect of iron and aluminum.
a) Roots transferred on day 4 and b) pictures taken on day 5. In both cases, a complete root extension arrest is observed next day.

4.2 Nanomechanical response with the *almt1* mutants

It is known that an aluminum stress in plant is tolerated by the release of small organic acids, the best-known being malate. The malate transporter located at the cytoplasmic membrane of plant cells allows the exudation of malate into the apoplast region. The almt1 gene codes this malate transporter. To test the importance of malate in our study system, we performed similar force-distance curves of an *almt1* mutant seedling. In these plants, the malate transporter is deficient and no malate exudation is observed. So, we seeded *almt1* mutants and measured its root elasticity as shown in Figure 4-10.

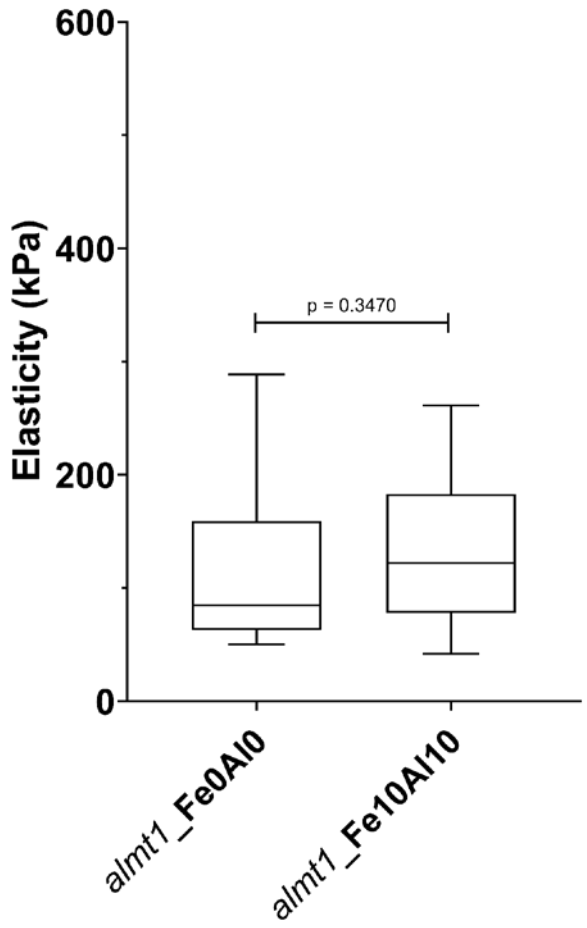

Figure 4-10: Elasticity values for mutant almt1 roots in control and Fe10Al10 condition.
Results indicate a lack of differences between the two experimental conditions. It indicates that in absence of malate there is no increase in the external epidermal cell wall. For plot box-and-whiskers plot details refer to Figure 4-1.

Only two conditions were tested: Fe0Al0 and Fe10Al10. As can be seen, no significant change in the elasticity values is observed (Table 4-5). In addition, plants exposed to both stress conditions grow normally when the phenotype was observed next day (Figure 4-11). This result indicates that the presence of malate does influence both the stiffness and root extension properties.

Table 4-5: Elasticity values in the almt1 mutant seedlings.

Stress condition		Elasticity (in kPa)	
	Number of plants	Average ± SD	Median
Fe0Al0	12	122 ± 76	88.3
Fe10Al10	11	139 ± 69	122.0

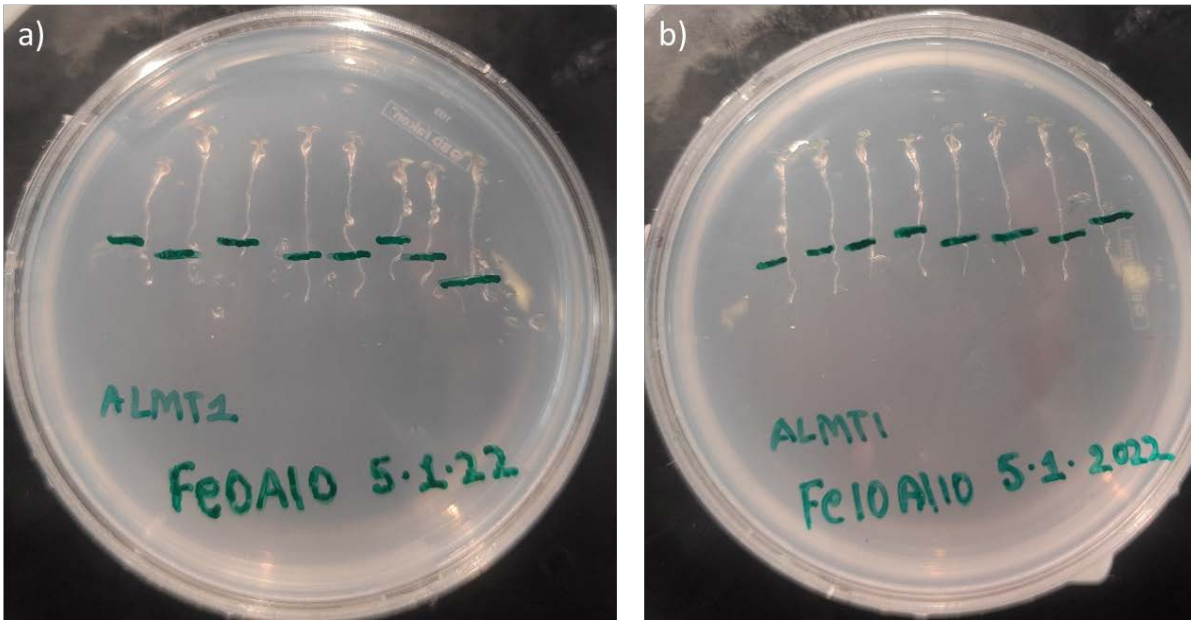

Figure 4-11: Root growth phenotype of the almt1 mutant seeds.
Pictures were taken on day 5 to observe any changes in root growth. a) Normal root growth for the Fe0Al0 condition, b) Normal root growth for the Fe10Al10 condition.

4.3 Nanomechanical response of WT in presence of phosphate

During the whole course of our research, we are only considering the changes in root structure in low phosphate condition. Changes observed in the elasticity results due to presence of metals is a direct consequence of the low phosphate conditions used in our experiments. This situation mimics the effect of acidic soils that are often deficient in phosphate, a known

chelator of cations that increases the solubility of toxic metals. To control our system in presence of phosphate on WT, we performed force-distance curves on the stress condition that creates a strong RGA phenotype: Fe10Al10, but in the presence of a large quantity of phosphate (500 µM).

In Figure 4-12, we tested two conditions Fe0Al0 (control) and Fe10Al10 in presence of 500 µM of phosphate. This elasticity plot shows that there is no significant difference observed in both conditions (Table 4-6). These elasticity results were further complemented by the phenotype observation next day. Roots grew normally with no inhibition observed (Figure 4-13).

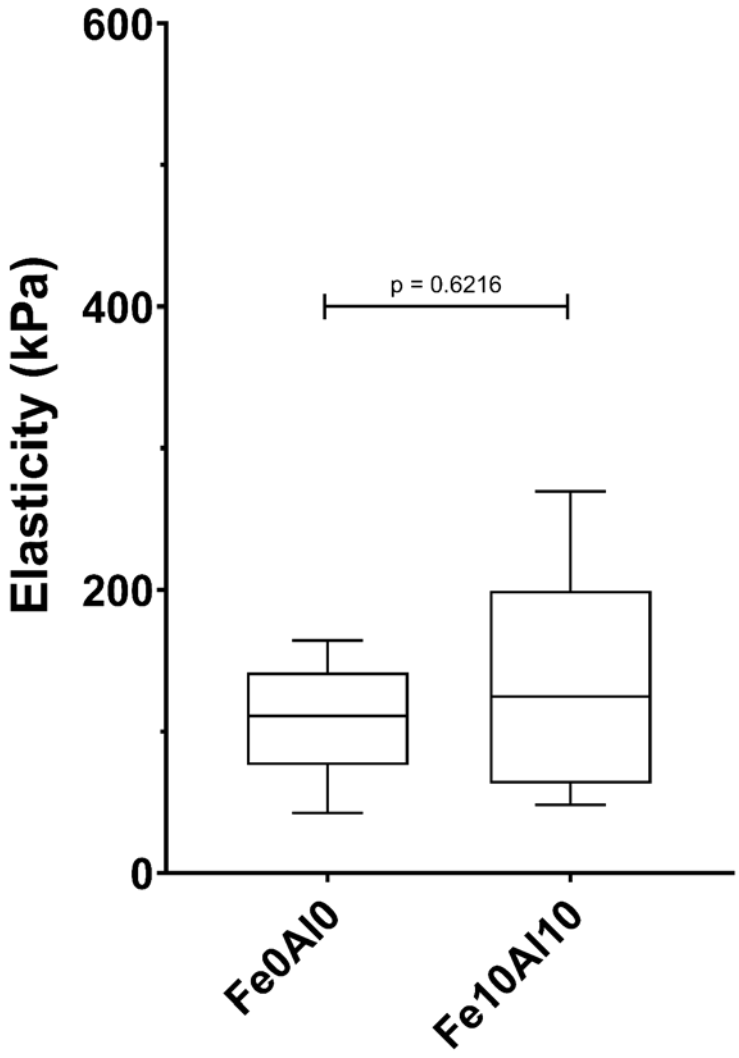

Figure 4-12: Elasticity values for WT roots in control and Fe10Al10 with 500 µM of Pi. For plot box-and-whiskers, plot details refer to Figure 4-1.

Table 4-6: Elasticity values in presence of phosphate.

Stress condition		Elasticity (in kPa)	
	Number of plants	Average ± SD	Median
Fe0Al0 (Control)	5	109 ± 44	110.7
Fe10Al10	8	133 ± 78	124.6

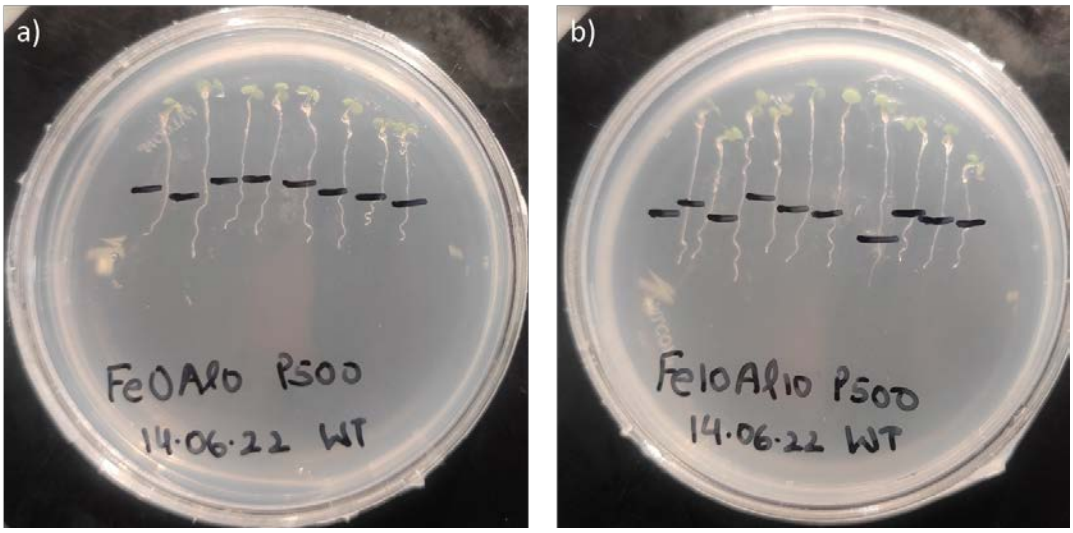

Figure 4-13: Root growth phenotype of WT Arabidopsis.
Control and stress conditions but in the presence of inorganic phosphate (Pi). When 500 µM of Pi is added, no root growth arrest is observed in the combined presence of iron and aluminum.

4.4 Phenotype in different conditions

Up to now, the root growth phenotype was expressed visually the following day of the nanoindentation experiment. We provide now a quantitative measurement of all the root lengths of various concentrations of plants (Figure 4-14). Roots were measured with the help of NeuronJ, a plugin found in ImageJ software. Roots were transferred to various stress conditions on day 4, but measured on day 6, i.e., two days after transfer. Although the phenotype is clearly visible after 24 hours (at day 5), we wanted to measure longer roots so that their differences in length could be better studied. Figure 4-14 shows results as a clear dichotomy: one group with long roots (Fe0Al5, Fe0Al10, Fe0Al20, Fe10Al0, Fe15Al0, and Fe20Al0) and the other group with short roots (Fe10Al5 and Fe10Al10). Results are so obvious that statistical significance is meaningless. Nevertheless, Table 4-7 covers statistical values for all the conditions that are discussed in this chapter.

Table 4-7: Seedling root lengths for WT and almt1 mutant

Plants	Exp. conditions	N	Root length (mm)
WT	Fe0Al0	19	25.0±3.1
	Fe0Al5	17	24.9±4.5
	Fe0Al10	18	27.6±3.1
	FeoAl20	26	26.8±2.8
	Fe10Al0	17	26.8±3.3
	Fe15Al0	19	24.3±2.5
	Fe20Al0	24	25.1±2.2
	Fe10Al5	**19**	**14.5±1.6**
	Fe10Al10	**19**	**13.4±1.3**
	Fe0Al0+P	25	26.2±4.6
	Fe10Al10+P	27	25.0±2.9
almt1	almt1_Fe0Al0	9	23.5±2.1
	almt1_Fe10Al10	9	22.0±4.9

As the root growth arrest phenotype can only be observed in Fe10Al5 and Fe10Al10 stress conditions, we further investigated the difference between Fe10Al5 and Fe10Al10 phenotype several days after transfer. When we observe the phenotype after 24-48 hours, roots do not show any growth and both the conditions seem to behave in a similar nature. It is only after 2 weeks that we see some differences where Fe10Al5 displays some lateral roots and lot of root hairs whereas Fe10Al10 has significantly fewer lateral roots and less root hairs (Figure 4-15). It clearly shows that the root extension arrest is not a definite phenotype. Even in stressed conditions, plant try to adapt themselves by changing their root architecture, but it takes a long time.

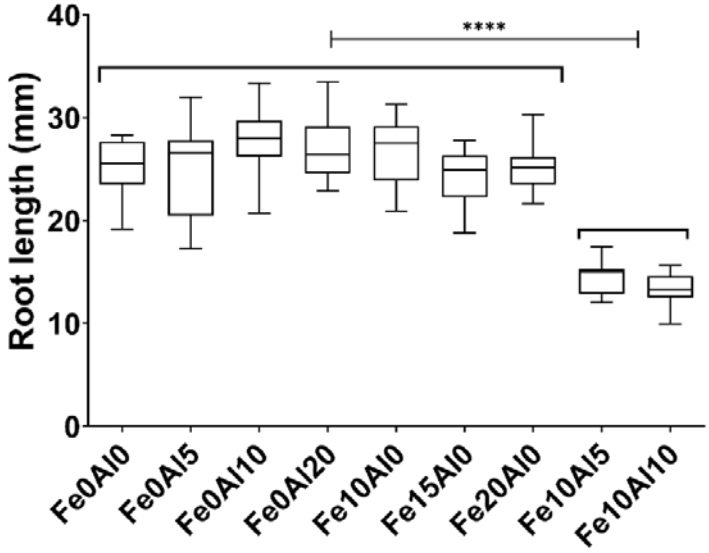

Figure 4-14: Quantitative root length measurements t day 6 of WT Arabidopsis seedlings. Roots were transferred from crystallization plate to Petri dishes on day 4. Pictures were taken on day 6. Root length measurements were performed with the help of NeuronJ, an ImageJ plugin software.

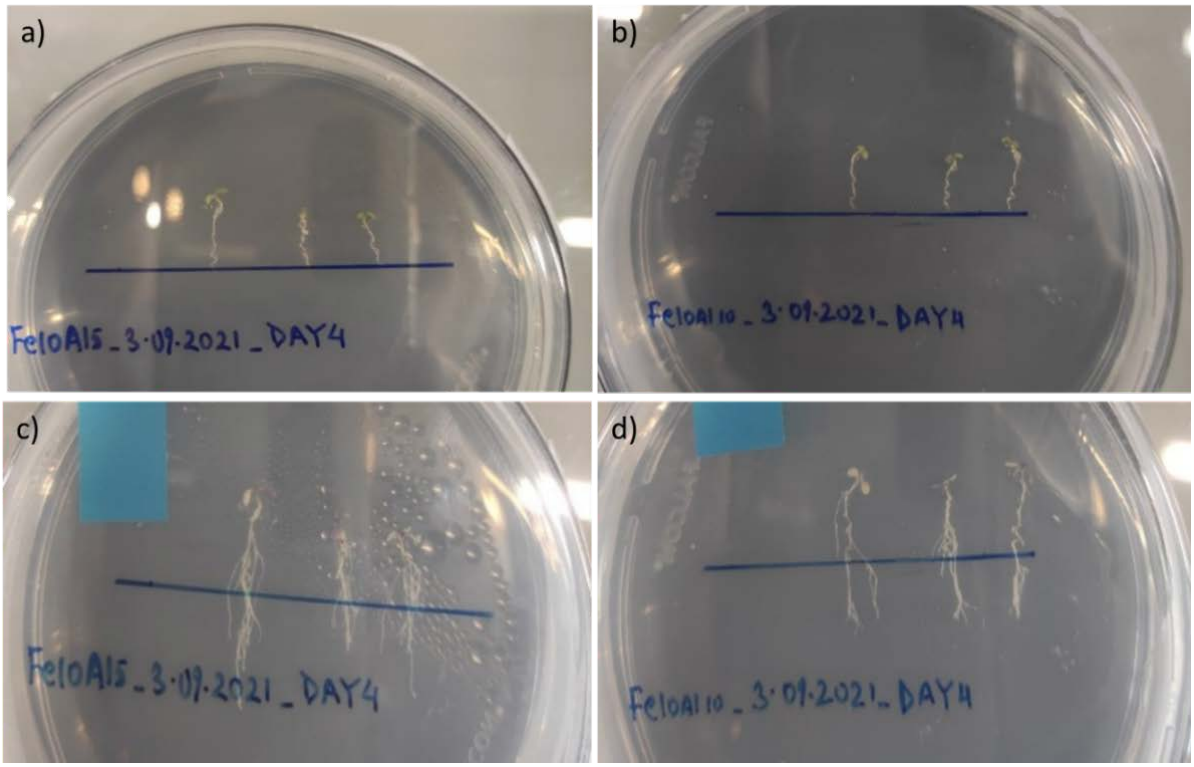

Figure 4-15: Root growth phenotype for Fe10Al5 and Fe10Al10 on a long term.
a-b) Roots were transferred to the Petri dish on day 4 and pictures were taken on day 5 for the first row. c-d) Pictures were again taken on day 21 where more lateral roots and root hairs are observed in Fe10Al5 as compared to that of Fe10Al10.

4.5 Additional nanomechanical results

During one of my secondment with our ITN partner laboratory (LAI, INSERM Marseille) I happened to have access to a JPK Nanowizard 4 AFM (NW4). Fortunately, this laboratory is near the plant lab (LGBP) that is attached to CEA Cadarache. They allowed us to grow seedlings in their premises. The NW4 belongs to the new generation of AFM and possess an inverted optical microscope, in addition to a classical AFM system. They are perfectly suited for biological samples. To investigate the reproducibility of our data, I performed indentation experiments.

Figure 4-16 shows the data results of a single day of experiment obtained on WT *Arabidopsis* plants. With NW4 it was possible to control the amount of applied force, and we set the total force to 10 nN. At this time, we used the second matrix design (see 3.7.2). Each plant had 3 x 3 matrix of 10 nodes, having total of 90 curves. Here, we take an average of each node and plot in the graph, Figure 4-16.

Three different conditions were investigated: Fe0Al0, Fe10Al0, and Fe10Al5. No change in previously described phenotypes is observed. Although we tested a small number of plants, results clearly showed a significant difference in the root elasticity behavior of Fe10Al5 compared with Fe0Al0 and Fe10Al0, Table 4-8.

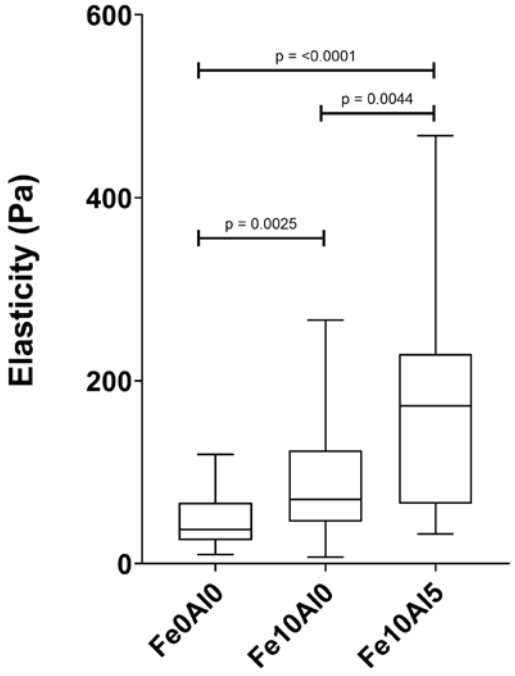

Figure 4-16: Indentation results of WT seedling roots acquired from JPK Nanowizard4. For plot box-and-whiskers plot details refer to Figure 4-1.

Table 4-8: Elasticity values from data of JPK AFM instrument.

Stress condition		Elasticity (in kPa)	
	Number of nodes	Average ± SD	Median
Control (Fe0Al0)	20	47.3 ± 30.6	37.1
Fe10Al0	30	88.8 ± 59.2	70.3
Fe10Al5	20	170 ± 107	172

If any shortcomings to this data is to be written, it can be the matrix design, which was not yet fully established as well as the number of plants tested.

DISCUSSION AND PERSPECTIVE

5 Discussion and Conclusion

Limited Pi condition has become an issue prevailing in about 70 % of cultivable land. Previous research studies showed that phosphate limitation leads, among other things, to apoplastic deposition of ferric (Fe^{3+}) iron in the growing root tip, and a root extension arrest (Muller et al. 2015; Balzergue et al. 2017; Mora-Macias et al. 2017). Our initial goal in this project was to determine changes in plant root stiffness at the nanoscale level in response to various iron concentration, always in a limiting phosphate condition (-Pi). We built our project based on previous studies of the AFM team of Marcoule (JL Pellequer) and the plant laboratory in Cadarache (Thierry Desnos). The working hypothesis was that the role of iron in -Pi condition was to stiffen the plant cell wall, which in turns lead to a root extension arrest. My work was thus under the benevolent guidance of the, now EBM, laboratory of Thierry Desnos in CEA Cadarache, who supported us with the genotypic and phenotypic aspects in plant science, i.e. the genetic and signaling pathways involved in this phenomenon.

Our primary technique in Grenoble, which we used during our entire project, is Atomic Force Microscopy (AFM) that allowed us to investigate the nanomechanical responses of epidermal cells forming the outermost layer of the root. Since these cells are at the frontier between plant and rhizosphere, they are the prime targets to sense changes in the environment and thus to react physiologically to these changes. By studying living roots *in situ,* inherent multicellular properties of the root is preserved, which is an improvement over studies performed on isolated living cells.

As for any new project, a learning experience often starts by repeating previous results. The initial nanomechanical studies on plant roots were initiated and done in 2014 by Christian Godon, with the help of Jean-Marie Teulon at the analysis, in CEA Marcoule. In 2017, preliminary nanomechanical experiments were tested in Grenoble with the help of Marjorie Cherry and Christian Godon (both from CEA Cadarache). Consequently, in my arrival in 2019, I started by repeating the protocol that was published in 2017. Excluding the training period, subsequent results were unexpectedly disastrous. In other words, not only there was no logic in determined elasticity properties, results were so variable for a similar condition that we had to question every step of the protocol, including a possible “aging disease” of our old

Dimension 3100 AFM. In fact, what takes a few lines to explain, took me almost two years to refine and set-up a robust protocol that has been submitted for publication (Kaur et al. 2023).

5.1 Protocol and challenges

To provide a quick overview of the protocol, it is made of four distinct steps. First, seeds must be sown in agar medium. Second, 4-day-old seedlings must be transferred from their growing condition to a stress condition (presence of metals). Third, seedlings must be fixed on glass slides and nanoindentation can be performed with an AFM. Fourth, force-distance curves must be analyzed, elastic properties determined, and the phenotype recorded (root length). Our current protocol allows for measuring about eight plant roots per day. However, it requires a precise organization to avoid waiting for a full two hours at each specific stress. The protocol was designed for plant roots but could be easily adapted to other plant organs such as hypocotyls, meristems, or leaves.

5.1.1 Protocol improvements

In my opinion, one of the significant improvements of the protocol was the seedling growing conditions. These improvements are explained in the method section and in the manuscript in the annex 2.

To refine the protocol, we have attempted to overcome loopholes whenever we came across any of it. Improvements were made in all four steps of the protocol. The living status of roots, which was not questioned before, has been tested during this present protocol and neither the fixation system with NuSil nor the horizontally positioned seedlings prevent roots from growing. We have shown that roots continue to grow at least two hours in such a position. Nevertheless, although root growth is a macroscopic sign of living tissue, it may not visibly indicate the presence of putative stress within the root.

Various experimental protocols can also be found in the recent literature. A recent work focused on indenting living root tissues with AFM (Cuadrado-Pedetti et al. 2021). They took particular care to indent the middle of the cell to avoid any cell-cell junctions. Similarly, to our camera on the D3100, they used an inverted microscope to locate the middle of a cell. Unfortunately, plant roots are quite thick unlike isolated cells, which makes it difficult to view our exact location on the root surface. Besides, locating the precise location of the tip beneath

the cantilever is another difficulty. In a somewhat similar work, Akita et al. performed indentation on various regions of living roots, which were growing between 3D printed micropillars (Akita et al. 2020). The goal was to use micropillars as a surrogate to avoid gluing plant roots. However, their measurements went into the µN force indentation, which might have made their final elasticity values less relevant to ours, and is likely a source of stress for plant roots. Performing force volumes is a faster way of data acquisition as done by Akita et al. but as per my experience it leads to rejection of almost 1/3rd of the data (either by incomplete data collection of poor indentation curves or by poor contact point fitting i.e. R^2 parameter). I tried acquiring force-volume maps on a few plants with a JPK NW2, which was generously provided to us by Dr. Claude Verdier at LiPhy laboratory in Grenoble. Despite a slight difficulty to orient plant roots under the indenting cantilever, final results follow the same trend as our result with the D3100, albeit a waste of 1/3 of acquired force-distance curves. Nevertheless, it provides a sense of robustness of our studies showing that plant roots in presence of Fe10Al10 condition have higher elasticity than those compared to Fe0Al0 condition.

5.1.2 Handling of roots complexity

While the plants are transferred to another Petri dish for two hours, I was keeping the Petri dish horizontally on the surface so that plants can have a better surface contact with agar and do not grow out of the agar medium to escape stress (when kept vertically ~ 80-90°). To our surprise, sometimes we noticed a bend at the end of the roots after two hours, which was due to gravitropism effect. Indentation experiments were still done on them. During our data analysis, we observed a co-relation between root bending and increased stiffness. Because we always took a snapshot of the plants under cantilever, it made it easy for us to detect this phenomenon. Of course, these plants were rejected at a later stage when compiling for our stiffness data. There were many other reasons why data from nanoindentation of plants were rejected. Sometimes, I had to stop indentation in the middle of my data acquisition only to realize that root was not well sealed. Sometimes it was visible that the root was moving and thus were discarded. It sounds OK, but because of the 2 h stress period, I had to wait for the next measuring schedule. Sometimes, for some still unknown reasons, I could not acquire force-distance curves on a seedling. After changing area, a couple of times, I have to give up

due to the measuring schedule (max 25-30 min per seedlings). Hence, so was the partially acquired data that were rejected later, despites some usable measures.

Roots are so strong that if not sealed correctly, they are capable of dislocating cantilevers or sometimes breaking the probe. Besides, if silicone adhesive is not spread well, it can get in contact with the cantilever support and tempers the AFM signal strength. In such a case, the cantilever had to be readjusted and our calibration must be performed again, which took almost two hours. If everything goes well, it was possible to continue experiments with the same tip for up to 14- 15 plants or 2 experimental days in general. Probe was always cleaned by dipping the cantilever into propanol and rinsed with ethanol at the end of the experiment. Because roots are so stiff, it is not advised to use it more than two days, it becomes blunt or contaminated with cellulose fibers.

5.1.3 Calibration evaluation

Bad data quality leads us to question our calibration practices. On our local AFM instrument, it is not possible to save thermals, but we took snapshots for the record. Hence, we made a practice of taking snapshots for every step whenever possible including calibration curves, root seedlings under the AFM camera, which lead us to have more *a posteriori* controls. I observed that improper fitting of the cantilever in the AFM sample holder could result in a bad calibration procedure. It might not be that evident when you get a good signal strength and a stable laser. Its impact could be faint during the acquisition of indentation curves, but have strong consequences later in the interpretation of curves. I found this step critical for our data quality, yet it is easy to be fooled by this step. To overcome this error, I followed very closely the spring constant value obtained during the calibration step so that it fits closest to the values provided by the manufacturer. If the value obtained deviates significantly from the nominal value (0.08 N/m for PNP-TR), I moved the laser around the cantilever and redo the whole calibration process. Sometimes, I had to slightly reorient the cantilever with a tweezer. This process stops when the values get between 0.075 and 0.085 N/m for our triangular PNP cantilever, and the power spectrum peak has a reasonable value. In the spirit, this process is reminiscent of the SNAP procedure used for calibrating AFM systems with pre-calibrated cantilevers (Schillers et al. 2017). In SNAP, the known spring constant of the cantilever is used

to calibrate the sensitivity, so that the thermal tuning method in AFM reproduces the known spring constant of the calibrated cantilever. In our case, we consider the manufacturer data as “a target” and refine our calibration procedure to obtain the expected values in spring constants. Although our approach is fundamentally different from SNAP, it allowed us to “standardize” the internal calibration of our AFM instrument.

5.1.4 Limitations

While we have described this protocol in a very detailed manner (see Annex 2), it was applied on *Arabidopsis thaliana* seeds, and yet the method is versatile enough that it can be applied to any seedling roots with a length of a few cm. There are nevertheless various limitations concerning the use of atomic force microscopes. Most modern instruments use round Petri dishes as a sample stage. In some AFM systems, it has been difficult to use standard glass slides because the lack of space prevented us to rotate a glass slide to orient the plant root according to the fixed position of the cantilever.

A main advantage of our protocol was the use of the Dimension 3100 AFM since it operates on a large motorized platform that can accommodate very large sample (ideal for large tissues such as plant roots). The downside of this instrument is its end of commercial life with no possible upgrade. Besides, our protocol has some peculiarity due to the open-loop scanner such as the lack of a performant force trigger for force-distance curve acquisitions. In addition, due to unfocused laser beam, we cannot use modern small cantilevers such as PF-QNM-LC. Nevertheless, modern instruments will not suffer with such problems (except the large motorized platform for most bio-systems).

A more worrisome limitation was the use of NuSil pressure sensitive adhesive. Its availability is unpredictable and we have tried alternatives but with moderate or no success. A key advantage of NuSil is its slow polymerization (min) and low viscosity, which allows us to manipulate with standard pipettes. The key property to look for a replacement is “pressure sensitive adhesive”. Some commercial alternatives can be found and were tested in our lab but never applied during this protocol.

Finally, the extensibility of the protocol to other possible stresses is limited to experimental conditions that can be translated into a chemical change of agar material. For instance,

insoluble compounds may not be homogeneously distributed in the agar and therefore the outcome of the phenotype may be unpredictable. In such cases, a different growing methodology should be used such as directly in liquid solutions.

5.2 Use of contact-based mechanical analysis

Our lab came up with a new methodology called 'Trimechanic-3PCS theory' that was implemented to extract elasticity parameters including not only the classical effective elastic constant, but also the stiffness along the indentation depth. We have covered the trimechanic-3PCS theory in the introduction section 1.1.6 and in the recently published article (Chen et al. 2023), see annex 1. Unfortunately, this methodology was not ready at the beginning of my work and I started using the free software AtomicJ (Hermanowicz et al. 2014).

5.2.1 Classic mechanical model

While analyzing data with AtomicJ, we figured out the limitations of classical analysis methodology available in AtomicJ. It is important to stress that AtomicJ is a processing software and is not being evaluated *per se*. It performs a data analysis in the traditional state of the art for contact-based Sneddon model, for instance. Moreover, AtomicJ contains dozens of parameters, which can all affect seriously the outcome of an analysis. In our experience, the greatest difficulty in standard analysis methods is the consideration that the contact point is an adjustable variable. Although, it makes sense in terms of computational analysis, in our point of view, the failure of a robust analysis resides in the automatic adjustment of the contact point, as it relies on a wrong hypothesis. Our biological samples, plant tissues such as seedling roots, have a complex and non-homogeneous architecture (Kasas et al. 2005; Digiuni et al. 2015; Chen et al. 2023). This cannot be truer than for the multi-layer organization of external plant cell walls. Besides the issue of the contact point (which, due to its critical importance, can explain some differences in the analysis of data), the presence of multiple zones in biological samples cannot be reliably fitted by a single curve. Consequently, assuming a perfect parabolic curve when using a pyramidal tip, classical methods adjust their region of fit (and consequently their contact point) to improve the quadratic fitting score. Sometimes, it ends with a contact point positioned too high almost on the steep slope region or sometimes

too low near the horizontal x-axis, i.e., the approach line. Of course, AtomicJ has the function of moving the contact point location as per our desire, but this will vary from person to person, which leads to manual errors. We need to rely on automating our data analysis. There is no magic bullet to solve this issue, including the fixed contact point concept of the Trimechanic-3PCS theory (Chen et al. 2023).

5.2.2 Trimechanics improvement over classical method

Because of the novelty of the Trimechanic-3PCS theory, I wanted to compare results from both approaches: AtomicJ and 3PCS. According to the trimechanic theory, nanoindentation is characterized in a zone-wise manner, with each zone j being quantified by a quadruplet: [ΔZ_j, $k_{C,j}$, $k_{T,j}$, $r_{S,j}$], the necessary and sufficient parameters to rebuild the fitting curves for F_T and three decomposed force components. Because our application of the 3PCS analysis focuses only on the first depth zone, k_C is null. All remaining triplets are shown in Table 5-1. It should be noted that the 3PCS approach characterizes an effective Young's modulus, i.e. without taking into account the Poisson's ratio (set to 0). Consequently, there is an inherent 25% difference in values obtained from AtomicJ, which uses the classical value of 0.5 as Poisson's ratio. Nevertheless, results are qualitatively similar, non-stressed conditions have lower Young's modulus than stressed conditions.

A global overview of the Table 5-1easily highlights the extreme cases (Fe0Al0 and Fe10Al10). It is also possible to detect trends among intermediate stress conditions; see for instance the stiffness or elastic constants of Fe10Al0, Fe15Al0, and Fe20Al0. However, due to the certain heterogeneity in plant roots, idiosyncrasies can also break the apparent linearity in elastic parameters; see for instance the stiffness of Fe0Al5 and Fe10Al5. It is one of the advantages of the trimechanic-3PCS theory to provide a full set of elastic-associated parameters such as the depth of the indentation zone (D_Z1), the stiffness (k_T), the effective Young's modulus ($\hat{E}$), and the relative strength of the tip-shape nanomechanics r_S. When looking carefully at the Table 5-1, a global trend is observed with a global increase in metal stress: stiffness and elasticity increase while the depth of indentation decreases. By taking these three elastic parameters together, idiosyncrasies that shed ambiguity at a single stress condition almost vanish. The last parameter (r_S) is of particular interest because it reflects the deformability of

the indented root. Interestingly, this parameter remains quite constant over all the stress conditions (Table 5-1). We attribute this constant behavior to the conserved chemical structure of the plant cell wall (cellulose, hemicellulose, pectin, and their specific bonding), irrespective of the amount of metal used. However, although being not significant, we can still divide r_S values into two categories: below 0.8 for some and above 0.8 for the others. Interestingly, almost all stress conditions with a r_S > 0.8 involve those with higher stiffness/elasticity. It is thus tempting to speculate that a slight change in chemical bonding appears in the presence of a large quantity of metals. The condition Fe10Al10 in presence of 500 µM Pi, which appears like a control condition with no increase in stiffness, may appear like an exception to this threshold of 0.8 but we do not know the proportion of metals bound to Pi versus free metals that could still get inside the root.

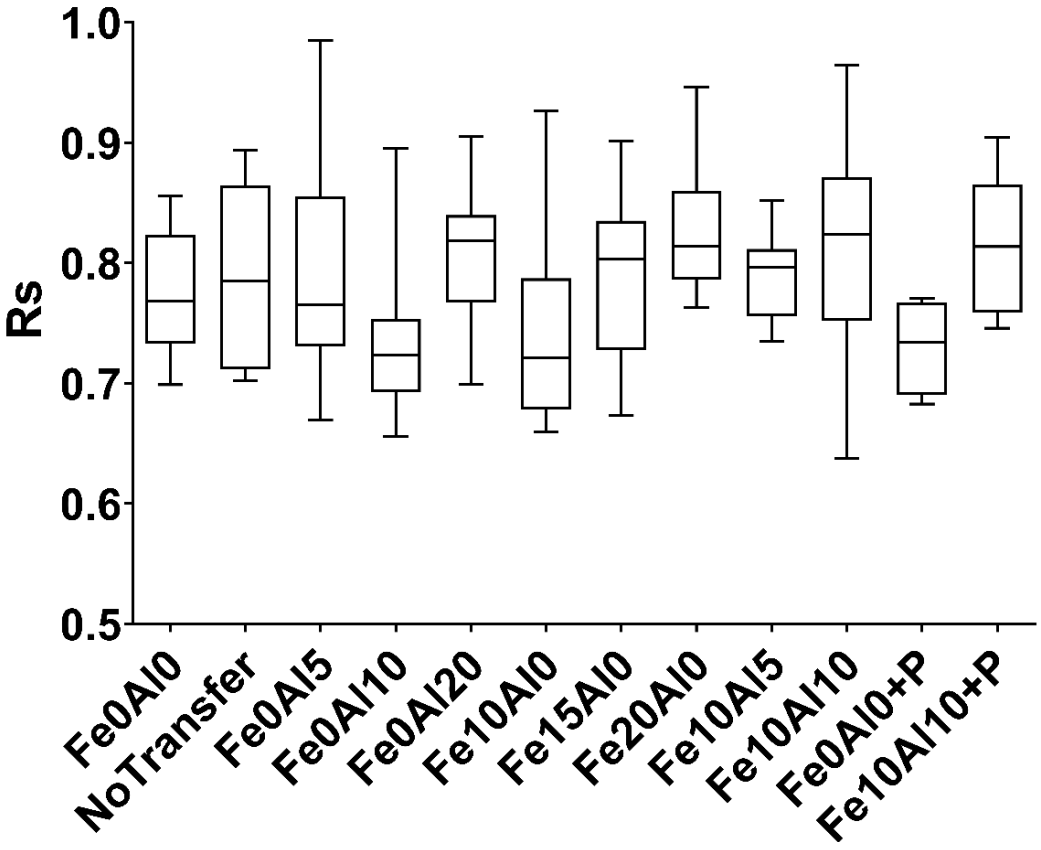

Figure 5-1: Stiffness ratio r_S values of plants in variable metal concentrations.
The uniform, non-significant values in all the conditions show that the stiffness parameter does not change and is independent of that of elasticity values. The similar data represents uniformity of the sample i.e. we used Arabidopsis thaliana seedlings only throughout our project.

Table 5-1: Nanomechanical properties of WT seedling roots as determined by the trimechanic theory

		Indentation depth	Ratio k_S/k_T	Average stiffness	Effective Young modulus (3PCS) (Chen et al. 2023)	Apparent Young modulus (AtomicJ) (Hermanowicz et al. 2014)
Stress conditions	n	D_Z1 (nm)	r_S_Z1	k_T_Z1 (10^{-3} N/m)	$\hat{E}$_Z1 (kPa)	Apparent
Fe0Al0	11	147 ± 55	0.78 ± 0.05	4.30 ± 1.16	53.9 ± 21.8	87.7 ± 45.3
Fe0Al0_No Transfer	5	161 ± 35	0.79 ± 0.08	5.40 ± 1.45	56.3 ± 20.1	64.9 ± 11.5
Fe0Al5	10	135 ± 42	0.79 ± 0.09	5.18 ± 3.88	64.3 ± 45.4	91.1 ± 24.7
Fe0Al10	10	150 ± 62	0.74 ± 0.07	4.26 ± 1.73	51.7 ± 30.9	99.9 ± 65.9
Fe0Al20	15	136 ± 41	0.81 ± 0.05	5.72 ± 2.18	76.9 ± 39.4	186 ± 112
Fe10Al0	14	153 ± 41	0.75 ± 0.08	4.94 ± 3.51	58.4 ± 50.4	94.8 ± 56.7
Fe15Al0	10	125 ± 15	0.79 ± 0.07	5.09 ± 2.55	69.2 ± 42.1	157 ±87.7
Fe20Al0	11	119 ± 29	0.83 ± 0.06	7.51 ± 3.77	106 ± 42	192 ± 122
Fe10Al5	13	115 ± 24	0.79 ± 0.04	4.98 ± 1.34	71.6 ± 17.2	153 ± 84
Fe10Al10	11	127 ± 57	0.81 ± 0.09	8.89 ± 8.63	105 ± 52	141 ± 57
Fe0Al0+P	5	137 ± 34	0.73 ± 0.04	4.86 ± 1.39	58.5 ± 26.3	109 ± 44
Fe10Al10+P	8	162 ± 25	0.81 ± 0.06	5.37 ± 1.97	59.6 ± 27.6	133 ± 78
almt1_Fe0Al0	14	162 ± 79	0.79 ± 0.08	4.6 ± 2.0	63.5 ± 50.4	122 ± 76
almt1_Fe10Al10	11	133 ± 28	0.74 ± 0.08	4.8 ± 2.8	58.3 ± 36.5	139 ± 69

From here on, when discussing our results, I would be discussing them based on Trimechanic-3PCS results, as shown in our submitted manuscript in the annex 1.

5.3 Correlation between phenotype with indentation results

5.3.1 Aluminum effect on roots

Our results show that the presence of aluminum has no effect on the plant phenotype (root length) up to 20 µM. Similarly, when compared with that of control, no change in elasticity, or stiffness, or indentation depth is observed in conditions up to 10 µM. Yet, at 20 µM Al higher stiffness and elasticity values among various conditions are observed.

REA phenotype for Al stress is multifactorial and the underlying mechanisms remain largely unknown (Kochian et al. 2015). However, we know that the presence of aluminum stimulates the expression of *ALMT1* gene (Godon et al. 2019), a malate transporter (ALMT1 (Sasaki et al. 2004)). When present in the medium, Al^{3+} ions bind to the extracellular ALMT1 channel. Binding of the ions triggers ALMT1 channel opening leading to malate exudation (Wang et al. 2022). Thus, high concentration of Al^{3+} leads to malate exudation that excretes Al outside of the root. In this whole process, not all the Al^{3+} ions are exudated and some ions manage to retain themselves in the CW and bind to negatively charged pectin (Yang et al. 2016), leading to an increase of stiffness (Ma et al. 2004), but without REA in our data.

5.3.2 Effect of iron on root stiffness.

A well-documented study has been done when it comes to effect of iron in case of low Pi condition. A preliminary work in 2017 linked the role of iron in root elongation arrest with cell wall stiffness (Balzergue et al. 2017). However, our present results show that no change in the phenotype in the presence of iron is observed. The roots still managed to grow even after reaching the concentration of 20 µM, whereas the previous work showed a total root growth arrest at 10 µM only. As explained in the current result section, this apparent contradiction was due to the presence of traces of other metals present in agar, which were critical in playing root inhibition effect.

It has already been observed that iron uptake increases in the presence of low Pi, over accumulating in root and shoot parts of the plant (Abel 2011, 2017). Iron accumulation occurs in the apoplastic region of the cell wall in the form of Fe^{3+}. At low Pi, the LOW PHOSPHATE ROOT 1 (LPR1) and PHOSPHATE DEFICIENCY RESPONSE 2 (PDR2) response genes contribute to the oxidation of Fe^{2+} into Fe^{3+}. Pectin, which contains negatively charged saccharides, has

high affinity for cations such Ca^{2+}, Fe^{3+}, or Al^{3+}, and it can be tempting to extrapolate the observation of Al^{3+} to Fe^{3+}, where Al^{3+} has been found itself bound to pectin leading to cell wall stiffening. Consequently, high iron concentration leads to high stiffness and elasticity parameters by binding to pectin in cell walls but no visible changes in root elongation are seen.

5.3.3 Role of iron and aluminum combination

From the previous results, we have shown that the presence of separated high concentrations (20 µM) of iron and aluminum gives rise to high elasticity values, but we do not see REA. However, the combination of both the metals (at only 10 µM) did give rise to a complete REA phenotype. Literature knowledge can help us to devise mechanisms that happen when two metals are combined. In addition to the physiological effects illustrated above for single metal stress, the presence of aluminum activates the ALMT1 transporter, which releases malate as explained before. Malate has affinity towards iron as it binds with it in the apoplast region of CW (Mora-Macias et al. 2017). Thus, in the presence of a large quantity of malate, iron accumulates in the apoplast region instead of going inside the cell for further transportation (Ravet et al. 2009). Consequently, iron accumulation in CW likely triggers a redox cycle that will eventually produce sufficient reactive oxygen species (ROS) ending to a root extension arrest. ROS generation itself also contributes to pectin de-mtyhlesterification which leads to cell wall stiffness (Awwad et al. 2019); ROS accumulation modifies QC position and root elongation zone (Abel 2011); the presence of ROS leads to Fe^{3+} accumulation leading to callous deposition and eventually meristem inhibition (Muller et al. 2015). Callous deposition impairs cell-to-cell communication leading to reduced stem cell activity. However, it takes around 2-3 days with up to a week to observe changes in RSA due to callous deposition. Simultaneously, there are various mechanisms leading to cell wall stiffness that can be linked with pectin dimethyl esterification. However, apart from cell wall stiffness, which has been shown to be simply due to metal accumulation, there must be some other mechanisms at the cell level, which results in the immediate root arrest behavior. The major question remains on how plants immediately sense such a high stress conditions and stop growing in such a short time (hours), before noticing RSA changes such as root hairs growing on the next day instead of primary root length growth.

Final conclusion: Graphical summary

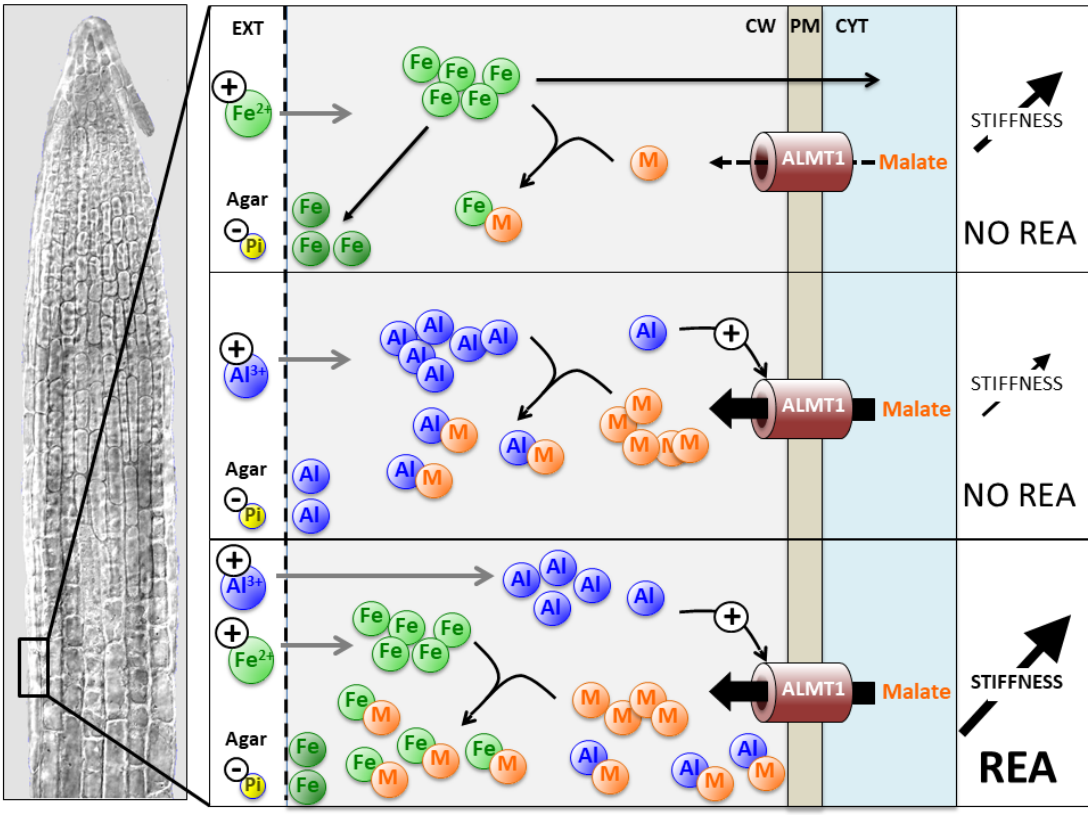

Figure 5-2: Model explaining effects of Fe and Al on CW stiffening and root extension.
Left panel shows a reconstituted picture of an Arabidopsis primary root tip; the square indicates part of the epidermis in the transition zone, where AFM measures were performed in this work. The top to bottom panels explains the phenomena that occur, depending on the Fe^{2+} and Al^{3+} content of the Pi-poor culture medium.

Top panel: the Fe^{2+} ions enter the apoplast of the cell wall (CW, in light gray background color), which subsequently can cross the plasma membrane (PM, in light tan color) through an unknown transporter (not presented here for clarity) and activates the STOP1-ALMT1 signaling (not shown), or accumulate into the apoplast in complex with small organic acids like malate (M). The ALMT1 transporter exports malate from the cytosol (CYT, light blue background) to the CW. The accumulation of Fe cations, possibly in the Fe^{3+} state (darker green on the bottom left) binds to pectin (not shown for simplicity), thereby increasing CW stiffness without triggering the root extension arrest (REA).

Middle panel: the Al^{3+} ions enter the CW and activate the transcription of ALMT1 (not shown) and the opening of ALMT1 transporter, thereby releasing malate in the apoplast. The accumulation of Al^{3+} leads to a modest increase of CW stiffness without REA.

Bottom panel: the combination of Fe^{2+} and Al^{3+} results in a large release of malate and a high accumulation of ROS-promoting iron-malate complexes in the CW. These ROS concomitantly greatly increase CW stiffness and strongly prevents root extension.

(M, malate; CW, cell wall; CYT, cytoplasm; PM, plasma membrane; REA, root extension arrest; -Pi, phosphate-poor medium; +Fe, adding Fe^{2+} in the medium; +Al, adding Al^{3+} in the medium)

Such a paradoxical result, i.e., the fact that an increase in single metal concentration does not provoke a REA, has been solved when studying the mutant Arabidopsis *almt1*. In this mutant plant, the malate transporter is deficient and the root cannot exudate malate. Thus, the

presence of Fe10Al10 in *almt1* seedlings did not increase the cell wall elasticity nor generated REA likely by a lack of accumulation of iron in the apoplast due to the absence of malate. It follows that the role of malate is of prime importance in the REA phenotype. It also follows that the kinetics of accumulation of iron in the apoplast is a critical parameter. To reconcile all our data, we generated a graphical summary illustration of our understanding regarding the combined metal stress in *Arabidopsis thaliana* seedlings (Figure 5-2).

5.4 Perspective

Our work was initiated by repeating experimental measurements of the effect of Fe on the stiffness of the external epidermal cell wall of *Arabidopsis thaliana*. It branched when our collaborators raised the importance of Al. It ended on highlighting the importance of organic acid in the root extension arrest phenotype. This progress of events raises a couple of perspective that is worth pursuing.

- Pectin function in metal stress: A first query could be to determine more precisely the role of pectin in the CW stiffening. This could be done using the long list of pectin-related plant mutants.

- Decellularized roots: Cell wall stiffness changes due to a change in the cross-linking bonds of pectin with or without the participation of ROS activity. Cell wall structure is regulated and sustained due to the turgor pressure of that of the cell. In fact, another aspect of exploring cell wall would be to perform the indentation on decellularized tissues of *Arabidopsis thaliana*. Of course, a different approach to the indentation protocol be needed, but that can be worked upon. These experiments can be helpful in providing comparative results of the cell wall component in the presence and absence of turgor pressure (in the presence and absence of metals).

- Use of microtips: At the beginning of my work, I did try using nanospherical tips but was unable to get productive results due to various limitations. Our nanoindentation results with the sharp tip was more in agreement with the structural biology of the cross-linking bonds responsible for stiffness. Quantitative experiments based on

micro-indentation on the root tissue may, however, be interesting to explore the root surface at the microscale, which will give rise to an averaging stiffness. Could it solve the problem of indenting the center vs junction of cells? Comparing them with the results of nanotip may lead to a better understanding of the characterization of both the root surface and the mechanical model itself.

- An obvious perspective, but still deserved to be placed in a list is the application: this model can be applied to other species to understand their stiffness behavior under various abiotic stress. In particular, crop plants of major agronomy interest could also be studied with our protocol. It could be useful to characterize the stiffness of the root cell wall of crop pants, in particular with available mutants that are capable of growing in nutrient deficient conditions to improve crop productivity.

- Deepening our understanding of root extension arrest: I will not mention the ROS black box, which is likely to remain dark for a long time. However, very little is known about the stiffness kinetics. In other words, what the time-course event is when the root is placed in the presence of abiotic stress.

  The presence of a low pH and traces of aluminum are sensed by the root, which triggers STOP1 regulatory factor in the nucleus, further activating ALMT1 production. This ALMT1 binds to Al^{3+} ions to open malate exudation channels. Malate exudation leads to chelation with metals Al^{3+}, Fe^{3+} ions depending upon their availability according to the variable stress concentrations. Throughout our project, we restricted the stress exposure of plant roots to two hours before performing indentation on them. That said, we still have not quantified the role of cell wall stiffness at different time intervals to which the roots are exposed to stress in different concentrations. This kind of experiment may be helpful in understanding the co-relation of malate exudation with respect to individual metallic concentrations in time space.

  Later, in the same pattern, the combined effect of iron and aluminum can be studied at different timing giving rise to understand more about ROS secretion kinetics together with malate secretion in this special case.

Bibliography

Abel S. 2011. "Phosphate sensing in root development." *Current Opinion in Plant Biology* 14 (3): 303-9. 10.1016/j.pbi.2011.04.007.

---. 2017. "Phosphate scouting by root tips." *Current Opinion in Plant Biology* 39: 168-77. 10.1016/j.pbi.2017.04.016.

Akita E., Yalikun Y., Okano K., Yamasaki Y., Ohtani M., Tanaka Y., Demura T., and Hosokawa Y. 2020. "In situ measurement of cell stiffness of Arabidopsis roots growing on a glass micropillar support by atomic force microscopy." *Plant Biotechnology* 37 (4): 417-22. 10.5511/plantbiotechnology.20.1016a.

Albersheim P., Darvill A., Roberts K., Sederoff R., and Staehelin A. 2011. *Plant cell walls. From chemitry to biology*. New York, NY, USA: Garland Science, Taylor & Francis Group, LLC.

Anderson C.T., Carroll A., Akhmetova L., and Somerville C. 2010. "Real-time imaging of cellulose reorientation during cell wall expansion in Arabidopsis roots." *Plant Physiology* 152 (2): 787-96. 10.1104/pp.109.150128.

Arabidopsis Genome I. 2000. "Analysis of the genome sequence of the flowering plant Arabidopsis thaliana." *Nature* 408 (6814): 796-815. 10.1038/35048692.

Awwad F., Bertrand G., Grandbois M., and Beaudoin N. 2019. "Reactive oxygen species alleviate cell death induced by thaxtomin A in *Arabidopsis thaliana* cell cultures." *Plants (Basel)* 8 (9). 10.3390/plants8090332.

Ayad N.M.E., Kaushik S., and Weaver V.M. 2019. "Tissue mechanics, an important regulator of development and disease." *Philosophical Transactions of Royal Society of London B Biological Sciences* 374 (1779): 20180215. 10.1098/rstb.2018.0215.

Balzergue C., Dartevelle T., Godon C., Laugier E., Meisrimler C., Teulon J.M., Creff A., Bissler M., Brouchoud C., Hagege A., Muller J., Chiarenza S., Javot H., Becuwe-Linka N., David P., Peret B., Delannoy E., Thibaud M.C., Armengaud J., Abel S., Pellequer J.L., Nussaume L., and Desnos T. 2017. "Low phosphate activates STOP1-ALMT1 to rapidly inhibit root cell elongation." *Nature Communications* 8: 15300. 10.1038/ncomms15300.

Bashline L., Lei L., Li S., and Gu Y. 2014. "Cell wall, cytoskeleton, and cell expansion in higher plants." *Molecular Plant* 7 (4): 586-600. 10.1093/mp/ssu018.

Bauer W.D., Talmadge K.W., Keegstra K., and Albersheim P. 1973. "The structure of plant cell walls: II. The hemicellulose of the walls of suspension-cultured Sycamore cells." *Plant Physiology* 51 (1): 174-87. 10.1104/pp.51.1.174.

Beauzamy L., Derr J., and Boudaoud A. 2015. "Quantifying hydrostatic pressure in plant cells by using indentation with an atomic force microscope." *Biophysical Journal* 108 (10): 2448-56. 10.1016/j.bpj.2015.03.035.

Beemster G.T., and Baskin T.I. 1998. "Analysis of cell division and elongation underlying the developmental acceleration of root growth in Arabidopsis thaliana." *Plant Physiology* 116 (4): 1515-26. 10.1104/pp.116.4.1515.

Bidhendi A.J., Chebli Y., and Geitmann A. 2020. "Fluorescence visualization of cellulose and pectin in the primary plant cell wall." *Journal of Microscopy* 278 (3): 164-81. 10.1111/jmi.12895.

Bidhendi A.J., and Geitmann A. 2016. "Relating the mechanics of the primary plant cell wall to morphogenesis." *Journal of Experimental Botany* 67 (2): 449-61. 10.1093/jxb/erv535.

---. 2019. "Methods to quantify primary plant cell wall mechanics." *Journal of Experimental Botany* 70 (14): 3615-48. 10.1093/jxb/erz281.

Bienfait H.F., Vandenbriel W., and Meslandmul N.T. 1985. "Free space iron pools in roots - Generation and mobilization." *Plant Physiology* 78 (3): 596-600. 10.1104/pp.78.3.596.

Binnig G., Quate C.F., and Gerber C. 1986. "Atomic force microscope." *Physical Review Letters* 56: 930-33. 10.1103/PhysRevLett.56.930.

Binnig G., Rohrer H., Gerber C., and Weibel E. 1982. "Surface studies by scanning tunneling microscopy." *Physical Review Letters* 49: 57 - 61. 10.1103/PhysRevLett.49.57.

Bonnot C., Pinson B., Clement M., Bernillon S., Chiarenza S., Kanno S., Kobayashi N., Delannoy E., Nakanishi T.M., Nussaume L., and Desnos T. 2016. "A chemical genetic strategy identify the PHOSTIN, a synthetic molecule that triggers phosphate starvation responses in Arabidopsis thaliana." *New Phytologist* 209 (1): 161-76. 10.1111/nph.13591.

Bournier M., Tissot N., Mari S., Boucherez J., Lacombe E., Briat J.F., and Gaymard F. 2013. "Arabidopsis ferritin 1 (AtFer1) gene regulation by the phosphate starvation response 1 (AtPHR1) transcription factor reveals a direct molecular link between iron and phosphate homeostasis." *Journal of Biological Chemistry* 288 (31): 22670-80. 10.1074/jbc.M113.482281.

Brown J.C. 1978. "Mechanism of iron uptake by plants." *Plant, Cell & Environment* 1 (4): 249-57. 10.1111/j.1365-3040.1978.tb02037.x.

Bruce D.M. 2003. "Mathematical modelling of the cellular mechanics of plants." *Philosophical Transactions of Royal Society of London B Biological Sciences* 358 (1437): 1437-44. 10.1098/rstb.2003.1337.

Bruker Corporation. 2011. "Fluid Imaging." https://www.nanophys.kth.se/nanolab/afm/icon/bruker-help/Content/Fluid%20Imaging/Fluid%20Imaging.htm.

Buchanan B.B., Gruissem W., and Jones R.L. 2015. *Biochemistry & molecular biology of plants*. second ed., edited by Buchanan B.B., Gruissem W. and Jones R.L. Chichester, UK: John Wiley & Sons.

Burgert I., and Keplinger T. 2013. "Plant micro- and nanomechanics: experimental techniques for plant cell-wall analysis." *Journal of Experimental Botany* 64 (15): 4635-49. 10.1093/jxb/ert255.

Carl P., and Schillers H. 2008. "Elasticity measurement of living cells with an atomic force microscope: data acquisition and processing." *Pflugers Archiv.* 457 (2): 551-59. 10.1007/s00424-008-0524-3.

Carpita N.C., and Gibeaut D.M. 1993. "Structural models of primary cell walls in flowering plants: consistency of molecular structure with the physical properties of the walls during growth." *The Plant Journal* 3 (1): 1-30. 10.1111/j.1365-313x.1993.tb00007.x.

Chang Y.-C., Yamamoto Y., and Matsumoto H. 1999. "Accumulation of aluminium in the cell wall pectin in cultured tobacco (Nicotiana tabacum L.) cells treated with a combination of aluminium and iron." *Plant, Cell & Environment* 22: 1009–17. 10.1046/j.1365-3040.1999.00467.x.

Chen S.-w.W., Teulon J.M., Kaur H., Godon C., and Pellequer J.L. 2023. "Nano-structural stiffness measure for soft biomaterials of heterogeneous elasticity." *Nanoscale Horizons* 8 (1): 75-82. 10.1039/d2nh00390b.

Chen W., Tang L., Wang J., Zhu H., Jin J., Yang J., and Fan W. 2022. "Research advances in the mutual mechanisms regulating response of plant roots to phosphate deficiency and aluminum toxicity." *International Journal of Molecular Sciences* 23 (3). 10.3390/ijms23031137.

Chighizola M., Puricelli L., Bellon L., and Podesta A. 2021. "Large colloidal probes for atomic force microscopy: Fabrication and calibration issues." *Journal of Molecular Recognition* 34 (1): e2879. 10.1002/jmr.2879.

Chiou T.J., and Lin S.I. 2011. "Signaling network in sensing phosphate availability in plants." *Annual Review of Plant Biology* 62: 185-206. 10.1146/annurev-arplant-042110-103849.

Cliffsnotes. 2023. "Plant biology: root structure and organisation." https://www.cliffsnotes.com/study-guides/biology/plant-biology.

Cordoba-Pedregosa M., Gonzalez-Reyes J.A., Canadillas M., Navas P., and Cordoba F. 1996. "Role of apoplastic and cell-wall peroxidases on the stimulation of root elongation by ascorbate." *Plant Physiology* 112 (3): 1119-25. 10.1104/pp.112.3.1119.

Cosgrove D.J. 1997. "Relaxation in a high-stress environment: the molecular bases of extensible cell walls and cell enlargement." *Plant Cell* 9 (7): 1031-41. 10.1105/tpc.9.7.1031.

---. 2005. "Growth of the plant cell wall." *Nature Reviews Molecular Cell Biology* 6 (11): 850-61. 10.1038/nrm1746.

---. 2014. "Re-constructing our models of cellulose and primary cell wall assembly." *Current Opinion in Plant Biology* 22: 122-31. 10.1016/j.pbi.2014.11.001.

---. 2016. "Plant cell wall extensibility: connecting plant cell growth with cell wall structure, mechanics, and the action of wall-modifying enzymes." *Journal of Experimental Botany* 67 (2): 463-76. 10.1093/jxb/erv511.

Cramer G.R., and Jones R.L. 1996. "Osmotic stress and abscisic acid reduce cytosolic calcium activities in roots of Arabidopsis thaliana." *Plant, Cell & Environment* 19 (11): 1291-98. 10.1111/j.1365-3040.1996.tb00007.x.

Cuadrado-Pedetti M.B., Rauschert I., Sainz M.M., Amorim-Silva V., Botella M.A., Borsani O., and Sotelo-Silveira M. 2021. "The Arabidopsis TETRATRICOPEPTIDE THIOREDOXIN-LIKE 1 gene is involved in anisotropic root growth during osmotic stress adaptation." *Genes* 12 (2). 10.3390/genes12020236.

De Lucas M., and Brady S.M. 2013. "Gene regulatory networks in the Arabidopsis root." *Current Opinion in Plant Biology* 16 (1): 50-55. 10.1016/j.pbi.2012.10.007.

Derbyshire P., Findlay K., McCann M.C., and Roberts K. 2007. "Cell elongation in Arabidopsis hypocotyls involves dynamic changes in cell wall thickness." *Journal of Experimental Botany* 58 (8): 2079-89. 10.1093/jxb/erm074.

Digiuni S., Berne-Dedieu A., Martinez-Torres C., Szecsi J., Bendahmane M., Arneodo A., and Argoul F. 2015. "Single cell wall nonlinear mechanics revealed by a multiscale analysis of AFM force-indentation curves." *Biophysical Journal* 108 (9): 2235-48. 10.1016/j.bpj.2015.02.024.

Dimitriadis E.K., Horkay F., Maresca J., Kachar B., and Chadwick R.S. 2002. "Determination of elastic moduli of thin layers of soft material using the atomic force microscope." *Biophysical Journal* 82 (5): 2798-810. 10.1016/S0006-3495(02)75620-8.

Dolan L., Janmaat K., Willemsen V., Linstead P., Poethig S., Roberts K., and Scheres B. 1993. "Cellular organisation of the *Arabidopsis thaliana* root." *Development* 119 (1): 71-84. 10.1242/dev.119.1.71.

Dunand C., Crevecoeur M., and Penel C. 2007. "Distribution of superoxide and hydrogen peroxide in Arabidopsis root and their influence on root development: possible interaction with peroxidases." *New Phytologist* 174 (2): 332-41. 10.1111/j.1469-8137.2007.01995.x.

Edelmann H.G. 1995. "Wall Extensibility during Hypocotyl Growth - a Hypothesis to Explain Elastic-Induced Wall Loosening." *Physiologia Plantarum* 95 (2): 296-303.

Eticha D., Stass A., and Horst W.J. 2005. "Cell-wall pectin and its degree of methylation in the maize root-apex: significance for genotypic differences in aluminium resistance." *Plant, Cell & Environment* 28 (11): 1410-20. 10.1111/j.1365-3040.2005.01375.x.

Fernandes A.N., Chen X., Scotchford C.A., Walker J., Wells D.M., Roberts C.J., and Everitt N.M. 2012. "Mechanical properties of epidermal cells of whole living roots of *Arabidopsis thaliana*: an atomic force microscopy study." *Physical review E: Statistical, nonlinear, and soft matter physics* 85 (2 Pt 1): 021916. 10.1103/PhysRevE.85.021916.

Fleischer A., O'Neill M.A., and Ehwald R. 1999. "The pore size of non-graminaceous plant cell walls is rapidly decreased by borate ester cross-linking of the pectic polysaccharide rhamnogalacturonan II." *Plant Physiology* 121 (3): 829-38. 10.1104/pp.121.3.829.

Foreman J., Demidchik V., Bothwell J.H., Mylona P., Miedema H., Torres M.A., Linstead P., Costa S., Brownlee C., Jones J.D., Davies J.M., and Dolan L. 2003. "Reactive oxygen species produced by NADPH oxidase regulate plant cell growth." *Nature* 422 (6930): 442-46. 10.1038/nature01485.

Forouzesh E., Goel A., Mackenzie S.A., and Turner J.A. 2013. "In vivo extraction of Arabidopsis cell turgor pressure using nanoindentation in conjunction with finite element modeling." *The Plant Journal* 73 (3): 509-20. 10.1111/tpj.12042.

Foy C.D., Chaney R.L., and White M.C. 1978. "The physiology of metal toxicity in plants." *Ann. Rev. Plant Physiol.* 29: 511-66. 10.1146/annurev.pp.29.060178.002455.

Fry S.C. 1979. "Phonolic components of the primary cell wall and their possible role in the hormonal regulation of growth." *Planta* 146 (3): 343-51. 10.1007/BF00387807.

---. 1986. "Cross-linking of matrix polymers in the growing cell-walls of angiosperms." *Annual Review of Plant Physiology* 37: 165-86. 10.1146/annurev.pp.37.060186.001121.

---. 1998. "Oxidative scission of plant cell wall polysaccharides by ascorbate-induced hydroxyl radicals." *Biochemical Journal* 332 (Pt 2): 507-15. 10.1042/bj3320507.

Gaff D.F., and Carr D.J. 1961. "Quantity of water in cell wall and its significance." *Australian Journal of Biological Sciences* 14 (3): 299-311. 10.1071/Bi9610299.

Garcia P.D., and Garcia R. 2018. "Determination of the elastic moduli of a single cell cultured on a rigid support by force microscopy." *Biophysical Journal* 114 (12): 2923-32. 10.1016/j.bpj.2018.05.012.

Gaspar T., Penel C., Castillo F.J., and Greppin H. 1985. "A 2-step control of basic and acidic peroxidases and its significance for growth and development." *Physiologia Plantarum* 64 (3): 418-23. 10.1111/j.1399-3054.1985.tb03362.x.

Gavara N. 2017. "A beginner's guide to atomic force microscopy probing for cell mechanics." *Microscopy Research and Technique* 80 (1): 75-84. 10.1002/jemt.22776.

Gavara N., and Chadwick R.S. 2012. "Determination of the elastic moduli of thin samples and adherent cells using conical atomic force microscope tips." *Nature Nanotechnology* 7 (11): 733-6. 10.1038/nnano.2012.163.

Geitmann A. 2006. "Experimental approaches used to quantify physical parameters at cellular and subcellular levels." *American Journal of Botany* 93 (10): 1380-90. 10.3732/ajb.93.10.1380.

Godon C., Mercier C., Wang X., David P., Richaud P., Nussaume L., Liu D., and Desnos T. 2019. "Under phosphate starvation conditions, Fe and Al trigger accumulation of the transcription factor STOP1 in the nucleus of Arabidopsis root cells." *The Plant Journal* 99 (5): 937-49. 10.1111/tpj.14374.

Goldbach H.E., and Wimmer M.A. 2007. "Boron in plants and animals: Is there a role beyond cell-wall structure?" *Journal of Plant Nutrition and Soil Science* 170 (1): 39-48. 10.1002/jpln.200625161.

Goldberg R., Liberman M., Mathieu C., Pierron M., and Catesson A.M. 1987. "Development of epidermal-cell wall peroxidases along the Mung Bean hypocotyl - Possible involvement in the cell-wall stiffening process." *Journal of Experimental Botany* 38 (193): 1378-90. 10.1093/jxb/38.8.1378.

Gruber B.D., Giehl R.F., Friedel S., and von Wiren N. 2013. "Plasticity of the Arabidopsis root system under nutrient deficiencies." *Plant Physiology* 163 (1): 161-79. 10.1104/pp.113.218453.

Hamant O., and Haswell E.S. 2017. "Life behind the wall: sensing mechanical cues in plants." *BMC Biology* 15 (1): 59. 10.1186/s12915-017-0403-5.

Hayot C.M., Forouzesh E., Goel A., Avramova Z., and Turner J.A. 2012. "Viscoelastic properties of cell walls of single living plant cells determined by dynamic nanoindentation." *Journal of Experimental Botany* 63 (7): 2525-40. 10.1093/jxb/err428.

Heath O.V.S., and Clark J.E. 1956. "Chelating agents as plant growth substances - Possible clue to the mode of action of Auxin." *Nature* 177 (4520): 1118-21. 10.1038/1771118a0.

Hermanowicz P., Sarna M., Burda K., and Gabrys H. 2014. "AtomicJ: An open source software for analysis of force curves." *Review of Scientific Instruments* 85 (6). 10.1063/1.4881683.

Heyn A.N.J. 1940. "The phyiology of cell elongation." *The Botanical Review* 6 (10): 515-74. 10.1007/BF02879296.

Hochmuth R.M. 2000. "Micropipette aspiration of living cells." *Journal of Biomechanics* 33 (1): 15-22. 10.1016/S0021-9290(99)00175-X.

Hoehenwarter W., Monchgesang S., Neumann S., Majovsky P., Abel S., and Muller J. 2016. "Comparative expression profiling reveals a role of the root apoplast in local phosphate response." *BMC Plant Biology* 16: 106. 10.1186/s12870-016-0790-8.

Hohl M., Greiner H., and Schopfer P. 1995. "The cryptic-growth response of maize coleoptiles and its relationship to H2O2-dependent cell wall stiffening." *Physiologia Plantarum* 94: 491-98. 10.1111/j.1399-3054.1995.tb00959.x.

Horst W.J. 1995. "The role of the apoplast in aluminum toxicity and resistance of higher-plants - a review." *Z. Pflanz. Bodenkunde* 158 (5): 419-28. DOI 10.1002/jpln.19951580503.

Houston K., Tucker M.R., Chowdhury J., Shirley N., and Little A. 2016. "The plant cell wall: A complex and dynamic structure as revealed by the responses of genes under stress conditions." *Frontiers in Plant Science* 7. 10.3389/fpls.2016.00984.

Huala E., Dickerman A.W., Garcia-Hernandez M., Weems D., Reiser L., LaFond F., Hanley D., Kiphart D., Zhuang M.Z., Huang W., Mueller L.A., Bhattacharyya D., Bhaya D., Sobral B.W., Beavis W., Meinke D.W., Town C.D., Somerville C., and Rhee S.Y. 2001. "The Arabidopsis Information Resource (TAIR): a comprehensive database and web-based information retrieval, analysis, and visualization system for a model plant." *Nucleic Acids Research* 29 (1): 102-05. 10.1093/nar/29.1.102.

Hutter J.L., and Bechhoefer J. 1993. "Calibration of atomic-force microscope tips." *Review of Scientific Instruments* 64 (11): 3342-42. 10.1063/1.1144449.

Jackman R.L., and Stanley D.W. 1995. "Perspectives in the textural evaluation of plant foods." *Trends Food Sci. Tech.* 6 (6): 187-94. 10.1016/S0924-2244(00)89053-6.

Kasas S., Wang X., Hirling H., Marsault R., Huni B., Yersin A., Regazzi R., Grenningloh G., Riederer B., Forro L., Dietler G., and Catsicas S. 2005. "Superficial and deep changes of cellular mechanical properties following cytoskeleton disassembly." *Cell Motility and the Cytoskeleton* 62 (2): 124-32. 10.1002/cm.20086.

Kaur H., Teulon J.-M., Foucher A.-E., Fenel D., Godon C., Chen S.-w.W., Desnos T., and Pellequer J.-L. 2023. "Measuring external primary cell wall elasticity of seedling roots using atomic force microscopy " *STAR Protocols* 4: 102265. 10.1016/j.xpro.2023.102265.

Keegstra K., Talmadge K.W., Bauer W.D., and Albersheim P. 1973. "The Structure of Plant Cell Walls: III. A Model of the Walls of Suspension-cultured Sycamore Cells Based on the Interconnections of the Macromolecular Components." *Plant Physiology* 51 (1): 188-97. 10.1104/pp.51.1.188.

Kerr T., and Bailey I.W. 1934. "The cambium and its derivative tissues X - structure, optical properties and chemical composition of the so called middle lamela." *Journal of the Arnold Arboretum* 15: 327-49. http://www.biodiversitylibrary.org/item/33591.

Kierzkowski D., Nakayama N., Routier-Kierzkowska A.L., Weber A., Bayer E., Schorderet M., Reinhardt D., Kuhlemeier C., and Smith R.S. 2012. "Elastic domains regulate growth and organogenesis in the plant shoot apical meristem." *Science* 335 (6072): 1096-9. 10.1126/science.1213100.

Kilpatrick J.I., Revenko I., and Rodriguez B.J. 2015. "Nanomechanics of cells and biomaterials studied by atomic force microscopy." *Advanced Healthcare Materials* 4 (16): 2456-74. 10.1002/adhm.201500229.

Kobayashi M., Matoh T., and Azuma J. 1996. "Two chains of rhamnogalacturonan II are cross-linked by borate-diol ester bonds in higher plant cell walls." *Plant Physiology* 110 (3): 1017-20. 10.1104/pp.110.3.1017.

Kochian L.V., Pineros M.A., Liu J., and Magalhaes J.V. 2015. "Plant adaptation to acid soils: The molecular basis for crop aluminum resistance." *Annual Review of Plant Biology* 66: 571-98. 10.1146/annurev-arplant-043014-114822.

Kontomaris S.V., and Malamou A. 2022. "Revisiting the theory behind AFM indentation procedures. Exploring the physical significance of fundamental equations." *European Journal of Physics* 43 (1): 015010. 10.1088/1361-6404/ac3674.

Koornneef M., and Meinke D. 2010. "The development of Arabidopsis as a model plant." *The Plant Journal* 61 (6): 909-21. 10.1111/j.1365-313X.2009.04086.x.

Kramer U. 2015. "Planting molecular functions in an ecological context with Arabidopsis thaliana." *eLife* 4. 10.7554/eLife.06100.

Krieg M., Flaschner G., Alsteens D., Gaub B.M., Roos W.H., Wuite G.J.L., Gaub H.E., Gerber C., Dufrene Y.F., and Muller D.J. 2019. "Atomic force microscopy-based mechanobiology." *Nature Reviews Physics* 1 (1): 41-57. 10.1038/s42254-018-0001-7.

Kutschera U. 1996. "Cessation of cell elongation in rye coleoptiles is accompanied by a loss of cell-wall plasticity." *Journal of Experimental Botany* 47 (302): 1387-94. 10.1093/jxb/47.9.1387.

Lampugnani E.R., Khan G.A., Somssich M., and Persson S. 2018. "Building a plant cell wall at a glance." *Journal of Cell Science* 131 (2). 10.1242/jcs.207373.

Le Gall H., Philippe F., Domon J.M., Gillet F., Pelloux J., and Rayon C. 2015. "Cell wall metabolism in response to abiotic stress." *Plants (Basel)* 4 (1): 112-66. 10.3390/plants4010112.

Le Poder L., Mercier C., Fevrier L., Duong N., David P., Pluchon S., Nussaume L., and Desnos T. 2022. "Uncoupling aluminum toxicity from aluminum signals in the STOP1 pathway." *Frontiers in Plant Science* 13: 785791. 10.3389/fpls.2022.785791.

Lekka M., Laidler P., Gil D., Lekki J., Stachura Z., and Hrynkiewicz A.Z. 1999. "Elasticity of normal and cancerous human bladder cells studied by scanning force microscopy." *European Biophysical Journal* 28 (4): 312-6. 10.1007/s002490050213.

Lockhart J.A. 1965. "An analysis of irreversible plant cell elongation." *Journal of Theoretical Biology* 8 (2): 264-75. 10.1016/0022-5193(65)90077-9.

---. 1967. "Physical nature of irreversible deformation of plant cells." *Plant Physiology* 42 (11): 1545-52. 10.1104/pp.42.11.1545.

Lynch J. 1995. "Root architecture and plant productivity." *Plant Physiology* 109 (1): 7-13. 10.1104/pp.109.1.7.

Ma J.F., Shen R., Nagao S., and Tanimoto E. 2004. "Aluminum targets elongating cells by reducing cell wall extensibility in wheat roots." *Plant and Cell Physiology* 45 (5): 583-9. 10.1093/pcp/pch060.

Magonov S.N., and Reneker D.H. 1997. "Characterization of polymer surfaces with atomic force microscopy." *Annual Review of Material Science* 27: 175-222.

Main K.H.S., Provan J.I., Haynes P.J., Wells G., Hartley J.A., and Pyne A.L.B. 2021. "Atomic force microscopy-A tool for structural and translational DNA research." *APL Bioengineering* 5 (3): 031504. 10.1063/5.0054294.

Majda M., Grones P., Sintorn I.M., Vain T., Milani P., Krupinski P., Zagorska-Marek B., Viotti C., Jonsson H., Mellerowicz E.J., Hamant O., and Robert S. 2017. "Mechanochemical polarization of contiguous cell walls shapes plant pavement cells." *Developmental Cell* 43 (3): 290-304 e4. 10.1016/j.devcel.2017.10.017.

McCann M.C., Wells B., and Roberts K. 1990. "Direct visualization of cross-links in the primary plant cell wall." *Journal of Cell Science* 96: 323-34. 10.1242/jcs.96.2.323.

McQueen-Mason S.J. 1995. "Expansins and cell wall expansion." *Journal of Experimental Botany* 46 (292): 1639-50. 10.1093/jxb/46.11.1639.

Meijering E., Jacob M., Sarria J.C., Steiner P., Hirling H., and Unser M. 2004. "Design and validation of a tool for neurite tracing and analysis in fluorescence microscopy images." *Cytometry A* 58 (2): 167-76. 10.1002/cyto.a.20022.

Meinke D.W., Cherry J.M., Dean C., Rounsley S.D., and Koornneef M. 1998. "Arabidopsis thaliana: a model plant for genome analysis." *Science* 282 (5389): 662, 79-82. 10.1126/science.282.5389.662.

Milani P., Gholamirad M., Traas J., Arneodo A., Boudaoud A., Argoul F., and Hamant O. 2011. "In vivo analysis of local wall stiffness at the shoot apical meristem in Arabidopsis using atomic force microscopy." *The Plant Journal* 67 (6): 1116-23. 10.1111/j.1365-313X.2011.04649.x.

Millet A. 2021. "A universal model for the Log-normal distribution of elasticity in polymeric gels and its relevance to mechanical signature of biological tissues." *Biology* 10 (1). 10.3390/biology10010064.

Mora-Macias J., Ojeda-Rivera J.O., Gutierrez-Alanis D., Yong-Villalobos L., Oropeza-Aburto A., Raya-Gonzalez J., Jimenez-Dominguez G., Chavez-Calvillo G., Rellan-Alvarez R., and Herrera-Estrella L. 2017. "Malate-dependent Fe accumulation is a critical checkpoint in the root developmental response to low phosphate." *Proceedings of the National Academy of Sciences of the USA* 114 (17): E3563-E72. 10.1073/pnas.1701952114.

Morrissey J., and Guerinot M.L. 2009. "Iron uptake and transport in plants: The good, the bad, and the Ionome." *Chemical Reviews* 109 (10): 4553-67. 10.1021/cr900112r.

Mueller T. 2016. "System for mesuring B cell receptor affinity maturation in germinal centres." Phd, Engineering & Physical Sciences, University of Birmingham.

Muller J., Toev T., Heisters M., Teller J., Moore K.L., Hause G., Dinesh D.C., Burstenbinder K., and Abel S. 2015. "Iron-dependent callose deposition adjusts root meristem maintenance to phosphate availability." *Developmental Cell* 33 (2): 216-30. 10.1016/j.devcel.2015.02.007.

Narciso M., Ulldemolins A., Junior C., Otero J., Navajas D., Farre R., Gavara N., and Almendros I. 2022. "Novel decellularization method for tissue slices." *Frontiers in Bioengineering and Biotechnology* 10: 832178. 10.3389/fbioe.2022.832178.

Naumann C., Heisters M., Brandt W., Janitza P., Alfs C., Tang N., Toto Nienguesso A., Ziegler J., Imre R., Mechtler K., Dagdas Y., Hoehenwarter W., Sawers G., Quint M., and Abel S. 2022. "Bacterial-type ferroxidase tunes iron-dependent phosphate sensing during Arabidopsis root development." *Current Biology* 32 (10): 2189-205 e6. 10.1016/j.cub.2022.04.005.

Nolte T., and Schopfer P. 1997. "Viscoelastic versus plastic cell wall extensibility in growing seedling organs: a contribution to avoid some misconceptions." *Journal of Experimental Botany* 48 (317): 2103-07. 10.1093/jxb/48.12.2103.

Norman M.D.A., Ferreira S.A., Jowett G.M., Bozec L., and Gentleman E. 2021. "Measuring the elastic modulus of soft culture surfaces and three-dimensional hydrogels using atomic force microscopy." *Nature Protocols* 16 (5): 2418-49. 10.1038/s41596-021-00495-4.

Otto O., Rosendahl P., Mietke A., Golfier S., Herold C., Klaue D., Girardo S., Pagliara S., Ekpenyong A., Jacobi A., Wobus M., Topfner N., Keyser U.F., Mansfeld J., Fischer-Friedrich E., and Guck J. 2015. "Real-time deformability cytometry: on-the-fly cell mechanical phenotyping." *Nature Methods* 12 (3): 199-202. 10.1038/nmeth.3281.

Palin R., and Geitmann A. 2012. "The role of pectin in plant morphogenesis." *Biosystems* 109 (3): 397-402. 10.1016/j.biosystems.2012.04.006.

Pandey B.K., Huang G., Bhosale R., Hartman S., Sturrock C.J., Jose L., Martin O.C., Karady M., Voesenek L., Ljung K., Lynch J.P., Brown K.M., Whalley W.R., Mooney S.J., Zhang D., and Bennett M.J. 2021. "Plant roots sense soil compaction through restricted ethylene diffusion." *Science* 371 (6526): 276-80. 10.1126/science.abf3013.

Paredez A.R., Somerville C.R., and Ehrhardt D.W. 2006. "Visualization of cellulose synthase demonstrates functional association with microtubules." *Science* 312 (5779): 1491-95. 10.1126/science.1126551.

Park Y.B., and Cosgrove D.J. 2012. "A revised architecture of primary cell walls based on biomechanical changes induced by substrate-specific endoglucanases." *Plant Physiology* 158 (4): 1933-43. 10.1104/pp.111.192880.

Passardi F., Penel C., and Dunand C. 2004. "Performing the paradoxical: how plant peroxidases modify the cell wall." *Trends in Plant Science* 9 (11): 534-40. 10.1016/j.tplants.2004.09.002.

Peaucelle A., Braybrook S., and Hofte H. 2012. "Cell wall mechanics and growth control in plants: the role of pectins revisited." *Frontiers in Plant Science* 3: 121. 10.3389/fpls.2012.00121.

Peaucelle A., Braybrook S.A., Le Guillou L., Bron E., Kuhlemeier C., and Hofte H. 2011. "Pectin-induced changes in cell wall mechanics underlie organ initiation in Arabidopsis." *Current Biology* 21 (20): 1720-26. 10.1016/j.cub.2011.08.057.

Preston R.D., and Hepton J. 1960. "The effect of indoleacetic acid on cell wall extensibility in Avena coleoptiles." *Journal of Experimental Botany* 11 (31): 13-27. 10.1093/Jxb/11.1.13.

Prevedel R., Diz-Munoz A., Ruocco G., and Antonacci G. 2019. "Brillouin microscopy: an emerging tool for mechanobiology." *Nature Methods* 16 (10): 969-77. 10.1038/s41592-019-0543-3.

Probine M.C., and Preston R.D. 1962. "Cell growth and structure and mechanical properties of wall in internodal cells of *Nitella opaca* .2. Mechanical properties of walls." *Journal of Experimental Botany* 13 (37): 111-27. 10.1093/jxb/13.1.111.

Provart N.J., Alonso J., Assmann S.M., Bergmann D., Brady S.M., Brkljacic J., Browse J., Chapple C., Colot V., Cutler S., Dangl J., Ehrhardt D., Friesner J.D., Frommer W.B., Grotewold E., Meyerowitz E., Nemhauser J., Nordborg M., Pikaard C., Shanklin J., Somerville C., Stitt M., Torii K.U., Waese J., Wagner D., and McCourt P. 2016. "50 years of Arabidopsis research: highlights and future directions." *New Phytologist* 209 (3): 921-44. 10.1111/nph.13687.

Pyne A.L., and Hoogenboom B.W. 2016. "Imaging DNA Structure by Atomic Force Microscopy." *Methods in Molecular Biology* 1431: 47-60. 10.1007/978-1-4939-3631-1_5.

Radmacher M., Fritz M., Hansma H.G., and Hansma P.K. 1994. "Direct observation of enzyme activity with the atomic force microscope." *Science* 265 (5178): 1577-9. 10.1126/science.8079171.

Radotic K., Roduit C., Simonovic J., Hornitschek P., Fankhauser C., Mutavdzic D., Steinbach G., Dietler G., and Kasas S. 2012. "Atomic force microscopy stiffness tomography on living Arabidopsis thaliana cells reveals the mechanical properties of surface and deep cell-wall layers during growth." *Biophysical Journal* 103 (3): 386-94. 10.1016/j.bpj.2012.06.046.

Ravet K., Touraine B., Boucherez J., Briat J.F., Gaymard F., and Cellier F. 2009. "Ferritins control interaction between iron homeostasis and oxidative stress in Arabidopsis." *The Plant Journal* 57 (3): 400-12. 10.1111/j.1365-313X.2008.03698.x.

Redei G.P. 1975. "Arabidopsis as a genetic tool." *Annual Review of Genetics* 9: 111-27. 10.1146/annurev.ge.09.120175.000551.

Refregier G., Pelletier S., Jaillard D., and Hofte H. 2004. "Interaction between wall deposition and cell elongation in dark-grown hypocotyl cells in Arabidopsis." *Plant Physiology* 135 (2): 959-68. 10.1104/pp.104.038711.

Roberts K. 1989. "The plant extracellular matrix." *Current Opinion in Cell Biology* 1 (5): 1020-7. 10.1016/0955-0674(89)90074-4.

Roduit C., Sekatski S., Dietler G., Catsicas S., Lafont F., and Kasas S. 2009. "Stiffness tomography by atomic force microscopy." *Biophysical Journal* 97 (2): 674-77. 10.1016/j.bpj.2009.05.010.

Roelofsen P.A. 1958. "Cell-wall structures as related to surface growth." *Acta Botanica Neerlandica* 7: 77-89. 10.1111/j.1438-8677.1958.tb00609.x.

Rongpipi S., Ye D., Gomez E.D., and Gomez E.W. 2018. "Progress and opportunities in the characterization of cellulose - An important regulator of cell wall growth and mechanics." *Frontiers in Plant Science* 9: 1894. 10.3389/fpls.2018.01894.

Routier-Kierzkowska A.L., Weber A., Kochova P., Felekis D., Nelson B.J., Kuhlemeier C., and Smith R.S. 2012. "Cellular force microscopy for in vivo measurements of plant tissue mechanics." *Plant Physiology* 158 (4): 1514-22. 10.1104/pp.111.191460.

Ryden P., Sugimoto-Shirasu K., Smith A.C., Findlay K., Reiter W.D., and McCann M.C. 2003. "Tensile properties of Arabidopsis cell walls depend on both a xyloglucan cross-linked microfibrillar network and rhamnogalacturonan II-borate complexes." *Plant Physiology* 132 (2): 1033-40. 10.1104/pp.103.021873.

Sampathkumar A., Krupinski P., Wightman R., Milani P., Berquand A., Boudaoud A., Hamant O., Jonsson H., and Meyerowitz E.M. 2014. "Subcellular and supracellular mechanical stress prescribes cytoskeleton behavior in Arabidopsis cotyledon pavement cells." *eLife* 3: e01967. 10.7554/eLife.01967.

Sánchez-Calderón L., Ibarra-Cortés M.E., and Zepeda-Jazo I. 2013. "Root development and abiotic stress adaptation." In *Abiotic Stress - Plant Responses and Applications in Agriculture*, edited by Vahdati K. and Leslie C., 135-68. IntechOpen.

Sanchez-Calderon L., Lopez-Bucio J., Chacon-Lopez A., Cruz-Ramirez A., Nieto-Jacobo F., Dubrovsky J.G., and Herrera-Estrella L. 2005. "Phosphate starvation induces a determinate developmental program in the roots of Arabidopsis thaliana." *Plant and Cell Physiology* 46 (1): 174-84. 10.1093/pcp/pci011.

Sasaki T., Yamamoto Y., Ezaki B., Katsuhara M., Ahn S.J., Ryan P.R., Delhaize E., and Matsumoto H. 2004. "A wheat gene encoding an aluminum-activated malate transporter." *The Plant Journal* 37 (5): 645-53. 10.1111/j.1365-313x.2003.01991.x.

Savitzky A., and Golay M.J.E. 1964. "Smoothing and differentiation of data by simplified least squares procedures." *Analytical Chemistry* 36 (8): 1627-39.

Scheller H.V., and Ulvskov P. 2010. "Hemicelluloses." *Annual Review of Plant Biology* 61: 263-89. 10.1146/annurev-arplant-042809-112315.

Scheres B., Benfey P., and Dolan L. 2002. "Root development." In *The Arabidopsis Book*, e0101. The American Society of Plant Biologists.

Schillers H., Rianna C., Schape J., Luque T., Doschke H., Walte M., Uriarte J.J., Campillo N., Michanetzis G.P.A., Bobrowska J., Dumitru A., Herruzo E.T., Bovio S., Parot P., Galluzzi M., Podesta A., Puricelli L., Scheuring S., Missirlis Y., Garcia R., Odorico M., Teulon J.M., Lafont F., Lekka M., Rico F., Rigato A., Pellequer J.L., Oberleithner H., Navajas D., and Radmacher M. 2017. "Standardized Nanomechanical Atomic force microscopy Procedure (SNAP) for measuring soft and biological samples." *Scientific Reports* 7 (1): 5117. 10.1038/s41598-017-05383-0.

Schneider C.A., Rasband W.S., and Eliceiri K.W. 2012. "NIH Image to ImageJ: 25 years of image analysis." *Nature Methods* 9 (7): 671-5. 10.1038/nmeth.2089.

Schopfer P. 2006. "Biomechanics of plant growth." *American Journal of Botany* 93 (10): 1415-25. 10.3732/ajb.93.10.1415.

Showalter A.M. 1993. "Structure and function of plant-cell wall proteins." *Plant Cell* 5 (1): 9-23. 10.1105/tpc.5.1.9.

Sirghi L., Ponti J., Broggi F., and Rossi F. 2008. "Probing elasticity and adhesion of live cells by atomic force microscopy indentation." *European Biophysical Journal* 37 (6): 935-45. 10.1007/s00249-008-0311-2.

Sneddon I.N. 1965. "The relation entre load and penetration in the axisymmetric boussinesq problem for a punch of arbitrary profile." *International Journal of Engineering Science* 3 (1): 47-57.

Sokolov I., Dokukin M.E., and Guz N.V. 2013. "Method for quantitative measurements of the elastic modulus of biological cells in AFM indentation experiments." *Methods* 60 (2): 202-13. 10.1016/j.ymeth.2013.03.037.

Somerville C., Bauer S., Brininstool G., Facette M., Hamann T., Milne J., Osborne E., Paredez A., Persson S., Raab T., Vorwerk S., and Youngs H. 2004. "Toward a systems approach to understanding plant cell walls." *Science* 306 (5705): 2206-11. 10.1126/science.1102765.

Somssich M., Khan G.A., and Persson S. 2016. "Cell wall heterogeneity in root development of Arabidopsis." *Frontiers in Plant Science* 7: 1242. 10.3389/fpls.2016.01242.

Svistoonoff S., Creff A., Reymond M., Sigoillot-Claude C., Ricaud L., Blanchet A., Nussaume L., and Desnos T. 2007. "Root tip contact with low-phosphate media reprograms plant root architecture." *Nature Genetics* 39 (6): 792-6. 10.1038/ng2041.

Tagawa T., and Bonner J. 1957. "Mechanical properties of the Avena coleoptile as related to Auxin and to ionic interactions." *Plant Physiology* 32 (3): 207-12. 10.1104/Pp.32.3.207.

Talbott L.D., and Ray P.M. 1992. "Molecular size and separability features of pea cell wall polysaccharides : implications for models of primary wall structure." *Plant Physiology* 98 (1): 357-68. 10.1104/pp.98.1.357.

Tan K.S., Hoson T., Masuda Y., and Kamisaka S. 1991. "Correlation between cell-wall extensibility and the content of diferulic and ferulic acids in cell-walls of *Oryza Sativa* coleoptiles grown under water and in air." *Physiologia Plantarum* 83 (3): 397-403. 10.1034/j.1399-3054.1991.830310.x.

Tenhaken R. 2015. "Cell wall remodeling under abiotic stress." *Frontiers in Plant Science* 5. 10.3389/fpls.2014.00771.

Teulon J.M., Delcuze Y., Odorico M., Chen S.-w.W., Parot P., and Pellequer J.-L. 2011. "Single and multiple bonds in (strept)avidin-biotin interactions." *Journal of Molecular Recognition* 24: 490-502. 10.1002/jmr.1109.

Valent B.S., and Albersheim P. 1974. "The structure of plant cell walls: v. On the binding of xyloglucan to cellulose fibers." *Plant Physiology* 54 (1): 105-8. 10.1104/pp.54.1.105.

Waidmann S., Sarkel E., and Kleine-Vehn J. 2020. "Same same, but different: growth responses of primary and lateral roots." *Journal of Experimental Botany* 71 (8): 2397-411. 10.1093/jxb/eraa027.

Wang J., Yu X., Ding Z.J., Zhang X., Luo Y., Xu X., Xie Y., Li X., Yuan T., Zheng S.J., Yang W., and Guo J. 2022. "Structural basis of ALMT1-mediated aluminum resistance in Arabidopsis." *Cell Research* 32 (1): 89-98. 10.1038/s41422-021-00587-6.

Wang T., Park Y.B., Caporini M.A., Rosay M., Zhong L., Cosgrove D.J., and Hong M. 2013. "Sensitivity-enhanced solid-state NMR detection of expansin's target in plant cell walls." *Proceedings of the National Academy of Sciences of the USA* 110 (41): 16444-9. 10.1073/pnas.1316290110.

Ward J.T., Lahner B., Yakubova E., Salt D.E., and Raghothama K.G. 2008. "The effect of iron on the primary root elongation of Arabidopsis during phosphate deficiency." *Plant Physiology* 147 (3): 1181-91. 10.1104/pp.108.118562.

Weinstein L.H., Meiss A.N., Uhler R.L., and Purvis E.R. 1956. "Growth-promoting effects of ethylenediamine tetra-acetic acid." *Nature* 178 (4543): 1188. 10.1038/1781188a0.

Whitney S.E.C., Gothard M.G.E., Mitchell J.T., and Gidley M.J. 1999. "Roles of cellulose and xyloglucan in determining the mechanical properties of primary plant cell walls." *Plant Physiology* 121 (2): 657-63. 10.1104/pp.121.2.657.

Wolf S., Hematy K., and Hofte H. 2012. "Growth control and cell wall signaling in plants." *Annual Review of Plant Biology* 63: 381-407. 10.1146/annurev-arplant-042811-105449.

Yang J., Qu M., Fang J., Shen R.F., Feng Y.M., Liu J.Y., Bian J.F., Wu L.S., He Y.M., and Yu M. 2016. "Alkali-soluble pectin is the primary target of aluminum immobilization in root border cells of Pea (*Pisum sativum*)." *Frontiers in Plant Science* 7: 1297. 10.3389/fpls.2016.01297.

Zhang H., and Liu K.K. 2008. "Optical tweezers for single cells." *Journal of The Royal Society Interface* 5 (24): 671-90. 10.1098/rsif.2008.0052.

Zhong Q., Inniss D., Kjoller K., and Elings V. 1993. "Fractured polymer/silica fiber surface studied by tapping mode atomic force microscopy." *Surface Science Letters* 290: L688-L92. 10.1016/0039-6028(93)90582-5.

ANNEX 1

Nanoscale Horizons

ROYAL SOCIETY OF CHEMISTRY

COMMUNICATION

Cite this: *Nanoscale Horiz.*, 2023, 8, 75

Received 17th August 2022,
Accepted 21st October 2022

DOI: 10.1039/d2nh00390b

rsc.li/nanoscale-horizons

Nano-structural stiffness measure for soft biomaterials of heterogeneous elasticity†

Shu-wen W. Chen, *[ab] Jean-Marie Teulon,[a] Harinderbir Kaur,[a] Christian Godon[c] and Jean-Luc Pellequer *[a]

Nanoscale Horizons

ROYAL SOCIETY OF CHEMISTRY

COMMUNICATION

Cite this: *Nanoscale Horiz.*, 2023, 8, 75

Received 17th August 2022,
Accepted 21st October 2022

DOI: 10.1039/d2nh00390b

rsc.li/nanoscale-horizons

Nano-structural stiffness measure for soft biomaterials of heterogeneous elasticity†

Shu-wen W. Chen, *[ab] Jean-Marie Teulon,[a] Harinderbir Kaur,[a] Christian Godon[c] and Jean-Luc Pellequer *[a]

Measuring the structural stiffness aims to reveal the impact of nanostructured components or various physiological circumstances on the elastic response of material to an external indentation. With a pyramidal tip at a nano-scale, we employed the atomic force microscopy (AFM) to indent the surfaces of two compositions of polyacrylamide gels with different softness and seedling roots of *Arabidopsis thaliana*. We found that the stiffness–depth curve derived from the measured force exhibits a heterogeneous character in elasticity. According to the tendency of stiffness–depth curve, we decomposed the responding force into depth-impact (F_C), Hookean (F_H) and tip-shape (F_S) components, called trimechanic, where F_S and its gradient should be offset at the surface or subsurfaces of the indented material. Thereby, trimechnic theory allows us to observe how the three restoring nanomechanics change with varied depth. Their strengths are represented by the respective spring constants (k_C, k_H, k_S) of three parallel-connected spring (3PCS) analogs to differentiate restoring nanomechansims of indented materials. The effective Young's modulus $\hat{E}$ and the total stiffness k_T (= k_H + k_S) globally unambiguously distinguish the softness between the two gel categories. Data fluctuations were observed in the elasticity parameters of individual samples, reflecting nanostructural variations in the gel matrix. Similar tendencies were found in the results from growing plant roots, though the data fluctuations are expectedly much more dramatic. The zone-wise representation of stiffness by the trimechanic-3PCS framework demonstrates a stiffness measure that reflects beneath nanostructures encountered by deepened depth. The trimechanic-3PCS framework can apply any mechanical model of power-law based force–depth relationship and is compatible with thin layer corrections. It provides a new paradigm for analyzing restoring nanomechanics of soft biomaterials in response to indenting forces.

New concepts

"New concept brought by this research is the trimechanic theory, the very concept of composite nanomechanics underlying the restoring mechanism of material under an external compression. It provides a disentanglement of the linear and tip-shape related mechanical responses at various indentation depth. The novel aspects of this research are (1) define the never explored application criteria for the Sneddon's model to the study of depth-heterogeneous elasticity. (2) Design a three parallel-connected spring (3PCS) analogy for quantifying the strengths of responding nanomechanics, allowing us to differentiate circumstances exhibiting the same stiffness yet with different restoring nanomechanisms. (3) Calculate the force–derived stiffness curve as the key element for analysis instead of the force values themselves, thereby the slope of stiffness curve essentially represents the intrinsic elasticity of the material. The trimechanic theory applies to all contact-based mechanical models with a power law force–depth relationship. The prospect of this research includes a standardization of the application of stiffness measure beyond model systems toward live or clinical tissues. Particularly, stiffness measure will not stay on a stage of global assessment but goes further to link elastic behaviors with substructure of the nanomaterial."

Introduction

Recently, mechanobiology has attracted a great deal of attention on how external forces can regulate the function of proteins, cells, and tissues.[1,2] In particular, it remains elusive on how cells transduce mechanical stresses, ranging from Pascals to mega Pascals, into physiological processes and end up with serious physiopathological consequences.[3] Many attempts have been made to accurately characterize elastic properties of these soft biomaterials, including micropipette aspiration,[4] optical tweezers,[5] deformability cytometry,[6] Brillouin microscopy,[7] and the most adopted strategy, atomic force microscopy (AFM).[8] AFM indentation results have brought to evidence that certain diseases are subject to abnormal cellular mechanics, for example, a

[a] *Université Grenoble Alpes, CEA, CNRS, IBS, F-38000 Grenoble, France. E-mail: cmft551@yahoo.com, jean-luc.pellequer@ibs.fr*
[b] *Rue Cyprien Jullin, Vinay, 38470, France*
[c] *Aix Marseille University, CEA, CNRS, BIAM, 13108 Saint Paul-Lez-Durance, Cadarache, France*
† Electronic supplementary information (ESI) available. See DOI: https://doi.org/10.1039/d2nh00390b

lowered stiffness measured for cancer cells compared to normal ones.[9] Similar results were found in extracellular matrix[10,11] and tissues during cancer progression.[12,13]

In the instrumental setup of AFM for indentation, the tip attached beneath the micro-sized cantilever plays as an indenter to compress the surface of cells or tissues. In this process, cantilever deflections are recorded as the so-called force–displacement data,[14,15] from which the Young's modulus is deduced.[16] In assessment of the Young's modulus, Hertzian[17] and Sneddon's models[18] are widely used to analyze the force–depth data acquired by AFM. The latter delineates the relation between the responding force of material and the indented depth, which depends on the shape of AFM tip. Hence, various shapes of tip have been exploited to study the tip-shape effect on the magnitude of Young's modulus.[19,20] Both Hertz and Sneddon models are restricted to sample systems of linear (homogeneous) elasticity with an infinite thickness (occupying the whole half space), and the employment of an axisymmetric punch to indent the material surface normally.[21,22] The Hertz model, used for spherical probes, has some other constrains such as the indented depth must be within 10% of the sample thickness,[23] relatively small compared to the spherical radius, and without adhesive interactions and frictions between the sample and the indenter upon contacting.[22] These limitations have been attenuated by the so-called bottom-effect correction for spherical tips[24] and conical tips;[25] or using a thin layer correction[26] that has been applied to two lipid layers.[21] The case of adhesion has been tackled by JKR[27] and DMT[28] models using spherical tips.

The architecture of cells and tissues is by essence complex and non-homogeneous.[29,30] The deformation of nano-structured component caused by external stresses depends on the bonding network and strengths of its chemical groups. Such a complication in stiffness measure brought by structural complexity makes conventional models difficult in interpretation of measured stiffness, especially in the study of soft biomaterials.[31] Moreover, the substratum may impact the stiffening behaviors.[21,32] It has been reported that stiffness difference can be detected from layered samples (separate elastic bodies) with different elasticity.[33–35] Therefore, a full analysis over the entire indentation trajectory is needed for our understanding on the above-mentioned issues.

Here, we propose a robust strategy, coined trimechanic theory, to encompass elastic behaviors of soft- and bio-materials in various circumstances. The change in elastic behaviors implicates the change in the context of the material. Trimechanic theory allows us to quantify the difference of elastic responses through different combinations of three nanomechanical actions governed, respectively, by a constant, a linear and a non-linear forces.

In this article, we illustrate the concept and application of the trimechanic theory to the force–depth measurements from AFM indentation. Besides the pyramidal tip used in this work, trimechanic theory will be shown to accommodate Hertz and other Sneddon's force–depth relations for spherical tips as well.

Methodology

A. Theory and model

A.1. Indentation force and stiffness. Consider the depth and force measurements by AFM indentation as a sequence of time events, $Z(t)$ and $F_T(t)$. In practice of AFM indentation, the data acquisition is carried out in a duration of T with an time interval Δt. $\{(Z(t), F_T(t))\}$ can be re-expressed as $\{(Z_i, F_{T,i})\}$, the enumeration index i indicates the data recorded at $t = (i-1)\cdot\Delta t$. This data series can be characterized by one single Young's modulus if the study material is a homogeneously elastic body. In the use of an axisymmetric tip with smooth surfaces, the Sneddon's solutions to Boussinesq's problem[36] relates the force F_T as a quadratic function of penetrated depth Z.[18] In this work, we employed a tip of pyramidal shape, of which the force–depth relation is given elsewhere;[19] omitting i, it is written as

$$F_T = \hat{E}\frac{\tan\alpha}{\sqrt{2}}Z^2 \tag{1}$$

where $\hat{E} = E/(1-\eta^2)$, denoted as the effective Young's modulus with E the Young's modulus and η the Poisson's ratio, and α corresponds to the face angle of the squared pyramidal tip. According to eqn (1), the stiffness $F'_T \equiv \partial F_T/\partial Z$ is explicitly a linear function of penetrated depth Z with a proportional constant R_S, thus

$$F'_T = R_S Z = (\sqrt{2}\hat{E}\tan\alpha)Z. \tag{2}$$

R_S can be conceived as stiffness slope, scoring the increment of stiffness per indented depth responded by the material, and directly linked to the effective Young's modulus $\hat{E}$.

For a material of homogeneous elasticity, the stiffness curve derived from F_T should be one single linear segment with one R_S or $\hat{E}$ based on the force–depth relationship. Thereby, we exploited this property to explore elastic heterogeneity of material by examining the slope of stiffness–depth curve during an indenting process. The change in R_S reflects a change in $\hat{E}$ as well as the restoring nanomechanics of material. From eqn (1) and (2), F_T and F'_T are both zero at $Z = 0$—initial boundary conditions for applying the Sneddon's model.

A.2. Trimechanic theory for general elastic response. For a material whose elastic properties vary with indented depth, we assume they exhibit a zone-wise pattern with a cone-like shape of the indenting tip. Within each depth-zone, the data points share similar elastic properties. Explicitly, the restoring force F_T at the total depth D can be expressed as a sequence of force segments:

$$\begin{aligned} F_T(D) &= \sum_{i=1}^{m}\int_{Z_{i-1}}^{Z_i} F'_T\mathrm{d}Z = F_T(Z_{j-1}) \\ &\quad + \sum_{i=j}^{m}\int_{Z_{i-1}}^{Z_i} F'_T\mathrm{d}Z = F_T(Z_{m-1}) + \int_{Z_{m-1}}^{D} F'_T\mathrm{d}Z \end{aligned} \tag{3}$$

The limits of integration define a zone-wise region of indented depth; by default, $F_T(Z_0 = 0)$ is zero. For each indented depth-zone, say Zone j, the F_T (*cf.* the second equality of eqn (3)) can be

expressed as a composite of three force components:

$$F_T(Z) = F_T(Z_{j-1}) + F'_T(Z_{j-1}) \times (Z - Z_{j-1}) + \int_{Z_{j-1}}^{Z} [F'_T(y) - F'_T(Z_{j-1})]\,dy \quad (4)$$

The first component is the force measured at the sub-surface of the zone, Z_{j-1}; it is a constant thus denoted by F_C. In effect, F_C represents the hitherto force against the indenting tip. The second component is a Hookean force, called F_H, with a proportional constant of $F'_T(Z_j - 1)$. Removing F_C and F_H from the total force F_T, the remaining force satisfies the initial boundary conditions for applying the Sneddon's model. We denote this force as F_S to attribute it to the tip shape, from which the magnitude of $\hat{E}$ is deduced. The three force components govern three nanomechanics modes—this is trimechanic theory. Trimechanic theory is the very concept of composite nanomechanics underlying the restoring mechanism of material in the indentation trajectory. Various elastic responses are expressed as a linear combination of the three basis nanomechanics, whose strengths quantify the difference in the elastic behaviors.

A.3. The three parallel-connected spring (3PCS) analogy. To quantify the strengths of the three basis nanomechanics in an elastic response, we designated a device with three parallel-connected spring (3PCS) analogs whose elastic actions represent the three different mechanical modes; see Fig. 1. The strength of each nanomechanical response is represented by the spring constant of the corresponding spring analog.

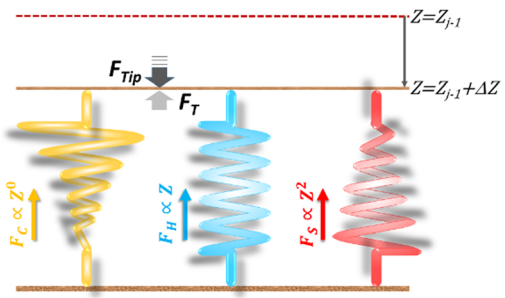

Fig. 1 Analogy of three parallel-connected springs: the elastic response (F_T) of a material to an applied force (F_{Tip}) is a composite action of three nanomechanics, respectively governed by F_C, F_H and F_S, which compose F_T. In the schematic diagram, the tip has arrived at the sub-surface of Zone j in the indentation trajectory, Z_{j-1}, and continues to indent the material with an additional compression, ΔZ. During the indentation from Z_{j-1} to $Z_{j-1} + \Delta Z$, the material exerts a restoring force F_T against the applied force F_{Tip} to form, microscopically, a quasi-equilibrium. Except the F_H-spring obeying the Hooke's law, the F_C-curve is a zero-power function of Z, while the nonlinear F_S function, in the diagram, has an exponent of 2 to exemplify the use of a pyramidal tip. The pseudo-stiffness function for the F_C-spring is inversely proportional to the indented depth, picturized by a spring with non-linearly shrinking width. The stiffness function of F_S-spring is proportional to Z, symbolized by a spring with linearly increasing width, and that of F_H-spring is a constant, thus represented by a spring of constant width. According to this spring analogy, $F_T = k_{3PCS} \cdot \Delta Z$, where $k_{3PCS} = k_C + k_H + k_S$, the sum of the spring constants of the three spring devices.

Among the 3PCS analogs, the F_H-spring is the only one having a typical spring constant, $k_{H,j} = F'_T(Z_j - 1)$ for zone j; it is essentially the total stiffness measured at the subsurface of the visited zone. Two other spring analogs for F_C and F_S do not have the standard spring constant, which will be represented by the average of their stiffness functions. As a constant, F_C contributes none to stiffness measure. Were there a stiffness function corresponding to F_C, it would be inversely proportional to the amount of compression to make up the force constant. Accordingly, F_C would act like a force thresholder, forbidding the tip without sufficient applied force continuing to indent the material. However, averaging such a pseudo-stiffness function cannot yield a finite number, thus we took $F_T(Z_{j-1})/\Delta Z_j$ as the spring constant of the F_C-spring, $k_{C,j}$, with $\Delta Z_j = Z_j - Z_{j-1}$.

For the F_S-spring, we averaged the corresponding stiffness function (eqn (2)) over the indented zone and obtained the spring constant:

$$k_{S,j} = R_{S,j} \cdot \Delta Z_j/2 \text{ or } \hat{E}_j \cdot \tan\alpha \cdot \Delta Z_j/\sqrt{2}. \quad (5)$$

We define $k_{T,j} = k_{H,j} + k_{S,j}$ as the stiffness measure for the indented material to represent the stiffness measure for the material indented through the depth-zone j. This zone-wise representation is based on behaviors of $F'_T - Z$ curve, to the contrary of stiffness tomography that slices the F_T–Z curve into segments (or layers for indentation depth) without care for the initial boundary conditions imposed on the nonlinear force and the contribution of Hookean nanomechanincs.[37–39] As shown, the relative strengths of Hookean and tip-shape nanomechanics, $r_{H,j}$ and $r_{S,j}$, are complementary to each other for $r_{H,j} = k_{H,j}/k_{T,j}$ and $r_{S,j} = 1 - r_{H,j}$. Taken together, an elastic response can be fully described by the trimechanic-3PCS framework in a quadruplet format: $[\Delta Z_j, k_{C,j}, k_{T,j}, r_{S,j}]$, the necessary and sufficient parameters to rebuild the fitting curves for F_T and three decomposed force components. Detailed calculations can be found in ESI.†

B. Material preparation and AFM instrumentation

B.1. The study systems of soft materials. System 1: the specimen is a 10.4% polyacrylamide gel of about 1.0 mm thickness. For this system, we used a triangular silicon nitride MLCT-BIO-DC cantilever D with nominal k = 0.03 N m^{-1}, L = 225 μm, W = 20 μm, F = 15 kHz (Bruker AFM probes, Camarillo, CA, USA), and a squared pyramid shape for the AFM tip with a nominal opening angle of 35°. The ingredient of 10.4% polyacrylamide gel includes 245 μL of acrylamide solution (40%, stored at 4 °C, Sigma-Aldrich A8887), 300 μL of Bis-acrylamide (2%, stored at 4 °C, Sigma-Aldrich 146072), 1.5 μL of tetramethylenediamine (TEMED, Euromedex, 50406) and 10 μL of ammonium persulfate (APS, 10%, Sigma-Aldrich, A3678) mixed in 443 μL of ultrapure water (MilliQ systems). The gel was assembled as reported previously[40] except that 50 μL of gel were deposited at the center of an O-ring from a polypropylene micro-tube (BRAND®, 780712) which was dipped in Sigmacote® (Sigma-Aldrich, SL2) beforehand.

System 2: the specimen is a 7.4% polyacrylamide gel of about 1.0 mm thickness. The same AFM instrumentation was used as for System 1. The 7.4% polyacrylamide gel was prepared by mixing with 176 μL of acrylamide solution, 210 μL of Bis-acrylamide, 1.5 μL of TEMED, and 10 μL of APS in 602 μL of ultrapure water. The two gel materials were made on the same day. A preparation protocol of polyacrylamide gels with tunable elastic properties can be found elsewhere.[41]

Experimental setups of AFM for System 1 and 2: we employed an AFM multimode 8 (Bruker, Santa Barbara, CA, USA) equipped with a J-scanner and nanoscope-V controller to perform indentations on gel specimen. The force–displacement measurements were acquired using the force volume mode of the Nanoscope 9.2 software, and the data were collected in a matrix fashion with 8 × 8 or 16 × 16 spots distributed over the material surface in a size of 2 × 2 μm^2, and each data curve consists of 512 data points with a ramp size smaller than 2 μm.

B.2. The study systems of live tissues. Systems 3 and 4: the specimens are a 4 day-old seedling root from *Arabidopsis thaliana* with a thickness of about 0.12 mm.[42] The sowing and growing of the plant seeds followed the procedures described elsewhere.[43] In brief, the roots were deposited on a glass covered with pressure sensitive adhesive NuSil MED1-1356 (NuSil Technology LLC, Carpinteria, CA, USA), and kept alive by covering with 200 μL growth solution (MES buffer 3.5 mM, pH 5.5–5.8 with MS liquid medium diluted to 1/10).[44] The indenter adopted for the system is the triangular pyrex silicon nitride PNP-TR cantilever #2 with nominal k = 0.08 N m^{-1}, L = 200 μm, W = 28 μm, F = 17 kHz, which holds a square pyramidal tip with an opening angle of 35° (NanoWorld, Neuchatel, Switzerland).

Experimental setups of AFM for Systems 3 and 4: the data values were acquired with a Dimension 3100 AFM (Bruker, Santa Barbara, CA, USA) equipped with a hybrid scanner and a nanoscope V controller. We recorded the data in a standard approach of force–distance measurements with the picoforce mode of the Nanoscope 7.3 software. Each data curve composed of 4096 points with a ramp size of 3 μm. All the indentation experiments on plants were performed in a single day.

Results and discussion

A. Elastic behaviors of soft materials

We present the results of AFM indentation for two gel composites with different concentrations of acrylamide and bis-acrylamide cross-linker, yet with the same molar ratio of acrylamide to bis-acrylamide, 16 : 1 (see Methodology). The gel system of higher (10.4%) concentration is presumably stiffer than that of the lower (7.4%) one. The former is thus called hard gel while the latter soft. The indentation (F_T–Z) and F_T-derived stiffness–depth (F'_T–Z) curves for the two gel systems are presented in Fig. 2. The computational tasks of generating F_T–Z and F'_T–Z curves from force–distance (F_d–z) data as well as the F_T decomposition into three components are described in the ESI.† In Fig. 2a, the F'_T–Z curves of both systems rise up

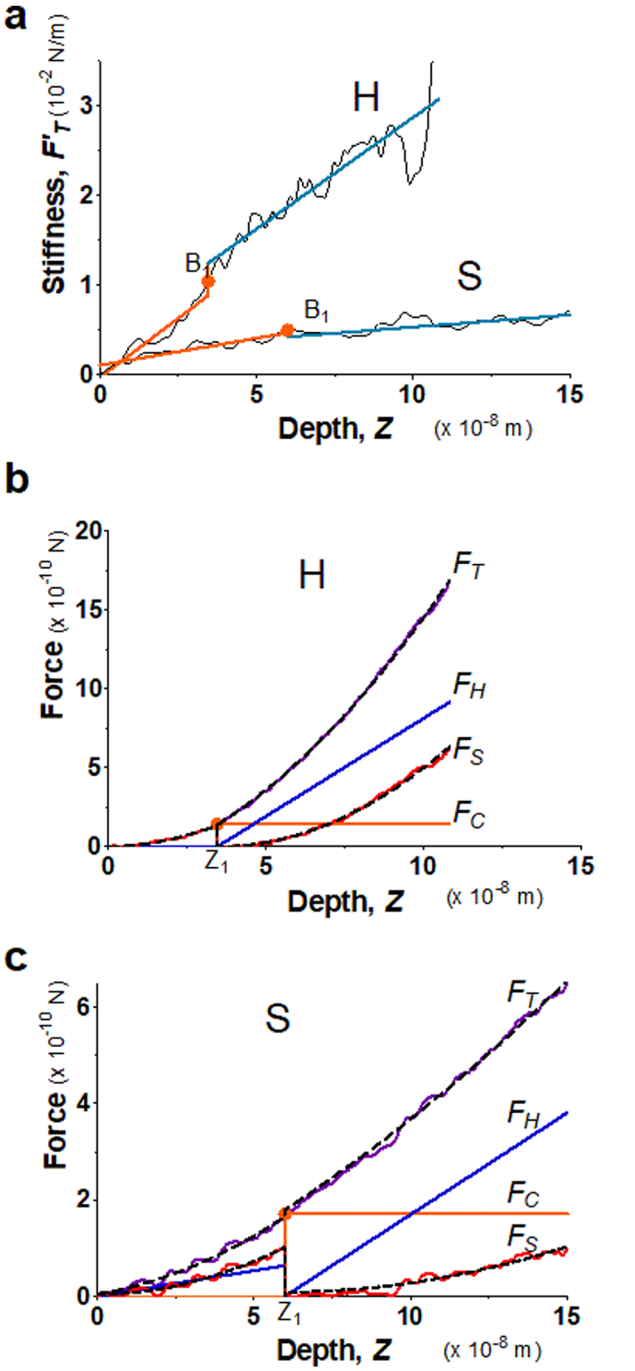

Fig. 2 Elastic behaviors of gel materials under the AFM indentation. (a) Stiffness–depth curves of two gel materials with different degrees of softness; "H" labels the hard gel while "S" labels the soft. The presenting graphs have been cut on the right for improving the clarity. In the full size, the total length of indented depth is 108 nm for the hard gel and 257.9 nm for the soft. The black solid lines present the F_T-derived stiffness data values. B_1 is the point breaking the F'_T–Z curve into two segments at a depth of Z_1. Here, Z_1 = 34.6 nm for "H" and Z_1 = 59.9 nm for "S". $\Delta Z_1 = Z_1 - Z_0 = Z_1$, $\Delta Z_2 = Z_2 - Z_1$, while Z_2 for both gels is the end of the indentation depth. Each stiffness segment was fitted to a linear function, drawn by an orange line for the first segment and in a light-blue color for the second one. (b) Decompose the restoring force of the hard gel (System 1) into three force components. F_T, F_C, F_H and F_S-curves are correspondingly presented by magenta, orange, blue and red lines, while fitting curves are drawn by black dashed lines. (c) Decompose the restoring force of the soft gel (System 2) into three force components. Similar to b, F_T, F_C, F_H and F_S are presented by magenta, orange, blue and red lines, respectively. The fitting results are drawn by black dashed lines.

with deeper indented depth. However, the one of the hard gel rises up faster and reaches a greater magnitude than that of the soft at the same depth, giving the stiffer property to the hard gel. The two curves have two linear segments with distinguished R_S values, indicating the entire indentation trajectory can be modeled as two depth-zones with different elasticity. We obtained $R_{S,1}$ = 265 and $R_{S,2}$ = 249 kPa for the hard gel. Similarly, $R_{S,1}$ = 60.5 and $R_{S,2}$ = 27.3 kPa for the soft gel. As seen later, the tendency of $\hat{E}$ would be closely related with that of R_S.

Fig. 2b and c present the curves of F_T as well as the three force components for the two gel systems. We deduced the $\hat{E}$ values from F_S-curves (Table 1) and shows that the hard gel has greater $\hat{E}$'s globally. We list the values of trimechanic-3PCS quadruplets in Table 1. We found that k_T unambiguously distinguishes the softness between soft and hard gels. As shown for this hard gel sample, the k_S dominates the total stiffness, k_T, in the first depth-zone, while k_H becomes greater than k_S at the end. Similarly, k_S is greater than k_H for the soft gel during the first depth-zone indentation while k_H is greater than to k_S in the second depth-zone.

Based on their nanomechanical types, k_H and k_S account for the resistances of material to surface displacement (non-bending action) and the extent of the surface penetrated, respectively. This behavior is illustrated by the change in r_S value, a numerical quantification for penetration ease. It is closely related to rigidity or deformability of the material. For either system, k_T steadily increases with deepened depth and accords with the tendency of $F_T'-Z$ curve. The structure of gel material formed by polymerization of acrylamide and bis-acrylamide depends on many factors such as gel concentration, molar ratio, pH and temperature.[45,46]

The k_H and k_S or r_S may provide detailed information on stiffening progresses of various indented spots of one gel or different gel composites. It is noteworthy that an effectively sharp tip should be employed instead of a large colloidal indenter for probing such a structural stiffness of material. For a nanostructured material, large spherical tips lead to a result averaged over heterogeneous elastic properties of the material. Consequently, stiffness variations attributed to different substructures and energetics on a nano-meter scale are often overlooked.

We compared the results from the trimechanic-3PCS model with the pyramid tip from AtomicJ software,[47] which aims to obtain the best fit of the indentation curve to the Sneddon's solution with a single segment by varying the location of the contact point. The fitting results of responding force from our model and AtomicJ-pyramid are shown in Fig. S2a and b (ESI†). Regarding the fitting goodness, the trimechanic-3PCS model yields a perfect fit, whereas AtomicJ-pyramid performed a poor fitting, particularly on the beginning of the indentation curve. From the data of $\hat{E}$ and k_T, it shows that the stiffness of material represented by AtomicJ-pyramid reflects an averaged value in contrast to the refined structural stiffness provided by the trimechanic-3PCS model. Moreover, the stiffness measure by trimechanic-3PCS model follows the tendency of the stiffness–depth curve accurately. It indicates that the trimechanic-3PCS model can be used to delineate the change in elasticity of the material in depth.

Table 1 The results of 3PCS quadruplet parameters for gel systems

	Hard		Soft	
Zone index	1	2	1	2
ΔZ (nm)	34.6	73.6	59.9	198
k_C (mN m^{-1})	0.00	1.92	0.00	0.86
k_T (mN m^{-1})	3.92	20.0	2.66	6.52
r_S	1.00	0.41	0.60	0.35
$\hat{E}$ (kPa)	230	236	54.4	23.4

r_s is dimensionless throughout the paper.

Beside the illustrating gel samples for the trimechanic-3PCS model shown in Fig. 2, we have applied this framework to 91 indentation curves of hard gel and 155 of soft gel; the results of k_T and $\hat{E}$ are presented in a graph format (see Fig. S3, ESI†). It shows that local elastic behaviors of these gel samples are not necessarily identical. Globally, the category of hard gel (upper sections of Fig. S3a and b, ESI†) exhibits a shorter length of indentation trajectory (the horizontal coordinate) yet much stiffer (brighter colors in intensity) than that of soft gel. It reveals that the hard gel accelerates the stiffening process shortly in depth against the deeper indentation by the AFM tip. Subsequently, the variation in the number of depth-zone is somewhat related to elasticity change in the indentation trajectory.

B. Elastic behaviors of live tissues

Biological tissues are often composed of complex structures. The probed surface of seeding roots of *A. thaliana* is formed of the external epidermal cell wall, which is structured with complex intertwining of cellulose, hemicellulose, and pectin,[48] including about 40% of water.[49] Two seedling roots (System 3 and 4) were chosen particularly for illustrating the advantages of using the trimechanic-3PCS model for analyzing elastic responses of live tissues with similar turgor pressure in a condition of constant temperature and buffer medium. In Fig. 3a, System 3 exhibits only one linear segment for the stiffness–depth curve while the other five. For the latter system, the slope of F_T-derive stiffness varies gradually and leads to a bent curve, unlike the former one that can be modeled by one straight line. These findings imply the impact of heterogeneous structure on the stiffness measure of plant root tissue, which cannot be modeled as one uniform shell structure.[50] Although System 4 has numerous depth-zones, the total depth of indentation is much shorter than that of System 3, 400 nm *vs.* ~1 μm. These depths indicate that the indentation was performed within the range of the external epidermal cell wall.[51] Fig. 3b and c show their corresponding force curves and the three force components.

In comparison with AtomicJ-pyramid (Fig. S2c and d, ESI†), we found that when the contact point and force fittings from both models are in good agreement, the deduced effective Young's moduli are unsurprisingly comparable, 45.2 and

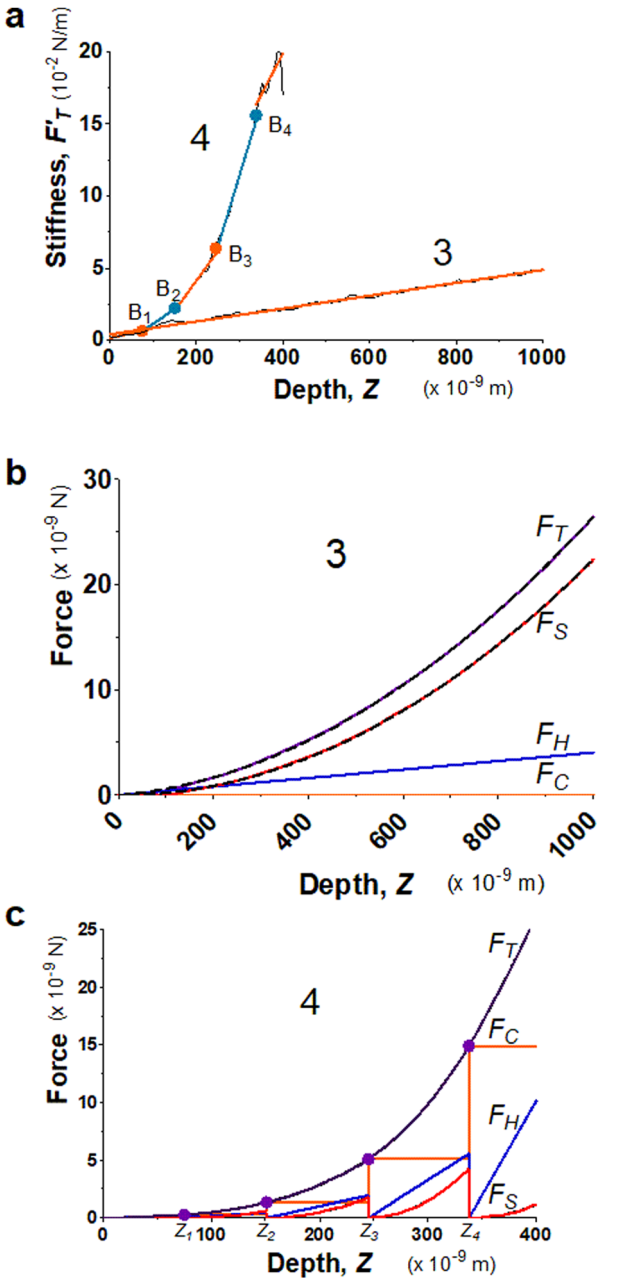

Fig. 3 Elastic behaviors of two 4 day-old seedling roots from *A. thaliana* (System 3 and 4) under AFM indentations. (a) The stiffness–depth curves of the two root systems, and labeled by 3 and 4, respectively. The black solid line presents F_T-derived stiffness curves, and the linear fitted segments are indicated by alternating colors, orange and light blue. The Z-coordinates of breaking points for System 4 are Z_1 = 74.8, Z_2 = 151, Z_3 = 245 and Z_4 = 338 nm. The single R_S of System 3 equals 44.7 kPa, and for the sequential segments of System 4, $R_{S,1}$ = 67.2, $R_{S,2}$ = 209, $R_{S,3}$ = 417, $R_{S,4}$ = 989, and $R_{S,5}$ = 570 kPa. (b) Application of trimechanic-3PCS model to System 3. The parameters of trimechanic-3PCS quadruplet are shown in Table 2. (c) Application of trimechanic-3PCS model to System 4. The trimechanic-3PCS quadruplets for the five depth-zones are listed in Table 2. All the plots of F_T as well as F_C, F_H and F_S against Z are respectively presented by magenta, orange, blue and red lines. The fitting results are delineated by black dashed lines.

45.5 kPa respectively from the trimechanic-3PCS model and AtomicJ-pyramid for System 3. On the contrary, for System 4,

Table 2 The results of 3PCS quadruplet parameters for plant seedling roots

	System 3	System 4				
Zone index	1	1	2	3	4	5
ΔZ (nm)	1000	74.8	76.0	94.2	92.9	62.0
k_C (mN m^{-1})	0.00	0.00	3.64	14.3	55.1	241
k_T (mN m^{-1})	27.2	3.93	13.9	39.4	105	182
r_S	0.85	0.63	0.57	0.48	0.43	0.10
$\hat{E}$ (kPa)	45.2	67.5	211	403	984	611

the discrepancy becomes severe between the two models (Fig. S2d, ESI†). As mentioned previously, the F_T-derived stiffness of this system cannot be modeled as one single linear segment, *i.e.* uniform elasticity. Nevertheless, the trimechanic-3PCS model reports the $\hat{E}$ values, ranging from 67.5 to 611 kPa, to describe the elasticity variation with depth. Results for the full plant datasets can be found graphically in Fig. S3c and d (ESI†).

For a live tissue of plant root, the magnitude and variation rate of stiffness with indented depth reflect the change of elastic properties through the thickness of the cell wall. In particular, the tip-shape nanomechanics (F_S) was found to exert a lower impact on the total response in deeper depth-zones, reflected by a decreased value of r_S or F_S weight. Such deeper indentations render the surface of the material so stiff that the surface hardly deforms itself to accord with the tip shape. One should not naively attribute the discrepancy between the results of trimechanic-3PCS and AtomicJ-pyramid models solely to the different choice of the contact point. We show in Fig. S1a (ESI†) that even the contact points determined by the two approaches are close, one still obtains incomparable results.

Conclusions

Trimechanic theory is a straightforward outcome of extending the applicability of the Sneddon's pyramid model to the study of elastic heterogeneity. The three force/nanomechanics components, F_C, F_H and F_S, carry information of the impact of hitherto indentation on the material. Analogous to the coordinates of a point in the three-dimensional space, (k_C, k_H, k_S) can be referred to the coordinates of an elastic response in the nanomechanical space, which is spanned by the three modes of nanomechanics. Excellent fittings of F_T curves by the trimechanic theory indicate that the best use of the Sneddon's model should be restricted to the F_S component instead of the total force F_T, and that the Hookean nanomechanics is substantial in the response. The stiffness-based approach to identification of same elasticity can extend to Hertz-spherical-tip model or a model whose force–depth relation follows the power law (a preliminary result for Hertz model is shown in Fig. S4, ESI†). The 3PCS quadruplet [ΔZ, k_C, k_T, r_S] contains all information on characterizing the elastic response of material, from which the modeled forces along the indentation depth can be reconstructed: $F_T = (k_C + k_T)\cdot\Delta Z$, k_T itself is the extrinsic stiffness, and $\hat{E}$ can be derived from k_T and r_S. Moreover, the combinatory ratio of r_S and r_H alludes to bonding deformability of the

composite material. With a nano-sized tip, AFM indentation combined with the trimechanic-3PCS framework provides us a technique to measure the structural stiffness of soft biomaterials, and to quantify the difference of restoring mechanisms from a variety of material conditions. The extended elasticity parameters bring a larger breadth on data comparison than one single parameter, leading to a finer differentiation between elastic properties of materials.

Author contributions

S. W. C. and J. L. P. conceived the study. S. W. C. developed the theory and performed the computational analysis. J. M. T. designed and made the gels and performed their indentation. H. K. and C. G. designed and performed indentation on plant roots. S. W. C. and J. L. P. wrote the manuscript with the contributions of all authors.

Conflicts of interest

There are no conflicts to declare.

Acknowledgements

IBS acknowledges integration into the Interdisciplinary Research Institute of Grenoble (IRIG, CEA). This work acknowledges the AFM platform at the IBS. Dr Anne-Emmanuelle Foucher (IBS, group EPIGEN) is acknowledged for her contribution to polyacrylamide gels. Dr Thierry Desnos (CEA, BIAM) is acknowledged for his contribution to the *Arabidopsis thaliana* project. Prof. Felix Rico (INSERM, Marseille) and Alessandro Podesta (Univ. Milano) are acknowledged for their useful discussions. Acknowledgment to the ANR project BioPhyt-18-CE20-0023-03 and the support of the European Union's Horizon 2020 research and innovation programme under the Marie Skłodowska-Curie grant agreement No. 812772, Project Phys2BioMed.

Notes and references

1 J. H. Wang and B. P. Thampatty, *Biomech. Model. Mechanobiol.*, 2006, **5**, 1–16.
2 V. Vogel, *Annu. Rev. Physiol.*, 2018, **80**, 353–387.
3 J. F. Stoltz and X. Wang, *Biorheology*, 2002, **39**, 5–10.
4 R. M. Hochmuth, *J. Biomech.*, 2000, **33**, 15–22.
5 H. Zhang and K. K. Liu, *J. R. Soc., Interface*, 2008, **5**, 671–690.
6 O. Otto, P. Rosendahl, A. Mietke, S. Golfier, C. Herold, D. Klaue, S. Girardo, S. Pagliara, A. Ekpenyong, A. Jacobi, M. Wobus, N. Topfner, U. F. Keyser, J. Mansfeld, E. Fischer-Friedrich and J. Guck, *Nat. Methods*, 2015, **12**, 199–202.
7 R. Prevedel, A. Diz-Munoz, G. Ruocco and G. Antonacci, *Nat. Methods*, 2019, **16**, 969–977.
8 M. Krieg, G. Flaschner, D. Alsteens, B. M. Gaub, W. H. Roos, G. J. L. Wuite, H. E. Gaub, C. Gerber, Y. F. Dufrene and D. J. Muller, *Nat. Rev. Phys.*, 2019, **1**, 41–57.
9 M. Lekka, P. Laidler, D. Gil, J. Lekki, Z. Stachura and A. Z. Hrynkiewicz, *Eur. Biophys. J.*, 1999, **28**, 312–316.
10 I. Sokolov, in *Cancer Nanotechnology*, ed. H. S. Nalwa and T. Webster, American Scientific Publishers, 2007, ch. 1, pp. 1–17.
11 S. Kumar and V. M. Weaver, *Cancer Metastasis Rev.*, 2009, **28**, 113–127.
12 M. Lekka, K. Pogoda, J. Gostek, O. Klymenko, S. Prauzner-Bechcicki, J. Wiltowska-Zuber, J. Jaczewska, J. Lekki and Z. Stachura, *Micron*, 2012, **43**, 1259–1266.
13 M. Plodinec, M. Loparic, C. A. Monnier, E. C. Obermann, R. Zanetti-Dallenbach, P. Oertle, J. T. Hyotyla, U. Aebi, M. Bentires-Alj, R. Y. Lim and C. A. Schoenenberger, *Nat. Nanotechnol.*, 2012, **7**, 757–765.
14 M. Radmacher, M. Fritz, C. M. Kacher, J. P. Cleveland and P. K. Hansma, *Biophys. J.*, 1996, **70**, 556–567.
15 M. Radmacher, *Methods Cell Biol.*, 2007, **83**, 347–372.
16 P. Carl and H. Schillers, *Pflugers Archiv.*, 2008, **457**, 551–559.
17 H. Hertz, *C. Vermischte Abhandlungen.*, 1882, pp. 449–464.
18 I. N. Sneddon, *Int. J. Eng. Sci.*, 1965, **3**, 47–57.
19 F. Rico, P. Roca-Cusachs, N. Gavara, R. Farre, M. Rotger and D. Navajas, *Phys. Rev. E: Stat., Nonlinear, Soft Matter Phys.*, 2005, **72**, 021914.
20 J. Zemla, J. Bobrowska, A. Kubiak, T. Zielinski, J. Pabijan, K. Pogoda, P. Bobrowski and M. Lekka, *Eur. Biophys. J.*, 2020, **49**, 485–495.
21 S. Chiodini, S. Ruiz-Rincon, P. D. Garcia, S. Martin, K. Kettelhoit, I. Armenia, D. B. Werz and P. Cea, *Small*, 2020, **16**, e2000269.
22 S. V. Kontomaris and A. Malamou, *Eur. J. Phys.*, 2022, **43**, 015010.
23 G. Persch, C. Born and B. Utesch, *Microelectron. Eng.*, 1994, **24**, 113–121.
24 E. K. Dimitriadis, F. Horkay, J. Maresca, B. Kachar and R. S. Chadwick, *Biophys. J.*, 2002, **82**, 2798–2810.
25 N. Gavara and R. S. Chadwick, *Nat. Nanotechnol.*, 2012, **7**, 733–736.
26 P. D. Garcia and R. Garcia, *Biophys. J.*, 2018, **114**, 2923–2932.
27 K. L. Johnson, K. Kendall and A. D. Roberts, *Proc. R. Soc. London, Ser. A*, 1971, **324**, 301–313.
28 B. V. Derjaguin, V. M. Muller and Y. P. Toporov, *J. Colloid Interface Sci.*, 1975, **53**, 314–326.
29 S. Kasas, X. Wang, H. Hirling, R. Marsault, B. Huni, A. Yersin, R. Regazzi, G. Grenningloh, B. Riederer, L. Forro, G. Dietler and S. Catsicas, *Cell Motil. Cytoskeleton*, 2005, **62**, 124–132.
30 S. Digiuni, A. Berne-Dedieu, C. Martinez-Torres, J. Szecsi, M. Bendahmane, A. Arneodo and F. Argoul, *Biophys. J.*, 2015, **108**, 2235–2248.
31 D. C. Lin, D. I. Shreiber, E. K. Dimitriadis and F. Horkay, *Biomech. Model. Mechanobiol.*, 2009, **8**, 345–358.
32 A. J. Engler, S. Sen, H. L. Sweeney and D. E. Discher, *Cell*, 2006, **126**, 677–689.
33 G. Kaushik, A. Fuhrmann, A. Cammarato and A. J. Engler, *Biophys. J.*, 2011, **101**, 2629–2637.
34 B. L. Doss, K. Rahmani Eliato, K. H. Lin and R. Ros, *Soft Matter*, 2019, **15**, 1776–1784.

35 V. G. Gisbert and R. Garcia, *ACS Nano*, 2021, **15**, 20574–20581.
36 J. Boussinesq, *Application des potentiels à l'étude de l'équilibre et du mouvement des solides élastiques, avec des notes étendues sur divers points de physique mathématique et d'analyse*, Gauthier-Villars Imprimeur-Libraire, Paris, 1885.
37 C. Roduit, S. Sekatski, G. Dietler, S. Catsicas, F. Lafont and S. Kasas, *Biophys. J.*, 2009, **97**, 674–677.
38 A. C. Dumitru, M. A. Poncin, L. Conrard, Y. F. Dufrene, D. Tyteca and D. Alsteens, *Nanoscale Horiz.*, 2018, **3**, 293–304.
39 S. Janel, M. Popoff, N. Barois, E. Werkmeister, S. Divoux, F. Perez and F. Lafont, *Nanoscale*, 2019, **11**, 10320–10328.
40 H. Schillers, C. Rianna, J. Schäpe, T. Luque, H. Doschke, M. Wälte, J. J. Uriarte, N. Campillo, G. P. Michanetzis, J. Bobrowska, A. Dumitru, E. T. Herruzo, S. Bovio, P. Parot, M. Galluzzi, A. Podestà, L. Puricelli, S. Scheuring, Y. Missirlis, R. Garcia, M. Odorico, J. M. Teulon, F. Lafont, M. Lekka, F. Rico, A. Rigato, J.-L. Pellequer, H. Oberleithner, D. Navajas and M. Radmacher, *Sci. Rep.*, 2017, **7**, 5117.
41 J. R. Tse and A. J. Engler, *Current Protocols in Cell Biology*, 2010, ch. 10, pp. 10–16.
42 C. Balzergue, T. Dartevelle, C. Godon, E. Laugier, C. Meisrimler, J.-M. Teulon, A. Creff, M. Bissler, C. Brouchoud, A. Hagège, J. Müller, S. Chiarenza, H. Javot, N. Becuwe-Linka, P. David, B. Péret, E. Delannoy, M.-C. Thibaud, J. Armengaud, S. Abel, J.-L. Pellequer, L. Nussaume and T. Desnos, *Nat. Commun.*, 2017, **8**, 15300.
43 H. Kaur, C. Godon, J.-M. Teulon, T. Desnos and J.-L. Pellequer, in *Mechanics of Cells and Tissues in Diseases*, ed. M. Lekka, D. Navajas, M. Radmacher and A. Podestà, Walter de Gruyter GmbH, Berlin/Boston, 2023, vol. 2, pp. 125–138.
44 T. Murashige and F. Skoog, *Physiol. Plant.*, 1962, **15**, 473–497.
45 D. P. Blattler, F. Garner, K. van Slyke and A. Bradley, *J. Chromatogr.*, 1972, **64**, 147–155.
46 A. Rath, F. Cunningham and C. M. Deber, *Proc. Natl. Acad. Sci. U. S. A.*, 2013, **110**, 15668–15673.
47 P. Hermanowicz, M. Sarna, K. Burda and H. Gabrys, *Rev. Sci. Instrum.*, 2014, **85**, 063703.
48 P. Albersheim, A. Darvill, K. Roberts, R. Sederoff and A. Staehelin, *Plant cell walls. From chemitry to biology*, Garland Science, Taylor & Francis Group, LLC, New York, NY, USA, 2011.
49 D. Gaff and D. Carr, *Aust. J. Biol. Sci.*, 1961, **14**, 299–311.
50 S. Tsugawa, Y. Yamasaki, S. Horiguchi, T. Zhang, T. Muto, Y. Nakaso, K. Ito, R. Takebayashi, K. Okano, E. Akita, R. Yasukuni, T. Demura, T. Mimura, K. Kawaguchi and Y. Hosokawa, *Sci. Rep.*, 2022, **12**, 13044.
51 P. Derbyshire, K. Findlay, M. C. McCann and K. Roberts, *J. Exp. Bot.*, 2007, **58**, 2079–2089.

Electronic Supplementary Material (ESI) for Nanoscale Horizons.

Supporting information:

Nano-structural stiffness measure for soft biomaterials of heterogeneous elasticity

Shu-wen W. Chen[a,b], Jean-Marie Teulon[a], Harinderbir Kaur[a], Christian Godon[c], and Jean-Luc Pellequer[a*]*

[a]Univ. Grenoble Alpes, CEA, CNRS, IBS, F-38000 Grenoble, France

[b]Rue Cyprien Jullin, F-38470 Vinay, France.

[c]Aix Marseille Univ, CEA, CNRS, BIAM, F-13108 Saint Paul-Lez-Durance, France

Corresponding authors : Shu-wen W. Chen (cmft551@yahoo.com); Jean-Luc Pellequer (jean-luc.pellequer@ibs.fr)

Computational procedure

1.a. Criteria of being a contact point

Determination of the contact point is the first step for the formation of indentation curve [1]. On a physical view, before reaching the contact point the tip experiences neither force nor force gradient (the first derivative of force) from the material. As a common practice in the study of nanomechanics, the location of the contact point is not pre-determined, it moves with which section of the curve yielding the best fitting results to the mechanical model used. As a consequence, the contact point lost its physical meaning. In this work, we follow the physical fact for determining the contact point, and we do not assume that the study material is necessarily elastically homogeneous.

Before starting with the curve of force (F_d) versus tip-sample separation (z), z being the cantilever-corrected piezo displacement; a small portion (10%) of initial pre-contacting data points are discarded to prevent unacceptable non-flatness and distortions from the baseline. We applied the Savitzky-Golay (SG) filter [2] to alleviate fluctuations of the data series (the smoothing effects can be seen from **Fig**. **S1**). Basically, the SG filter processes a series of data points in a convolution fashion with a matrix of $(n+1) \times (2w+1)$ convolution coefficients, where w is the half size of the smoothing window, n is the degree of the fitting polynomial function and is the highest order for the derivative function. In this work, we used $n = 3$ and $w = 15$ for all the testing systems. The great advantage of using the SG filter is not only to smoothen noisy data but also to simultaneously calculate the derivative functions.

Fig. S1 describes the detail of locating the contact points (z_c's) of all the study systems based on the criteria, $F_d = 0$ and $\partial F_d/\partial z = 0$. For calculations of $\partial F_d/\partial z$, we first used the SG filter to calculate the first derivative with respect to t or enumeration indexes of data points, $\partial F_d/\partial t$ and $\partial d/\partial t$, at each data point, then $\partial F_d/\partial z$ is calculated as $(\partial F_d/\partial t)/(\partial z/\partial t)$, i.e., the ratio of $\partial F_d/\partial t$ to $\partial z/\partial t$.

1.b. Formation of indentation and stiffness-depth curves

Once the contact point was decided, we generated the plot of F_T against Z (the indentation curve) straightforwardly with that $Z = -(z - z_c)$ and $F_T(Z) = F_d(z) - F_d(z_c)$, then the tip effects were removed from the F_T–Z curve [3]. Since $z = z_c$ was chosen as the origin of the F_T–Z curve, $Z_0 = 0$ and $F_T(Z_0) = 0$. Similar to the calculations for $\partial F_d/\partial z$, the curve of F_T-derived stiffness vs. depth was generated by the following steps: 1) calculate $\partial F_T/\partial t$ and $\partial Z/\partial t$ using the SG filter;

2) calculate the ratio of $\partial F_T/\partial t$ to $\partial Z/\partial t$ as the value of $F_T'(\partial F_T/\partial Z)$; 3) smoothen the F_T'-Z curve using a moving average filter.

2. Heterogeneity of elasticity and segmental analysis of stiffness-depth curve

We adopted a stiffness-based approach to identify the regions of different elasticity in the indentation trajectory. Based on Sneddon's model with pyramidal tips, the stiffness-depth curve (F_T' vs. Z) would appear as a series of linear segments joined at breaking points, B_j's. The Z coordinates of B_j's are referred to as generalized contact points that interface two adjacent depth-zones of different elastic properties. The following describes how linear segments delimiting the depth-zones of different elastic properties are determined from the stiffness-depth curve.

The segmentation of stiffness-depth curve was performed using clusterwise linear regression with the minimal distance method [4]. For a curve consisting of m linear segments, the clusterwise linear regression optimizes all the segments simultaneously with $2m$ fitting parameters. Subsequently, consecutive points were re-grouped from a cluster and an initial set of linear segments was established. Linearity of two consecutive segments was tested by their intersection angle. If the angle was within 5°, then the two segments were merged together to become one. Each segment required at least $(2w+1)$ data points. For a stiffness segment corresponding to, say Zone j, it has a generic form of a linear function: $c_j + R_{S,j}\times Z$ with c_j and $R_{S,j}$ two fitting parameters. The two parameters are exploited for decomposing F_T into F_C, F_H and F_S.

3. Force decomposition for the trimechanic theory

As F_H component of Zone j is formulated as $k_{H,j}\times(Z-Z_{j-1})$, $k_{H,j} = c_j + R_{S,j}\times Z_{j-1}$ and equals $F_T'(Z_{j-1})$ in Eq. (4). More important, the heterogeneity of material elasticity in the indentation trajectory is differentiated by $R_{S,j}$. F_C is set to $F_T(Z_{j-1})$, whereas the F_S component is the total force F_T subtracting the sum of F_C and F_H. In general, F_C and F_H do not need a fitting function, only F_S needs one. For example, F_S will fit to a parabolic function when a cone-like

or pyramidal tip is in use: $f_{p,j}(Z - Z_{j\text{-}1})^2 + \delta_j$, where $f_{p,j}$ and δ_j are two fitting parameters. The effective Young's modulus can be deduced as $\hat{E}_j = \sqrt{2}\, f_{p,j}/tan(\alpha)$ (cf. Eq. (2)) by ignoring the contribution attributed to the modulus of indenting tip itself. The weight of F_S contribution w_S is defined as $F_S(Z_j)/F_T(Z_j)$ to decide whether F_S to be neglected. If $w_S < 0.1$, then F_S is set to zero. Its data values are joined to F_H and the resultant F_H will be re-fitted to $k_{H,j} \times (Z - Z_{j\text{-}1})$, where $k_{H,j}$ now is a fitting parameter instead of an analytical quantity. Consequently, the fitted F_T data values, as presented in **Fig**. **2** and **3**, are the sum of the fitted force and, at most, two other non-fitted ones.

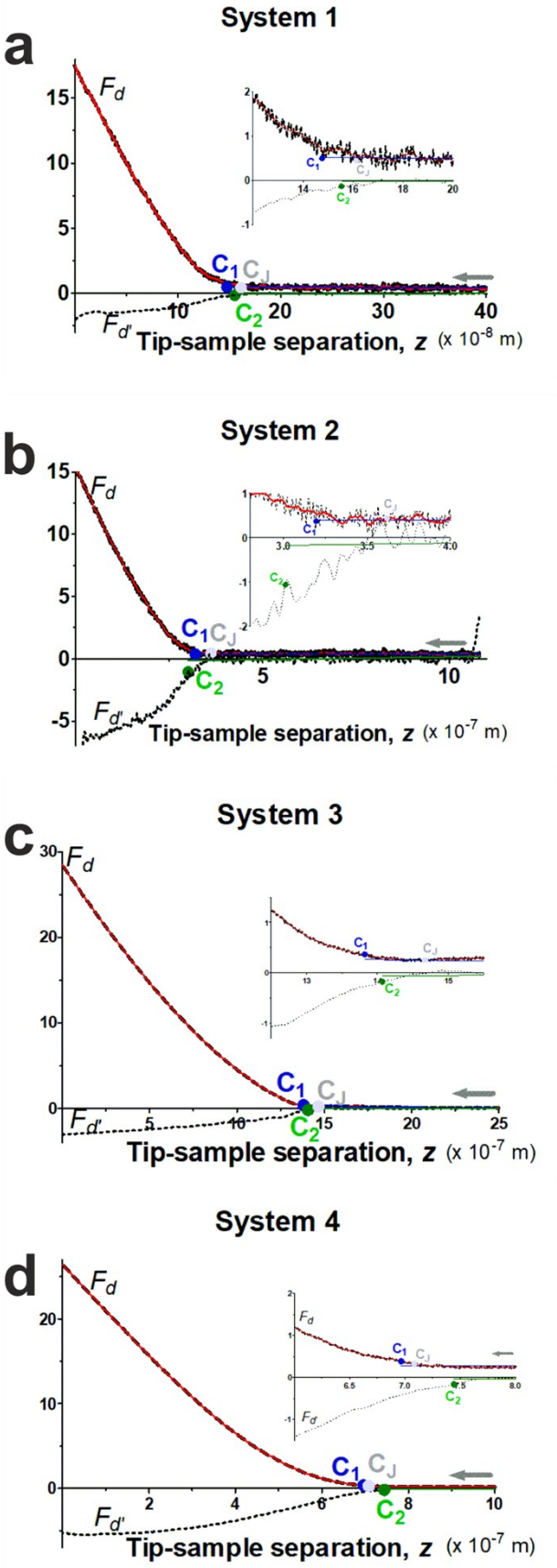
System 1
a
F_d
$F_{d'}$
C_1
C_J
C_2
Tip-sample separation, z (x 10^-8 m)
System 2
b
F_d
$F_{d'}$
C_1
C_J
C_2
Tip-sample separation, z (x 10^-7 m)
System 3
c
F_d
$F_{d'}$
C_1
C_J
C_2
Tip-sample separation, z (x 10^-7 m)
System 4
d
F_d
$F_{d'}$
C_1
C_J
C_2
Tip-sample separation, z (x 10^-7 m)

Figure S1: Contact points of all the illustrating systems. The determination of contact point is based on the criteria: $F_d(z) = 0$ and $F_d'(z)=0$ (see the main text). The plots of deflection force, $F_d(z)$, and $F_d'(z)$ have been smoothened by the SG filter beforehand and presented by black dashed lines in the figure. Inset graphs illustrate the smoothing effects of the SG filter. Red lines represent smoothed data of $F_d(z)$. The gray arrow along the z coordinate indicates the approaching direction of the tip toward the material surface. The blue and green lines are the baselines obtained by clusterwise linear regression respective to $F_d(z)$ and $F_d'(z)$. Correspondingly, blue and green spots mark the potential contact points along the $F_d(z)$ and $F_d'(z)$ baselines, and denoted by $\mathbf{C_1}$ and $\mathbf{C_2}$. For comparison, gray spots mark the contact point determined by the AtomicJ-pyramid algorithm, and labeled with $\mathbf{C_J}$. In practice, $\mathbf{C_1}$ and $\mathbf{C_2}$ were chosen as close as possible toward the material surface, where $F_d(z_1)$ and $F_d'(z_2)$ are within, 2.5 for gels and 2.9 for plant roots, standard deviations relative to the respective baselines. From our experience, $F_d'(z)$ is better to reflect the tendency of $F_d(z)$ than $F_d(z)$ itself. Consequently, z_2 is taken as the final location of the contact point. The units of F_d and F_d' are in 10^{-7} m, 10^{-8} N, and 10^{-3} N/m, respectively. (**a**) The hard gel (System 1): $z_1 = 14.9$, $z_2 = 14.9$, and $z_J = 16.1$ ($\times 10^{-8}$ m); F_d and F_d' are in 10^{-10} N, and 10^{-2} N/m. (**b**) The soft gel (System 2): $z_1 = 3.19$, $z_2 = 3.01$, and $z_J = 3.62$ ($\times 10^{-7}$ m); F_d and F_d' are in 10^{-10} N and 10^{-3} N/m. (**c**) The plant root of System 3: $z_1 = 13.8$, $z_2 = 14.1$ and $z_J = 14.68$ ($\times 10^{-7}$ m); F_d and F_d' are in 10^{-9} N and 10^{-2} N/m. (**d**) The plant root of System 4: $z_1 = 6.97$, $z_2 = 7.44$ and $z_J = 7.09$ ($\times 10^{-7}$ m); F_d and F_d' are in 10^{-9} N and 10^{-2} N/m.

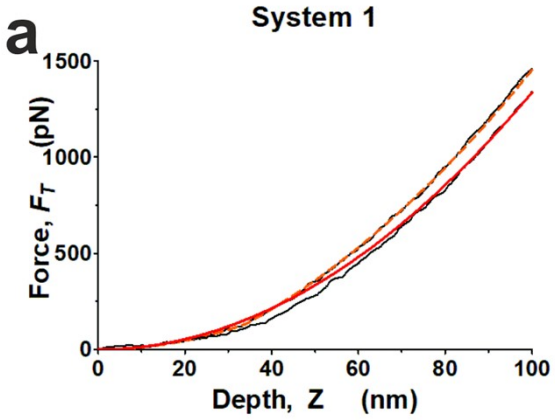
a
System 1
Force, F_T (pN)
1500
1000
500
0
0
20
40
60
80
100
Depth, Z (nm)

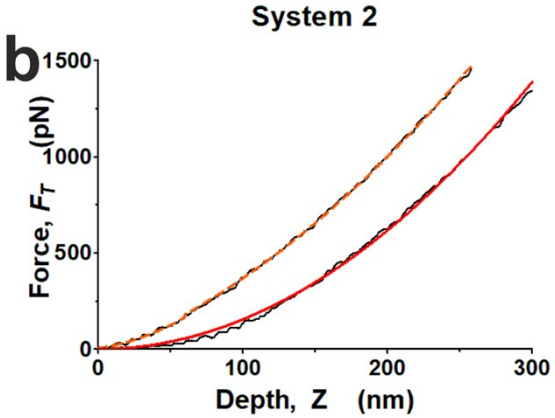
b
System 2
Force, F_T (pN)
1500
1000
500
0
0
100
200
300
Depth, Z (nm)

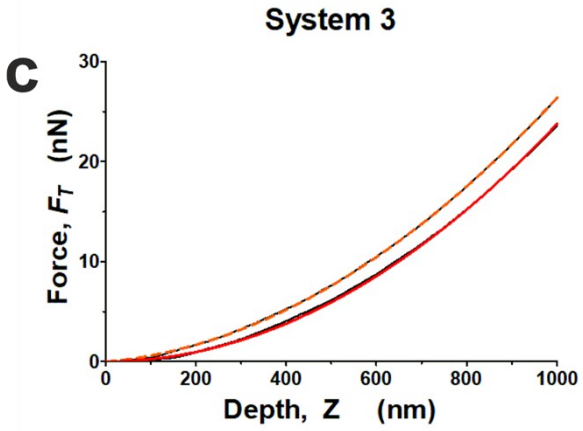
c
System 3
Force, F_T (nN)
30
20
10
0
0
200
400
600
800
1000
Depth, Z (nm)

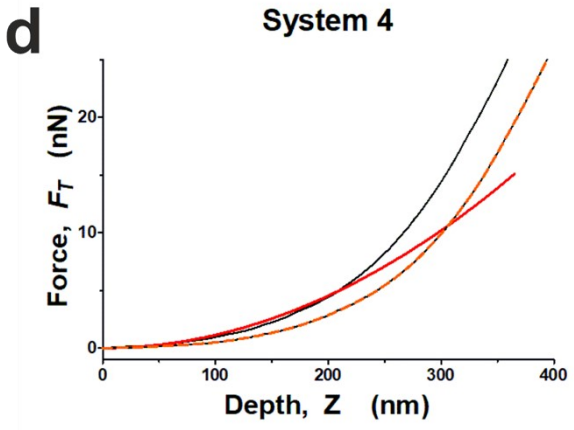
d
System 4
Force, F_T (nN)
20
10
0
0
100
200
300
400
Depth, Z (nm)

Figure S2: The fitting results of responding force from AtomicJ-pyramid and the trimechanic-3PCS models. The pyramid model of AtomicJ uses the conventional approach to fitting the responding force where the initial contact point is sought for improving the goodness of the fitting by a robust exhaustive method, LTA [5]. In the parameter setup of AtomicJ, the same semi-vertical angle of the pyramidal tip, 35˚, and a Poisson ratio of 0.0 were used for best comparison with the tri-mechanic-3PCS model to illustrate different consequences from the conventional usage of the Sneddon's model and our strategy. Derived indentation curves from AFM measurements are drawn by thin black lines for both models and the fittings by AtomicJ-pyramid are shown in red whereas that of the trimechanic-3PCS model are in orange dashed lines. (**a**) System 1: the hard gel. AtomicJ-pyramid provides a value of 256 kPa for the effective Young's modulus, equivalent to a stiffness measure of 14.4 mN/m using an indentation transition of 113 nm (see Eq. 5), while our model obtains 230 and 236 kPa for Zone 1 and 2, and the corresponding k_S equals 3.91 and 20.0 mN/m, respectively. (**b**) System 2: the soft gel. The effective Young's modulus deduced from AtomiJ-pyramid is 29.5 kPa, equivalent to a stiffness of 4.37 mN/m at indentation depth of 298 nm. From the trimechanic-3PCS framework, we observed that $\hat{E}1$ = 54.4 and $\hat{E}2$ = 23.4 kPa with $k_{S,1}$ = 2.66 and $k_{S,2}$ = 6.52 mN/m, respectively. (**c**) System 3, only one value of effective Young's modulus was deduced from both methods, 45.5 kPa from AtomicJ-pyramid and 45.2 kPa from the trimechanic-3PCS model. (**d**) System 4, AtomicJ-pyramid yields $\hat{E}$ = 214 kPa, while the trimechanic-3PCS model reports five $\hat{E}$ values attributed to the five force/stiffness segments, ranging from 67.5 to 611 kPa (see **Fig. 3**). From the fitting results, one can see by adopting the conventional strategy for stiffness measure, AtomicJ-pyramid displays a poor fitting to the response of material in the initial indentation which is essential for accurately describing the elastic properties of material surface. $\hat{E}$ = 214 kPa from AtomicJ-pyramid is too high to account for the response of material in the initial indentation while it is too low to describe the impact of deepened depth brought on the stiffness magnitude for a material of heterogeneous elasticity.

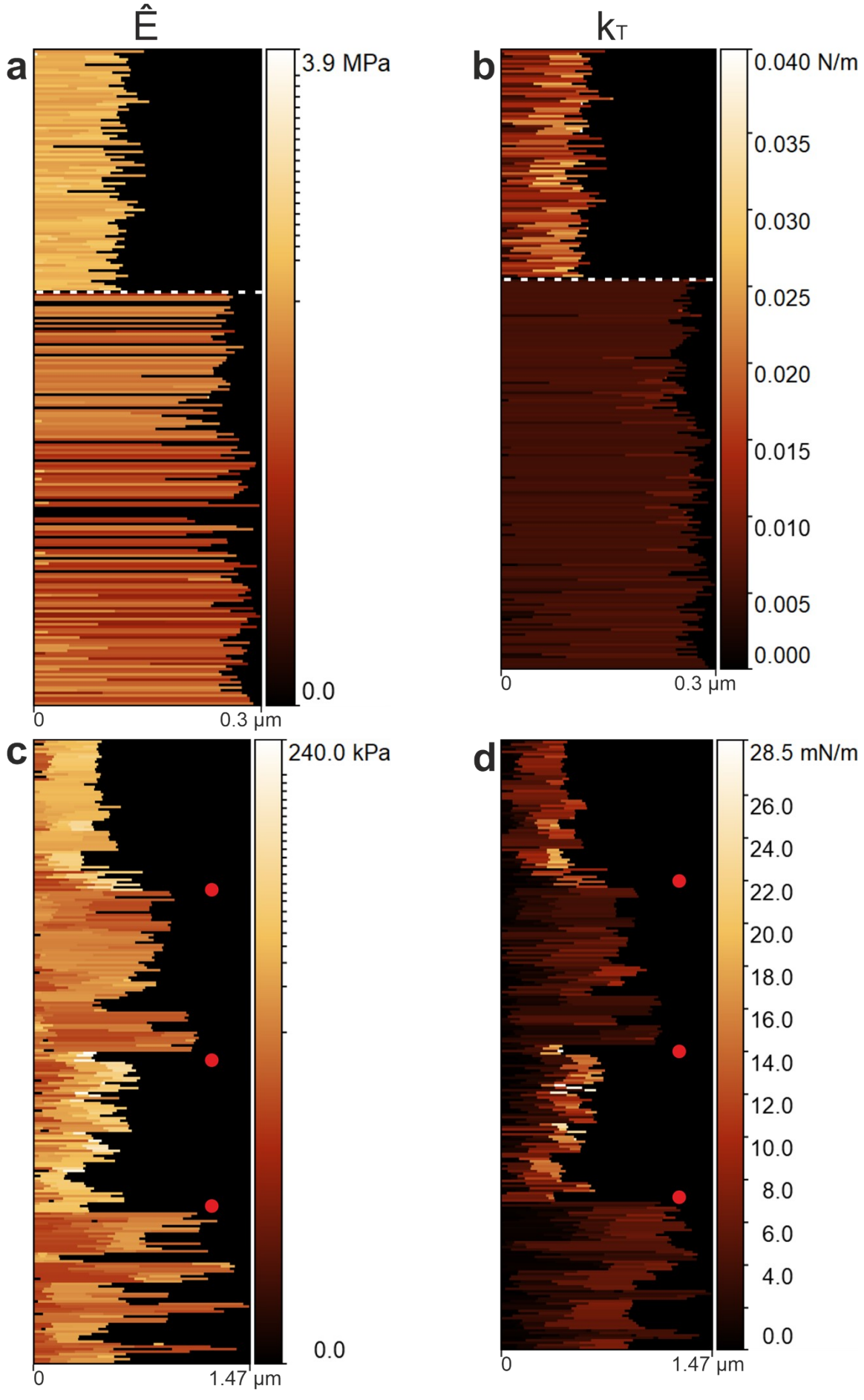
Ê
a
3.9 MPa
0.0
0
0.3 µm
kT
b
0.040 N/m
0.035
0.030
0.025
0.020
0.015
0.010
0.005
0.000
0
0.3 µm
c
240.0 kPa
0.0
0
1.47 µm
d
28.5 mN/m
26.0
24.0
22.0
20.0
18.0
16.0
14.0
12.0
10.0
8.0
6.0
4.0
0.0
0
1.47 µm

Figure S3: Bar graphs of effective Young's modulus and the stiffness measure k_T for polyacrylamide gels and plant roots. The horizontal-axis corresponds to the indented depth; the results of each indentation curve are represented with one line. The color bar on the right of the graph displays the value in the measured quantities. The graphics were generated using the Gwyddion software [6]. (**a**, **b**) The values of $\hat{E}$ and k_T of 91 sampled indentations for the hard gel as prepared for System 1, and beneath are 155 measurements for the soft gel for System 2. The separation of the two groups is marked by white dotted lines. By the naked eye, one can observed that the colors of $\hat{E}$ and k_T for the hard gel are much brighter than for the soft gel. Take the first depth-zone as an example, $\hat{E}_{\mathbf{hard}} = 2.96 \pm 4.02$ MPa (median = 2.27 MPa) vs. $\hat{E}_{\mathbf{soft}} = 0.41 \pm 0.62$ MPa (median = 0.32 MPa); $k_{T,\mathbf{hard}} = 9.96 \pm 4.90$ mN/m (median = 9.68 mN/m) vs. $k_{T,\mathbf{soft}} = 5.02 \pm 1.33$ mN/m (median = 5.51 mN/m). As for the first depth-zone, large standard deviations are observed for all depth-zones and underlie heterogeneity of cross-linker arrangement and inter-subgroup bonding properties. (**c**, **d**) The results of $\hat{E}$ and k_T of 248 indentation experiments on four different plant roots, maximum 64 curves for each root. The red spots mark the separation between the measurements on each roots. We observed that the values of $\hat{E}$, k_T and indentation length fluctuate widely, yet they vary more homogeneously within the same plant root. Recall that these root tissues are living organisms, their physiological conditions continuously change, e.g. the growth rate. For the first depth-zone, the averaged $\hat{E} = 94.9 \pm 101$ kPa with a median value of 58.4 kPa, and $k_T = 12.3 \pm 17.8$ with the median of 4.1 (in mN/m).

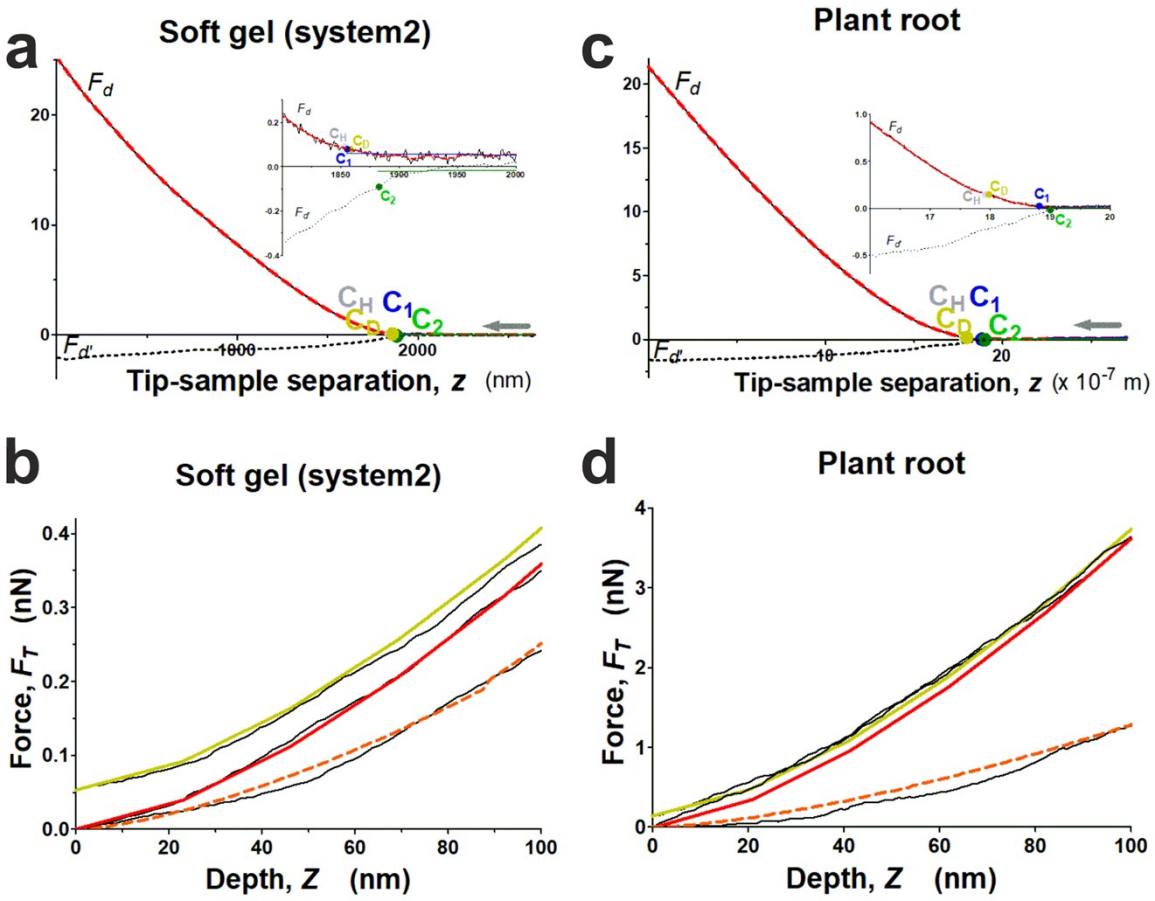

Figure S4: Preliminary test for the trimechanic-3PCS model applied to force-depth curves using a small spherical probe with a radius of 100 nm. The results from the present model are compared with other contact-based models. Locations of the contact points and the fittings of a F_T–Z curve from a soft gel sample **(a**,**b)** and that on a plant root **(c**,**d)**. The results from classical paraboloid Hertz and DMT models were obtained using AtomicJ robust exhaustive method, LTA [5] (JKR model from AtomicJ is not shown for lack of successful fitting). Parameter setup of AtomicJ includes the radius of the spherical probe, 0.1 µm, a Poisson ratio of 0, and the data smoothing by the SG filter (w = 10, n = 3). **(a)** Determination of the contact point for the soft gel. $\mathbf{C_1}$ and $\mathbf{C_2}$ mark the potential contact points obtained from $F_d(z)$ and $F_d'(z)$ baselines (cf. **Fig**. **S1**), whereas $\mathbf{C_H}$ and $\mathbf{C_D}$ mark the contact points identified by the Hertz and DMT models using AtomicJ. Inset graphs show a zoomed area around the contact points. **b)** Comparison of fitting results to individual indentation curves from respective models (thin black lines) within the first 100 nm of indentation depth. Fittings by AtomicJ-Hertz and AtomicJ-DMT are shown in red and olive, respectively, whereas that of the trimechanic-3PCS model are in orange. The effective Young's moduli deduced from AtomicJ-Hertz and AtomicJ-DMT are 26.8 and 26.6

kPa, respectively (both models consider the entire curve as one depth-zone). The trimechanic-3PCS framework yields Ê1 = 17.3 and Ê2 = 21.0 kPa for two depth-zones. **(c**,**d)** same descriptions as **(a**,**b)** except the system is a plant root. The effective Young's moduli from AtomicJ-Hertz and AtomicJ-DMT are respectively 272 and 270 kPa, while from the trimechanic-3PCS framework, Ê1 = 96.2 in the depth range considered. For this case, the greater difference in comparison of Young's moduli is attributed to the large discrepancy in the determined location for the contact point.

References

1. S. L. Crick and F. C. Yin, *Biomech. Model. Mechanobiol.*, 2007, **6**, 199-210.
2. A. Savitzky and M. J. E. Golay, *Anal. Chem.*, 1964, **36**, 1627-1639.
3. P. Carl and H. Schillers, *Pflugers Archiv.*, 2008, **457**, 551-559.
4. H. Spath, *Cluster dissection and analysis theory, fortran programs, examples*, Ellis Horwood Limited, Chichester, 1985.
5. P. Hermanowicz, M. Sarna, K. Burda and H. Gabrys, *Rev. Sci. Instrum.*, 2014, **85**, 063703.
6. D. Nečas and P. Klapetek, *Cent. Eur. J. Phys.*, 2012, **10**, 181-188.

ANNEX 2

STAR ✦ Protocols

CellPress

Measuring external primary cell wall elasticity of seedling roots using atomic force microscopy

Harinderbir Kaur[1,5], Jean-Marie Teulon[1], Anne-Emmanuelle Foucher[1], Daphna Fenel[1], Shu-wen W. Chen[1,2], Christian Godon[3,5], Thierry Desnos[4,*], and Jean-Luc Pellequer[1,5,6,]**

[1]Univ. Grenoble Alpes, CEA, CNRS, IBS, F-38000 Grenoble, France

[2]Rue Cyprien Jullin, F-38470 Vinay, France

[3]Aix Marseille Université, CNRS, CEA, Institut de Biosciences et Biotechnologies Aix-Marseille, Laboratoire de Signalisation pour l'adaptation des végétaux à leur environnement, CEA Cadarache, F-13115 Saint-Paul lez-Durance, France

[4]Aix Marseille Université, CNRS, CEA, Institut de Biosciences et Biotechnologies Aix-Marseille, Equipe Bioénergies et Microalgues, CEA Cadarache, F-13115 Saint-Paul-lez-Durance, France

[5]Technical contact

[6]Lead contact

*Correspondence: thierry.desnos@cea.fr

**Correspondence: jean-luc.pellequer@ibs.fr

STAR Protocols

CellPress
OPEN ACCESS

Protocol

Measuring external primary cell wall elasticity of seedling roots using atomic force microscopy

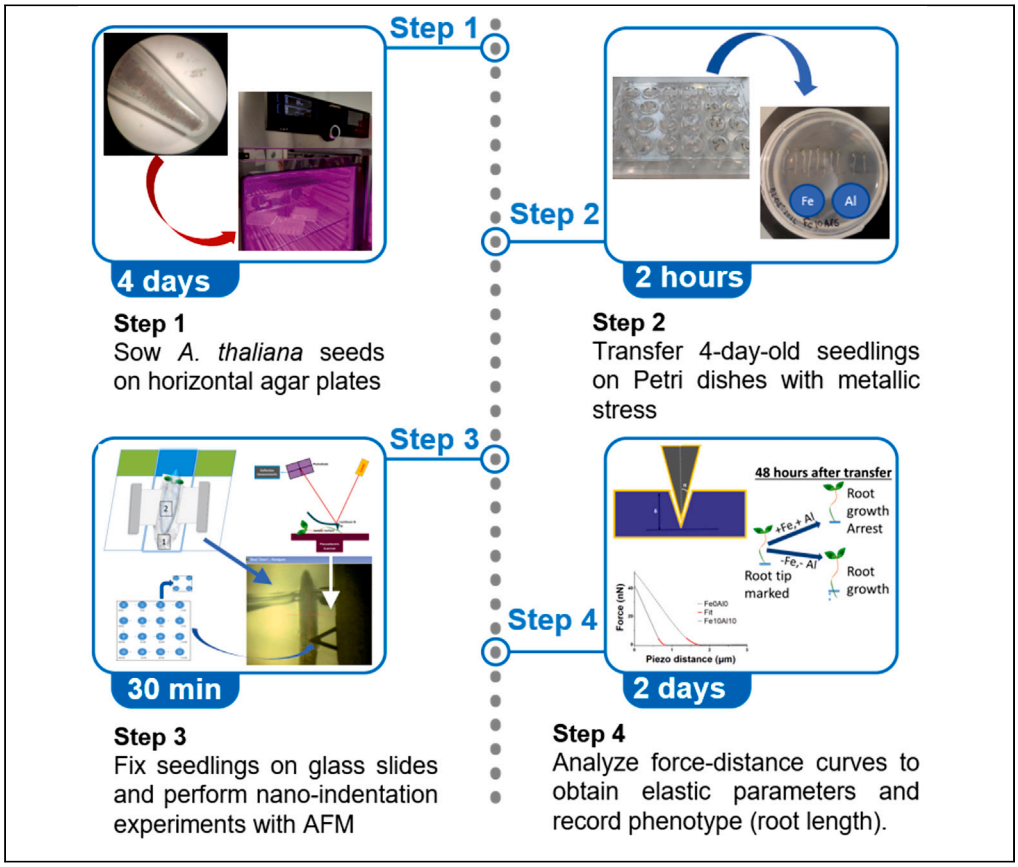

Stiffness plays a central action in plant cell extension. Here, we present a protocol to detect changes in stiffness on the external epidermal cell wall of living plant roots using atomic force microscopy (AFM). We provide generalized instructions for collecting force-distance curves and analysis of stiffness using contact-based mechanical model. With this protocol, and some initial training in AFM, a user is able to perform indentation experiments on 4- and 5-day-old *Arabidopsis thaliana* and determine stiffness properties.

Publisher's note: Undertaking any experimental protocol requires adherence to local institutional guidelines for laboratory safety and ethics.

Harinderbir Kaur, Jean-Marie Teulon, Anne-Emmanuelle Foucher, ..., Christian Godon, Thierry Desnos, Jean-Luc Pellequer

thierry.desnos@cea.fr (T.D.)
jean-luc.pellequer@ibs.fr (J.-L.P.)

Highlights

Growing *Arabidopsis thaliana* in flat crystallization plates

Transferring 4-day-old seedlings into Petri dishes with various Fe and Al metals

Nanoindentation of seedlings in the transition zone with atomic force microscopy

Determining elastic properties of stress roots using the trimechanic theory

Kaur et al., STAR Protocols 4, 102265
June 16, 2023
https://doi.org/10.1016/j.xpro.2023.102265

STAR Protocols

CellPress
OPEN ACCESS

Protocol

Measuring external primary cell wall elasticity of seedling roots using atomic force microscopy

Harinderbir Kaur,[1,5] Jean-Marie Teulon,[1] Anne-Emmanuelle Foucher,[1] Daphna Fenel,[1] Shu-wen W. Chen,[1,2] Christian Godon,[3,5] Thierry Desnos,[4,*] and Jean-Luc Pellequer[1,5,6,*]

[1]Univ. Grenoble Alpes, CEA, CNRS, IBS, 38000 Grenoble, France

[2]Rue Cyprien Jullin, 38470 Vinay, France

[3]Aix Marseille Université, CNRS, CEA, Institut de Biosciences et Biotechnologies Aix-Marseille, CEA Cadarache, 13115 Saint-Paul lez-Durance, France

[4]Aix Marseille Université, CNRS, CEA, Institut de Biosciences et Biotechnologies Aix-Marseille, Equipe Bioénergies et Microalgues, CEA Cadarache, 13115 Saint-Paul-lez-Durance, France

[5]Technical contact

[6]Lead contact

*Correspondence: thierry.desnos@cea.fr (T.D.), jean-luc.pellequer@ibs.fr (J.-L.P.)
https://doi.org/10.1016/j.xpro.2023.102265

SUMMARY

Stiffness plays a central action in plant cell extension. Here, we present a protocol to detect changes in stiffness on the external epidermal cell wall of living plant roots using atomic force microscopy (AFM). We provide generalized instructions for collecting force-distance curves and analysis of stiffness using contact-based mechanical model. With this protocol, and some initial training in AFM, a user is able to perform indentation experiments on 4- and 5-day-old *Arabidopsis thaliana* and determine stiffness properties.

For complete details on the use and execution of this protocol, please refer to Godon et al.[1]

BEFORE YOU BEGIN

Sterilize seeds and prepare agar before sowing. Then, grow seeds on agar plates for 4 days. This protocol requires a rigorous planning to avoid unavailability of any instrument/facility on the measurement day.

Seed sterilization

Timing: 1.5 h

The surface of Arabidopsis seeds must be sterilized before sowing. The seeds harvested in a natural environment tend to have contamination by bacterial or fungi spores. Thus, sterilization and filtering becomes necessary after harvesting to avoid contamination. All these steps are performed in a sterile hood.

1. Pour a small quantity of seeds (an equivalent of around 50 µL or less) in the microfuge tube.
   a. Label the microfuge tube with the name of the seeds and add the date.
   b. Cover the label with Parafilm or tape so that the label does not fade out.
2. Add 1 mL of washing solution (SDS 0.05%, EtOH 70%) using a sterile pipette tip.
3. Close the cap and gently invert the tube upside down for 2–3 min to expose all the seeds to the liquid solution.
4. Remove the liquid from the microfuge tube.

a. Place the pipette tip at the bottom of the tube; push twice in the washing solution gently so that seeds distribute along the sidewall.
b. Carefully pipette out the liquid with the help of the tip and discard; avoid taking out the seeds!

5. Wash the seeds with Ethanol.
   a. Add 1 mL of ethanol (100%).
   b. Gently shake the microfuge tube for 1 min minimum.
   c. Pipette out the ethanol the same way as the step 4b; avoid taking out the seeds!
6. Dry the seeds.
   a. Keep the microfuge tube open for at least 1 h under the laminar flow hood, or until dry.
7. Store the seeds.
   a. Seeds can be kept at 20°C–24°C for short storage, and in 4°C with low hygrometry for long storage.

Note: Moisture content affects the germination capacity of seeds. If not dried enough, the moisture content left can damage the outer seed coat, opening it before germination. Sterile seeds can be stored for up to 3 months. When kept for a longer time, the germination rate decreases with time, seeds do not germinate synchronously, or seeds do not germinate at all.

Agar media preparation

Timing: 1 h

Agar medium requires a sterilization step and thus must be prepared in advance.

8. Pour 4 g of agar powder in a 500 mL glass bottle (8 g/L).
9. Add 2.5 g of sucrose to the bottle (5 g/L).
10. Add 490 mL of deionized water and stir to dissolve the powders.
11. Take the bottle to laminar hood and open a new sealed 10 mL pipette.
12. Add 10 mL of the solution nutritive to the bottle in the sterile laminar flow hood.

Note: Keep the nutrient solution in a sterile environment and at 4°C.

13. Label the bottles with the autoclave tape and autoclave (120°C, 30 min).

Note: Do not forget to autoclave microfuge tubes, pipette tips, and wooden toothpicks. After autoclaving, open all the sterilized materials in the clean laminar hood only. It is better to make small batches of agar bottles instead of big bottles (1 L). Repeated heating of the medium leads to a loss of water and an increase in salt concentration.

Medium and culture plate preparation

Timing: 1.5 h

The seedlings need to be grown for four days before nanoindentation experiments. Steps 14–15 explain how to grow seedlings on horizontally standing crystallization plates, a very critical improvement over the usage of vertically positioned Petri dish.

14. Heating the agar.
    a. Normally agar is in solidified form at room temperature. Slightly unscrew/loosen the lid of the bottle without fully opening it.

Note: Opening the lid in air will make the solution non-sterile. But remember to loosen the cap slightly; if not, bottle will burst during heating. It is important to wear a protective glove and goggles.

b. Place the bottle in the microwave at full power (1450 W).

Note: Timing for heating is proportional to the volume of the solution in the bottle. Take out the bottle after 1–2 min, or when it is partially melted, swirl gently for 2–3 min. It helps to even out the heat and dissolve agar completely. The goal is to melt and not boil the agar. If needed, place it back into the microwave for 30–40 s. Excessive heating can lead to water evaporation, which changes the concentration of nutrients.

Note: Make sure to wear thermo-protective gloves to handle the hot bottle.

15. Preparing a culture plate (perform all steps in laminar flow hood, 30 min).
    a. In a 50 mL polypropylene tube, add 30 mL of melted agar solution and 600 µL of MES buffer solution.
    b. Add 1 µM of $FeCl_2$ (or 3 µL from a 10 mM stock).
    c. Gently invert upside down the polypropylene tube to mix well.
    d. Pour carefully medium solution to the wells up to the brim of the crystallization plate. The number of wells to use depends on the total number of seeds that you need to grow for your daily experiment. Troubleshooting problem 1.
    e. Allow the medium to cool down at room temperature until solidifies.
    f. Spread the seeds onto the agar and align them evenly with a sterile wooden stick. Approximately 10–12 seeds in each well.

Note: If more seeds are poured, they will have less space to grow and reduced amount of nutrients available.

    g. Slightly dip the seeds inside agar so that the seeds have better contact with agar. This helps the roots to grow downwards and straight.
    h. Pour some water in 2 or 3 empty wells of the culture plate to keep high hygrometry for the next 4 days.
    i. Seal the plate with the micro-pore tape. Porous nature of the tape allows aeration and prevents water evaporation outside the plate.
    j. Place the plate in the Peltier-cooled incubator for next 4 days with a day/night cycle of 18/6 h and corresponding temperature of 24°C/21°C.

KEY RESOURCES TABLE

REAGENT or RESOURCE	SOURCE	IDENTIFIER
Biological samples		
Arabidopsis thaliana wild-type seeds	Thierry Desnos (CEA/BIAM)	Col^{er105}
Arabidopsis thaliana mutant seeds	Thierry Desnos (CEA/BIAM)	$almt1^{51\ (*)}$
Chemicals, peptides, and recombinant proteins		
Agar powder	Sigma-Aldrich	Cat# A7921 (BCBZ7284)
Aluminum chloride ($AlCl_3$)	Sigma-Aldrich	Cat# 237051
Ammonium nitrate (NH_4NO_3)	Sigma-Aldrich	Cat# A3795
Boric acid (H_3BO_3)	Sigma-Aldrich	Cat# B6768
Calcium chloride dihydrate ($CaCl_2 \cdot 2H_2O$)	Sigma-Aldrich	Cat# C7902
Cobalt(II) chloride hexahydrate ($CoCl_2 \cdot H_2O$)	Sigma-Aldrich	Cat# C8661
Copper(II) sulfate pentahydrate ($CuSO_4 \cdot 5H_2O$)	Sigma-Aldrich	Cat# C3036
Ethanol absolute	Carlo Erba	Cat# 4145872
Iron chloride ($FeCl_2$)	Sigma-Aldrich	Cat# 44939
Magnesium sulfate heptahydrate ($MgSO_4 \cdot 7H_20$)	Sigma-Aldrich	Cat# M2773
Manganese sulfate monohydrate ($MnSO_4 \cdot H_20$)	Sigma-Aldrich	Cat# M7899

(*Continued on next page*)

Continued

REAGENT or RESOURCE	SOURCE	IDENTIFIER
MES-(2-(N-morpholino)ethanesulfonic acid	Sigma-Aldrich	Cat# M8250
Milli-Q water	Milli-Q	Direct 8
Potassium hydroxide	Sigma-Aldrich	Cat# 221473
Potassium iodide (KI)	Sigma-Aldrich	Cat# 221945
Potassium nitrate (KNO_3)	Sigma-Aldrich	Cat# P8291
Potassium phosphate monobasic (KH_2PO_4)	Sigma-Aldrich	Cat# P5655
Sucrose	Mpbio	Cat# 02 904713-CF
Silicon pressure sensitive adhesive (PSA)	NuSil Technology LLC	MED1-1356
Sodium Dodecyl Sulfate (SDS) solution 0.05%	Sigma-Aldrich	Cat# L4390
Sodium molybdate dehydrate ($Na_2MoO_4 \cdot 2H_2O$)	Sigma-Aldrich	Cat# M1651
Zinc sulfate heptahydrate ($ZnSO_4 \cdot 7H_20$)	Sigma-Aldrich	Cat# Z1001
Software and algorithms		
AtomicJ, version 2.0	Hermanowicz et al.[2]	https://sourceforge.net/projects/jrobust/
ImageJ, version 1.51j8	Schneider et al.[3]	https://imagej.nih.gov/ij/
NeuronJ_.jar 1.4.3 (with imagescience.jar 3.0.0)	Meijering et al.[4]	https://imagescience.org/meijering/software/neuronj/
Prism, v5 or v8	GraphPad	https://www.graphpad.com/
Other		
AFM cantilevers	Nanoworld AG	PNP-TR-50
AFM Dimension 3100	Bruker	D3100
AFM Nanowizard IV	JPK	NW4
AFM probe holder	Bruker	DTFML-DD
Binocular	Nikon	SMZ800N (C-PS stand)
Cover slips (glass 24 × 40 mm)	Agar Scientific	Cat# AGL462440-1
Crystallization plate VDX	Hampton Research	Cat # HR3-140
Glass bottle (500 mL)	Duran, Dutscher	Cat # 818014407
Glass slide StarFrost 3 × 1 in	Knittel Glass	Cat# VS1137#1FKB.01
Horticole Indoor Led, 45 W, 169 LEDs, 276 × 276 × 14 mm, full spectrum	www.cultureindoor.com	Cat# 003-300-370
Laminar flow hood FlowFAST	Faster Air	H 09 SA7010
Microfuge tubes 1.5 mL	Eppendorf	Cat# 0030.120.086
Micro tape Anapore 9.14 m × 1.25 cm	Euromedis	Cat# 135312
Microwave 900W	Severin	mw7825
Peltier-cooled incubator	Memmert	IPP110+
Petri dish 60 × 15 mm	Falcon	Cat# 353004
Pipette motor Ergo one FAST	Starlab	Cat# S7166-0010
Pipette tips 20 µL	TipOne	Cat# S1110-3700
Pipette tips 200 µL	TipOne	Cat# S1111-0700
Pipette tips 1000 µL	TipOne	Cat# S1111-6701
Pipette P20L	Gilson	Cat# FA10003M
Pipette P200L	Gilson	Cat# FA10005M
Pipette P1000L	Gilson	Cat# FA10006M
Polypropylene centrifuge tubes 50 mL	Falcon, Greiner Bio-One	Cat# 227261
Programmable timer	Otio	93022
Screw thread vials, amber, 12 × 32 mm	Thermo Scientific	Cat# C4013-2
Septa TEF/SIL 8 mm	Thermo Scientific	Cat# C4013-60
Shimadzu 8-425 caps	Thermo Scientific	Cat# C4013-3A
Syringe filter 0.22 µm, 33 mm	Millipore Millex-GV	Cat# SLGV033RB
Syringe needle 0.8 × 40 mm	Terumo Neolus	Cat# NN-2138R
Thermal gloves	VersaTouch	
Tweezer Style SM104 4.7″	Techni-Tool	Cat# 758TW401
Wooden toothpick sticks	N/A	N/A

(*) almt1[51]: mutation G881A that results in a defective splicing of intron 3.

MATERIALS AND EQUIPMENT

⚠ CRITICAL: When handling the reagents wearing of lab coat, gloves and goggles is advised. Follow the waste disposal rules as per your institute and country's safety guidelines. Reagents should be stored and prepared according to the manufacturer's recommendation. Refer to the appropriate material's safety data sheet.

Preparation of individual stock solutions of each nutrient

- 1 M $MgSO_4 \cdot 7H_2O$ (246.5 g in 1 L milliQ H_20).
- 1 M NH_4NO_3 (80 g in 1 L milliQ H_20).
- 1 M KNO_3 (101.1 g in 1 L milliQ H_20).
- 1 M $CaCl_2 \cdot 2H_2O$ (147 g in 1 L milliQ H_20).
- 10 mM KI (166 mg in 100 mL milliQ H_20).
- 100 mM H_3BO_3 (618 mg in 100 mL milliQ H_20).
- 1 M $MnSO_4 \cdot H_2O$ (6.76 g in 40 mL milliQ H_20).
- 1 M $ZnSO_4 \cdot 7H_2O$ (28.7 g in 100 mL milliQ H_20).
- 25 g/L $Na_2MoO_4 \cdot 2H_2O$ (1.25g in 50 mL milliQ H_20).
- 2.5 g/L $CuSO_4 \cdot 5H_2O$ (125 mg in 50 mL milliQ H_20).
- 2.5 g/L $CoCl_2 \cdot 6H_2O$ (125 mg in 50 mL milliQ H_20).

Filtrate all solutions (0.2 μm) and store at 4°C for months or years unless contaminated.

Composition of the 50× nutrient solution stock (1 L):

Reagent	Final concentration	Amount
$MgSO_4 \cdot 7H_2O$	23.4 mM	23.4 mL
NH_4NO_3	103 mM	103 mL
KNO_3	94.5 mM	94.5 mL
$CaCl_2 \cdot 2H_2O$	33.5 mM	33.5 mL
KI	25 μM	2.5 mL
H_3BO_3	39.3 mM	39.3 mL
$MnSO_4 \cdot H_2O$	523 μM	523 μL
$ZnSO_4 \cdot 7H_2O$	251 μM	251 μL
$Na_2MoO_4 \cdot 2H_2O$	52 μM	400 μL
$CuSO_4 \cdot 5H_2O$	7.3 μM	728 μL
$CoCl_2 \cdot 6H_2O$	5.26 μM	500 μL
milliQ H_2O	N/A	701.398 mL
Total	**N/A**	**1 L**

Filtrate (0.2 μm) and store it at 4°C for several months.

Growth solution

Reagent	Final concentration	Amount
50× nutrient solution	N/A	20 mL
Sucrose	5 g/L	5 g
milliQ H_20	N/A	960 mL
Total	**N/A**	**980 mL**

Autoclave this solution and keep it in sterile condition, at 20°C–24°C for 6 months. During the protocol, starting at step 3 below, take 980 μL of the growth solution and add 20 μL of MES solution (3.4 mM final concentration); this is the final composition of the "growth solution" which must be used only one day.

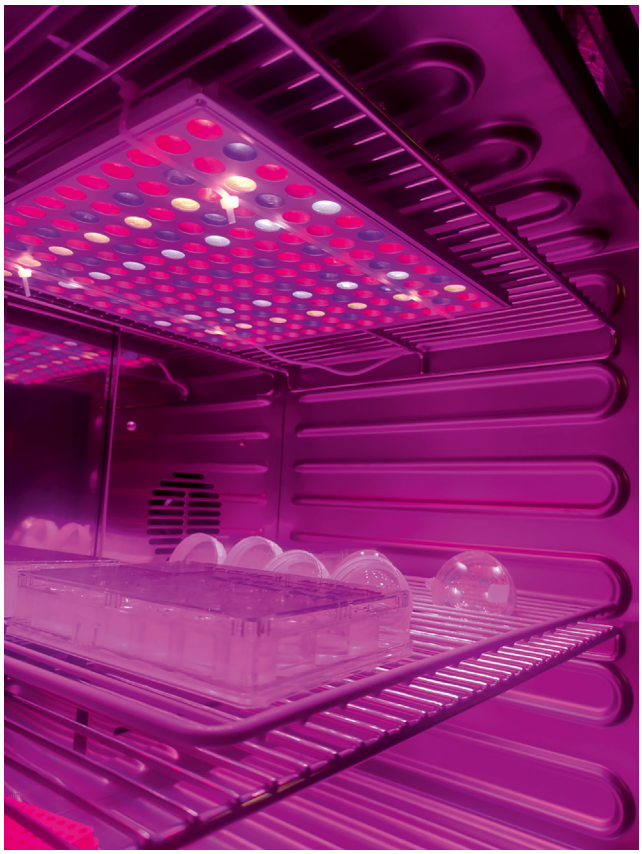

Figure 1. Peltier cooled incubator to grow *Arabidopsis thaliana* seedlings

Light is provided by an added LED box covering the "full spectrum" of light and made of 196 LEDS: 98 at 630 nm, 42 at 470 nm, 28 at 660 nm, 14 white at 3000 K, and 14 white at 6500 K. A day/night program on the incubator requires the development of a short running sequence of events using a Memmert proprietary software (AtmoCONTROL 2.9.2.0 29/01/2019, provided by Memmert). A caveat is found on the IPP+ 110 when activating the program, it automatically starts at the beginning of the programed cycle (likely the next morning). It implies that the program must be activated 24 h before use.

Other individual stock solutions:

- 500 µM phosphate solution KH_2PO_4 (1 M stock = 13.61 g in 100 mL milliQ H_20).
- 10 µM $FeCl_2$ solution (10 mM stock = 0.12 g in 100 mL milliQ H_20).
- 10 µM $AlCl_3$ solution (10 mM stock = 0.13 g in 100 mL milliQ H_20). This stock solution should be prepared with caution in a fume hood (use gloves and safety glasses) as the addition of water to the $AlCl_3$ powder releases vapors of hydrochloric acid. Furthermore, this solution must be prepared in a glass beaker as the dissolution of $AlCl_3$ is exothermic. Slowly add the water onto the powder and swirl the beaker until the complete dissolution of the powder (few minutes). Do not autoclave this solution.
- MES Buffer (pH 5.7) (170 mM stock solution = 3.62 g in 100 mL H_20); adjust the pH with 10 N KOH.

Filtrate all solutions (0.2 µm) except $AlCl_3$, store all solutions at 4°C.

- Peltier-cooled incubator.

The incubator Memmert IPP+ 110 controls the temperature of a chamber. There is a sidewall opening to accommodate the power cords of the artificial LED box made of a mixture of red, blue, and white color (Figure 1). Both the chamber and LED lights run on a programmable timer with the light being on for 16 h during the day at a controlled temperature of 24°C and 8 h at night without light at 21°C.

Alternatives: Any growth chamber or light box system can be used for growing *Arabidopsis thaliana* seeds. We have also used natural light, but to maintain homogeneity it is safer to use a reproducible system. Light boxes with LEDs are cheap and easy to find. We have noticed that some LED light boxes do produce a significant heating so by adjusting their height above the growing plates, one can simulate a change in temperature when the light is on (vs off). However, when the light is off, the room temperature should be constant and slightly cooler.

- Pressure sensitive silicon adhesive (NuSil).

NuSil is a pressure sensitive adhesive (PSA) that has a property to stretch while polymerizing. It has a composition of 50% of silicone and 50% of ethyl acetate. NuSil has a low viscosity (245 mPa s), which makes it possible to pipet. Ethyl acetate evaporates with time leaving behind only silicone that gets polymerized with time. Troubleshooting problem 2.

⚠ CRITICAL: We prefer NuSil over other adhesives because it has a particular characteristic of stretching while drying, which was not reproduced with some other PSAs. For the nano-mechanical experiment, it is crucial that the end of the root tip is appropriately fixed on the glass slide since measurements are performed about 500 μm from the root tip. Because of the root capping, the macroscopic rigidity of the root tip was the major source of trouble in the attachment of root tips on glass slides.

Alternatives: The NuSil used in our work is difficult to obtain because of logistical issues with the supplier that hardly delivers small bottles. However, there are alternative PSA available, and we experimented with Silicolease PSA 408/toluene (cat #117149, Elkem, France). Nonetheless, we chose not to pursue it due to its higher viscosity (from 40,000–120,000 mPa·s compared to 245 mPa·s for NuSil) and a compatible tack around 20 kPa (Avantor Sciences).

- Atomic Force Microscopy (AFM) set-up.

Indentation experiments are performed in liquid medium with a Bruker Dimension 3100 AFM. The DTFML-DD probe holder holds triangular Pyrex nitride cantilevers (PNP). The PNP tip has a square pyramidal symmetry, a low sharpness (~10 nm nominal radius), a half-opening angle of 35°, which was verified by SEM measurements, and a proper spring constant for plant root tissues (nominally 0.08 N/m). The total mass of such a cantilever is about 130 ng, a very negligible mass compared to a single seedling root (~0.5 mg). AFM runs with a Nanoscope V controller and the Nanoscope 7.3 software using the picoforce module. Indentation of plant root surface was performed with approach-retract curves using a ramp size of 3–4 μm, a scan rate of 0.5 Hz, and 4096 points per curve. Ramp size was adjusted using its z-start position so that an indentation of about 0.5 μm was achieved.

Alternatives: Other AFM instruments can also be used for these experiments on the condition that they have a large enough stage for glass slides. Most modern bio-AFM complies with this specificity.

STEP-BY-STEP METHOD DETAILS

Culture plate preparation for the transfer of seedlings

Timing: 0.5 h

To stress seedlings with various abiotic metals, seedlings need to be transferred from their original growing conditions to the stress conditions. These Petri dishes are prepared on the day of the experiment.

1. Prepare small Petri dishes (60 × 15 mm style). Troubleshooting problem 3.

a. Label the bottom of the Petri dish with the stress condition; also include the plating date.
b. Warm-up the agar bottle, as described in step 14 (before you begin). Make sure the agar is liquid enough.
c. Mix 15 mL of agar and 300 µL of MES buffer in a polypropylene tube.
d. If Al stress of 5 µM is needed, then add 7.5 µL of $AlCl_3$ in the polypropylene tube.
e. If Fe stress of 10 µM is needed, then add 15 µL of $FeCl_2$ in the polypropylene tube.
f. Homogenize the polypropylene tube and deposit the mix in the Petri dish.

Note: Always keep the small Petri dishes in the incubator throughout the whole experiment. Seedlings are systematically transferred to a Petri dish for 2 h, even in the absence of metallic stress. Troubleshooting problem 4.

Nanomechanical experiments

Timing: 2 days

Nanoindentation experiments are performed with an AFM using a square-pyramidal tip. Living seedling roots are fixed on glass slides. Steps 2 to 8 describe all the procedures from cantilever attachments to force-distance curve collection. Several steps require the supervision of an AFM expert due to some fragile components of AFM (cantilevers or piezo scanners). Although the procedures are generic, details may vary from one AFM to another.

2. Attach cantilever to the AFM scanner (2 min).
   a. Using the binocular and dedicated tweezer , gently lift the cantilever and place it straight into the groove of the liquid cell holder. Troubleshooting problem 5.
   b. Attach the liquid cell holder to the piezo scanner.

   Note: In case of the Dimension 3100, lift the piezo significantly upward (away from the sample). Make sure that the scanner is far from the sample stage so that the tip will not hit the root surface and break.

3. Calibrate the AFM system (60 min).
   a. Perform calibration in air.
      i. Adjust the laser beam on the cantilever while preserving the highest sum.
      ii. Perform a contact-based force-distance curve (ramp size of 3 µm, frequency of 0.5 Hz, 4096 points per curve).
      iii. Determine the deflection sensitivity by measuring the slope of the curve in contact with the surface.
      iv. Repeat the previous step several times until sensitivity values are constant.
      v. Perform a thermal tuning to determine the spring constant of the cantilever.
      vi. Save the computed spring constant and repeat the previous step until the spring constant values are uniform.
   b. Perform calibration in liquid.
      i. Repeat previous step 3.a but in liquid environment.

   Note: For the Dimension 3100, only the deflection sensitivity can be performed in liquids.

      ii. Wait for half an hour after adding the growth solution to thermally stabilize the AFM cantilever.
      iii. Set the sensitivity values obtained in liquid as final values.
      iv. If the AFM system can perform thermal tuning with frequencies below 1 kHz, then also perform the thermal tune in liquid, otherwise, keep the spring constant obtained during the previous calibration in air.

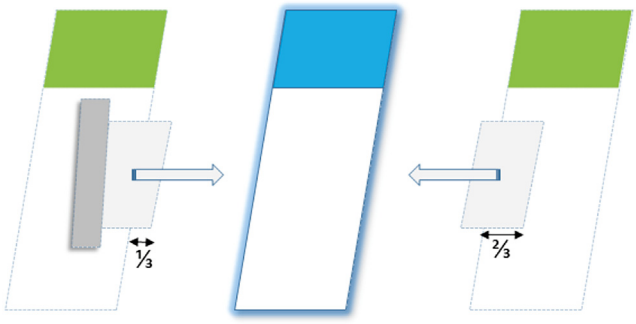

Figure 2. Assembling the glass slides to mount plant seedlings for nanoindentation analysis with AFM
Cover slips glued to the green Starfrost glass slides are colored in light gray. A small piece of micropore tape (dark gray) is used to fix the cover slips (for clarity on the left side is shown, but both sides should be fixed in the same way).

4. Fixing a plant root on a glass slide (5 min).
   a. Glass slide set up (2 min for the set-up and 1.5 min for sealing).
      i. Take two standard glass slides plus two rectangular cover slips and assemble them as shown in Figure 2.
      ii. Take a micropore tape and place it over the cover slip to bind to the glass slide.

Note: Make sure that both cover slips are at the same height in the middle of the slide and that 2/3rd of the width is touching the slide and 1/3rd of it stays outside.

      iii. Take a third glass slide and place it in the middle of the other two glass slides such that a little rectangular space is left in between (Figure 3).
      iv. At one end of the glass slide deposit a drop of silicone adhesive (approx. 100–150 μL).

⚠ CRITICAL: Never store NuSil in any clear plastic container like Eppendorf or Falcon tubes. Always store it in dark glass bottle, due to the presence of ethyl acetate solvent.

      v. After depositing NuSil on the glass slide, spread it with the help of another cover slip (Figure 3) dragging upwards to the other end. When we spread a drop of NuSil on the glass slide, it has the thickness of the cover slip and is evenly distributed.

⚠ CRITICAL: A constant thickness of glue is important for reducing the height fluctuation of deposited plant. Do not add more than two drops of NuSil. More amount will lead to longer polymerization time.

      vi. After spreading NuSil, wait for 20–25 s, so that the adhesive starts polymerizing, yet it is still wet for the sealing purpose.

Note: The goal is to place the root onto the adhesive when it is semi-solid so that it stays on the surface and does not dip into the adhesive. It might be tempting to place the plant sooner. Sometimes the plant can dip inside the NuSil and can affect its living state, in particular due the presence of un-evaporated ethyl acetate.

      vii. Take one seedling from the Petri dish and, using a dedicated tweezer (NuSil is a glue and it is difficult to fully remove from the tweezer. Thus, a dedicated tweezer should be used to NuSil threads sealing); gently lift it from the shoot area preferably under the cotyledon without pinching the seedling.

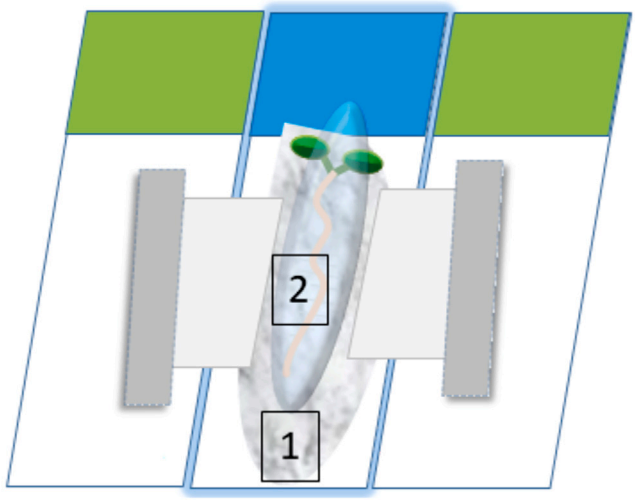

Figure 3. Principle of mounting plant seedlings on glass slides

The goal of this setup is to deposit a uniform layer of NuSil glue on the middle glass slide. The adhesive layer shown in light gray and labeled with the number 1. A long primary root in orange and two green cotyledons schematizes the seedling. The seedling is finally covered with a growth medium shown in light transparent blue color and labeled with the number 2. Cover slips are in light gray whereas micropore tapes are in dark gray.

⚠ CRITICAL: if not lifted properly, this might lead to breakage of the plant into two pieces. In case of longer roots, it might be stuck inside the agar gel and extra caution is required to extract the seedling from the agar. Always lift from the cotyledon part because that area has the center of mass. This way the root can balance itself during the transfer from the Petri dish to the glass slide.

b. Depositing a seedling on the glass slide.
   i. Place the plant on the slide such that the root tip is placed first, followed by the shoot part.[5,6] Troubleshooting problem 6.
   ii. Lay down the root straight to enable the indentation in the transition zone. In case the root is bent around the transition zone it is difficult to perform indentation around that area. Troubleshooting problem 7.
   iii. Fastening the seedling root by sealing it with the semi-solid adhesive present on the glass slide, starting from the top, then the middle and the very end (root tip) to prevent any movement of the root (Figure 4). Troubleshooting problem 8.

⚠ CRITICAL: Seal only 50–100 μm of the root tip area. It preserves the transition zone from any presence of glue.

   iv. Immediately cover entirely the plant root (at least 100 μL) with growth solution (square #2, Figure 3) to prevent drying during measurement. Make sure to cover the root tip first as it is the most sensitive part of the plant. The system is ready for measurements (Figure 4).

⚠ CRITICAL: Do not use water to cover the root, as it will generate an osmotic imbalance that causes excess water to enter into the cell, which in turn either break or escape from the fastening NuSil bands.

5. Nano-Indentation on the living root tissues (max 25 min).

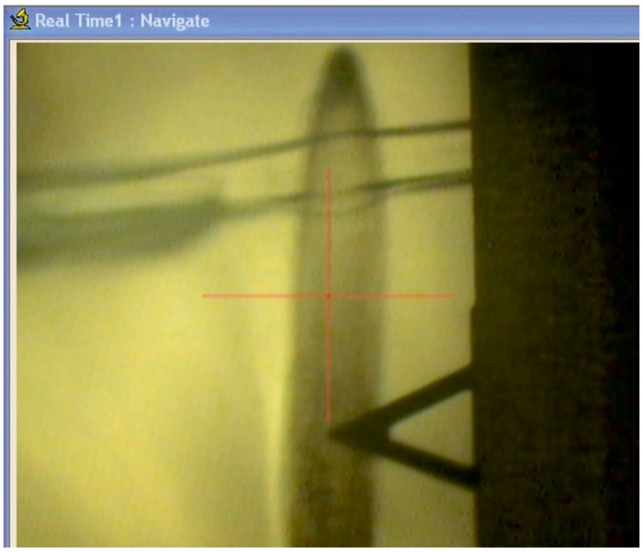

Figure 4. Picture showing how the root should be laid down for AFM measurements

The sealing with NuSil should be very thin so that cantilever support is not touching the sealing bands. After sealing carefully, place the middle glass slide of Figure 3 under the piezo scanner. At this point, we need to rotate the glass slide manually so that the root tip is positioned under the cantilever as seen through the camera.

⚠ CRITICAL: Although the seedling is alive, the horizontal position is not its favorite. Consequently, the experiment should be performed as quickly as possible. A time longer than 30 min gave us unpredictable results as global stress may occur within the root.

a. Before positioning the plant root under the AFM cantilever, retract the piezo to a safe distance between the cantilever and the plant root.
b. Lift the scanner head carefully and insert the glass slide with the plant. Buffer is already on the top of the root, thus carefully lower the scanner head so that the cantilever will not bend upon contact with water (adding a drop of buffer on the cantilever is usually necessary to have a smooth insertion in liquid).
c. Orient the glass slide, so that the root orientation is close to vertical and its tip is on the top of the camera (Figure 4).
d. The target working area is located approximately 500 μm away from the root tip. This distance can be estimated knowing the length of the PNP cantilever (about 200 μm). Use the stage positioning controls to move the cantilever on the right zone.

⚠ CRITICAL: Difficulty in using PNP cantilever: because the seedling root is pseudo-cylindrical and the PNP tip height rather small (<3.5 μm), it is not advised to probe the root beyond the longitudinal median line of the root. Note that there is a small setback of the tip of PNP cantilever (4 μm), see Figure 5.

e. Focus the camera so that the root surface is clearly visible.
f. Wait for a few minutes for the laser to stabilize.
g. Center laser spot at (0,0) position. Keep deflection set point to 2.5 V.
h. Make a new folder for each node and mention its co-ordinate in the filename.
i. Lower the piezo down manually until the root is clearly visible, then start engaging.
j. When the surface is detected, then run continuous force-distance (FD) curves to adjust the ramp parameters. With the Dimension 3100, we have to modify the z-ramp start so that our 3 μm-long ramp could be performed correctly. With our open-loop scanner, we did not use a trigger force threshold, and consequently, the ramp must be manually adjusted prior a full record.
k. With appropriate FD curves, start collecting and recording curves.

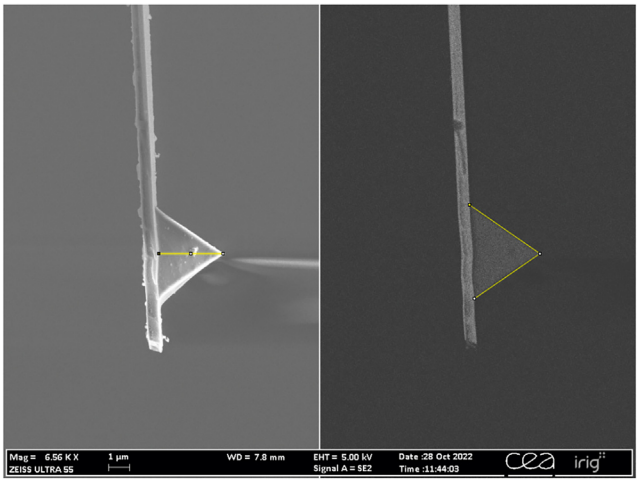

Figure 5. Scanning electron microscopy image of a PNP-TR cantilever used in the AFM experiment

A secondary electron image is on the left and a backscattered electron image is on the right. Tip height and opening angle are highlighted in yellow and were measured using ImageJ: 3.05 µm in height (left) and an opening angle of 69.27°. The manufacturer's data indicates a tip height of 3.5 µm and a half-opening angle of 35°. Image is magnified 6560× under a tension of 5 kV and a working distance of 7.8 mm.

l. Because of the limited time (before plant roots display additional stress), we can only probe a limited number of areas. Our best protocol contains 16 physically different areas (called nodes) and each node is composed of a matrix of 2 × 2 FD curves, using the autoramp tool with 50 nm of distance between each point (Figure 6).

m. Withdraw the cantilever every time after the recording of the curves and engage again after changing the piezo offset co-ordinates. Troubleshooting problem 9.

Alternatives: Modern AFM instruments use force-volume mode that allows the collection of a matrix of nodes with a single FD curve per node. The analysis of data will thus be slightly different as in our protocol (see the quantification and statistical analysis section below).

n. After completion of all 16 nodes, for the record, take a screen shot of the plant root under the cantilever.

o. Move the piezo upward to a safe distance and discard the glass slide.

p. Repeat from step 4 for additional seedlings.

q. At the end of the day, remove the cantilever holder by lifting the piezo scanner gently.

r. On a bench, clean the tip by pouring 100 µL of propanol over. Repeat twice.

s. Remove extra propanol with the help of filter paper placed on the edge of the holder.

t. Add 100 µL ethanol for further cleaning.

u. We can keep the probe inside the holder for future experiments. Always recalibrate before experiment.

6. Prepare plant roots for checking their growth status (10 min).
   a. With the remaining roots, not taken for the indentation experiment, transferred them to the Petri dishes containing stressed medium or control medium, try to align them properly and mark the position of the root tip with a pen. Troubleshooting problem 10.
   b. Use the binoculars to mark the root end for next-day visual assessment.
   c. Observe phenotype (root extension) after 24 h and take a photograph.
7. Root length measurement (2 days after the initial experiment).
   a. Measure the root length 48 h after the transfer to have a clear distinction in the root extension phenotype.

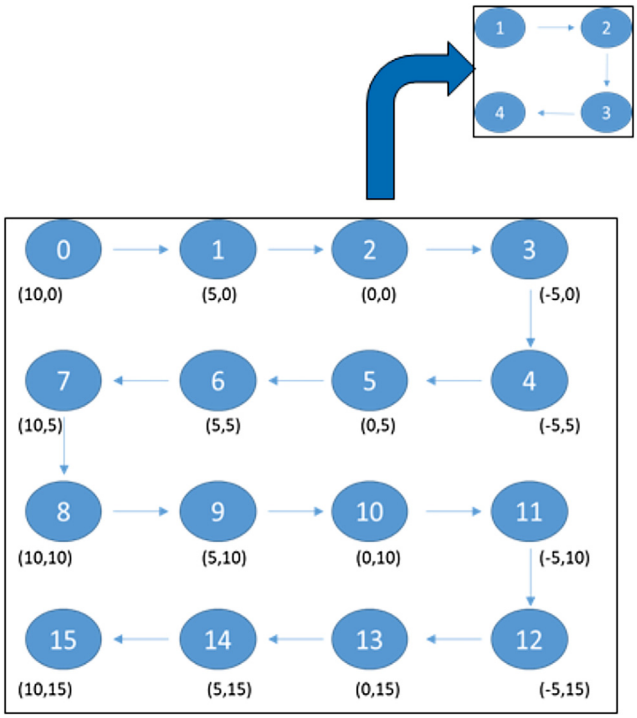

Figure 6. Pictorial version of the matrix strategy used to collect force-distance curves

The measurement starts at position 0 and proceed according to blue arrows. Offsets of the piezo scanner at each node of the matrix are indicated below (values in µm). At each node, a submatrix of 2 × 2 FD curves are recorded. Do not forget to update filenames at each node in order to keep track of the matrix (it helps during the data analysis).

Alternatives: Classically, we measure the root length contiguously to AFM measurements. It is also possible to dedicate a specific experiment (excluding AFM) purely for root length measurements.

b. Take pictures of the whole roots under stressed and non-stressed conditions. Do not forget to add a ruler in the field of view to calibrate the length measurement with ImageJ.
c. Export these pictures to imageJ where they can be opened with the NeuronJ plugin. The NeuronJ plugin allows you to trace the root paths with the computer mouse. The default standard length unit is in pixels.

Note: NeuronJ requires an 8-bit gray scale image in a GIF format, so use ImageJ to transform your picture prior to opening it with NeuronJ.

d. If NeuronJ is not installed yet, please follow the steps e-f first, otherwise jump to step g.
e. Install NeuronJ from https://imagescience.org/meijering/software/neuronj/. Download both jar files: NeuronJ_.jar (version 1.4.3) and imagescience.jar (version 3.0.0).
f. Move the two .jar files into the plugins directory of ImageJ software installed on your computer (see the installation manual of ImageJ for your specific computer system).
g. Open a gif image of your plant root.
h. Add a tracing by selecting the leftmost menu of NeuronJ in Figure 7. First, click at one end of a root and wait a few seconds until the plugin sets up (do not click again).
i. After 2–3 s, move the mouse following the root shape and the plugin should automatically track the root feature.

Figure 7. Partial menu of the NeuronJ plugin

Click on the icon to add (1st left) or to remove (2nd left) a tracing. To remove a tracing, it must be finalized, i.e., ended by a double click. To measure tracing data click on the last-right icon.

Note: Sometimes the plugin loses track of the root, then just click on the last pixel of the root where the tracking was lost. It concatenates a new tracking segment from that click and proceeds like before. You can click as many times as needed to follow perfectly the root.

j. When you reach the end of the root, then double-click to exit the tracking.
k. Click on the measure-tracing icon to display the results (Figure 7).

Note: You can perform the entire tracing of all roots first and, only at the end, select the measurement. Then, you can export all the data using the plugin menu. It provides the global average length of all roots and displays their individual values. It is then possible to save this data as text files.

l. Save the results of NeuronJ in text file or spread sheet format. Also, save the labeled path in PNG format, for the record.
m. Reopen ImageJ with the original image that contains the ruler and calibrate (set scale) the pixel length of your image. Report the conversion factor to your spreadsheet result to convert NeuronJ pixel size into mm.
n. Use any graphical software to plot histograms or boxplots of the root lengths, we used Prism 5.

8. Data analysis (15 min per plant).

The reproducibility of the experimental protocol is of prime interest. In particular, measurements of stress and non-stress plant roots must be performed in the same manner because there is a link between the elastic constant and the experimental indentation depth. Therefore, we tried to keep everything as constant as possible to perform our nanoindentation experiments. In our protocol, we used the contact-based mechanical model of Sneddon[7] and a novel extension known as the trimechanic theory[8] to determine the elastic property of the external cell wall. This model allows us to extract the effective Young's modulus by fitting the force-indentation curve, after correcting the FD curve.[9] The relationship between the force (F) and the indentation (Z) is described by:

$$F = \hat{E}\frac{\tan\alpha}{\sqrt{2}}Z^2$$

where $\hat{E}$ is the effective Young's modulus ($\hat{E} = E/(1-\eta^2)$) and E the Young's modulus with η the Poisson's ratio, and α the half-opening angle of the squared pyramidal tip (35° for PNP tips). Sample FD curves of stressed and non-stressed plant roots are shown in Figure 8. The trimechanic theory is used to fit the indentation curves in multiple depth zones and to extract the effective Young's modulus as well as the corresponding stiffness.[8]

Alternatives: AtomicJ, an open source package,[2] was also used in our study, and several methods can also be used to obtain the Young's modulus values *e.g.*, manufacturer software (Bruker, JPK, …).[2] A graphical interface for calculating the Young's modulus is available with the Force V1.1.0 program.[10] Details of the computation steps of FD curve analysis are described by Domke & Radmacher.[11] It is possible to linearize the force-indentation curve and then fitting with a simple linear regression[9]; this process can be obtained with basic programing skills in Matlab (or equivalent) or simply with Excel spreadsheets. A recent review on determining elastic properties of biological object has been recently released.[12] One of the

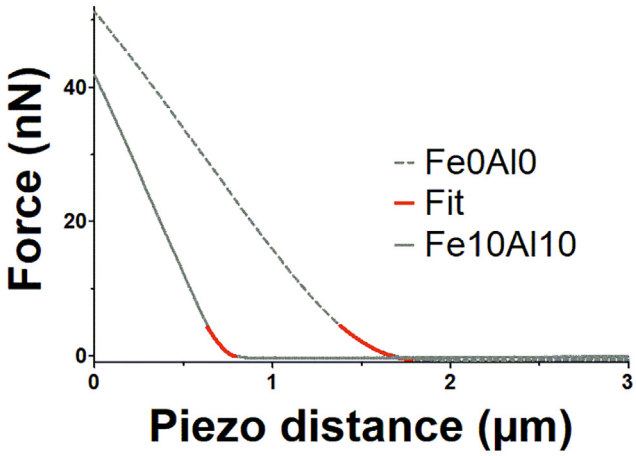

Figure 8. Sample of force-distance curves and their fitting using AtomicJ software

Approach curves are in gray with a plain line for the stress condition (10 µM $FeCl_2$ + 10 µM $AlCl_3$) and with a dashed line for the control condition (no metals). The fitting was capped to 5 nN and is highlighted by a red line. From the stress-condition fit (plain line), the Young's modulus value is 506 kPa whereas it is 60 kPa for the control condition (dashed lines).

main differences between all these alternative fitting methods is the strategy to obtain the contact point, which influence greatly the numerical values of *E*. Nevertheless, when comparing measurements between control and a stress condition, it is reasonable to choose any model, on the condition of always using it the same way for all FD curves.

Filtering and collecting fitting data from FD curves are described in the quantification and statistical analysis section. In the end, our protocol provides a single average value (Elasticity, Stiffness, Depth, …) per plant as provided by the trimechanic theory.[8] The protocol is applied with the same experimental conditions on three or four plants per day, usually four times, providing a total of about 10–15 plants per condition. Once all the experimental conditions are tested, a boxplot is produced and statistical tests can be applied. A sample of a box-and-whiskers plot drawn with Prism v5 is shown in Figure 9.

EXPECTED OUTCOMES

AFM and nanoindentation have the power to quantify variation in the mechanical response of biological tissues such as plant roots in this protocol. Changes in mechanical response can be a consequence of internal stress (oxidative damages) or external abiotic stress (metal toxicity).

The current protocol allows the measuring of about eight plant roots per day. However, it requires a precise organization to avoid waiting for a full 2 h at each specific stress. Note that a 2-h transfer step is always included even in the absence of stress condition (control conditions). The protocol is designed for plant roots but could be easily adapted to other plant organs such as hypocotyls, meristems, or leaves. This protocol could also be adapted for measuring putative change in stiffness connected with the gravitropism effect on plant roots. We have already noticed a correlation between root bending and increased stiffness during our measurements (unpublished data).

The current protocol leads to the measurement of force-distance curves that are translated into force-indentation curves using a contact-based mechanical model. Here we used the model of Sneddon[7] as well as a very recent extension called the trimechanic theory.[8] The force-distance curves allow us to extract effective elastic constants (effective Young's modulus). Only the trimechanic theory allows us to obtain the effective elastic constants, stiffness, and associated deformability. In addition, the trimechanic theory analyzes the global stiffness response of the root along the indentation depth.[8] This protocol was used to determine the stiffness of plant roots during an abiotic stress caused by the additional presence

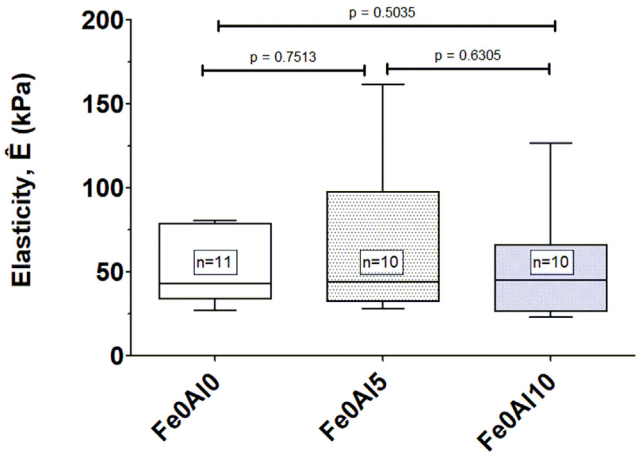

Figure 9. Box-and-whiskers plot of elastic properties of WT seedling roots in absence or presence of aluminum stress

Elasticity is represented by the effective Young's modulus (Ê) in kPa units. Fe0Al0 indicates the nutrient solution without Fe and without Al. Fe0Al5 indicates the nutrient solution without Fe and with 5 μM of Al. Each box edge represents the first and third quartiles around the median. The whiskers represent the min and max values for each group. The label inserted within a box indicates the total number of measured plants. Exact p-values are obtained according to the Mann-Whitney non-parametric t-test. Results indicate that there are no significant differences in the elasticity of seedling roots grown in absence or in presence of 5 or 10 μM Al.

of Fe and/or Al metal (in preparation). The protocol could be adapted to any kind of metallic stress or complex stresses allying metals, chelator, or pH changes that can be translated into a chemical change, which in turn can be added to the agar composition in a Petri dish.

Indentation on living plants has clear advantages over isolated cells. In particular, it has been demonstrated that fixed root on glass slides remained alive for the duration of an AFM experiment.[13] The living status of roots has been tested during this present protocol and neither the fixation system with NuSil nor the horizontally positioned seedlings prevent roots from growing. We have shown that roots continue to grow at least 2 h in such a position. Nevertheless, although root growth is a macroscopic sign of living tissue, it is not a clear indication of the lack of putative stress within the root.

In our protocol, a square pyramidal tip is used to determine the stiffness of plant root surfaces. The protocol could be adapted to any kind of tip shape including paraboloid or spherical tips as well as other types of indentation systems.[14] In addition, the same protocol has been used for a preliminary test of rheology on *Arabidopsis thaliana* roots (unpublished data). Moreover, this methodology is also applicable to decellularized plants. A preliminary decellularization experiment has been tested and suggests that the following protocol can also be applied on decellularized plant roots.

QUANTIFICATION AND STATISTICAL ANALYSIS

In this protocol, we adopted a hierarchical approach for analyzing experimental data. With the final version of the protocol, 16 data points (nodes) are collected on each single plant. At each data node, redundant data is collected using a 2 × 2 matrix (4 FD curves). We test the homogeneity of data by evaluating the extracted elastic properties from all these four curves. If any value is not within 2 sigma from the mean, then the corresponding FD curve is removed. If more than two FD curves are removed in a node, then the node is removed. If half of the nodes of a plant are removed, then the whole plant data is discarded. A distribution histogram of effective Young's modulus values obtained at each node of all plants revealed, most of the time, a log-normal distribution. This is not particularly rare in biology.[15] Consequently, we decided to compute the geometric mean of all nodes of a plant and provide this value as the final result of this single plant. A quick survey of other averaging methods did not change the overall conclusions of the work.

Finally, but not less important, is the use of an appropriate statistical test (we used non-parametric Mann-Whitney) and a low threshold for the p-value calculation ($\alpha = 0.01$). The threshold is not yet classical in biology, but not rare[16] and in our opinion, it should become a standard due to the inherent variability of biological materials. Equally important is to provide the exact p-value in the manuscripts so that the reader may also perform their own interpretation of the significance of presented data. The critical assumption of t-tests is that data used in the statistical test are obtained from a random sampling, in other words, that these data are independent. This is a very sensitive issue since "true" independent experiments are unreachable under practical laboratory constraints (money, time, instrument availability,…). Thus, it is critical to identify what a reasonable independent experiment is. In our case, we decided that a single experiment was the characterization of a single plant. Consequently, the data used in the statistical tests are average values of elastic properties obtained on several single plants. In practice, we performed experiments on different days with a certain number of plants: usually our results cover at least 4 independent days in which 2 to 4 plants are measured.

LIMITATIONS

Our protocol uses classical force-distance curves to measure nanomechanical properties of roots. We used a contact-based mechanical model to obtain the elasticity of plant roots[7] and a recently modified version, called the trimechanic theory.[8] Alternative analysis could be performed such as shell models,[17] hyper-elastic models,[18] or visco-elastic models.[19] Nevertheless, the protocol intends to focus on the handling of root samples. The same protocol remains valid with other mechanical model. Illustrated details about similar AFM measurements can be found elsewhere.[20,21]

Our protocol was applied on *Arabidopsis thaliana* seedlings but could be adopted to any seedling roots having a few cm in length. There are nevertheless various limitations concerning the use of AFM. Most modern instruments use small round Petri dishes as a sample stage. In some AFM systems, it has been difficult to use standard rectangular glass slides. Indeed, to orient the plant root according to the fixed position of the cantilever, it is easier to rotate a glass slide.

A main advantage of our protocol was the use of the Dimension 3100 AFM since it operates on a large motorized platform that can accommodate very large samples such as plant roots. The downside of this instrument is its end of commercial life with no possible upgrade. The AFM used in this protocol has some peculiarity due to the open-loop scanner such as the lack of a performant force trigger set-up for force-distance curves acquisition. In addition, due to unfocused laser beam, modern small cantilevers such as PF-QNM-LC cannot be used. Nevertheless, modern instruments will not suffer with such problems.

A more worrisome limitation was the use of NuSil pressure sensitive adhesive. Its availability is unpredictable and we have tried alternatives but with moderate or no success. A key advantage of NuSil is its slow polymerization (min) and low viscosity, which allows us to manipulate with standard pipettes. For alternative, the key property to look for is "pressure sensitive adhesive". Some commercial alternatives can be found and were tested in our lab but never applied during this protocol.

The extensibility of the protocol to other possible stresses is limited to experimental conditions that must be translated into a chemical change of agar material (the central step of this protocol). For instance, insoluble compounds may not be homogeneously distributed in the agar and therefore the outcome of the phenotype may be unpredictable. In such cases, a different growing methodology should be used such as directly in liquid solutions.

TROUBLESHOOTING

Problem 1

Classically, seedlings grow in large Petri dishes that are oriented vertically (step 15). However, to perform nanoindentation experiments, it is critical to have straight root ends; thus preventing artefact from curling effects as seen on Figure 10.

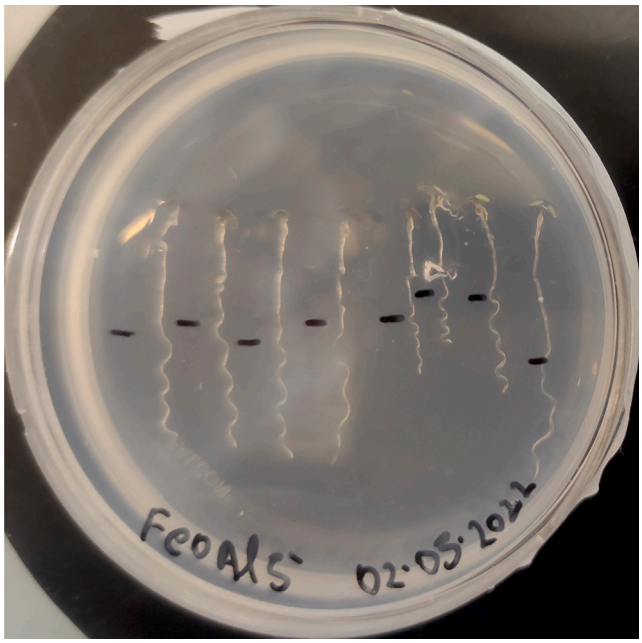

Figure 10. Example of curled *Arabidopsis thaliana* seedlings grown almost vertically on agar Petri dish

Because our experiments do not use additional phosphate than the one already present in the agar, it is possible that adding Pi should also reduce the curling effect. The black lines locate the end of the root tip when deposited in the Petri dish. If the root grows, the root tip will extend beyond the black line.

Potential solution

- Flat horizontal crystallization plates (Figure 11) are ideal replacement and suitable for growing plants for 4-5day-old only.

Problem 2

In Materials and Equipment, Pressure sensitive silicon adhesive: NuSil adhesive tends to polymerize with time when stored in any plastic material. If they are stored with a half-empty bottle for longer duration, the air inside the bottle can lead to drying of the adhesive.

Potential solution

- NuSil must be stored in glass aliquots of 2 mL. One of the great advantages of NuSil is its low viscosity that allows relatively easy manipulation. These glass tubes are filled up to the brim with NuSil, then sealed with a rubber-seal cap tightly. To fill the vials, it is necessary to use a sealed syringe instead of a classical pipette tip. This way they are stored in small quantities and last long. Over a three-year period (about 110 experiments), almost $^{1}/_{2}$ of the 1 L bottle of NuSil was used. Use dark-glass bottles because it is the native storage condition of ethyl acetate.

Problem 3

We sometimes observed that one side of the Petri dish displays one phenotype and another side a different phenotype (1). We attributed this phenomenon to a lack of homogeneous distribution of metals on the Petri dishes.

Potential solution

- It is important to mix the added metal solutions well into the liquid agar. This can be slightly tricky, as agar must be liquid enough to mix but not too hot.

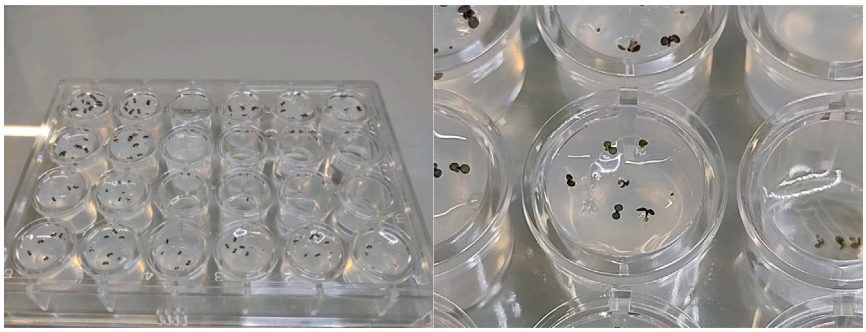

Figure 11. Example of a crystallization plate used to grow *Arabidopsis thaliana* seedlings

The plate is on the left and a zoom over a single well on the right. Agar is deposited in some wells and seeds are sown under a laminar hood. No more than 10 seeds should be sown in each well to allow enough space for roots to grow. Some wells are filled with water to provide humidity in the plate. The size of these wells is adapted for 2 cm long seedlings (4-5-day-old for *Arabidopsis*).

Problem 4

Timing of the experiment is critical (1). Because we want to compare physiological and mechanical responses from different experimental conditions, it is critical to keep a strict timing (age of plants and duration of stress). One of the difficulties is that pausing is not possible after starting the experiment (since the sowing). The 2 h transfer period imposes a strict agenda in the progress of the main experiment.

Potential solution

- Make a monthly and weekly calendar with planned experiments.
- Include a detailed daily calendar of the AFM measurement day to avoid any loss of time. Timing included in this protocol is defined after several months of practice; it is thus underestimated for a newcomer.

Problem 5

Improper fitting of the cantilever into the probe holder might lead to errors during AFM calibration steps: sensitivity and force constant of cantilever (Step 2a). Sometimes, the baseline at the beginning of the FD curve is not flat and may hint about poor cantilever positioning in the holder or a poorly fixed root (Figure 12). In case of incorrect sensitivity characterization, the thermal tuning will provide an erroneous cantilever spring constant.

Potential solution

- Do not hesitate to remove the probe holder and reposition the cantilever delicately into the groove of the holder. Perform the calibration again. There is no escape from the calibration steps, any improper action will systematically impact all the AFM measurements and their interpretation.
- We suggest the reader to access a complete description of calibration steps here[22] and particularly the supplementary information.

Problem 6

Pay attention to the face of the root that is in contact with agar during the transfer time of 2 h (step 4.b.i). Because it is transferred just for 2 h, the side touching the metal-excess agar is most likely to experience the full stress level than the whole root itself.

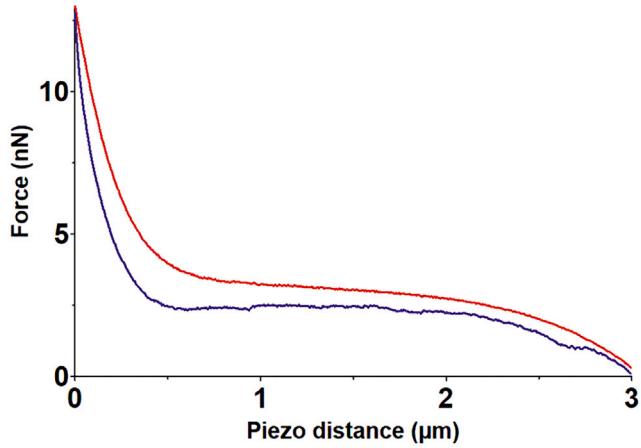

Figure 12. Example of a FD curve with a bent "baseline" (between 1 and 3 µm)

The approach and retract curves are in red and blue, respectively. The total ramp size is 3 µm while the maximum applied force is about 13 nN. Sometimes such a bending is a sign of a poor set-up in the optical AFM system. Other reasons could also explain the non-flat baseline such as a poorly fixed root on the NuSil or a cantilever is still in contact with the surface at the end of the retract ramp.

Potential solution

- It is best to present the side of the root that was in contact with agar to the top access of the glass slide, i.e., facing the tip of the cantilever. We have experienced a reduced heterogeneity in our data after such trick.

Problem 7

The curl effect makes the root rounded and more stretched (Figure 13); it complicates measurements and their interpretation (step 4.b.ii). In some cases, part of the root might be under the cantilever, which will not allow the cantilever to take the measurements properly as it might not touch the desired area. Note that the cantilever support may also touch the NuSil glue before the tip is reaching the surface of the root.

Potential solution

- In any case, bent roots do experience various mechanical stresses and should not be measured, unless it is a property specifically sought.

Problem 8

Sealing by adhesive is done such that the height shall remain constant throughout the slide (step 4.b.iii). With an excess of adhesive, the tip may touch the adhesive during the positioning under the AFM scanner or the edge of cantilever support may also touch the adhesive that will bias nanoindentation measurements.

Potential solution

- The sealing starts from the top just to make sure of the stiffening of the glue. A minimum of three seals is required so that the root does not move.
- See Figure 14 as an example for fastening the very tip of the root

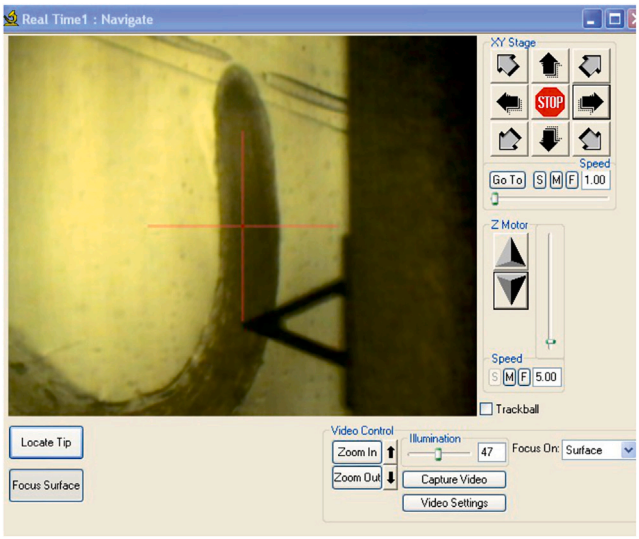

Figure 13. Image showing a bend root fixed on a glass slide

We found that such bending leads to high elasticity values of the external cell wall structure. The curvature often comes from the growing condition, likely induced by gravitropism. This is likely the most inconvenient aspect of growing seedlings in agar plates.

Problem 9

Performing a large-scale lateral displacement on the top of a root (step 5.m). Because of the inherent curvature and topography of a plant root, it is not advised to move over long distances (> 1 μm) using piezo scanner offsets.

Potential solution

- We found that withdrawing the cantilever works best on our system. It will avoid any tip damage.
- Re-engage at each measurement node. This practice helps in a better landing of the tip at the correct spot, fewer plant surface scratches, and less biological material deposition on the tip. All these parameters lead to better data acquisition.

Problem 10

The reading of the plant root phenotype (step 6.a) in our experiment is the root extension (measured in mm). Sometimes, plant seeds have different germination "power" and some seedlings may grow slower or faster.

Potential solution

- Always try to transfer roots of similar length so that their growth rate would be similar. This will help in overcoming any errors when measuring root length the next days.

RESOURCE AVAILABILITY

Lead contact

Jean-Luc Pellequer (jean-luc.pellequer@ibs.fr).

Materials availability

This study did not generate new unique reagents.

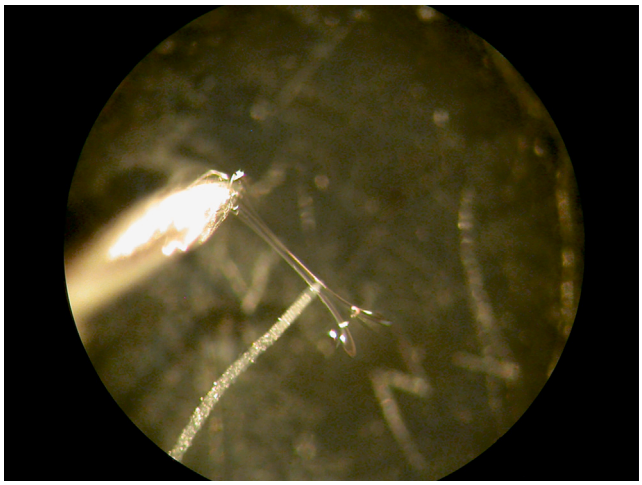

Figure 14. Optical magnification of deposited seedling roots on NuSil adhesive over a glass slide

A thin needle (bright color on the left) is used to fasten the position of the root on the adhesive by picking hardening adhesive over the root. Several fastening strips are required along the root but keep a significant room for the investigation zone, which is about 500 μm from the root tip (about five times the root diameter).

Data and code availability

This study did not generate/analyze datasets/code.

ACKNOWLEDGMENTS

IBS acknowledges integration into the Interdisciplinary Research Institute of Grenoble (IRIG, CEA). This work acknowledges the AFM platform at the IBS and the ANR project BioPhyt - 18-CE20-0023-03 and the support of the European Union's Horizon 2020 research and innovation programme under the Marie Skłodowska-Curie grant agreement No 812772, Project Phys2BioMed. We thank Bérangère Moreau (CEA Grenoble DRF/IRIG/DEPHY/MEM/LEMMA) for her help in SEM images. We also thank Isabel Ayala and Lionel Imbert (IBS/NMR) for their support in lab experiments.

AUTHOR CONTRIBUTIONS

H.K. established the current protocol and performed the mechanical measurements. J.-M.T. performed the initial mechanical analysis. A.-E.F. provided critical improvements in the protocol. D.F. performed scanning electron microscopy on PNP and other cantilevers. C.G. established the initial preliminary protocol and performed initial AFM measurements. S.-w.W.C. developed the trimechanic theory used to interpret the mechanical data. T.D. initiated the project in 2014 and provided plant materials. J.-L.P. directed the study and wrote the manuscript with the help of all co-authors.

DECLARATION OF INTERESTS

The authors declare no competing interests.

REFERENCES

1. Godon, C., Kaur, H., Teulon, J.-M., Chen, S.W.W., Desnos, T., and Pellequer, J.-L. (2023). Plant root cell wall stiffening induced by a metallic stress. In Mechanics of Cells and Tissues in Diseases, M. Lekka, D. Navajas, M. Radmacher, and A. Podestà, eds. (Walter de Gruyter GmbH), pp. 335–344. https://doi.org/10.1515/9783110989380-021.

2. Hermanowicz, P., Sarna, M., Burda, K., and Gabryś, H. (2014). AtomicJ: an open source software for analysis of force curves. Rev. Sci. Instrum. *85*, 063703. https://doi.org/10.1063/1.4881683.

3. Schneider, C.A., Rasband, W.S., and Eliceiri, K.W. (2012). NIH Image to ImageJ: 25 years of image analysis. Nat. Methods *9*, 671–675. https://doi.org/10.1038/nmeth.2089.

4. Meijering, E., Jacob, M., Sarria, J.C.F., Steiner, P., Hirling, H., and Unser, M. (2004). Design and validation of a tool for neurite tracing and analysis in fluorescence microscopy images. Cytometry A *58*, 167–176. https://doi.org/10.1002/cyto.a.20022.

5. Balzergue, C., Dartevelle, T., Godon, C., Laugier, E., Meisrimler, C., Teulon, J.-M., Creff, A., Bissler, M., Brouchoud, C., Hagège, A., et al. (2017). Low phosphate activates STOP1-ALMT1 to rapidly inhibit root cell elongation. Nat. Commun. *8*,

15300. https://doi.org/10.1038/ncomms15300.

6. Kaur, H., Godon, C., Teulon, J.-M., Desnos, T., and Pellequer, J.-L. (2023). Preparation and deposition of plant roots for AFM nanomechanical measurements. In Mechanics of Cells and Tissues in Diseases, M. Lekka, D. Navajas, M. Radmacher, and A. Podestà, eds. (Walter de Gruyter GmbH), pp. 125–138. https://doi.org/10.1515/9783110989380-010.

7. Sneddon, I.N. (1965). The relation between load and penetration in the axisymmetric boussinesq problem for a punch of arbitrary profile. Int. J. Eng. Sci. *3*, 47–57.

8. Chen, S.W.W., Teulon, J.M., Kaur, H., Godon, C., and Pellequer, J.L. (2022). Nano-structural stiffness measure for soft biomaterials of heterogeneous elasticity. Nanoscale Horiz. *8*, 75–82. https://doi.org/10.1039/D2NH00390B.

9. Carl, P., and Schillers, H. (2008). Elasticity measurement of living cells with an atomic force microscope: data acquisition and processing. Pflugers Arch. *457*, 551–559. https://doi.org/10.1007/s00424-008-0524-3.

10. Lekka, M., Laidler, P., Gil, D., Lekki, J., Stachura, Z., and Hrynkiewicz, A.Z. (1999). Elasticity of normal and cancerous human bladder cells studied by scanning force microscopy. Eur. Biophys. J. *28*, 312–316. https://doi.org/10.1007/s002490050213.

11. Domke, J., and Radmacher, M. (1998). Measuring the elastic properties of thin polymer films with the atomic force microscope. Langmuir *14*, 3320–3325. https://doi.org/10.1021/la9713006.

12. Kontomaris, S.V., Stylianou, A., Chliveros, G., and Malamou, A. (2023). Determining spatial variability of elastic properties for biological samples using AFM. Micromachines *14*, 182. https://doi.org/10.3390/mi14010182.

13. Fernandes, A.N., Chen, X., Scotchford, C.A., Walker, J., Wells, D.M., Roberts, C.J., and Everitt, N.M. (2012). Mechanical properties of epidermal cells of whole living roots of Arabidopsis thaliana: an atomic force microscopy study. Phys. Rev. E Stat. Nonlin. Soft Matter Phys. *85*, 021916. https://doi.org/10.1103/PhysRevE.85.021916.

14. Routier-Kierzkowska, A.L., Weber, A., Kochova, P., Felekis, D., Nelson, B.J., Kuhlemeier, C., and Smith, R.S. (2012). Cellular force microscopy for in vivo measurements of plant tissue mechanics. Plant Physiol. *158*, 1514–1522. https://doi.org/10.1104/pp.111.191460.

15. Millet, A. (2021). A universal model for the Log-normal distribution of elasticity in polymeric gels and its relevance to mechanical signature of biological tissues. Biology *10*, 64. https://doi.org/10.3390/biology10010064.

16. Kozlova, L., Petrova, A., Ananchenko, B., and Gorshkova, T. (2019). Assessment of primary cell wall nanomechanical properties in internal cells of non-fixed Maize roots. Plants *8*, 172. https://doi.org/10.3390/plants8060172.

17. Tsugawa, S., Yamasaki, Y., Horiguchi, S., Zhang, T., Muto, T., Nakaso, Y., Ito, K., Takebayashi, R., Okano, K., Akita, E., et al. (2022). Elastic shell theory for plant cell wall stiffness reveals contributions of cell wall elasticity and turgor pressure in AFM measurement. Sci. Rep. *12*, 13044. https://doi.org/10.1038/s41598-022-16880-2.

18. Jorba, I., Beltrán, G., Falcones, B., Suki, B., Farré, R., García-Aznar, J.M., and Navajas, D. (2019). Nonlinear elasticity of the lung extracellular microenvironment is regulated by macroscale tissue strain. Acta Biomater. *92*, 265–276. https://doi.org/10.1016/j.actbio.2019.05.023.

19. Peaucelle, A., Braybrook, S.A., Le Guillou, L., Bron, E., Kuhlemeier, C., and Höfte, H. (2011). Pectin-induced changes in cell wall mechanics underlie organ initiation in Arabidopsis. Curr. Biol. *21*, 1720–1726. https://doi.org/10.1016/j.cub.2011.08.057.

20. Bovio, S., Long, Y., and Moneger, F. (2019). Use of atomic force microscopy to measure mechanical properties and turgor pressure of plant cells and plant tissues. J. Vis. Exp. *149*, e59674. https://doi.org/10.3791/59674.

21. Rauschert, I., Benech, J.C., Sainz, M., Borsani, O., and Sotelo-Silveira, M. (2022). Atomic force microscopy to study the physical properties of epidermal cells of live Arabidopsis roots. J. Vis. Exp. *181*, e63533. https://doi.org/10.3791/63533.

22. Schillers, H., Rianna, C., Schäpe, J., Luque, T., Doschke, H., Wälte, M., Uriarte, J.J., Campillo, N., Michanetzis, G.P.A., Bobrowska, J., et al. (2017). Standardized Nanomechanical Atomic force microscopy Procedure (SNAP) for measuring soft and biological samples. Sci. Rep. *7*, 5117. https://doi.org/10.1038/s41598-017-05383-0.

ANNEX 3

Correlation between plant cell wall stiffening and root extension arrest phenotype in the combined abiotic stress of Fe and Al

Harinderbir Kaur[1], Jean-Marie Teulon[1], Christian Godon[2], Thierry Desnos[2], Shu-wen W. Chen[1,3], Jean-Luc Pellequer[1]

1 Univ. Grenoble Alpes, CEA, CNRS, IBS, F-38000 Grenoble, France.

2 Aix Marseille Univ., CEA, CNRS, BIAM, F-13108 Saint Paul-Lez-Durance, Cadarache, France

3 Rue Cyprien Jullin, Vinay, 38470, France

Correlation between plant cell wall stiffening and root extension arrest phenotype in the combined abiotic stress of Fe and Al

Harinderbir Kaur[1], Jean-Marie Teulon[1], Christian Godon[2], Thierry Desnos[2], Shu-wen W. Chen[1,3], Jean-Luc Pellequer[1]

1 Univ. Grenoble Alpes, CEA, CNRS, IBS, F-38000 Grenoble, France.

2 Aix Marseille Univ., CEA, CNRS, BIAM, F-13108 Saint Paul-Lez-Durance, Cadarache, France

3 Rue Cyprien Jullin, Vinay, 38470, France

Author for correspondance :

Jean-Luc Pellequer

Institut de Biologie Structurale

Jean-luc.pellequer@ibs.fr

Keywords: Primary root, Atomic Force Microscopy, Nanoindentation, Root extension arrest, abiotic stress, elasticity

Summary statement: We record the change in stiffness of the external primary cell wall of living *Arabidopsis thaliana* seedlings in presence of metallic stress using atomic force microscopy. Results reveals for the first time the uncoupling between mechanical response (CW stiffening) and root extension arrest.

Abstract

The plasticity and growth of plant cell walls (CWs) remain poorly understood at the molecular level. In this work, we used atomic force microscopy (AFM) to observe elastic responses of the root transition zone of 4-day-old *Arabidopsis thaliana* wild type and *almt1* mutant seedlings grown under Fe or Al stresses. The elastic parameters were deduced from force-distance measurements by AFM using the trimechanic-3PCS framework. In all metal stresses tested, the presence of single metal species Fe^{2+} or Al^{3+} at 10 µM exerts no noticeable effect on the root growth compared with the control conditions. On the contrary, a mix of both the metal ions produced a strong root extension arrest concomitant with significant increase of CW stiffness. This was not found for the *almt1* mutant which substantially abolishes the ability to exude malate. By raising the concentration of either Fe^{2+} or Al^{3+} to 20 µM, no root extension arrest was observed; nevertheless, a rise of root stiffness occurred. Our results indicate that the combination of Fe^{2+} and Al^{3+} with exuded malate is crucial for both CW stiffening and root extension arrest. However, stiffness increase induced by single Fe or Al metal is not sufficient for arresting root growth.

Introduction

The cell wall (CW) of land plants has been depicted as a highly intertwining architecture by cellulose microfibrils, hemicellulose, and pectin (Carpita & Gibeaut, 1993), which compose the three major components of the primary CW. Cellulose microfibrils are the stiffest component, playing a load-bearing role, and their orientation creates a mechanical anisotropy, restricting cell expansion in the microfibril direction (Majda et al., 2017). Hemicelluloses (xyloglucan chains) bind to cellulose microfibrils using hydrogen bonds (Valent & Albersheim, 1974); they also bind covalently to pectin (Bauer, Talmadge, Keegstra, & Albersheim, 1973), a network made of matrix pectin polysaccharides and soluble proteins (Kerr & Bailey, 1934). Water is also a major constituent of primary CWs (Gaff & Carr, 1961), up to 65% (Jackman & Stanley, 1995), and an essential element for chemical reactions within the CW. The thickness of the primary CW was suggested around 80 to 100 nm for meristematic and parenchymatous cells, in accordance with a layered structure of cellulose microfibrils with a layer spacing of ~20-40 nm (McCann, Wells, & Roberts, 1990). However, the accurate thickness measurement of external primary CWs remains challenging, roughly estimated as ~0.1 to 1 µm (Derbyshire, Findlay, McCann, & Roberts, 2007).

Cell growth is characterized by an irreversible increase in cell volume and surface area, concomitant with a CW loosening. The complexity of CW growth results in poorly known pathways and mechanisms that control root CW plasticity (Somssich, Khan, & Persson, 2016). Upon various environmental stresses, a reduction of cell growth associated with CW stiffening is a well-known phenomenon observed in plants (Schopfer, 2006), tightly linked to dynamic behaviors of primary CWs. It has been proposed that strain-stiffening limits growth and restricts organs bulging (Kierzkowski et al., 2012). During the plant growth, some cells enlarge their volumes by 10-to-1000 times (Cosgrove, 1997) that is regulated by external stimuli such as temperature, light, water, xenobiotics, and internal factors like growth hormones (Preston & Hepton, 1960).

The cessation of coleoptile growth was attributed to the loss of CW plasticity but not to turgor pressure which implicates an increase of CW stiffness (Kutschera, 1996). One pioneer work on CW nanomechanics used atomic force microscopy (AFM) to observe stiffness heterogeneity in the meristem surfaces at regional, cellular and even subcellular levels (Milani et al., 2011). AFM has been shown powerful for stiffness measure on plant tissues (Cuadrado-Pedetti et al., 2021; Milani et al., 2014; Peaucelle et al., 2011). For characterizing the nano-stiffness of a sample in response to a given stress, AFM nanoindentation provides a promising strategy of detecting changes in physico-chemical properties of cellular or tissue surfaces on a nanoscale.

Recently, stiffening plant roots have been observed in the early 30 min after exposition to iron stress (Balzergue et al., 2017). In a condition of low phosphate, low pH (<6) and the presence of iron, a primary root extension arrest (REA) was observed and a signaling pathway involving STOP1 and ALMT1 proteins was found to inhibit CW expansions (Balzergue et al., 2017; Mora-Macias et al., 2017). Therein, STOP1 abundance in the nucleus of plant cell was found controlled by the presence of iron (Fe) and aluminum (Al) metals, of which both induced malate exudation through the ALMT1 channel (Godon et al., 2019; Le Poder et al., 2022). Although Fe is a fundamental nutrient for plants, a defense mechanism somehow occurs in a Fe-rich environment, implying that an excess of Fe is deleterious to plants (Oliveira de Araujo et al., 2020). The deleterious effect of Fe is linked with the ferritin capacity of plant cell for storing free reactive iron (Ravet et al., 2009) instead of being driven to the vacuole (Hirsch et al., 2006; Ward, Lahner, Yakubova, Salt, & Raghothama, 2008). Indeed, ferritin encapsulates the Fe^{3+} cation after oxidizing Fe^{2+} prior to storage (Macara, Hoy, & Harrison, 1972). In bean roots, the apoplast provides a storage space for Fe^{3+}, where it could be extracted for nutrition use in case of iron deficiency (Bienfait, Vandenbriel, & Meslandmul, 1985). The *Arabidopsis lpr1/lpr2* mutants lack the capability of oxidizing Fe^{2+} to Fe^{3+} and were shown to reduce the amount of iron in the apoplast, exhibiting a Fe-insensitive phenotype in a low-phosphate condition (Svistoonoff et al., 2007).

Inhibition of root elongation is a well-known plant response to the tolerance of Al (Clarkson, 1965), especially at low pH (Bian, Zhou, Sun, & Li, 2013). Al toxicity resides

in its cationic binding to negatively charged sites (membranes, proteins, saccharides) available in the root (Nichol, Oliveira, Glass, & Siddiqi, 1993). One creep-extension analysis showed that Al accumulation in the CW provoked a reduction of CW extensibility in wheat roots (Ma, Shen, Nagao, & Tanimoto, 2004).Within one hour of Al supply, callose deposition was observed in the root tip of soybean seedlings (Wissemeier, Diening, Hergenroder, Horst, & Mixwagner, 1992). In addition to callose deposition, the main physiological mechanism of Al tolerance is the exclusion of Al from the root apex (Kochian, Pineros, Liu, & Magalhaes, 2015), where Al usually accumulates in the root apex symplast and mostly in the apoplast (Delhaize & Ryan, 1995) and binds directly to negatively charged pectins of the CW of root border cells (Yang et al., 2016). This exclusion is accomplished by exudation of organic acids (Miyasaka, Buta, Howell, & Foy, 1991) such as malate and citrate (Liu, Magalhaes, Shaff, & Kochian, 2009). In cultured tobacco, Al accumulation in plant cell walls was found depending on the presence of ferrous iron (Fe^{2+}) (Chang, Yamamoto, & Matsumoto, 1999). However, unlike Al, Fe does not stimulate malate excretion (Delhaize, Ryan, & Randall, 1993).

Fe^{2+} in phosphate-deficient conditions is able to arrest the primary root growth (Abel, 2011; Godon et al., 2019). Potential harmfulness of excessive Fe to cells is attributed to ROS (reactive oxygen species) production either by the Fenton (involving Fe^{2+}) or by the Haber-Weiss reactions (Fe^{3+}) (Gill & Tuteja, 2010). Above 40 µM of mixed Fe with Al resulted in a drastic reduction of root length, likely through the ROS production (Cakmak & Horst, 1991). The presence of Fe^{2+} in *Arabidopsis* roots stimulates ROS production with peroxidase activity (Balzergue et al., 2017; Muller et al., 2015; Naumann et al., 2022), particularly together with the class III peroxidase to stiffen and loosen the plant CWs (Francoz et al., 2015; Passardi, Cosio, Penel, & Dunand, 2005; Wolf & Hofte, 2014). In grass, peroxidase activity was linked to leaf growth arrest and CW cross-linking (MacAdam & Grabber, 2002); in rice, the peroxidase was found present in coleoptile growth arrest of shoots with increased ferulic and diferulic acids (Wakabayashi, Soga, & Hoson, 2012); similar findings were obtained for maize (Uddin et al., 2014). However, the causality between CW stiffness and REA remains to be elucidated.

In order to investigate Al and Fe effects on physiology and morphology of growing roots, we performed AFM indentations on *Arabidopsis* seedling roots under Fe and Al stresses of various metal concentrations and compositions. The present research provides a link of the structural stiffness measure (Chen, Teulon, Kaur, Godon, & Pellequer, 2023) with stress effects of metal ions in the root growth. Through the correspondence between the variations in the magnitude of elasticity parameters and the length of seedling roots in these stress conditions, it can improve our understanding of molecular mechanisms of metal ions in CW stiffening and root growth.

Materials and Methods

Seedling growth and manipulation

The experimental specimens are *A. thaliana* L. (Heynh.) lines of Columbia (Col-0) or the Col^{er105} background as specified in (Bonnot et al., 2016). The production of *almt1*^{51} mutant was previously described (Balzergue et al., 2017). Seeds were surface sterilized by 70% ethanol + 0.05% SDS for 1 min, followed by twice washing with 95% ethanol for 1 min each time and left in a laminar airflow for drying. To alleviate gravitropism effects on seedling growth such as inducing root wriggling or waving by growing vertically in a Petri dish, the seeds sown on day 0 were placed in a 24-well crystallographic plate (VDX plate HR3-140, Hampton Research). Plates were placed in a growing chamber (IPP100+ incubator, Memmert, Fisher Scientific, Illkirch, France) for 4 days with a 16-h photoperiod with 24˚C/21˚C day/night, respectively. During the 4 days, seedlings grew under the –Pi condition (no phosphate added) in the nutrient solution. The chemical content of the agar presently used is particularly poor in phosphate and metals, as determined by ICP analysis (Mercier et al., 2021), which is different from the agar used in our previous study (Balzergue et al., 2017).

After 4 days, seedlings were transferred into 60-mm agar Petri dishes in the –Pi condition while supplemented with or without 10 µM or 20 µM of $FeCl_2$ and/or $AlCl_3$for 2 hours. Then, seedlings were transferred from the agar plates to a glass slide for AFM nanoindendation experiments, and classical force–distance curves were collected within 30

min after mounting the glass slide. A control experiment, named No Transfer, in which seedlings were moved directly from the growing plate to the glass slide, was used to evaluate the impact of root transferring (from plates to Petri dishes).

Length measurement of primary root

The root lengths were measured on day 6 after sowing with seedlings directly deposited in the Petri dishes. The photos were taken with a camera and the root lengths in the photos were measured using the NeuronJ plugin (Meijering et al., 2004) of ImageJ software (Schneider, Rasband, & Eliceiri, 2012) with a 5 mm grid paper as distance calibration. Snapshots from NeuronJ root tracing were saved in the PNG format and data were plotted using GraphPad Prism 5.0.

Nanoindentation experiments with atomic force microscopy

Force–distance (F-D) curves were obtained using an AFM Dimension 3100 (Bruker, Santa Barbara, USA) with a nanoscope five controller running the Nanoscope 7.3 software. Triangular pyrex nitride cantilever with pyramidal tips of a max nominal radius 10 nm, a half-opening angle of 35˚, and a nominal spring constant k = 0.08 N/m were used (PNP-TR, NanoWorld AG, Neuchatel, CH).

Calibration of photodiode sensitivity was done first using the approach-retract curve in air on the glass substrate followed by a thermal tuning to determine the cantilever spring constant (Kaur *et al.* 2023, submitted). The determined spring constants were about 0.08 ± 0.01 N/m. In case of a large divergence, the cantilever was manually readjusted inside the probe holder and the calibration was repeated (Schillers et al., 2017). Then the photodiode sensitivity was performed again in a liquid medium with an average value of 65 nm/V. In our case, a SUM value of 3.5-4 V was usually achieved with PNP-TR cantilevers. The engaging deflection setpoint was kept at 2.5 V while the initial vertical deflection on the photodiode was set to 0 V. For performing the indentation experiment, a ramp size of 3 µm, a scan rate of 0.5 Hz, and 4096 data points per curve were set. Trigger was set off and no trigger value was used, implying that z-start value for the ramp at each

new engagement may need adjustments. To limit the maximal force during the measurement, a range of 25-40 nN was usually adopted for F-D data values.

The glass slide with a glued seedling (see the procedure in supplementary data and **Fig. S1**) was positioned under the AFM cantilever with the help of AFM optical camera. Thanks to the large motorized sample stage, we adjusted the glass slide in such a way that the cantilever could be positioned perpendicularly at the longitudinal middle of the glued root. The target working area, the transition zone, was 500 µm away from the root apex, almost twice the length of PNP cantilever.

Hierarchical statistics and reproducibility of experiments.

Owing to the roughness of root surfaces, indentations were performed at various locations in a matrix form. Different sizes of matrices were used: 5×2, 4×3, 4×4, representing 10, 12, or 16 indenting nodes. The optimal distance between nodes was 5 µm. Each node was formed of a sub-matrix with 3×3 or 2×2 F-D curves spaced by 50 nm in X and Y directions. Most of the presented results were obtained with a 4×4 node matrix of a 2×2 sub-matrix. Measurements from various forms of matrices were merged altogether. It usually took 25 min to record a full set of F-D curves for a single plant root; the manipulation time should be kept as short as possible to avoid additional stress effects.

For each stress condition, experiments were repeated 3 to 5 times. Each time involved 2 to 4 plants. The robustness of our protocol is ascertained by reproducible results from experiments repeated in a remote institute with another AFM instrument (Nanowizard IV, JPK-Bruker). Here, we considered all the measurements on one plant as one independent experiment. To synthesize the overall measurements into one comprehensive result for elasticity of the plant, hierarchical statistics were adopted. Explicitly, each elasticity parameter of one plant was obtained by averaging all the collected data (with 3×3 or 2×2 sub-matrices) of a node, then subsequently averaged over all the nodes of the plant. For one stress condition, at least 10 plants were analyzed ($n \geq 10$).

Regarding the reproducibility of results, two criteria were imposed: a valid node should have more than half of its F-D curves within 2 sigma from the mean; a valid plant needs at least half of its measured nodes valid. The distribution of elastic parameters from all nodes of a given stress condition was most often log-normal. Therefore, we computed geometric

means for the average value of elastic parameters of the plant. We also applied non-parametric Mann–Whitney t-tests to evaluating the statistical significance of these parameters among different stress conditions using a null hypothesis that assumes no difference on average among these conditions. A p-value was calculated using Graphpad Prism 5.0 with an α-threshold of 0.01. The box-and-whiskers plots were drawn using Graphpad Prism 8.

Characterization of plant elasticity by the trimechanic-3PCS framework

The trimechanic-3PCS framework (Chen et al., 2023) allows us to investigate the variation of stiffness with varied depth for biomaterials of heterogeneous elasticity responding to an external force. For a depth of indentation trajectory exhibiting a linear-elasticity behavior, this theory states that the responding force F_T of that depth zone can be expressed as a linear combination of three force components: F_C, F_H and F_S. In this work, the elasticity parameters of the very surface of CWs, i.e., the first depth zone with depth Z_1, are of concern.

The three force types (F_C, F_H and F_S) govern three modes of restoration mechanics, namely, depth impact, Hookean and tip-shape nanomechanics, respectively. The contributions (or strengths) of the three nanomechanics to the overall response are represented by the spring constants (k_C, k_H, k_S) of three parallel-connected spring (3PCS) analogs. The stiffness is defined as $k_T = k_H + k_S$. Another important elastic parameter is $r_S = k_S/k_T$, which quantifies penetration ease of the material and the composition of responding nanomechanics; it can represent material rigidity or deformability. Moreover, the F_S–deduced effective Young's modulus, $\hat{E} = E/(1-\eta^2)$ with E the Young's modulus and η the Poisson's ratio, represents the intrinsic property of elasticity. The calculations of these parameters were detailedly described previously (Chen et al., 2023).

Results

Elasticity of WT seedling roots in the absence of metals

The non-stressed (control) systems were characterized as the seedling roots grown in no metals supplemented (Fe**0**Al**0**) with or without a transfer step. Systematically, the transfer step is always included, unless mentioned otherwise. Nanoindentation experiments were performed on these non-stressed seedlings 2 hours later after being transferred, or immediately in case of no transfer. The average of root length was obtained on day 6 (4 days growth + 2 days after transferring from the Fe**0**Al**0** condition) as 25.0 mm (**Table 1**). According to p-values with the significance threshold $\alpha = 0.01$, no single group in the control systems significantly distinguishes itself from the others (**Fig. 1**). Averaged elasticity parameters are listed in **Table 2**. All pairs of groups tested by the standard non-parametric t-test were connected by a line with the exact p-value indicated above (**Fig**. **1**). The results show that the averaged effective Young modulus $\hat{E}$ is about 55 kPa, the stiffness k_T ~4.64 mN/m, and indentation depth Z_1 ~151 nm.

Elasticity of WT plant roots in the presence of metals

To assess the effect of the –Pi growth medium with Fe^{2+} and Al^{3+} ions, several combinatory concentrations of Fe and Al were applied to the test on the growth and CW stiffening of seedling roots. Systematically, the seedling roots were placed in various stressed environments for two hours. These stress conditions were prepared with 10 µM of $FeCl_2$ or 10 µM of $AlCl_3$, or mixing both, and labeled as Fe**10**Al**0**, Fe**0**Al**10** and Fe**10**Al**10**, respectively. No REA is observed in both Fe**0**Al**10** and Fe**10**Al**0** whereas a full REA is observed in the Fe**10**Al**10** condition (**Fig. 2A**), see T**able 1** for root lengths.

The results from nanoindentation experiments in 10 µM metal conditions are shown in **Fig**. **2**. The hierarchical averages of their elasticity parameters are presented in **Table 2**. The elastic behaviors of conditions Fe**10**Al**0** and Fe**0**Al**10** exhibit no remarkable distinction from Fe**0**Al**0**; their combined result of $\hat{E}$ is about 55 kPa. It indicates that the total amount

of metal ions at 10 μM changes little in the effective Young's modulus, stiffness or indentation depth compared to no metal at all. However, the elasticity of roots grown with mixed Fe and Al (Fe**10**Al**10**) yields a value of 127 kPa for the effective Young's modulus $\hat{E}$, a significant increase in CW stiffness. Accordingly, the averaged k_T of 8.89 mN/m for Fe**10**Al**10** is also much higher than all the conditions of a single metal element at 10 μM (cf. 4-5 mN/m in **Table 2**) (**Fig**. **2C**).

We further explored the concentration impact of metal ions by doubling the concentration from 10 to 20 μM. We found that Fe**20**Al**0** displays a significantly higher $\hat{E}$ and k_T than the control systems, while Fe**0**Al**20** exhibits a moderate effect (**Fig**. **3**). The results show that the average of $\hat{E}$ and k_T have a similar value between Fe**20**Al**0** and Fe**10**Al**10** conditions (**Table 2**) whereas the corresponding values of Fe**0**Al**20** are intermediate. Very interestingly, doubling the cationic concentration of single metal does not provoke the occurrence of REA (**Table 1**).

Elasticity of *almt1* mutant plant roots in the presence of metals

Unlike WT plant roots, no REA phenotype was found from *almt1* mutants in the Fe**10**Al**10** condition (**Fig**. **4**). The elasticity parameters for *almt1* mutant seedlings grown in Fe**0**Al**0** and Fe**10**Al**10** conditions are listed in **Table 3**. No significant difference was found in the magnitudes of $\hat{E}$ and k_T between the two stress conditions (**Fig. 4**). However, these values are comparable to WT in Fe**0**Al**0** (**Tables 2, 3**). It implies that without exuded malate, the two metal ions cannot exert substantial effects on elastic responses of mutant roots.

Discussion

The present results show that the elastic responses of external epidermal cell walls of *Arabidopsis* seedling roots to external forces vary in terms of concentration and

composition of Fe and Al metal ions. It indicates that elasticity of plant cell CW is sensitive and can be used as to assess abiotic stresses on plant growth and stiffening. However, unexpectedly, the stiffening and the phenotype of seedling roots such as REA are not directly correlated.

Root extension arrest (REA) and metallic stress

The root lengths of *Arabidopsis* seedlings were measured from the root tip to the cotyledon base (**Fig. S2**). Among all the stress conditions (Fe**10**Al**0**, Fe**0**Al**10**, Fe**20**Al**0**, Fe**0**Al**20**, and Fe**10**Al**10**), we observed the REA phenotype appeared only in the WT roots grown in Fe**10**Al**10** condition (**Table 1**). It is surprising that no REA was observed with doubled concentrations of single metal species (either Fe or Al). It reveals that the excess of single metal species did not urge the occurrence of REA. To ascertain that the REA phenotype is only due to the mixture of the two metal species, we carried out an experiment in a condition with the same metal ingredients and 500 µM phosphate (Pi). Phosphate is known for binding cations (Foy, Chaney, & White, 1978) but do not completely abolish the entry of metals into seedling roots (Balzergue et al., 2017). Results show no REA in the presence of Pi (**Table 2**, **Fig**. **S5**).

To further resolve the origin of REA occurrence, the WT results were compared with those of the *almt1* mutant. Lacking the malate-transporter ALMT1, the *almt1* mutant is strongly altered in exuding malate, a small organic anion known to chelate Fe^{3+} and Al^{3+}. The root growth of *almt1* mutant was known to be insensitive to Fe^{2+} (under -Pi condition) and exhibited no REA phenotype (Balzergue et al., 2017; Mora-Macias et al., 2017). The absence of REA phenotype was explained as a consequence of reduced accumulation of iron in the apoplast due to a dramatic decrease of malate exudation. From our results, the mixed Fe and Al stress also lacks the ability to stimulate REA in the *almt1* mutants, and these mixed metal cations act like single metal ions of 10 µM in WT roots. In other words, without the malate exudation, the mixed Al and Fe are no longer growth inhibitors, leading to a normal growth. It further suggests that trapping metal ions by malate molecules is a key step to promote REA in WT. Taken all the data together, the factors to simulate REA

include the amount of metal ions, the composition of metal species and the exudation of malate.

Metallic stress and elasticity of living seedling roots

When the interlaced architecture of CWs is perturbed by metal ions, the bonding modes are accordingly justified; these changes can be reflected by altered elastic responses. It is noteworthy that the used AFM indenting tip has a small apex (~10 nm radius), enabling us to sense structural strengths of beneath constituents in primary CWs such as cellulose microfibrils. Applying the trimechanic-3PCS framework to data analysis, the elasticity parameters defined therein helped us to differentiate elastic properties modulated by various stressed environments. The force decomposition of the theory unveils that the F_S-deduced $\hat{E}$ is a sensitive parameter to varying metal contents in the growing medium, whereas the values of k_T, representing the overall stiffness, are less distinguishable (**Table 2**). The change in penetration ease r_S underlies the varying modes of nanomechanics and network bonding of CW architecture under different stresses (Chen et al., 2023). The r_S parameter is provided only by the trimechanic-3PCS framework and cannot be accessed by the conventional methods (Hermanowicz, Sarna, Burda, & Gabrys, 2014). This r_S parameter can also represent the deformability of the indented root.

According to comparable r_S values of WT roots in Fe**0**Al**0**, Fe**10**Al**0** and Fe**0**Al**10** conditions, the bonding properties of CW structure are inferred alike. However, with higher concentration of metal ions (Fe**20**Al**0**, Fe**0**Al**20**, and Fe**10**Al**10**), an increase in r_S is visible ($r_S > 0.8$, **Table 2**). It follows that in all these conditions of high metal amount, the bonding properties of CW are differentiated from that of low metal amount. As already demonstrated, Al binds directly to negatively charged pectins of CWs and provokes a reduction in CW extensibility (Ma et al., 2004; Yang et al., 2016). In addition, expression profiling experiments suggested that pectins do bind with Fe (Hoehenwarter et al., 2016), which therefore, like Al, changes the bonding elasticity of the external primary cell wall. It is noteworthy that elastic parameters presented here are referred to the indentation depth of about 150 nm, which locates most likely the pectin constituents of CW (as opposed to

cellulose microfibrils). Thus, the increased stiffness of CW for seedlings grown from Fe**20**Al**0** and Fe**0**Al**20** conditions likely involve the binding of Fe and Al to the pectin components of CW.

From the results of Z_1, $\hat{E}$ or k_T, the increase of the total amount of metal ions is closely related to CW stiffening. At 10 μM of either iron or aluminum, the elastic properties of WT roots are similar to that of the control system that contains no metal ions. At 20 μM (regardless of metal composition), the parameters $\hat{E}$, k_T and r_S increase while Z_1 slightly reduces; see the results from Fe**10**Al**10**, Fe**20**Al**0** and Fe**0**Al**20** in **Table 2**. However, the Fe**20**Al**0** and Fe**0**Al**20** (single metal species) conditions exhibit no REA phenotype. It ensues that the increase of CW stiffness is not causal or not sufficient to trigger to REA, at least not in the operational conditions of our experiments.

Root extension arrest and CW stiffening

REA phenotype induced by the Al stress is multifactorial and its mechanism remains largely unknown (Kochian et al., 2015). However, from our previous work and others, REA phenotype due to Fe stress is documented in its initial steps of Fe redox cycle that produces ROS in the CW and promotes peroxidase-dependent cell wall stiffening in the transition zone (Balzergue et al., 2017; Naumann et al., 2022). The major tolerance mechanism of Al toxicity is through the stimulation of the expression of *ALMT1* gene (Godon et al., 2019), a malate transporter (ALMT1 (Sasaki et al., 2004)). The rate-limiting step in this mechanism is the transport of organic acids rather than the cellular synthesis of these molecules (Ryan, Delhaize, & Jones, 2001). Indeed, Al^{3+} binding to the extracellular face of the ALMT1 channel opens the channel thereby stimulating the exudation of malate (Wang et al., 2022).

We have shown that the CW stiffness increases without REA at high Fe^{2+}concentrations (≥ 20 μM) for seedling roots grown from an agar medium with poor phosphate and other metals, probably reflecting a lack of ROS production (**Fig. 5**). In the ferrous state, the Fe ion has multiple possible outcomes: adsorbed by the cell via its importing receptor,

chelated with some organic acids in the CW, and oxidized to a ferric ion that may non-specifically bind to pectins of the CW. However, at 20 µM Fe^{2+}, none of these outcomes are important enough to form the necessary redox condition for REA occurrence. At the same high concentration, Al^{3+} activates the exudation of malate that chelates Al to move it out of the root. The remaining Al^{3+} ions in the CW then bind to negatively-charged pectins, leading to an increase of stiffness though without REA occurrence (**Fig. 5**). The stress effect of co-presence of Fe and Al highlights the importance of malate accumulated in the apoplast. A current model postulates that, in combination with the apoplastic ferroxidase LPR1, malate-Fe^{3+} complexes trigger ROS in the apoplast (Naumann et al., 2022). Based on this model, our results show that Al^{3+} increases exudation of malate in the apoplast, thereby accumulating Fe in the apoplast followed by an accumulation of ROS to end up with a root extension arrest (**Fig. 5**).

Conclusions

Root extension arrest was observed from *Arabidopsis* WT seedlings only stressed by a mix of 10 µM $FeCl_2$ and 10 µM $AlCl_3$ in a low phosphate agar medium. This REA is concomitant with a stiffening of the external primary cell walls. However, single metal, even at a higher concentration (20 µM), did not induce REA despite an increase in CW stiffness. Thus, the increase in the stiffness of CW may have independent origins: one associated with the binding of metals to pectin components of CW, and another associated with the redox cycle that produces ROS in the CW and promotes the peroxidase-dependent stiffening of CW. Consequently, the REA occurs in a balance of metabolic events (chemical and/or mechanical) that depends upon a change in the contribution of each factors including the chelating effect of malate in the combined Fe-Al stress.

Acknowledgments

IBS acknowledges integration into the Interdisciplinary Research Institute of Grenoble (IRIG, CEA). This work acknowledges the AFM platform at the IBS. Acknowledgment to the ANR project BioPhyt -18-CE20-0023-03 and the support of the European Union's Horizon 2020 research and innovation programme under the Marie Skłodowska-Curie grant agreement No 812772, Project Phys2BioMed. We thank Dr. Anne-Emmanuelle Foucher (IBS/EPIGEN) for critical improvements of the plant growth protocol. We also thank Isabel Ayala and Lionel Imbert (IBS/NMR) for their support in lab experiments.

Author contributions

HK established the current protocol and performed the mechanical measurements. Jean-Marie Teulon performed the initial mechanical analysis. Christian Godon established the initial preliminary protocol and performed initial AFM measurements. Shu-wen W. Chen developed the trimechanic theory used to interpret the mechanical data. Thierry Desnos initiated the project and provided plant materials. Jean-Luc Pellequer directed the study and wrote the manuscript. All authors contributed to revisions of the manuscript.

Data Availability

Data available on request from the authors

ORCID

Harinderbir Kaur: https://orcid.org/0000-0002-2418-2449

Christian Godon: https://orcid.org/0000-0002-1535-9855

Thierry Desnos: https://orcid.org/0000-0002-6585-1362

Shu-wen W. Chen: https://orcid.org/0000-0003-4205-4931

Jean-Luc Pellequer: https://orcid.org/0000-0002-8944-2715

References

Abel, S. (2011). Phosphate sensing in root development. *Current Opinion in Plant Biology, 14*(3), 303-309. doi:10.1016/j.pbi.2011.04.007

Balzergue, C., Dartevelle, T., Godon, C., Laugier, E., Meisrimler, C., Teulon, J.-M., . . . Desnos, T. (2017). Low phosphate activates STOP1-ALMT1 to rapidly inhibit root cell elongation. *Nature Communications, 8*, 15300. doi:10.1038/ncomms15300

Bauer, W. D., Talmadge, K. W., Keegstra, K., & Albersheim, P. (1973). The Structure of Plant Cell Walls: II. The Hemicellulose of the Walls of Suspension-cultured Sycamore Cells. *Plant Physiology, 51*(1), 174-187. doi:10.1104/pp.51.1.174

Bian, M., Zhou, M., Sun, D., & Li, C. (2013). Molecular approaches unravel the mechanism of acid soil tolerance in plants. *The Crop Journal, 1*, 91–104. doi:10.1016/j.cj.2013.08.002

Bienfait, H. F., Vandenbriel, W., & Meslandmul, N. T. (1985). Free Space Iron Pools in Roots - Generation and Mobilization. *Plant Physiology, 78*(3), 596-600. doi:10.1104/pp.78.3.596

Bonnot, C., Pinson, B., Clement, M., Bernillon, S., Chiarenza, S., Kanno, S., . . . Desnos, T. (2016). A chemical genetic strategy identify the PHOSTIN, a synthetic molecule that triggers phosphate starvation responses in Arabidopsis thaliana. *New Phytologist, 209*(1), 161-176. doi:10.1111/nph.13591

Cakmak, I., & Horst, W. J. (1991). Effect of aluminium on lipid peroxidation, superoxide dismutase, catalase, and peroxidase activities in root tips of soybean (*Glycine max*). *Physiologia Plantarum, 83*, 463-468. doi:10.1111/j.1399-3054.1991.tb00121.x

Chang, Y.-C., Yamamoto, Y., & Matsumoto, H. (1999). Accumulation of aluminium in the cell wall pectin in cultured tobacco (Nicotiana tabacum L.) cells treated with a combination of aluminium and iron. *Plant, Cell & Environment, 22*, 1009–1017. doi:10.1046/j.1365-3040.1999.00467.x

Chen, S. W. W., Teulon, J. M., Kaur, H., Godon, C., & Pellequer, J. L. (2023). Nano-structural stiffness measure for soft biomaterials of heterogeneous elasticity. *Nanoscale Horizons, 8*, 75-82. doi:10.1039/D2NH00390B

Clarkson, D. T. (1965). The effect of aluminium and some other trivalent metal cations on cell division in the root apices of *Allium cepa*. *Annals of Botany, 29*(114), 309-315. doi:10.1093/oxfordjournals.aob.a083953

Cosgrove, D. J. (1997). Relaxation in a high-stress environment: the molecular bases of extensible cell walls and cell enlargement. *Plant Cell, 9*(7), 1031-1041. doi:10.1105/tpc.9.7.1031

Cuadrado-Pedetti, M. B., Rauschert, I., Sainz, M. M., Amorim-Silva, V., Botella, M. A., Borsani, O., & Sotelo-Silveira, M. (2021). The Arabidopsis TETRATRICOPEPTIDE THIOREDOXIN-LIKE 1 gene is involved in anisotropic root growth during osmotic stress adaptation. *Genes, 12*(2), 236. doi:10.3390/genes12020236

Delhaize, E., & Ryan, P. R. (1995). Aluminum Toxicity and Tolerance in Plants. *Plant Physiology, 107*(2), 315-321. doi:10.1104/pp.107.2.315

Delhaize, E., Ryan, P. R., & Randall, P. J. (1993). Aluminum Tolerance in Wheat (Triticum aestivum L.) (II. Aluminum-Stimulated Excretion of Malic Acid from Root Apices). *Plant Physiology, 103*(3), 695-702. doi:10.1104/pp.103.3.695

Derbyshire, P., Findlay, K., McCann, M. C., & Roberts, K. (2007). Cell elongation in Arabidopsis hypocotyls involves dynamic changes in cell wall thickness. *Journal of Experimental Botany, 58*(8), 2079-2089. doi:10.1093/jxb/erm074

Foy, C. D., Chaney, R. L., & White, M. C. (1978). The physiology of metal toxicity in plants. *Annual Review of Plant Physiology, 29*, 511-566. doi:10.1146/annurev.pp.29.060178.002455

Francoz, E., Ranocha, P., Nguyen-Kim, H., Jamet, E., Burlat, V., & Dunand, C. (2015). Roles of cell wall peroxidases in plant development. *Phytochemistry, 112*, 15-21. doi:10.1016/j.phytochem.2014.07.020

Gaff, D., & Carr, D. (1961). The quantity of water in the cell wall and its significance. *Australian Journal of Biological Sciences, 14*(3), 299-311 doi:10.1071/BI9610299

Gill, S. S., & Tuteja, N. (2010). Reactive oxygen species and antioxidant machinery in abiotic stress tolerance in crop plants. *Plant Physiology and Biochemistry, 48*(12), 909-930. doi:10.1016/j.plaphy.2010.08.016

Godon, C., Mercier, C., Wang, X., David, P., Richaud, P., Nussaume, L., . . . Desnos, T. (2019). Under phosphate starvation conditions, Fe and Al trigger accumulation of the transcription factor STOP1 in the nucleus of Arabidopsis root cells. *The Plant Journal, 99*(5), 937-949. doi:10.1111/tpj.14374

Hermanowicz, P., Sarna, M., Burda, K., & Gabrys, H. (2014). AtomicJ: An open source software for analysis of force curves. *Review of Scientific Instruments, 85*(6), 063703. doi:10.1063/1.4881683

Hirsch, J., Marin, E., Floriani, M., Chiarenza, S., Richaud, P., Nussaume, L., & Thibaud, M. C. (2006). Phosphate deficiency promotes modification of iron distribution in Arabidopsis plants. *Biochimie, 88*(11), 1767-1771. doi:10.1016/j.biochi.2006.05.007

Hoehenwarter, W., Monchgesang, S., Neumann, S., Majovsky, P., Abel, S., & Muller, J. (2016). Comparative expression profiling reveals a role of the root apoplast in local phosphate response. *BMC Plant Biology, 16*, 106. doi:10.1186/s12870-016-0790-8

Jackman, R. L., & Stanley, D. W. (1995). Perspectives in the Textural Evaluation of Plant Foods. *Trends in Food Science & Technology, 6*(6), 187-194. doi:10.1016/S0924-2244(00)89053-6

Kerr, T., & Bailey, I. W. (1934). The cambium and its derivative tissues X - structure, optical properties and chemical composition of the so called middle lamela. *Journal of the Arnold Arboretum, 15*, 327-349. doi:http://www.biodiversitylibrary.org/item/33591

Kierzkowski, D., Nakayama, N., Routier-Kierzkowska, A. L., Weber, A., Bayer, E., Schorderet, M., . . . Smith, R. S. (2012). Elastic domains regulate growth and organogenesis in the plant shoot apical meristem. *Science, 335*(6072), 1096-1099. doi:10.1126/science.1213100

Kochian, L. V., Pineros, M. A., Liu, J., & Magalhaes, J. V. (2015). Plant adaptation to acid soils: The molecular basis for crop aluminum resistance. *Annual Review of Plant Biology, 66*, 571-598. doi:10.1146/annurev-arplant-043014-114822

Kutschera, U. (1996). Cessation of cell elongation in rye coleoptiles is accompanied by a loss of cell-wall plasticity. *Journal of Experimental Botany, 47*(302), 1387-1394. doi:10.1093/jxb/47.9.1387

Le Poder, L., Mercier, C., Fevrier, L., Duong, N., David, P., Pluchon, S., . . . Desnos, T. (2022). Uncoupling aluminum toxicity from aluminum signals in the STOP1 pathway. *Frontiers in Plant Science, 13*, 785791. doi:10.3389/fpls.2022.785791

Liu, J., Magalhaes, J. V., Shaff, J., & Kochian, L. V. (2009). Aluminum-activated citrate and malate transporters from the MATE and ALMT families function independently to confer Arabidopsis aluminum tolerance. *The Plant Journal, 57*(3), 389-399. doi:10.1111/j.1365-313X.2008.03696.x

Ma, J. F., Shen, R. F., Nagao, S., & Tanimoto, E. (2004). Aluminum targets elongating cells by reducing cell wall extensibility in wheat roots. *Plant and Cell Physiology, 45*(5), 583-589. doi:10.1093/pcp/pch060

MacAdam, J. W., & Grabber, J. H. (2002). Relationship of growth cessation with the formation of diferulate cross-links and p-coumaroylated lignins in tall fescue leaf blades. *Planta, 215*(5), 785-793. doi:10.1007/s00425-002-0812-7

Macara, I. G., Hoy, T. G., & Harrison, P. M. (1972). The formation of ferritin from apoferritin. Kinetics and mechanism of iron uptake. *Biochemical Journal, 126*(1), 151-162. doi:10.1042/bj1260151

Majda, M., Grones, P., Sintorn, I. M., Vain, T., Milani, P., Krupinski, P., . . . Robert, S. (2017). Mechanochemical polarization of contiguous cell walls shapes plant pavement cells. *Developmental Cell, 43*(3), 290-304. doi:10.1016/j.devcel.2017.10.017

McCann, M. C., Wells, B., & Roberts, K. (1990). Direct visualization of cross-links in the primary plant cell wall. *Journal of Cell Science, 96*, 323-334.

Meijering, E., Jacob, M., Sarria, J. C., Steiner, P., Hirling, H., & Unser, M. (2004). Design and validation of a tool for neurite tracing and analysis in fluorescence microscopy images. *Cytometry A, 58*(2), 167-176. doi:10.1002/cyto.a.20022

Mercier, C., Roux, B., Have, M., Le Poder, L., Duong, N., David, P., . . . Desnos, T. (2021). Root responses to aluminium and iron stresses require the SIZ1 SUMO ligase to modulate the STOP1 transcription factor. *The Plant Journal, 108*(5), 1507-1521. doi:10.1111/tpj.15525

Milani, P., Gholamirad, M., Traas, J., Arneodo, A., Boudaoud, A., Argoul, F., & Hamant, O. (2011). In vivo analysis of local wall stiffness at the shoot apical meristem in Arabidopsis using atomic force microscopy. *The Plant Journal, 67*(6), 1116-1123. doi:10.1111/j.1365-313X.2011.04649.x

Milani, P., Mirabet, V., Cellier, C., Rozier, F., Hamant, O., Das, P., & Boudaoud, A. (2014). Matching Patterns of Gene Expression to Mechanical Stiffness at Cell Resolution through Quantitative Tandem Epifluorescence and Nanoindentation. *Plant Physiology, 165*(4), 1399-1408. doi:10.1104/pp.114.237115

Miyasaka, S. C., Buta, J. G., Howell, R. K., & Foy, C. D. (1991). Mechanism of aluminum tolerance in snapbeans : root exudation of citric Acid. *Plant Physiology, 96*(3), 737-743. doi:10.1104/pp.96.3.737

Mora-Macias, J., Ojeda-Rivera, J. O., Gutierrez-Alanis, D., Yong-Villalobos, L., Oropeza-Aburto, A., Raya-Gonzalez, J., . . . Herrera-Estrella, L. (2017). Malate-dependent Fe accumulation is a critical checkpoint in the root developmental response to low phosphate. *Proceedings of the National Academy of Sciences of the USA, 114*(17), E3563-E3572. doi:10.1073/pnas.1701952114

Muller, J., Toev, T., Heisters, M., Teller, J., Moore, K. L., Hause, G., . . . Abel, S. (2015). Iron-dependent callose deposition adjusts root meristem maintenance to phosphate availability. *Developmental Cell, 33*(2), 216-230. doi:10.1016/j.devcel.2015.02.007

Naumann, C., Heisters, M., Brandt, W., Janitza, P., Alfs, C., Tang, N., . . . Abel, S. (2022). Bacterial-type ferroxidase tunes iron-dependent phosphate sensing during Arabidopsis root development. *Current Biology, 32*(10), 2189-2205 e2186. doi:10.1016/j.cub.2022.04.005

Nichol, B. E., Oliveira, L. A., Glass, A. D. M., & Siddiqi, M. Y. (1993). The fffects of aluminum on the influx of calcium, potassium, ammonium, nitrate, and phosphate in an aluminum-sensitive cultivar of barley (*Hordeum vulgare*). *Plant Physiology, 101*, 1263-1266. doi:10.1104/pp.101.4.1263

Oliveira de Araujo, T., Isaure, M. P., Alchoubassi, G., Bierla, K., Szpunar, J., Trcera, N., . . . Mari, S. (2020). *Paspalum urvillei* and *Setaria parviflora*, two grasses naturally adapted to extreme iron-rich environments. *Plant Physiology and Biochemistry, 151*, 144-156. doi:10.1016/j.plaphy.2020.03.014

Passardi, F., Cosio, C., Penel, C., & Dunand, C. (2005). Peroxidases have more functions than a Swiss army knife. *Plant Cell Reports, 24*(5), 255-265. doi:10.1007/s00299-005-0972-6

Peaucelle, A., Braybrook, S. A., Le Guillou, L., Bron, E., Kuhlemeier, C., & Hofte, H. (2011). Pectin-induced changes in cell wall mechanics underlie organ initiation in Arabidopsis. *Current Biology, 21*(20), 1720-1726. doi:10.1016/j.cub.2011.08.057

Preston, R. D., & Hepton, J. (1960). The Effect of Indoleacetic Acid on Cell Wall Extensibility in Avena Coleoptiles. *Journal of Experimental Botany, 11*(31), 13-27. doi:10.1093/Jxb/11.1.13

Ravet, K., Touraine, B., Boucherez, J., Briat, J. F., Gaymard, F., & Cellier, F. (2009). Ferritins control interaction between iron homeostasis and oxidative stress in Arabidopsis. *The Plant Journal, 57*(3), 400-412. doi:10.1111/j.1365-313X.2008.03698.x

Ryan, P., Delhaize, E., & Jones, D. (2001). Function and Mechanism of Organic Anion Exudation from Plant Roots. *Annual Review of Plant Physiology and Plant Molecular Biology, 52*, 527-560. doi:10.1146/annurev.arplant.52.1.527

Sasaki, T., Yamamoto, Y., Ezaki, B., Katsuhara, M., Ahn, S. J., Ryan, P. R., . . . Matsumoto, H. (2004). A wheat gene encoding an aluminum-activated malate transporter. *The Plant Journal, 37*(5), 645-653. doi:10.1111/j.1365-313x.2003.01991.x

Schillers, H., Rianna, C., Schäpe, J., Luque, T., Doschke, H., Wälte, M., . . . Radmacher, M. (2017). Standardized Nanomechanical Atomic force microscopy Procedure (SNAP) for measuring soft and biological samples. *Scientific Reports, 7*, 5117. doi:10.1038/s41598-017-05383-0

Schneider, C. A., Rasband, W. S., & Eliceiri, K. W. (2012). NIH Image to ImageJ: 25 years of image analysis. *Nature Methods, 9*(7), 671-675. doi:10.1038/nmeth.2089

Schopfer, P. (2006). Biomechanics of plant growth. *American Journal of Botany, 93*(10), 1415-1425. doi:10.3732/ajb.93.10.1415

Somssich, M., Khan, G. A., & Persson, S. (2016). Cell wall heterogeneity in root development of Arabidopsis. *Frontiers in Plant Science, 7*, 1242. doi:10.3389/fpls.2016.01242

Svistoonoff, S., Creff, A., Reymond, M., Sigoillot-Claude, C., Ricaud, L., Blanchet, A., . . . Desnos, T. (2007). Root tip contact with low-phosphate media reprograms plant root architecture. *Nature Genetics, 39*(6), 792-796. doi:10.1038/ng2041

Uddin, M. N., Hanstein, S., Faust, F., Eitenmuller, P. T., Pitann, B., & Schubert, S. (2014). Diferulic acids in the cell wall may contribute to the suppression of shoot growth in the first phase of salt stress in maize. *Phytochemistry, 102*, 126-136. doi:10.1016/j.phytochem.2014.02.014

Valent, B. S., & Albersheim, P. (1974). The structure of plant cell walls: v. On the binding of xyloglucan to cellulose fibers. *Plant Physiology, 54*(1), 105-108. doi:10.1104/pp.54.1.105

Wakabayashi, K., Soga, K., & Hoson, T. (2012). Phenylalanine ammonia-lyase and cell wall peroxidase are cooperatively involved in the extensive formation of ferulate network in cell walls of developing rice shoots. *Journal of Plant Physiology, 169*(3), 262-267. doi:10.1016/j.jplph.2011.10.002

Wang, J., Yu, X., Ding, Z. J., Zhang, X., Luo, Y., Xu, X., . . . Guo, J. (2022). Structural basis of ALMT1-mediated aluminum resistance in Arabidopsis. *Cell Research, 32*(1), 89-98. doi:10.1038/s41422-021-00587-6

Ward, J. T., Lahner, B., Yakubova, E., Salt, D. E., & Raghothama, K. G. (2008). The effect of iron on the primary root elongation of Arabidopsis during phosphate deficiency. *Plant Physiology, 147*(3), 1181-1191. doi:10.1104/pp.108.118562

Wissemeier, A. H., Diening, A., Hergenroder, A., Horst, W. J., & Mixwagner, G. (1992). Callose formation as parameter for assessing genotypic plant tolerance of aluminum and manganese. *Plant Soil, 146*(1-2), 67-75. doi:10.1007/Bf00011997

Wolf, S., & Hofte, H. (2014). Growth Control: A Saga of Cell Walls, ROS, and Peptide Receptors. *Plant Cell, 26*(5), 1848-1856. doi:10.1105/tpc.114.125518

Yang, J., Qu, M., Fang, J., Shen, R. F., Fong, Y. M., Liu, J. Y., . . . Yu, M. (2016). Alkali-soluble pectin is the primary target of aluminum immobilization in root border cells of pea (Pisum sativum). *Frontiers in Plant Science, 7*, 1297. doi:10.3389/fpls.2016.01297

Table 1: The average of seedling root length for all study systems

Plant type	Stress conditions	n	Length (mm)
WT	Fe**0**Al**0**	19	25.0 ± 3.1
	Fe**0**Al**10**	18	27.6 ± 3.1
	Fe**10**Al**0**	17	26.8 ± 3.3
	Fe**10**Al**10**	19	13.4 ± 1.3
	Fe**0**Al**20**	26	26.8 ± 2.8
	Fe**20**Al**0**	24	25.1 ± 2.2
	Fe**10**Al**10**+P	27	25.0 ± 2.9
almt1	ALMT1_Fe**0**Al**0**	9	23.5 ± 2.1
	ALMT1_Fe**10**Al**10**	9	22.0 ± 4.9

Table 2: Elastic properties of WT seedling roots

	n	Z_1 (nm)	$\hat{E}$ (kPa)	r_S	k_T (10^{-3} N/m)
Fe**0**Al**0**	11	147 ± 55	53.9 ± 21.8	0.78 ± 0.05	4.30 ± 1.16
Fe**0**Al**0**_NoTransfer	5	161 ± 35	56.3 ± 20.1	0.79 ± 0.08	5.40 ± 1.45
Fe**0**Al**10**	10	150 ± 62	51.7 ± 30.9	0.74 ± 0.07	4.26 ± 1.73
Fe**10**Al**0**	14	153 ± 41	58.4 ± 50.4	0.75 ± 0.08	4.94 ± 3.51
Fe**10**Al**10**	11	127 ± 57	105 ± 52	0.81 ± 0.09	8.89 ± 8.63
Fe**0**Al**20**	15	136 ± 41	76.9 ± 39.4	0.81 ± 0.05	5.72 ± 2.18
Fe**20**Al**0**	11	119 ± 29	106 ± 42	0.83 ± 0.06	7.51 ± 3.77
Fe**10**Al**10**+P	8	162 ± 25	59.6 ± 27.6	0.81 ± 0.06	5.37 ± 1.97

Table 3: Elastic properties of *almt1* mutant seedling roots

	n	Z_1 (nm)	$\hat{E}$ (kPa)	r_S	k_T (10^{-3} N/m)
Fe**0**Al**0**	14	162 ± 79	63.5 ± 50.4	0.79 ± 0.08	4.6 ± 2.0
Fe**10**Al**10**	11	133 ± 28	58.3 ± 36.5	0.74 ± 0.08	4.8 ± 2.8

Figure legends

Figure 1: Phenotype and the box-and-whiskers plots of elastic parameters of WT seedling roots without metal stress. The whiskers represent minimal and maximal values, with the edge representing the first and third quartiles around the median, for each root system with stress condition specified. Fe**0**Al**0** indicates the nutrient solution for the system was not supplemented with Fe and Al. NoTransfer denotes seedlings that were not transferred from crystallography plates to Petri dishes, and elastic parameters were measured directly after being taken out of the growing plate. The control0 is referred to the overall results over both Fe**0**Al**0** and NoTransfer conditions. **A**) Snapshot of seedling roots, where length measurements were performed using the NeuronJ plugin of ImageJ. The purple color highlights the selected pixel used to calculate the root length. **B**) Effective Young's modulus (Ê in the kPa unit) is presented for the control system. **C**) The values of stiffness k_T in the N/m unit.

Figure 2: Box-and-whiskers plots of elastic parameters of WT seedling roots in the stress of 10 μM metal concentration. **A**) Average root lengths measured on day 6. **B**) Effective Young's modulus ($\hat{E}$) in the kPa unit. **C**) Stiffness measure, k_T, in the N/m unit.

Figure 3: Box-and-whiskers plots of elastic properties of WT seedling roots with 20 μM of metallic ions. For comparisons, the results from WT Fe**0**Al**0** and Fe**10**Al**10** are co-presented. **A**) Average root lengths measured on day 6. **B**) Effective Young's modulus ($\hat{E}$) in kPa. **C**) Stiffness k_T in N/m.

Figure 4: Box-and-whiskers plots of elastic properties of *almt1* mutant roots in comparison with WT (cf. **Fig**. **2**) in two stressed conditions, Fe**0**Al**0** and Fe**10**Al**10**. **A**) Average root lengths measured on day 6. **B**) Effective Young's modulus, $\hat{E}$, (in kPa). **C**) Presentation of k_T in the N/m unit

Figure 5: Model explaining the effects of Fe and Al on CW stiffening and root extension. Left panel shows a reconstituted picture of an Arabidopsis primary root tip; the square indicates part of the epidermis in the transition zone, where AFM measures were performed in this work. The top to bottom panels explain the phenomena that occur, depending on the Fe^{2+} and Al^{3+} content of the Pi-poor culture medium.

Top panel: the Fe^{2+} ions enter the apoplast of the cell wall (CW, in light gray background color), which subsequently can cross the plasma membrane (PM, in light tan color) through an unknown transporter (not presented here for clarity) and activates the STOP1-ALMT1 signaling (not shown), or accumulate into the apoplast in complex with small organic acids like malate (M). The ALMT1 transporter exports malate from the cytosol (CYT, light blue background) to the CW. The accumulation of Fe cations, possibly in the Fe^{3+} state (darker green on the bottom left) binds to pectins, thereby increasing CW stiffness without triggering the root extension arrest (REA).

Middle panel: the Al^{3+} ions enter the CW and activate the transcription of *ALMT1* (not shown) and the opening of ALMT1 transporter, thereby releasing malate in the apoplast. The accumulation of Al^{3+} leads to a modest increase of CW stiffness without REA.

Bottom panel: the combination of Fe^{2+} and Al^{3+} results in a large release of malate and a high accumulation of ROS-promoting iron-malate complexes in the CW. These ROS concomitantly greatly increase CW stiffness and strongly prevents root extension.

(M, malate; CW, cell wall; CYT, cytoplasm; PM, plasma membrane; REA, root extension arrest; -Pi, phosphate-poor medium; +Fe, adding Fe^{2+} in the medium; +Al, adding Al^{3+} in the medium)

Figure 1

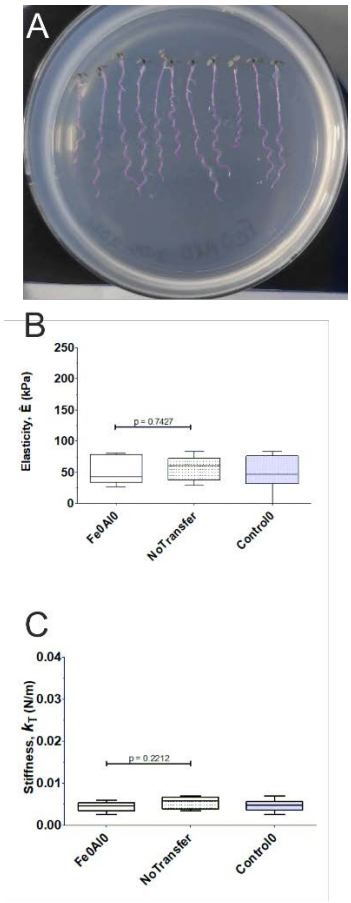

Figure 1: Phenotype and the box-and-whiskers plots of elastic parameters of WT seedling roots without metal stress. The whiskers represent minimal and maximal values, with the edge representing the first and third quartiles around the median, for each root system with stress condition specified. Fe**0**Al**0** indicates the nutrient solution for the system was not supplemented with Fe and Al. NoTransfer denotes seedlings that were not transferred from crystallography plates to Petri dishes, and elastic parameters were measured directly after being taken out of the growing plate. The control0 is referred to the overall results over both Fe**0**Al**0** and NoTransfer conditions. **A**) Snapshot of seedling roots, where length measurements were performed using the NeuronJ plugin of ImageJ. The purple color highlights the selected pixel used to calculate the root length. **B**) Effective Young's modulus (Ê in the kPa unit) is presented for the control system. **C**) The values of stiffness k_T in the N/m unit.

Figure 2

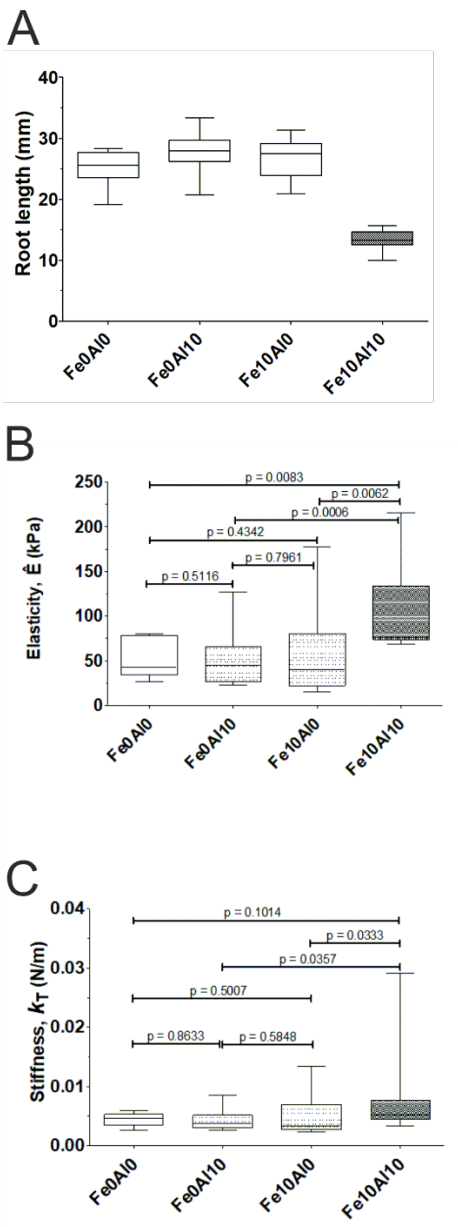

Figure 2: Box-and-whiskers plots of elastic parameters of WT seedling roots in the stress of 10 µM metal concentration. **A**) Average root lengths measured on day 6. **B**) Effective Young's modulus ($\hat{E}$) in the kPa unit. **C**) Stiffness measure, k_T, in the N/m unit.

Figure 3

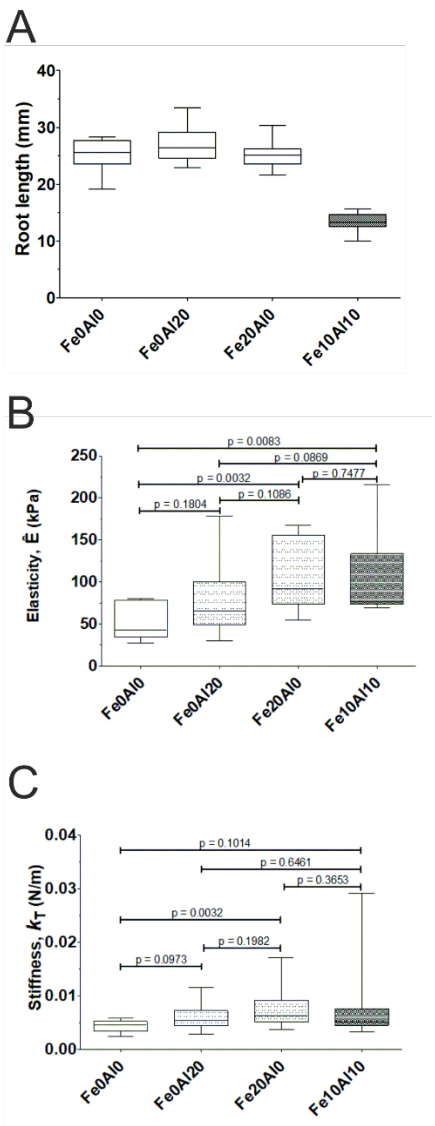

Figure 3: Box-and-whiskers plots of elastic properties of WT seedling roots with 20 µM of metallic ions. For comparisons, the results from WT Fe**0**Al**0** and Fe**10**Al**10** are co-presented. **A**) Average root lengths measured on day 6. **B**) Effective Young's modulus ($\hat{E}$) in kPa. **C**) Stiffness k_T in N/m.

Figure 4

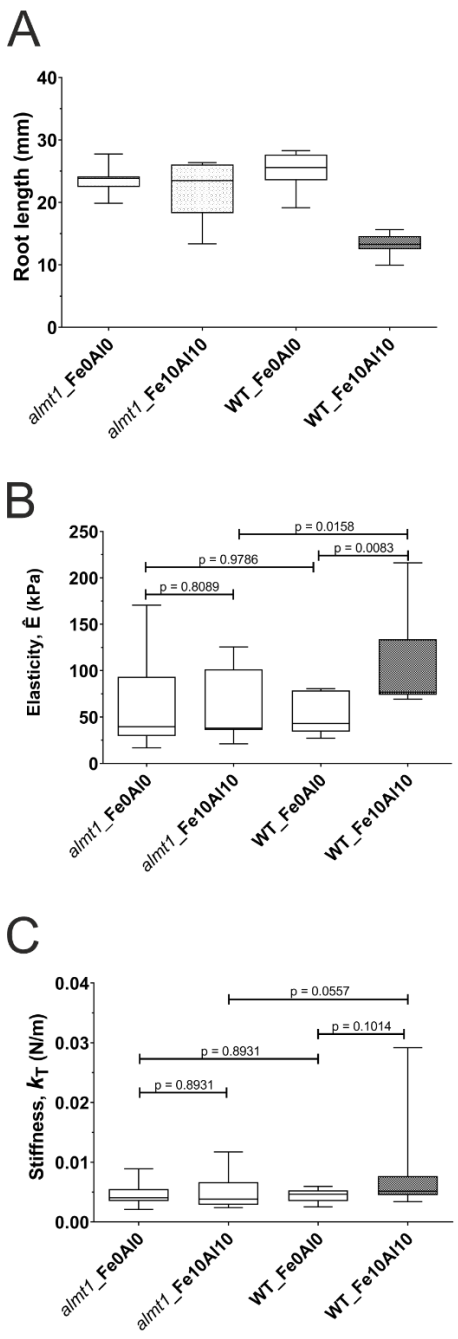

Figure 4: Box-and-whiskers plots of elastic properties of *almt1* mutant roots in comparison with WT (cf. **Fig**. **2**) in two stressed conditions, Fe**0**Al**0** and Fe**10**Al**10**. **A**) Average root lengths measured on day 6. **B**) Effective Young's modulus, $\hat{E}$, (in kPa). **C**) Presentation of k_T in the N/m unit

Figure 5

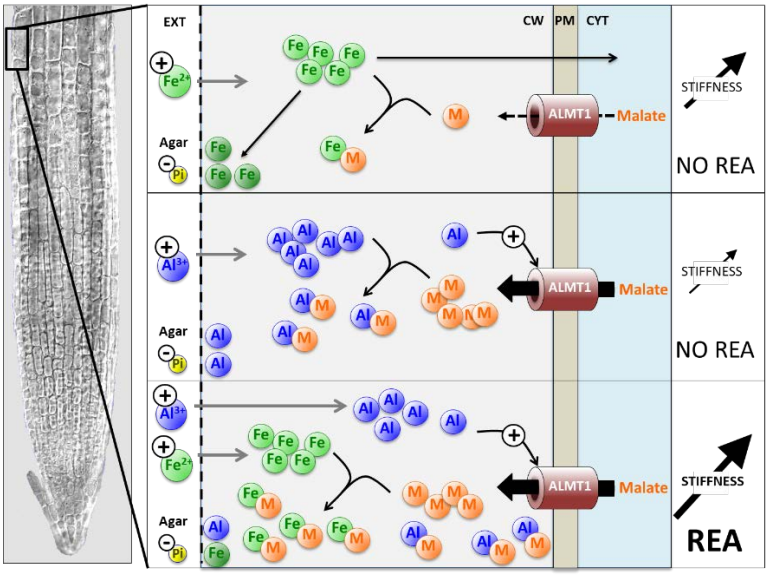

Figure 5: Model explaining the effects of Fe and Al on CW stiffening and root extension.

Left panel shows a reconstituted picture of an Arabidopsis primary root tip; the square indicates part of the epidermis in the transition zone, where AFM measures were performed in this work. The top to bottom panels explain the phenomena that occur, depending on the Fe^{2+} and Al^{3+} content of the Pi-poor culture medium.

Top panel: the Fe^{2+} ions enter the apoplast of the cell wall (CW, in light gray background color), which subsequently can cross the plasma membrane (PM, in light tan color) through an unknown transporter (not presented here for clarity) and activates the STOP1-ALMT1 signaling (not shown), or accumulate into the apoplast in complex with small organic acids like malate (M). The ALMT1 transporter exports malate from the cytosol (CYT, light blue background) to the CW. The accumulation of Fe cations, possibly in the Fe^{3+} state (darker green on the bottom left) binds to pectins, thereby increasing CW stiffness without triggering the root extension arrest (REA).

Middle panel: the Al^{3+} ions enter the CW and activate the transcription of *ALMT1* (not shown) and the opening of ALMT1 transporter, thereby releasing malate in the apoplast. The accumulation of Al^{3+} leads to a modest increase of CW stiffness without REA.

Bottom panel: the combination of Fe^{2+} and Al^{3+} results in a large release of malate and a high accumulation of ROS-promoting iron-malate complexes in the CW. These ROS concomitantly greatly increase CW stiffness and strongly prevents root extension.

(M, malate; CW, cell wall; CYT, cytoplasm; PM, plasma membrane; REA, root extension arrest; -Pi, phosphate-poor medium; +Fe, adding Fe^{2+} in the medium; +Al, adding Al^{3+} in the medium).

Supplementary data of

Correlation between plant cell wall stiffening and root extension arrest phenotype in the combined abiotic stress of Fe and Al

Harinderbir Kaur[1], Jean-Marie Teulon[1], Christian Godon[2], Thierry Desnos[2], Shu-wen W. Chen[1,3], Jean-Luc Pellequer[1]

1 Univ. Grenoble Alpes, CEA, CNRS, IBS, F-38000 Grenoble, France.

2 Aix Marseille Univ., CEA, CNRS, BIAM, F-13108 Saint Paul-Lez-Durance, Cadarache, France

3 Rue Cyprien Jullin, Vinay, 38470, France

Preparation of agar

The nutrient solution contained 0.47 mM $MgSO_4$, 2.1 mM NH_4NO_3, 1.89 mM KNO_3, 0.67 mM $CaCl_2$, 0.5 mM KI, 0.79 mM H_3BO_3, 10 mM $MnSO_4$, 5 mM $ZnSO_4$, 1 mM Na_2MoO_4, 0.1 mM $CuSO_4$ and 0.1 mM $CoCl_2$. The growth solution contains 20 ml/L of nutrient solution and 5 g/L sucrose. The agar medium contains 20 ml/L of nutrient solution with 5 g/L of sucrose and 8 g/L of agar powder (Sigma-Aldrich,A7921 Lot BCBZ7284). The elemental composition of the agar indicates a poor metal content (Mercier et al., 2021). The agar medium was buffered extemporaneously with 3.4 mM 2-(N-morpholino) ethanesulfonic acid (MES) for pH 5.5-5.8 range.

Plant sealing under NuSil

A thin layer of silicone, NuSil MED1-1356 (NuSil Technology LLC, Carpinteria, CA, USA), was spread on the glass slide as described elsewhere (Kaur, Godon, Teulon, Desnos, & Pellequer, 2023). Partial polymerization was allowed for a few seconds before the root is laid over the silicone. Then, several thin silicone bands were stretched using a syringe needle to fasten the root over all its length except the transition zone, which is located about 500 µm from the root apex (**Fig. S1**). To prevent drying, a droplet of the growth medium (without the agar powder) was deposited to cover the entire seedling. After AFM calibration, the mounted seedling was positioned under the AFM for data acquisition (**Fig. S1**).

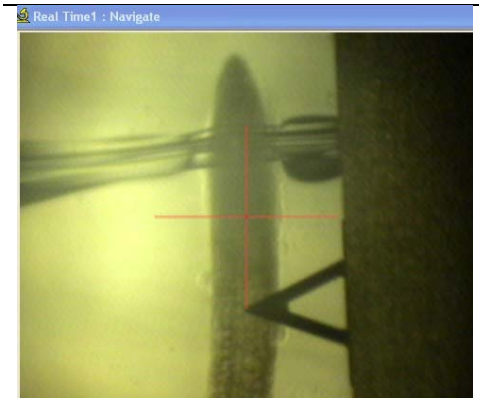

Figure S1: Photo of a root placed under the AFM cantilever taken by the AFM optical

camera. The triangular shape cantilever (200 µm long) was placed 500 µm away from the root tip in the transition zone where nanoindentation measurements proceeded. The band of NuSil glue was near the root tip. The thickness of the fastening band must be thin enough to avoid hindering the AFM cantilever, but thick enough to withstand the bending of the root tip.

Plant primary-root extension phenotype

Roots were transferred on day 4 in a Petri dish with stress agar medium, some of them were taken for nanoindentation experiments, while the remaining ones were labeled with a marker at their ends when the nanoindentation experiment finished. In the next day, a photo of the Petri dish is taken and archived with the experimental data. In **Fig. S2**, there is a clear demonstration of root extension arrest for the seedlings deposited in the agar medium with both Fe and Al, whereas the plant grew normally in the absence of metal stress.

On day 6, another photo was taken and saved as a GIF image format, which is compatible with the NeuronJ plugin (Meijering et al., 2004) of ImageJ software (Schneider, Rasband, & Eliceiri, 2012). NeuronJ was used to trace the whole root body until the base of the cotyledon to obtain the length (in mm) by an internal ImageJ calibration. The average of root lengths in different experimental conditions is shown in **Fig. S2E**.

a)


Fe0Al0 2.05.2022

b)

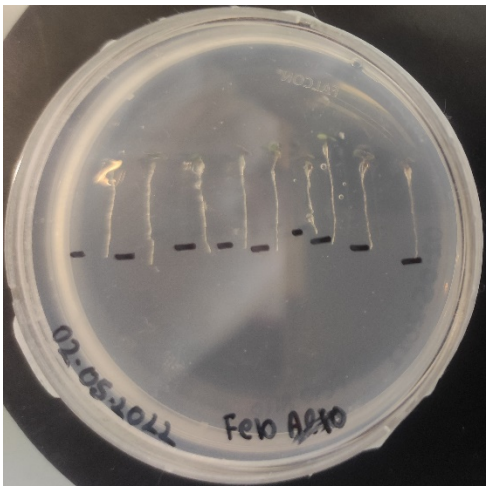
02.05.2022
Fe0 Al10

c)

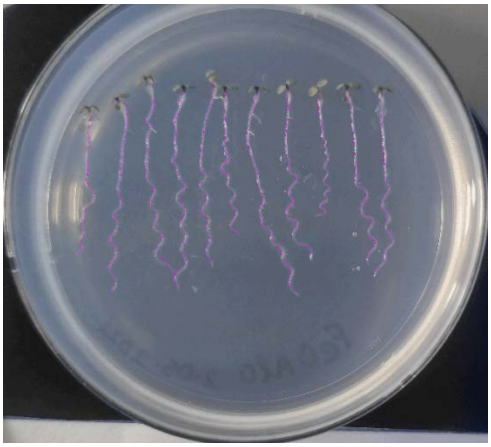

d)

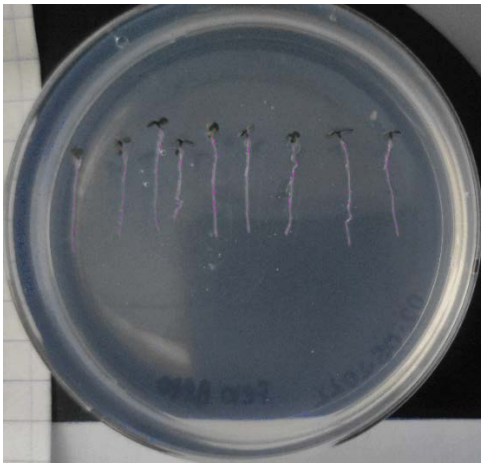

e)

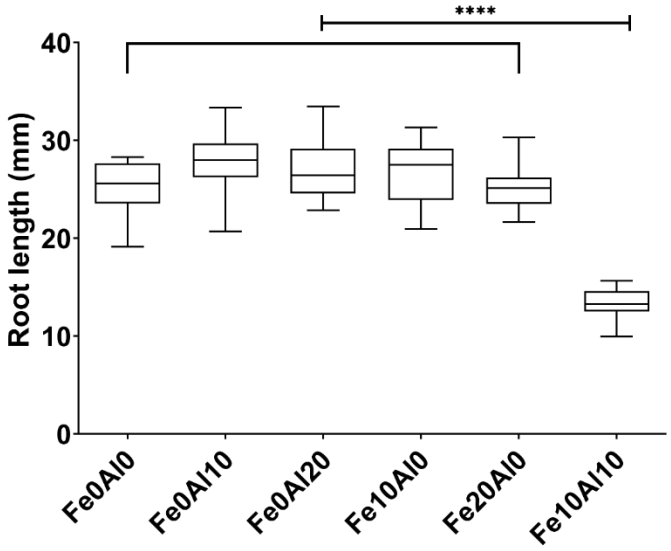
****
Root length (mm)
0
10
20
30
40
Fe0Al0
Fe0Al10
Fe0Al20
Fe10Al0
Fe20Al0
Fe10Al10

Figure S2: Root extension phenotypes. **a**) Control system: roots in the absence of metallic stress shows a normal root extension. **b**) Fe**10**Al**10** system: root extension arrest was observed by the lack of additional length measured below the marker. **c-d**) Snapshots for root length measurements using the NeuronJ plugin of ImageJ in the two systems of Fe**0**Al**0** and Fe**10**Al**10**. **e**) Box-and-whiskers plot of root lengths measured from all stress systems using NeuronJ expressed in mm units. Each box edge represents the first and third quartiles around the median. The whiskers represent the min and max values for each group. The nomenclature follows the metal stress conditions such as Fe**0**Al**0** for 0 µM of Fe^{2+} and 0 µM of Al^{3+}, and so others for different combinations of both metals. Among all the metal stress conditions, only Fe**10**Al**10** shows a total root extension arrest, observed two days after AFM indentation experiments, and the statistical significance is labeled with **** toward every single condition ($p < 0.0001$).

Data analysis by AtomicJ.

For comparison, force-distance curves were also analyzed using AtomicJ (Hermanowicz, Sarna, Burda, & Gabrys, 2014), a standard nanomechanical analysis software. Parameters are as follows: robust exhaustive contact estimator with the robust (LTA) fitting method based on the Sneddon model for pyramidal tips of 35° half-opening. The approach force curve was capped to 5 nN. We regularly observed curves showing a poor R^2 fitting; we removed all the fitting data with $R^2 < 0.9$ (**Fig. S3**). Elasticity parameters for each measured node were grouped into a single value, each node produces an arithmetic average over all its force curves (4 or 9 curves), and finally all the arithmetic mean values from nodes were geometrically averaged to get one value per plant. Then, the final averages over all the plants from individual experimental conditions at one time were calculated and clubbed together (**Fig. S4**) and **Table S1**.

(a)

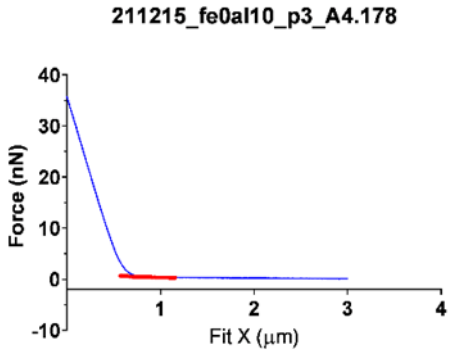

(b)

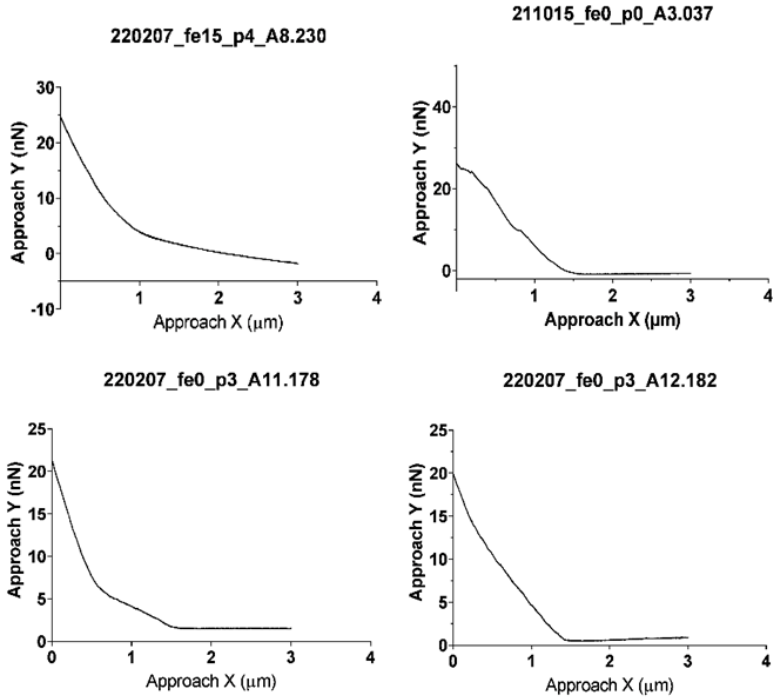

Figure S3: Representative force-distance curves excluded from AtomicJ analysis. **a**) A typical fine curve but with a poor fitting. Without optimizing the contact point manually, the curve was classified as a series of unqualified data and removed based on the value of R^2. From experiences, manually adjusting the location of the contact point for better curve fitting lacks an objective criterion for the user, leading to an unreliable outcome. Roughly, 5-10 curves were manually deleted per plant. If the number of deleted curves exceeded 30, then all the measurements from the plant were totally rejected and considered as a global poor data acquisition. **b**) Examples of excluded curves according to visual inspection. These curves visibly do not have a good approaching trace, therein several slopes or tilted baselines are present, indicating nanoindentation measurements were not properly acquired by AFM.

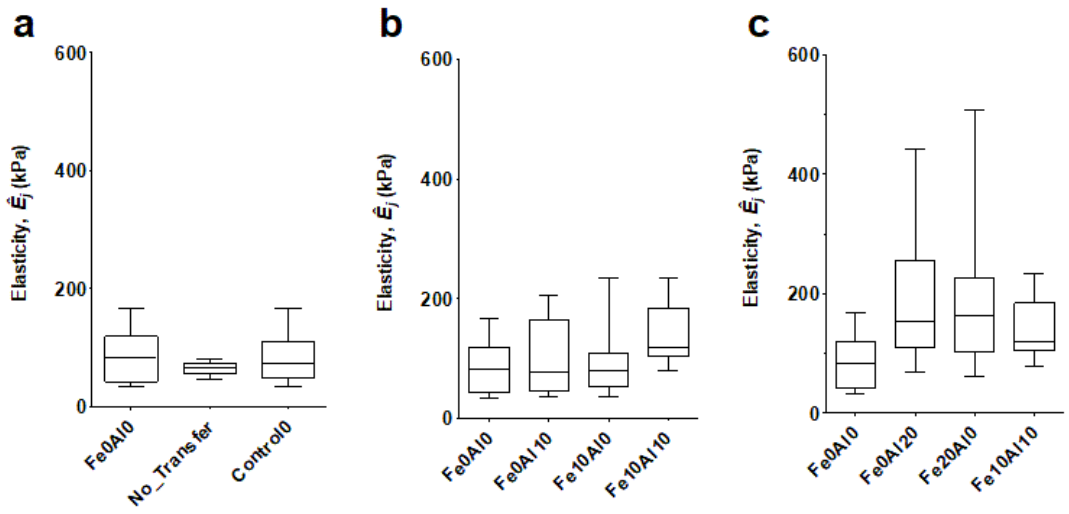

Figure S4: Box-and-whiskers plots of elastic properties of WT seedling roots analyzed by the pyramid model in the AtomicJ software. These plots **a-c** mirror those from **Figs**. **1-3** in the main text. The effective Young's modulus presented are in the kPa unit. See **Fig**. **S2** for numerical meanings of the box-and-whiskers plot. Fe**0**Al**0** indicates the nutrient solution without Fe and Al. No_Transfer denotes the seedlings lack the transfer step from crystallography plates to Petri dishes and elasticity nanoindentation experiments were performed directly after being taken out of the growing plates. Control0 is referred to the overall results from both Fe**0**Al**0** and No_Transfer conditions. In parallel, Fe**10**Al**10** contains 10 µM of Fe^{2+} and 10 µM of Al^{3+}, and the rest of other stress systems can be perceived from their names.

Performing the statistical analysis using the same strategy, the elasticity results from the AtomicJ-pyramid method are globally similar to that from the trimechanic-3PCS framework. They show that under stress of Fe**10**Al**10**, the stiffness of CWs is higher than the other stress conditions. Moreover, the increase of metal amount (up to 20 µM) also stiffens the root. The data values from AtomicJ use a Poisson's ratio of 0.5 which is different from the effective Young's modulus used in the trimechanic-3PCS framework (η = 0); consequently $\hat{E}_J$ values from AtomicJ are, by definition, systematically 25% higher than $\hat{E}$ from the trimechanic-3PCS.

Table S1: The values of the effective Young's modulus $\hat{E}_J$ by the AtomicJ-pyramid method

Stress Conditions	$\hat{E}_J$ (in kPa)
Fe**0**Al**0**	87.7±45.3
No_Transfer	64.9±11.5
Fe**0**Al**10**	99.9±65.9
Fe**10**Al**0**	94.8±56.7
Fe**10**Al**10**	141±57
Fe**20**Al**0**	192±123
Fe**0**Al**20**	186±112

Nanomechanical measurement in presence of phosphate

Below are the nanomechanical results of WT seedlings when measured in presence of 500 µM of inorganic phosphate (Pi) using the trimechanic theory (**Fig. S5**). No significant change in elasticity, stiffness, or root length, are observed with Fe**10**Al**10** in presence of phosphate.

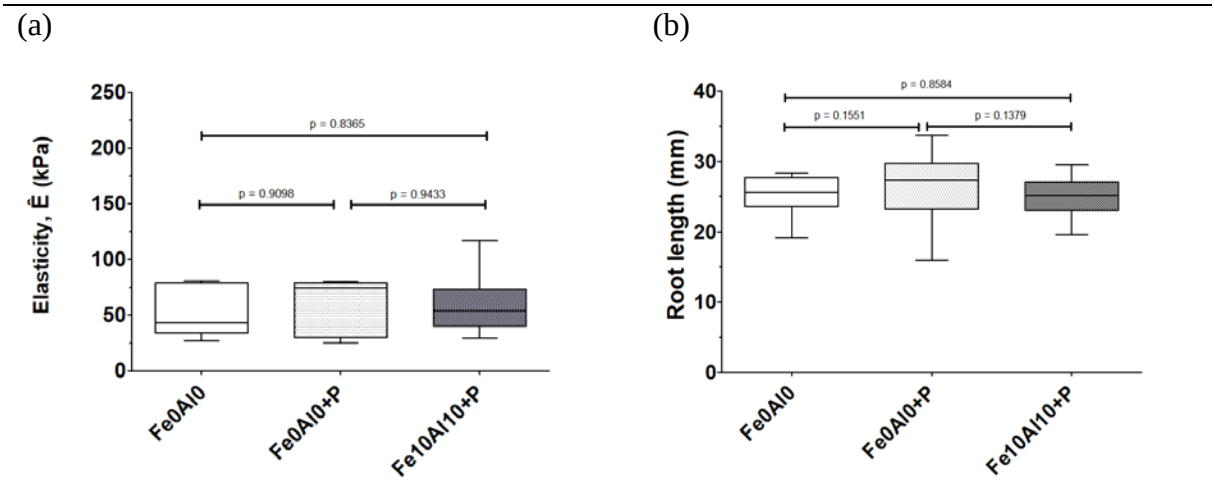

Figure S5: Box-and-whiskers plot of nanomechanical properties of WT seedling roots with the help of trimechanic theory. **a**) Elasticity values represented by the Young's modulus expressed in kPa units. **b**) The lengths of seedling roots (in mm). See **Fig**. **S2** for the use of Box-and-Whiskers plots. The nomenclature of stress conditions follows the description presented elsewhere in the paper, where "P" in Fe**0**Al**0**+P denotes 500 µM of inorganic

phosphate (Pi) added in. There were 5 and 8 plants for the conditions Fe**0**Al**0**+P and Fe**10**Al**10**+P, respectively?

References

Hermanowicz, P., Sarna, M., Burda, K., & Gabrys, H. (2014). AtomicJ: An open source software for analysis of force curves. *Review of Scientific Instruments, 85*(6), 063703. doi:10.1063/1.4881683

Kaur, H., Godon, C., Teulon, J.-M., Desnos, T., & Pellequer, J.-L. (2023). Preparation and deposition of plant roots for AFM nanomechanical measurements. In M. Lekka, D. Navajas, M. Radmacher, & A. Podestà (Eds.), *Mechanics of Cells and Tissues in Diseases* (Vol. 2, pp. 125-138). Berlin/Boston: Walter de Gruyter GmbH,.

Meijering, E., Jacob, M., Sarria, J. C., Steiner, P., Hirling, H., & Unser, M. (2004). Design and validation of a tool for neurite tracing and analysis in fluorescence microscopy images. *Cytometry A, 58*(2), 167-176. doi:10.1002/cyto.a.20022

Mercier, C., Roux, B., Have, M., Le Poder, L., Duong, N., David, P., . . . Desnos, T. (2021). Root responses to aluminium and iron stresses require the SIZ1 SUMO ligase to modulate the STOP1 transcription factor. *The Plant Journal, 108*(5), 1507-1521. doi:10.1111/tpj.15525

Schneider, C. A., Rasband, W. S., & Eliceiri, K. W. (2012). NIH Image to ImageJ: 25 years of image analysis. *Nature Methods, 9*(7), 671-675. doi:10.1038/nmeth.2089